ABSTRACT

Title of Dissertation: THE NORMAL-SUPERCONDUCTING PHASE TRANSITION OF YBCO IN ZERO MAGNETIC FIELD

Matthew C. Sullivan, Doctor of Philosophy, 2004

Dissertation directed by: Professor Christopher J. Lobb
Department of Physics

We have investigated the superconducting phase transition of $YBa_2Cu_3O_{7-\delta}$ in zero magnetic field. Most of our data were taken on thin films, grown by pulsed laser deposition. To ensure we are looking at intrinsic properties of the phase transition, we have endeavored to optimize our films, which we characterize using ac susceptibility, x-ray diffraction, and surface analysis using SEM and AFM.

We examined voltage vs. current measurements at temperatures close to the transition temperature, T_c. Previous work in our group by D. R. Strachan has suggested that the standard scaling analysis fails at low current, contrary to what is widely accepted, and finds evidence for the transition at higher currents. Using data at higher currents, we can unambiguously find T_c and the dynamic critical exponent z, and show $z = 2.1 \pm 0.15$, as expected for the three-dimensional XY model with diffusive dynamics.

At lower currents, we find significant finite-size effects, due to the thickness of the films. The crossover to two-dimensional behavior has been seen by other researchers

in thinner films ($d \leq 500$ Å), but were considered irrelevant for thicker films. We show that even in our thickest film ($d = 3200$ Å), the finite-size effects obscure the transition in zero field. This effect would also occur in a magnetic field, and may explain the wide range of critical exponents found in the literature.

Finally, we report on work with bulk single crystals. Our measurements of specific heat in crystals disagrees with the critical exponent $\nu > 1$ as is widely reported in the literature. We will also discuss voltage vs. current measurements on crystals.

THE NORMAL-SUPERCONDUCTING PHASE TRANSITION OF YBCO IN ZERO MAGNETIC FIELD

by

Matthew C. Sullivan

Dissertation submitted to the Faculty of the Graduate School of the
University of Maryland at College Park in partial fulfillment
of the requirements for the degree of
Doctor of Philosophy
2004

Advisory Committee:

Professor Christopher J. Lobb, Chairman
Professor Richard L. Greene
Professor J. Robert Anderson
Professor Ichiro Takeuchi
Professor Lourdes G. Salamanca-Riba

DEDICATION

To my grandfather,

who even now guides me in all I am and do.

ACKNOWLEDGEMENTS

Many people contributed directly and indirectly to this dissertation, without whose help I would never have finished, much less stayed in school.

First and foremost I must thank my advisor, Professor Christopher J. Lobb, for taking me on as a starry-eyed first year graduate student, letting me leave, and then luring me back to finish my Ph.D. He always supported me in what I wanted to do and the avenues of research I found more interesting, even if (and when) it was not what he had planned or intended. Chris Lobb has a deep knowledge and love of physics, especially experimental physics, and I have learned much about the pursuit of scientific knowledge from him.

Douglas Strachan taught me everything I know about this project, and I owe my experimental expertise as well as a good deal of healthy cynicism about other researchers' results to him. My work is founded on what he did and attempts to continue the high quality of his work.

A major reason I managed not to quit graduate school was the timely arrival of Thomas Frederiksen from Denmark. He only worked with me for six months, but Thomas did more work in six months than many graduate students do in years. His work complemented mine perfectly, and he was a pleasure to work with. I would also like to thank Richard Ott for a years' worth of hard work and ideas, and it has

been a pleasure to pass on some of my knowledge to Hua Xu and Su Li, and to see them carry this project forward. I would especially like to thank Monica Lilly for all the work she did – it was a challenge at times to find things for her to do, as every project I had she completed in half the time it would have taken me.

Other people in other labs helped me complete this dissertation. In particular, Josh Higgins, housemate and coworker, helped me both professionally and personally, and his support, ideas, and suggestions were instrumental in the completion of this dissertation. In Greene's lab, Amlan Biswas, Mumtaz Qazilbash, Chris Hill, and Rachel Headley all helped me when I came in to use their equipment. Yoram Dagan taught me a lot about YBCO when I thought I knew everything. Towards the end of my research, Hamza Balci took time from writing his own thesis to devote days helping me with my YBCO crystals, and to him I owe an especially deep debt of gratitude.

In my own lab, deep in the dungeon of the sub-basement, I have benefitted from the suggestions and discussions with many graduate students, in particular David Tobias, who suggested (albeit obliquely) the experiment that led to the major point of this thesis. I also thank Andrew Berkley for his suggestions and encyclopedic knowledge of physics, and Huizong Xu, Sudeep Dutta, Su-Young Lee, and Kao-Shuo Chang for their friendship.

Another member of the Center who supported me was Professor Richard Greene, who offered suggestions and help, especially when I attempted to measure heat capacity. I also received valuable technical assistance from Brian Straughn and Doug Bensen. Additionally, I received support from the staff of the Center's main office: Belta Pollard, Grace Sewlall, Cleopatra White, and Brian Barnaby.

My parents were also invaluable for their support and understanding. I thank my father for tricking me into attending graduate school in the first place and doing all the legwork, and my mother for ensuring that I survived the emotional ups and downs of the past six years.

Şi vreau să zic o mulţumire personală prietenei mele: Kelley Dunbar, te iubesc. Mă bucur, şi mă mir, că eşti cu mine.

TABLE OF CONTENTS

LIST OF TABLES

LIST OF FIGURES

Chapter 1

Introduction

Superconductivity was discovered by Heike Kammerlingh Onnes in 1911[1]. After liquifying helium in 1908, Kammerlingh Onnes used it to cool mercury and measured mercury's resistance at temperatures very close to absolute zero. He saw that at 4.2 K (-269 °C, or -450 °F), the resistance vanished abruptly. Below 4.2 K, an electrical current could pass without dissipation through the sample. This led him to declare that the mercury had "passed into a new state, which on account of its extraordinary electrical properties may be called the superconducting state."[1] The temperature at which this sudden change occurred he called the "critical temperature," and nowadays is given the symbol T_c.

Researchers realized that as the temperature of mercury falls below the critical temperature, the electrons which carry the current undergo a phase transition. Phase transitions occur whenever a material passes from one state into another, and as such are quite commonplace – as ordinary as water condensing on the bathroom mirror while someone showers, or ice melting in a glass on a hot day. Phase transitions have been studied for centuries, and today we inherit coherent theories regarding many different types of phase transitions. The theory which describes the superconducting phase transition is well established, however, the rub is that

[1]The information in the introduction on the history and basics of superconductivity was taken from Ref. [2] and Ref. [3]

experiments offer conflicting evidence regarding this phase transition.

In the end, understanding how electrons in superconductors undergo the transition from the "normal" state (at $T > T_c$, where they act like normal metals) to the superconducting state will help researchers understand the mechanism that creates superconductivity in the first place (we hope). At the very least, that is our goal.

1.1 Phase Transitions

Phase transitions, as we said, are everywhere.[2] They seem more rare than they actually are (water-steam and water-ice are the only two most people can recall) because typically we only see one state: the state that occurs at room temperature, atmospheric pressure, and in the Earth's ambient magnetic field. We know that if we cool water at atmospheric pressure, it becomes ice. We also know that if we apply pressure to ice, it will turn it back into water. Thus for water, there are actually two parameters which determine its state: temperature and pressure. For any given material and transition, there can be more than two parameters which affect its state.

For a given temperature T and pressure P, how does the material decide which phase to be in? Clearly, the material will choose the phase that has the lowest free energy at that T and P. A plot of the lowest-energy phase as a function of T and P is called a phase diagram. The phase diagram for water is shown in Fig. 1.1. The lines between the phases are called the coexistence curves, and show where two phases can exist simultaneously. Where all three phases can coexist is called the triple point, and is used to calibrate thermometers and pressure gauges.

Of course, water is not the only material which undergoes a phase transition. Other much-studied phase transitions include the magnetic transitions and the superconducting transition. For these two transitions, the important parameters are

[2] A nice overview of phase transitions can be found in Ref. [4].

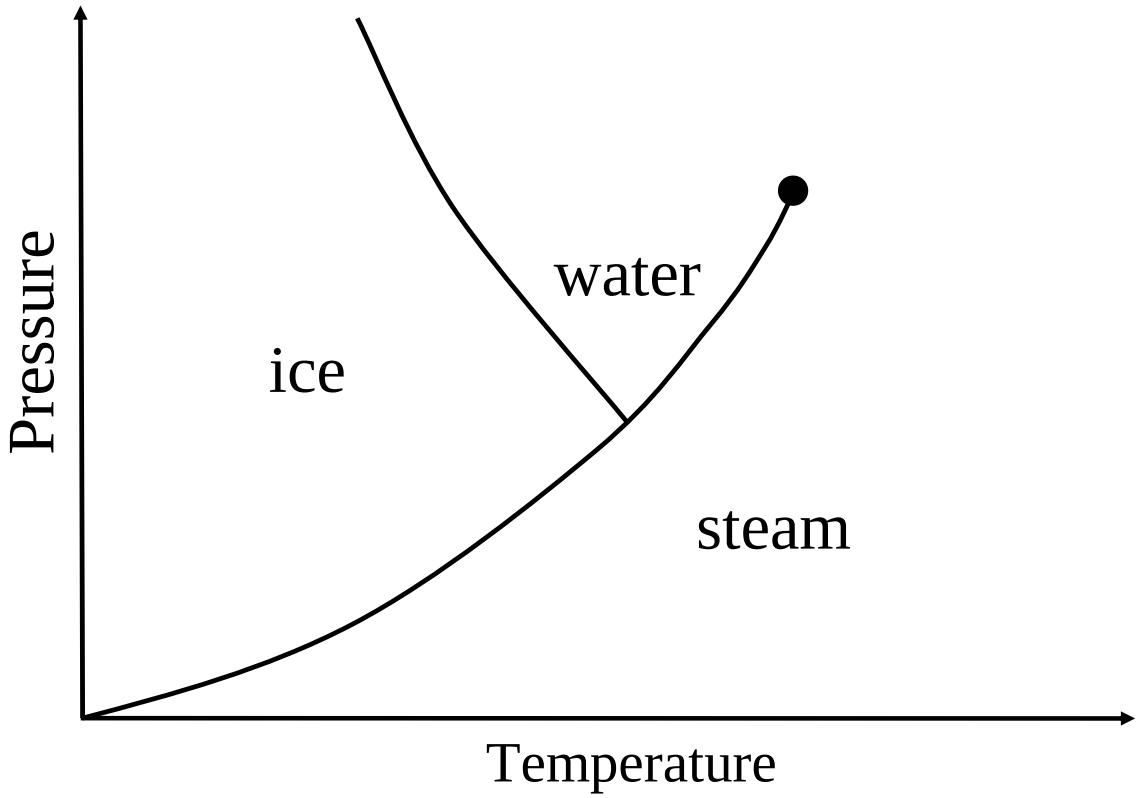

Figure 1.1: Phase diagram of water. Along any coexistence curve, the transition is first order. The water-ice coexistence curve continues up in pressure and does not end. The critical point at the end of the water-steam coexistence curve is second order.

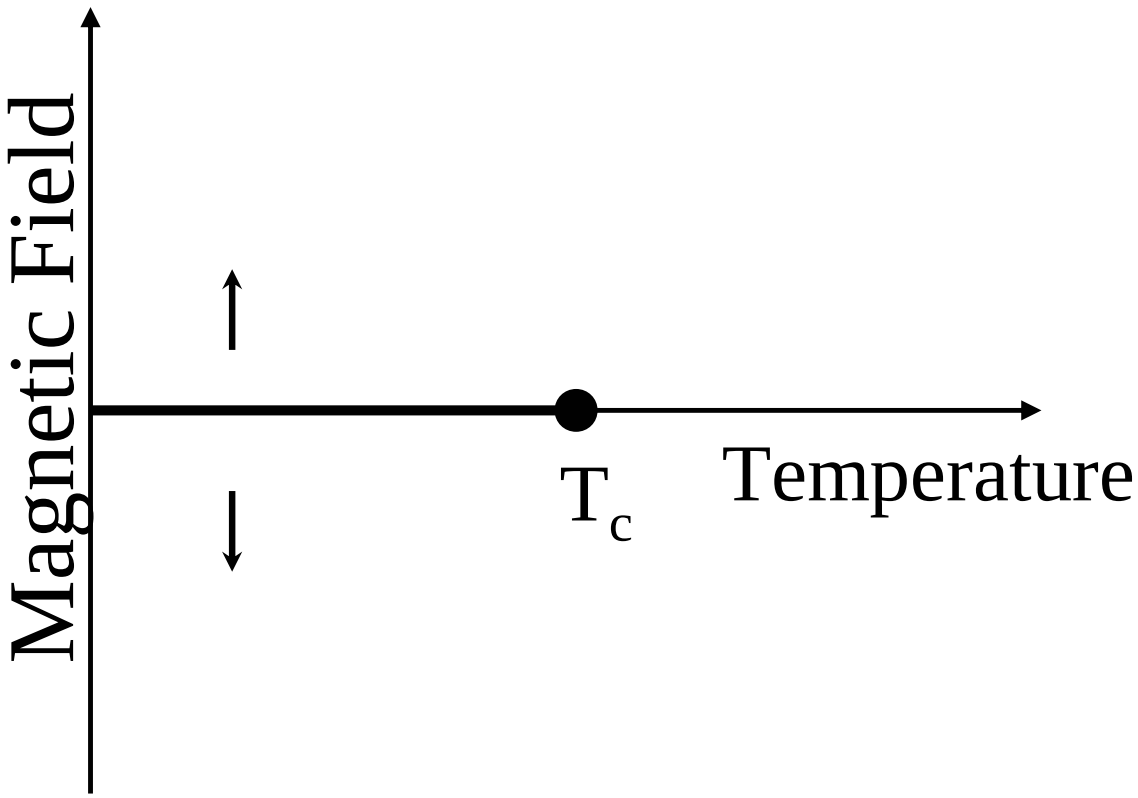

Figure 1.2: Phase diagram of a ferromagnet. For all temperatures a ferromagnet aligns spin-up for $H > 0$ or spin-down for $H < 0$. For zero magnetic field, the spin-up and spin-down coexist for $T < T_c$ (here T_c is called the Curie temperature). The co-existence curve at $H = 0$ is analogous to the water-steam curve, and at T_c and $H = 0$ there is a critical point, similar to the critical point in water.

not pressure and temperature, but magnetic field H and temperature T. The ferromagnetic phase transition is shown in Fig. 1.2. In a ferromagnet the two phases are spin-up and spin-down (referring to the alignment of the domains in the ferromagnet). The coexistence curve occurs at $H = 0$.

First-Order Transitions

A phase transition is equivalent to crossing a coexistence curve on the phase diagram. Heating water to become steam is the same as starting in water at a given

temperature and pressure, and increasing the temperature at a fixed pressure until it crosses over into steam; or, similarly, fixing the temperature and increasing the pressure can take you from steam to water.

How exactly does water become steam? Any high school science student will tell you that it takes heat to convert ice to water and water to steam. Thus, heating water to its boiling point is not enough, you must supply additional energy to turn it to steam. In a similar manner, energy must be added to a ferromagnet to flip all the domains. This additional energy is called the latent heat. At every point (except the one discussed below) along the coexistence curves in Figs. 1.1 and 1.2, there is a latent heat.

Any transition which requires a latent heat is called a first-order (or discontinuous) transition. This is because the first derivative of the free energy (and thus the entropy) is discontinuous. This also means that a physical property is discontinuous (density for water, magnetization for a ferromagnet).

Second-Order Transitions

There is a special point in the water and ferromagnet phase diagrams that is not a first-order transition. At high temperatures and pressures, the coexistence curve between water and vapor ends at the critical point, and beyond the critical point, you cannot distinguish between water and steam. In a ferromagnet, beyond the Curie temperature (also called T_c), you can vary the state continuously from spin-up to spin-down without going through a phase transition, thus $T = T_c$ and $H = 0$ is a critical point. At the critical point, there is no latent heat – it requires no energy for water to become steam and vice versa, in the ferromagnet, it requires no energy to flip a domain. Because it requires no additional energy to switch phases, small variations in energy will cause local changes in the phase of the material. These variations are called fluctuations, and have a limited size and lifetime. Fluctuations near a second-order transition are the focus of this dissertation.

A transition that has no latent heat is called a second-order (or continuous) transition. They are also sometimes called critical phase transitions. In these transitions, the first derivative of the free energy (and the entropy) is continuous.

For this work we are only interested in the second-order normal-superconducting transition. As Ref. [4] points out, this is not because second-order phase transitions are intrinsically more interesting than first-order transitions, but because there is a large body of theory accompanying second-order transitions.

1.2 Superconductivity

Much work has been done on superconductors since their discovery in 1911. Researchers soon discovered that not only high temperatures destroy superconductivity, but also high magnetic fields and high applied currents. These maximum fields and currents are called the critical field, H_c, and critical current density, J_c. In 1933, Meissner and Ochsenfeld discovered that in magnetic fields lower than H_c, superconductors expel any magnetic field inside the sample. This is now called the Meissner effect. One would expect a perfect conductor to conserve rather than expel magnetic flux, thus it is clear that superconductivity is more than just perfect conductivity.

Type I Superconductors

The first superconductors discovered (mercury, lead, tin) were all what today are called type I superconductors. Type I superconductors have a relatively simple phase diagram, shown in Fig. 1.3. The coexistence curve, akin to the coexistence curves in Figs. 1.1 and 1.2, defines the critical field for different temperatures, and so is also called $H_c(T)$. $H_c(T)$ separates the normal (resistive) state from the superconducting state (resistance $R = 0$). For type I, below $H_c(T)$ the material is always in the Meissner state, and always expels magnetic field.

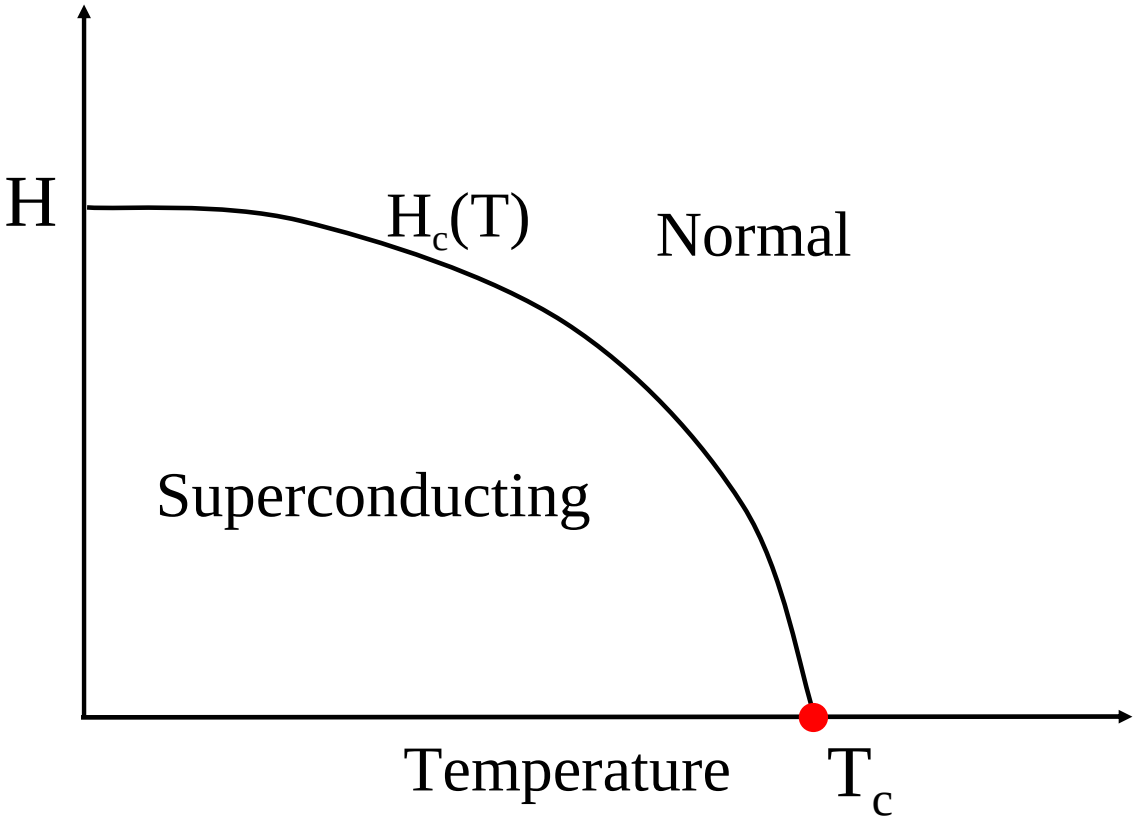

Figure 1.3: Phase diagram of a type I superconductor. The critical point at zero applied magnetic field is a second-order transition.

Just from these facts, we can see that this phase transition is first order. Imagine we are at some temperature in a field $H > H_c$. As the temperature is lowered below the critical temperature, the superconductor will expel all the magnetic field inside its bulk. To do so will require additional energy – a latent heat – and thus the transition is first order.

There is one point on the phase diagram where this argument fails, namely, at zero applied magnetic field. There is no magnetic field to expel, and the transition in zero field is second-order. This is a critical point, similar to the critical point at the end of the water-steam coexistence curve.

Type II Superconductors

If there is type I, there must also be (at least!) type II. Type II superconductors were discovered in 1930 and explained theoretically by Abrikosov in 1957. Type II superconductors have a somewhat more complicated and controversial phase diagram. The simplest model phase diagram is shown in Fig. 1.4.[3]

In the simplest theory of type II superconductors, there are two thermodynamic critical fields, H_{c1} and H_{c2}. Below H_{c1}, type II superconductors behave similarly to type I, that is, they are superconducting ($R = 0$) and expel magnetic fields. Above H_{c2}, they are in the normal state.

Between the two critical fields, type II superconductors differ significantly from type I. For $H_{c1} < H < H_{c2}$, magnetic flux will penetrate the superconductor, but only in small tubes, each tube carrying a quantized amount of magnetic flux. This amount is called the magnetic flux quantum, $\Phi_0 = h/2e = 2.07 \times 10^{-15}$ T-m^2. The electrons at the cores of these magnetic flux tubes are in the normal state, whereas the electrons outside the cores are in the superconducting state. The normal core is surrounded by a circulating supercurrent, which is why this phenomenon is called

[3]Basic information on type II superconductors is from Refs. [3] and [2].

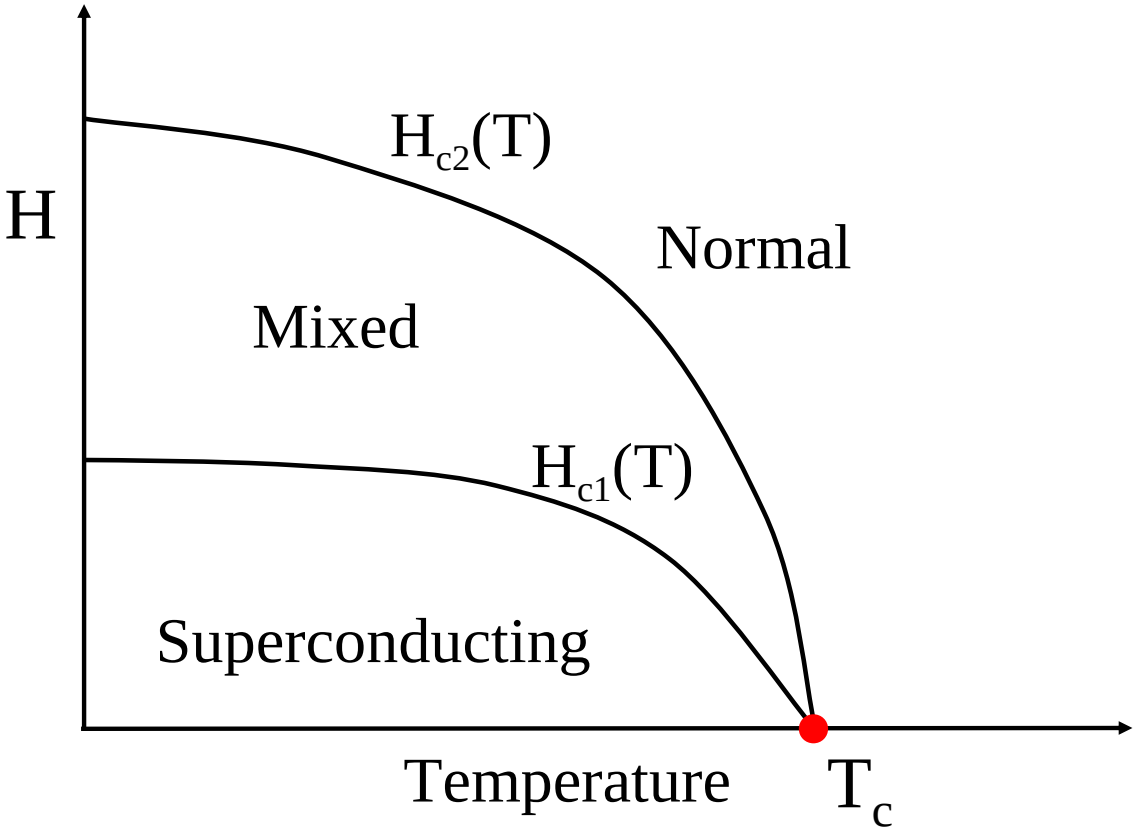

Figure 1.4: Phase diagram of a type II superconductor. Both $H_{c1}(T)$ and $H_{c2}(T)$ are second-order transitions. The critical point at zero applied magnetic field is also second-order.

a "vortex." When vortices enter a superconductor, it is called the "mixed" state. If a current is applied, the vortices will move due to the Lorentz force, and the normal electrons in the cores can dissipate energy. Thus in the strict sense of zero resistance, the mixed state is not superconducting. In practice, the vortices often become pinned on defects in the material and stop moving, thus the resistance, even in the mixed state, becomes immeasurably small. Note that even in a perfect defect-free superconductor, for $H_{c1} \leq H \leq H_{c2}$, the superconducting electrons are correlated over all length scales, so in this sense the system is superconducting. Regardless of the definition of superconductivity ($R = 0$ or long-range electronic coherence), there is a phase transition at $H_{c2}(T)$.

As you approach $H_{c2}(T)$ from below, the field inside the superconductor smoothly approaches the applied field, making $H_{c2}(T)$ a second-order transition. In typical type II superconductors, $H_{c1}(T)$ is also a second-order transition separating a superconducting ($R = 0$) from the non-superconducting mixed state.[4]

The Vortex-Glass Transition

In 1985, the highest T_c of any known superconductor was 23 K. In 1986, a new type of superconductor was discovered with $T_c = 35$ K[5], and shortly thereafter, a new material with $T_c = 92$ K (-181 °C, -294 °F)[6, 7, 8]. These new materials, called high-temperature superconductors, brought about a re-examination of all aspects of superconductivity. One of the many new ideas to result, due to Fisher, Fisher and Huse (FFH), was that Fig. 1.4 may be incorrect. FFH predicted the existence of a new phase in superconductors, called the "vortex-glass" phase[9, 10, 11].

FFH predicted that in the mixed state, the vortices in high-temperature superconductors would move about, causing dissipation, as in previous type II superconductors. However, at sufficiently low temperatures, the vortices should become

[4]See p. 157 of Ref. [3]. In low-κ systems, H_{c1} can be a first-order transition.

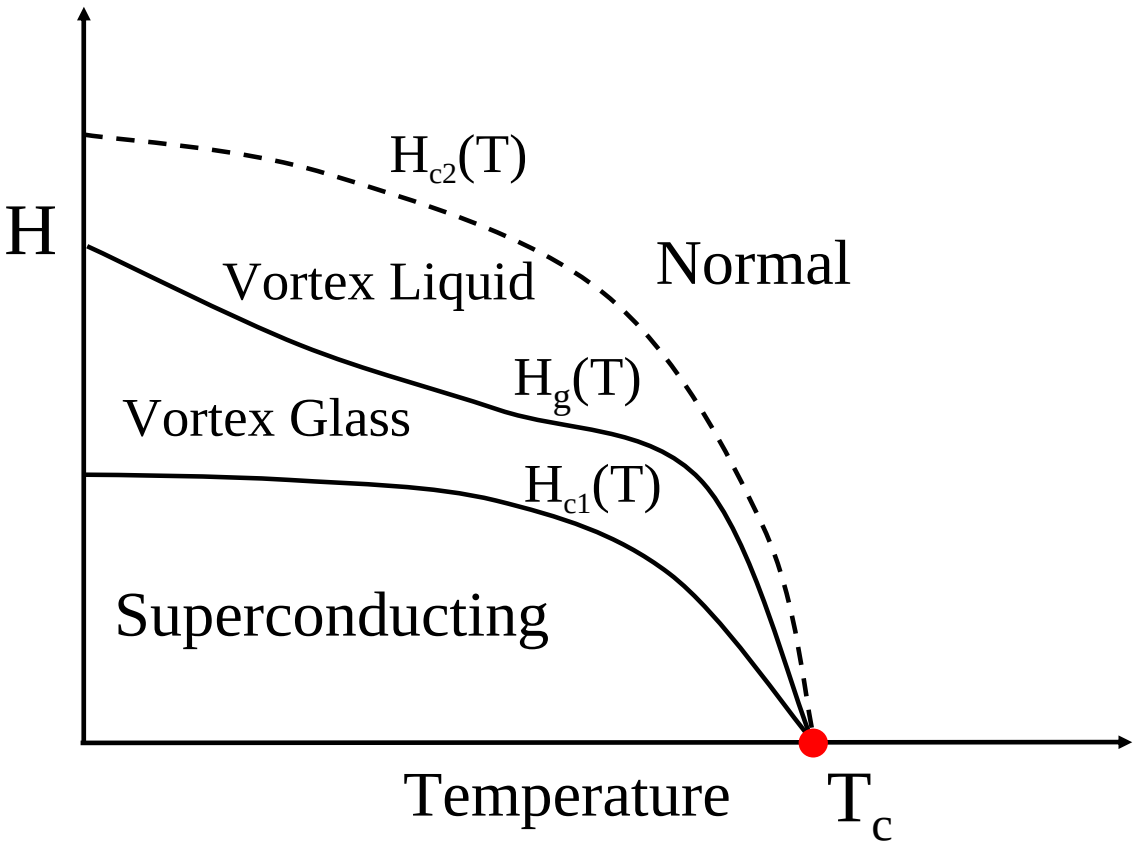

Figure 1.5: Phase diagram of a type II superconductor with the vortex-glass transition. The proposed phase transition within the mixed state ($H_g(T)$) is predicted to be second order. $H_{c2}(T)$ is no longer a phase transition, but rather a broad crossover from vortex-liquid to normal states. There is still a critical point at $H = 0$.

pinned, thus allowing a transition to a superconducting state at $H > H_{c1}$. This is called the "vortex-glass" phase, shown in Fig. 1.5. Raising the temperature will allow the vortices to begin to move and dissipate energy, thus H_{c2} is no longer a phase transition but a broad, continuous crossover to the normal state. Thus, the normal-superconducting transition is expected as the vortices freeze at $H_g(T)$. Because the vortices are not expelled from the superconductor and there is no energy cost to slow the dynamics of the vortices, the vortex-glass transition is expected to be second-order.

A consensus has emerged that the vortex-glass transition does, in fact, exist.

Recent work by D. R. Strachan[12] (in which I participated as a beginning graduate student) investigated this transition, and has called into question the validity of how researchers determine the parameters governing the transition – and indeed, whether the vortex-glass transition truly exists at all.

This dissertation does not directly investigate the vortex-glass transition. The controversy surrounding the vortex-glass transition motivated us to investigate the normal-superconducting transition in zero field, where the existence of a second-order phase transition is not in doubt and the critical parameters for the transition are well known theoretically (at least in principle). However, much of what we have learned about second-order phase transitions in the high temperature superconductors in zero field can be applied to the transition in field, and hopefully will help to clarify the controversial vortex-glass transition.

1.3 Outline

There is a large body of work regarding second-order phase transitions. Most researchers examine this superconducting transition in a magnetic field. However, we have chosen to reduce the complexity of the problem and study the phase transition in zero field where, as noted above, the transition is well understood. In particular, we are looking for the *critical exponents* ν and z. We expect $\nu \approx 0.67$ and $z \approx 2$.

To study this transition, we will use the high-temperature cuprate superconductor $YBa_2Cu_3O_{7-\delta}$ (YBCO). A discussion of the sample follows immediately in Ch. 2. In Ch. 3, we will describe the experimental apparatus and the measurement methods we use.

Ch. 4 serves as a brief introduction to the body of theory that underlies our work on phase transitions, and serves to inform our expectations as to how the data should look.

The main body of our work is presented in Ch. 5 in the form of voltage vs.

current ($I - V$) measurements on thin films of YBCO. In the analysis of the data, we find unexpected ohmic behavior at low currents in the critical regime, which (after much effort) we find are due to finite size effects.

Finally, in Ch. 6 we present specific heat data on large bulk single crystals of YBCO, as well as preliminary measurements of $I - V$ curves on crystals.

Chapter 2

Sample Preparation and Characterization

We use a high-temperature superconductor (HTSC) to investigate the properties of the normal-superconducting transition in zero field. There are many parameters in this experiment, but none more important than the sample. As a post-doc once advised us, "If the sample is garbage, then everything else is garbage."

In this chapter we will discuss the samples: How we fabricate them, pattern them, and put contacts on them in preparation for measurement.

2.1 The Material: YBCO

The material we have used for our experiments is $YBa_2Cu_3O_{7-\delta}$, also called Y-Ba-Cu-O, Y-123, or YBCO. YBCO, discovered in 1987, was the first superconductor known to have a T_c above the boiling point of nitrogen[6, 7, 8]. It has been extensively studied in the last seventeen years, and our work follows a large body of research.

YBCO is very different from low-temperature superconductors, which tend to be elements (e.g. mercury, tin) or simple compounds (e.g. NbN, Nb_3Ge). YBCO has a complicated structure, shown in Fig. 2.1. The unit cell of YBCO is orthorhombic, with $a \neq b \neq c$. However, it is often considered tetragonal, as $a \approx b$.[1] Also note

[1]Information on crystal structures and properties taken from Ref. [13].

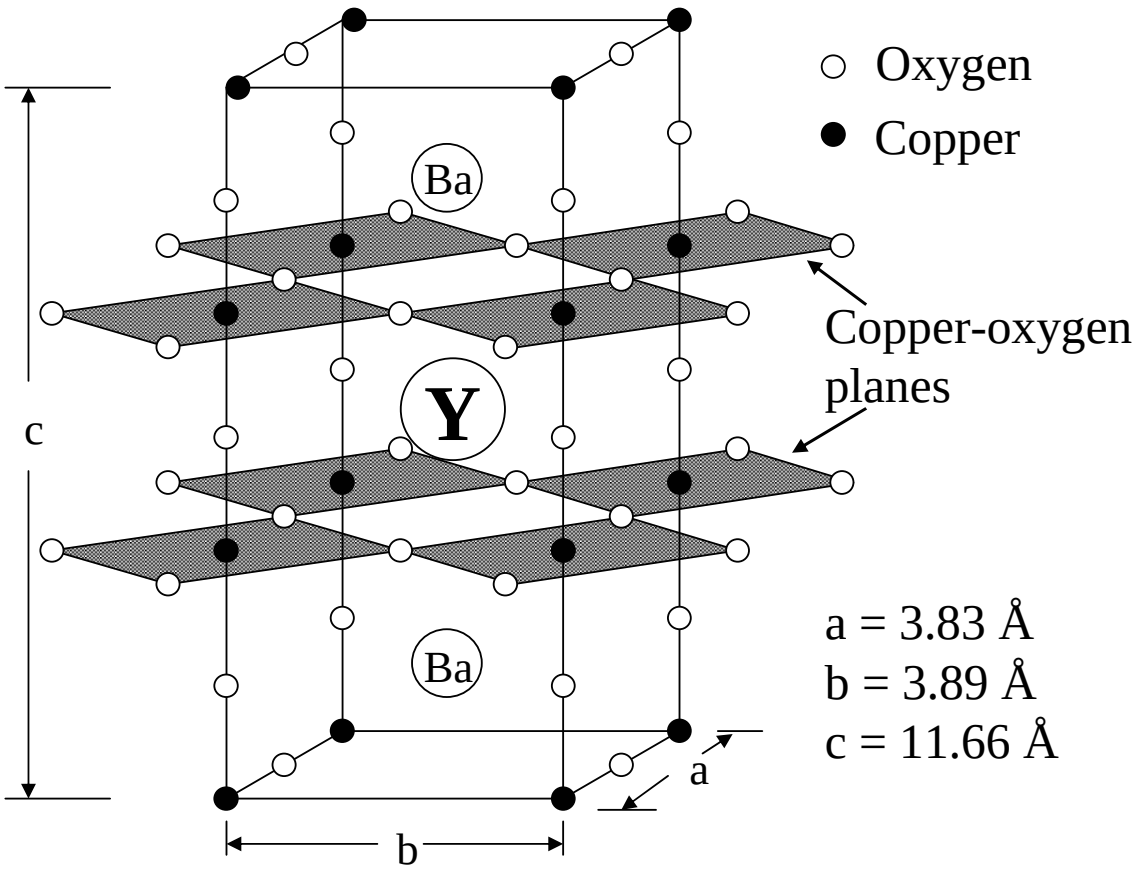

Figure 2.1: The unit cell of YBCO. The additional oxygen atoms indicate the copper-oxygen planes, where superconductivity occurs in this material. The lengths of the unit cell axes a, b, and c are given.

that $c \approx 3a \approx 3b$. This will be important for growth issues later.

YBCO and other HTSCs with similar acronyms (BSCCO, LSCO, PCCO, NCCO) all share an important feature emphasized in Fig. 2.1, namely, the copper-oxygen planes. Superconductivity occurs in these planes. For this reason, HTSCs tend to be naturally anisotropic. Compared to other HTSCs with $T_c \approx 90$ K, YBCO is the most isotropic – a lucky coincidence for us, as the simplest theories which describe the phase transition are for isotropic materials.

As the formula suggests, oxygen vacancies are important in YBCO. These oxygen vacancies determine the carrier concentration. Because oxygen typically supplies

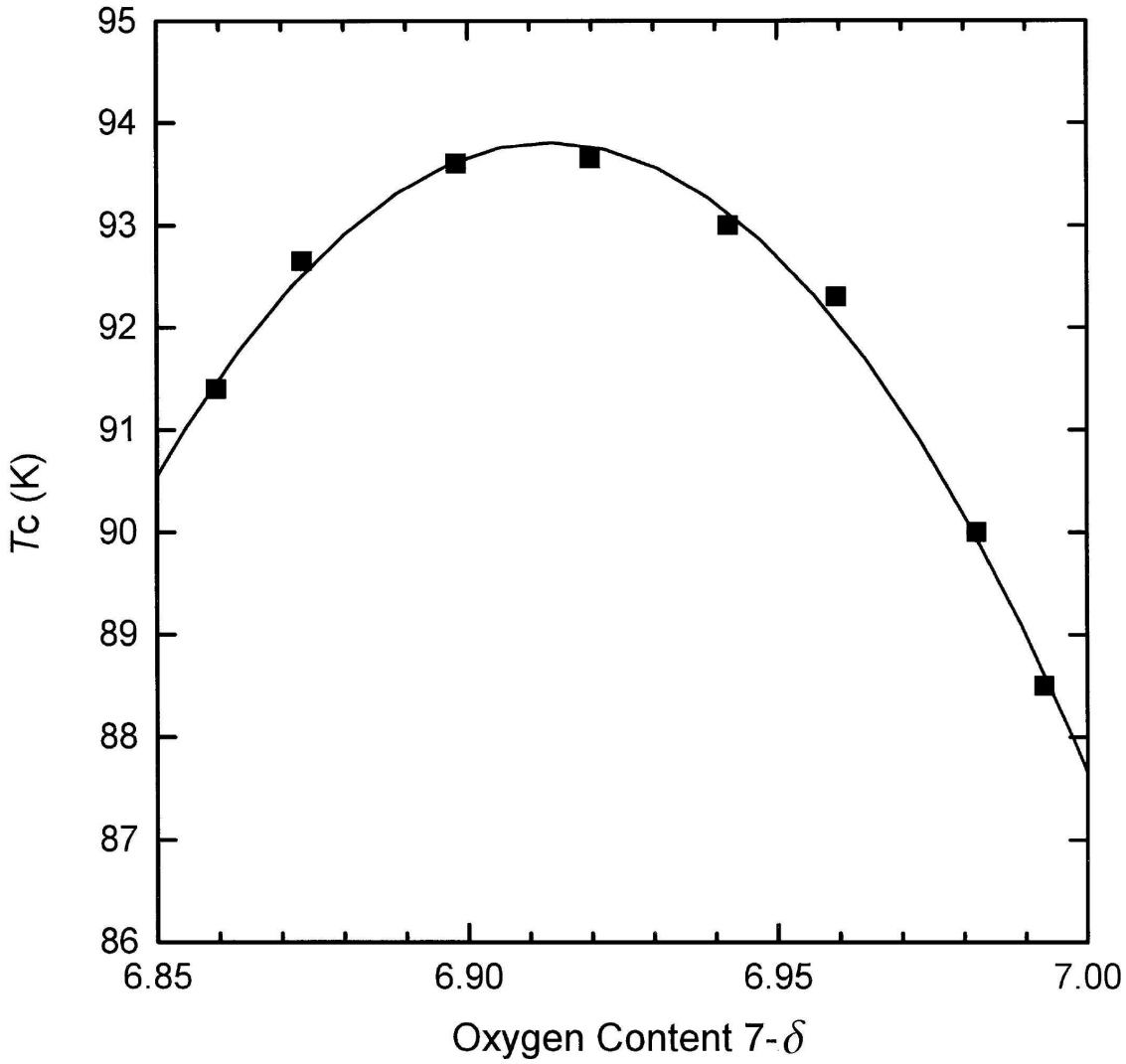

Figure 2.2: Transition temperature vs. doping in YBCO. Graph from Ref. [14].

electrons, oxygen vacancies supply holes, and so YBCO is a hole-doped superconductor. The transition temperature of YBCO varies strongly with oxygen doping, as shown in Fig. 2.2.

In this work we investigate optimally-doped YBCO. Because the T_c vs. doping curve has a maximum at optimal doping, small changes in doping do not affect T_c as much as they do for over- and under-doped samples. Thus, optimally-doped films are more homogenous in T_c and also in their superconducting properties. We do not directly measure oxygen content in our samples.

2.2 Films

The lion's share of our data was taken using thin films. The moniker "thin films" is a catch-all for any sample with a thickness $\lesssim 1\mu$m and (more importantly) grown on a substrate. Our films are typically 2000 Å thick.

In this section we will discuss how we grow our films, characterize and optimize their properties, pattern them, and prepare them for measurement.

2.2.1 Film Growth via Pulsed Laser Deposition

There are several preferred methods of film growth. The three most popular are sputtering, molecular beam epitaxy, and pulsed laser deposition (PLD) (also called laser ablation).[2] PLD is attractive because of ease of growth, fast turn-around time, and multi-functionality of the vacuum chamber. The schematic of the system is shown in Fig. 2.3.

In PLD, a high-energy laser pulse is fired into a vacuum chamber onto a stoichiometrically correct target. The energy density on the surface of the target is controlled by the aperture size and shape as well as the lens distance from the target. At high energies, the surface layers of the target will be ejected from the target in a plasma. This plasma combines with the oxygen in the chamber and is deposited on the heater and substrate. At sufficiently high temperatures (typically 850°C), an epitaxial crystalline film will grow on top of the substrate.

High-quality films are necessary in order to study the intrinsic properties of YBCO; copper-oxygen planes must align, oxygen content must be uniform, etc. There are a plethora of parameters which have to be carefully controlled in order to make high-quality films. These parameters include: aperture size, lens distance from the target, target distance from the heater, heater temperature, thermal link

[2]Generally, PLD is considered by many researchers to give the worst films in terms of sample homogeneity and surface roughness.

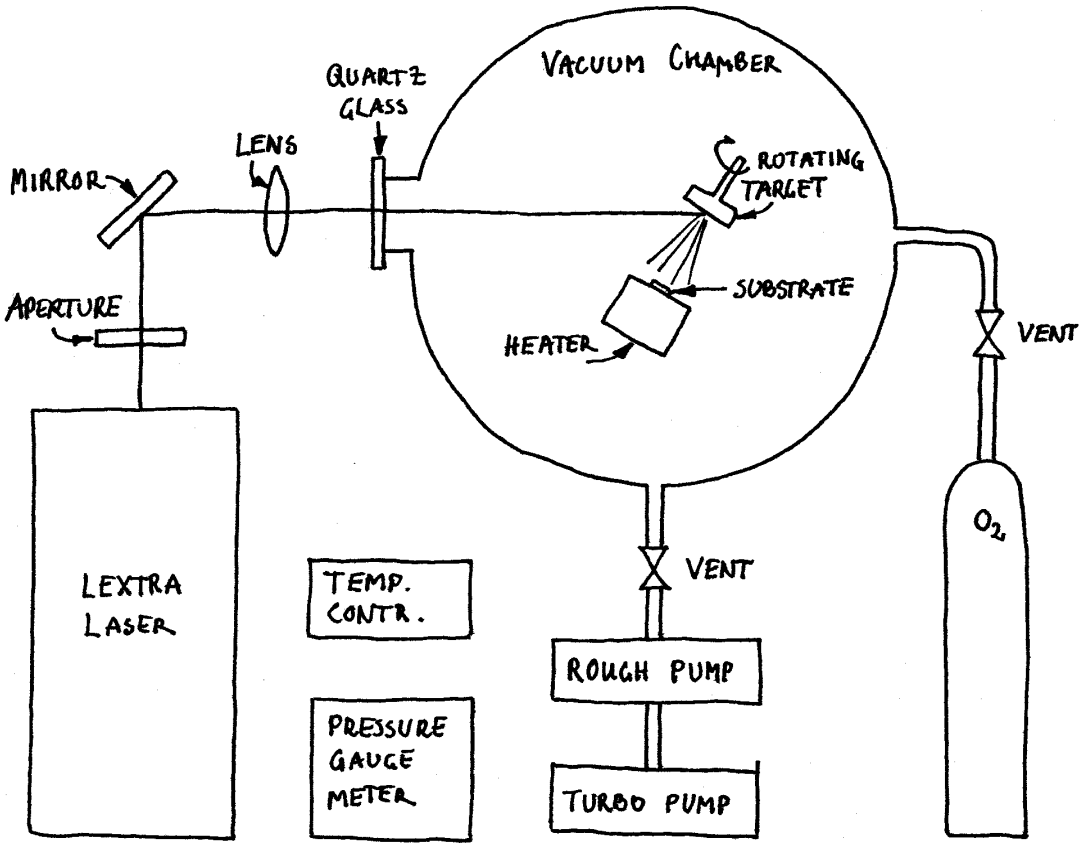

Figure 2.3: Schematic of PLD setup, showing laser, vacuum chamber, target and heater. Schematic drawn by T. Frederiksen.

from the substrate to the heater, laser energy, oxygen pressure during deposition, annealing conditions, and more. A table of parameters and a detailed drawing is given in Appendix A of Ref. [15]. We have chosen not to repeat such a table here because we have found the parameters to be dependant on the target, condition of the laser, condition of the heater, etc., and thus even the most detailed description of deposition conditions would not allow another user to make similar films. In general, our films were grown with an ultra-violet Kr-F laser ($\lambda = 248$ nm), at a heater temperature of $\approx 850°$C, in a 150 mTorr O_2 environment, with an energy density of ≈ 1 J/cm^2, and a pulse rate of 10 Hz. More important than the parameters, though, is the step-by-step description of PLD film growth given in Appendix A of Ref. [15], which does not need to be repeated here.

For YBCO films, most researchers use one of three different substrates: $LaAlO_3$ (LAO), $SrTiO_3$ (STO), or $NdGaO_3$ (NGO). LAO is less often used because it has significant warping when heating and cooling, which causes structural damage in the YBCO films. STO is popular because its lattice is better matched to YBCO than LAO, and it has no structural changes when heated and cooled. STO has a high dielectric constant (≈ 300), however, and thus is not ideal for high-frequency measurements. NGO has a small dielectric constant (≈ 20), and a smaller lattice mismatch to YBCO than STO, and is thus an ideal candidate for film growth. In practice, we found films on NGO difficult to grow, and because our measurements were at dc, most of our films were grown on STO.

2.2.2 Film Characterization

Once a proper substrate is chosen, growing a film of YBCO that superconducts is, by all standards, quite easy (some wags joke that all one needs do is rub the substrate on the target). Growing a *good* film is not so easy, and we have a set of tools to help us quantify the film's quality: x-ray diffraction, ac susceptibility measurements, and

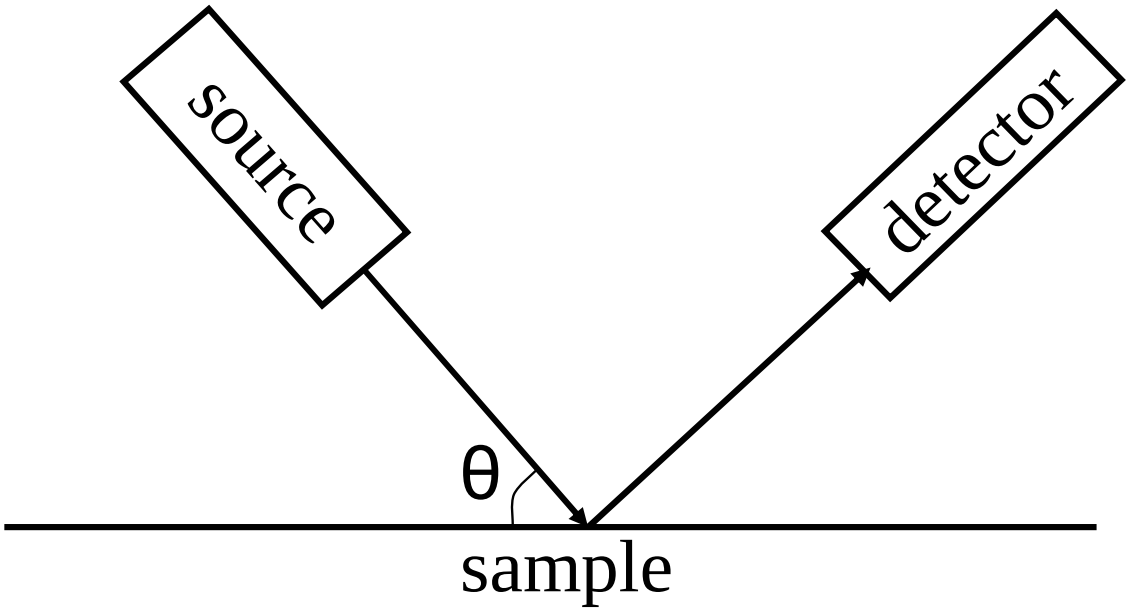

Figure 2.4: Schematic of the x-ray diffractometer. X-rays are reflected off the surface of the film, giving constructive interference at certain angles.

surface analysis using an atomic force microscope (AFM) and a scanning electron microscope (SEM).

X-ray diffraction

In order to make the best measurements on the superconducting state in YBCO, our films must have the c-axis perpendicular to the surface of the substrate. This will give us many large-area copper-oxygen planes stacked on top of each other, with current flowing parallel to the surface of the substrate. Such a film with the c-axis perpendicular to the substrate is called a c-axis film. One of the major problems we hope to avoid is a- and b-axis grains, which puts the copper-oxygen planes perpendicular to the direction of current flow, causing a non-uniform current density.

X-ray diffraction is the fastest and simplest method to look at the crystallinity of our films and to determine whether they are c-axis films. An x-ray diffractometer

shines x-rays of a certain frequency at our sample at a given angle θ, measured between the source and the sample, as sketched in Fig. 2.4. These x-rays reflect off the surface of the film and also off the lattice planes inside the film. Thus, at certain angles, when the extra distance travelled by the light reflected off planes inside the film equals an integer multiple of a wavelength, you will get constructive interference. The angles where constructive interference occurs will tell you the lattice spacings of your film.[3]

Data is usually plotted as counts (i.e. number of photons reaching the detector) vs. 2θ (this is a historical convention, from when the source was fixed, thus a rotation of the sample of amount θ required that the detector moved an amount 2θ). The x-rays are created when high-energy electrons strike a copper target, liberating electrons from the inner K-shell. As electrons fall from the outer shells to the inner shell, they create photons of two very similar wavelengths, $K_{\alpha 1} = 1.541$ Å and $K_{\alpha 2} = 1.5444$ Å.[4] Constructive interference shows up as large peaks about certain angles. From the position of the peaks and the wavelength of the incident photons, we can determine the lattice spacing that created that peak. A table of crystal orientations (using the Miller indices (hkl) in the reciprocal lattice of the crystallographic planes), expected lattice spacings, $2\theta_1$, and $2\theta_2$ values for YBCO, STO, and some common impurity phases are given in Table 2.1. The expected values for the lattice spacing d were taken from Ref. [16].

The x-ray diffraction pattern for a "good" sample is shown in Fig. 2.5. A separate measurement of the substrate and the aluminum base which holds the sample is necessary to insure that their peaks are not mistaken for impurities in the film. In Fig. 2.5, all of the peaks can be identified as c-axis YBCO, substrate, or peaks from the holder. The largest peaks are from the substrate, which is not surprising, considering the regular crystal structure of the substrate and the fact that it is

[3]A discussion of Bragg diffraction is given in Ref. [13].

[4]Here, "K" refers to the electronic K-shell, as opposed to "k", wave number.

YBCO	d (Å)	$2\theta_1$ (deg.)	$2\theta_2$ (deg.)	STO	d (Å)	$2\theta_1$ (deg.)	$2\theta_2$ (deg.)
002	5.83	15.19	15.22	100	3.94	22.55	22.61
003	3.89	22.86	22.92	200	1.97	46.06	46.18
004	2.92	30.65	30.72	300	1.31	71.82	72.03
005	2.33	38.58	38.68	110	2.79	32.08	32.16
006	1.94	46.70	46.83	220	1.39	67.25	67.44
007	1.67	55.09	55.24	111	2.27	39.60	39.70
008	1.46	63.81	63.99	CuO			
009	1.30	72.96	73.17	002	2.53	35.44	35.53
$00\overline{1}\overline{0}$	1.17	82.70	82.95	111	2.52	35.54	35.63
010	3.89	22.87	22.92	200	2.31	38.94	39.04
020	1.94	46.71	46.84	Cu_2O			
030	1.30	72.98	73.19	111	2.47	36.42	36.51
100	3.83	23.24	23.29	200	2.14	42.30	42.41
200	1.91	47.50	47.63	220	1.51	61.35	61.51
300	1.28	74.34	74.55	$BaCuO_2$			
013	2.75	32.56	32.64	600	3.05	29.28	29.35
103	2.73	32.83	32.91	530	3.14	28.44	28.51
110	2.73	32.83	32.91	611	2.97	30.10	30.17

Table 2.1: X-ray diffraction peaks for YBCO, STO, and common impurities, given that $K_{\alpha 1} = 1.541$ Å and $K_{\alpha 2} = 1.5444$ Å.

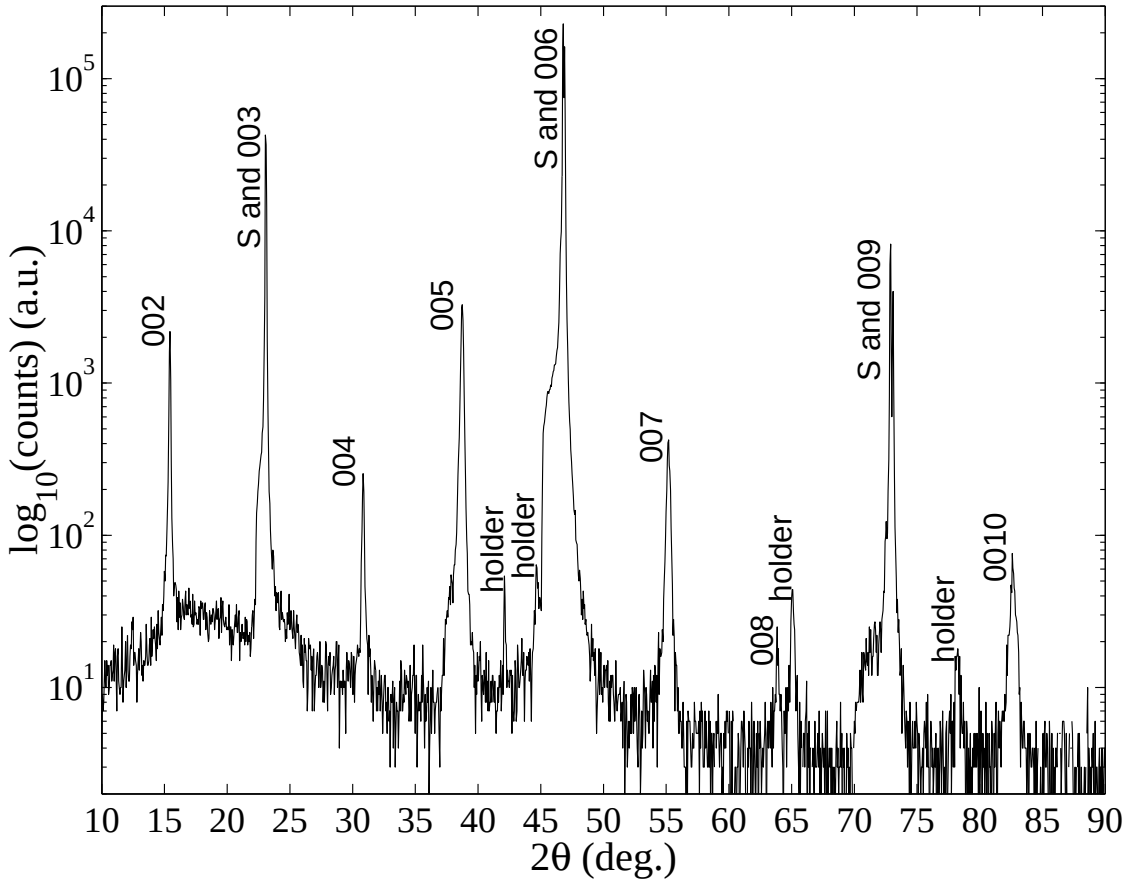

Figure 2.5: Typical x-ray diffraction pattern for a YBCO thin film (sample mcs89). All peaks are accounted for and indicate only c-axis YBCO, Al sample holder (holder), or substrate (S).

many times thicker (0.5 mm thick) than the superconducting film. In fact, because the signal from the substrate is so large, each substrate peak is actually split into two peaks from the two wavelengths $K_{\alpha 1}$ and $K_{\alpha 2}$. The signals from the sample peaks are too small to distinguish the two wavelengths. Impurities would show up as separate peaks in the graph (unless, of course, the occur at the same angles as the substrate or YBCO peaks).

One of the major problems in c-axis YBCO films that can be identified with an x-ray diffractometer is a-axis grain growth. Because $c \approx 3a$, a substrate matched to the a and b axes of YBCO can still grow a-axis films. In fact, very thick films

($d \gtrsim 4000$ Å) are a mixture of c- and a-axis. For this reason, most films tend to be in the range 1000 Å $< d <$ 4000 Å. Films thinner than this generally have a lower T_c, and thicker films have a-axis inclusions. But even films in this optimum thickness range can grow a-axis. In particular, during annealing, a-axis grains form as an outgrowth on the surface of the c-axis films[17]. Again, because $c \approx 3a$, these outgrowths form rectangular structures at 90° to one another on top of the c-axis structures.

A quick glance at Table 2.1 shows that the a-axis peaks occur unfortunately close to the substrate peaks, so small amounts of a-axis can be drowned out by the substrate. The a-axis peak easiest to see is the YBCO (200) peak, which appears just to the right of the STO (200) and YBCO (006) peaks. In Fig. 2.6, sample mcs89 (solid) shows no a-axis, whereas sample mcs141 (dashed) shows a small a-axis peak at $2\theta = 48°$.[5]

These a-axis outgrowths on the surface of the films can be seen using an atomic force microscope (AFM), but because the c- and a-axes have very different conductivities, a-axis outgrowths on the surface can be seen more readily using a scanning electron microscope (SEM). SEM pictures of the surfaces of the same films from Fig. 2.6 are shown in Fig. 2.7. The a-axis growths on mcs141 in Fig. 2.7(a) are the rectangular structures at 90° to one another. In these rectangular structures, the c-axis points parallel to the long side of the rectangle. Away from the rectangular structures, the c-axis points out of the paper. These structures are absent from mcs89 (Fig. 2.7(b)), as we expect from the x-ray data.

[5]The peaks do not occur at exactly the values predicted in Table 2.1. The diffractometer has a slight offset which changes as a function of θ, and our lattice spacings never match exactly those found in references.

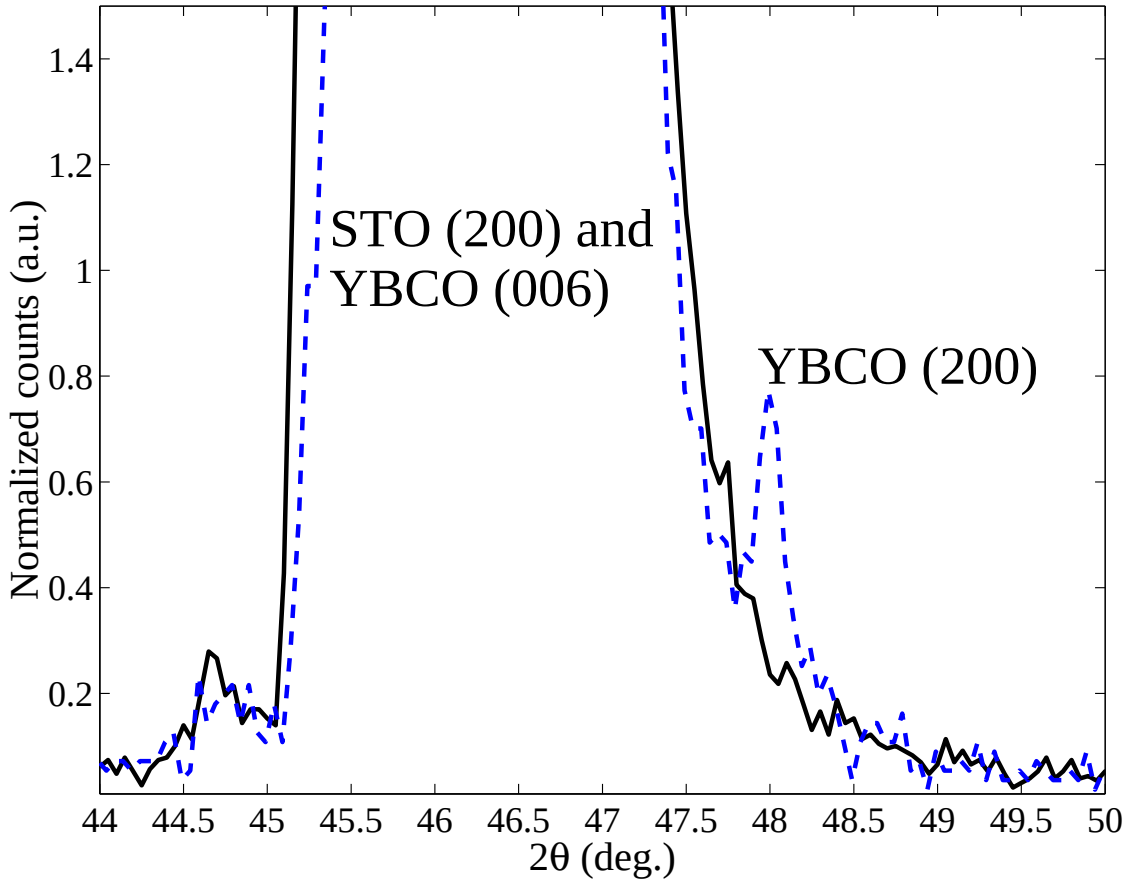

Figure 2.6: X-ray diffraction pattern for mcs89 (solid) and mcs141 (dashed). The large peak is STO (200) and YBCO (006). At $2\theta = 48°$, mcs141 has a small a-axis peak (YBCO (200)).

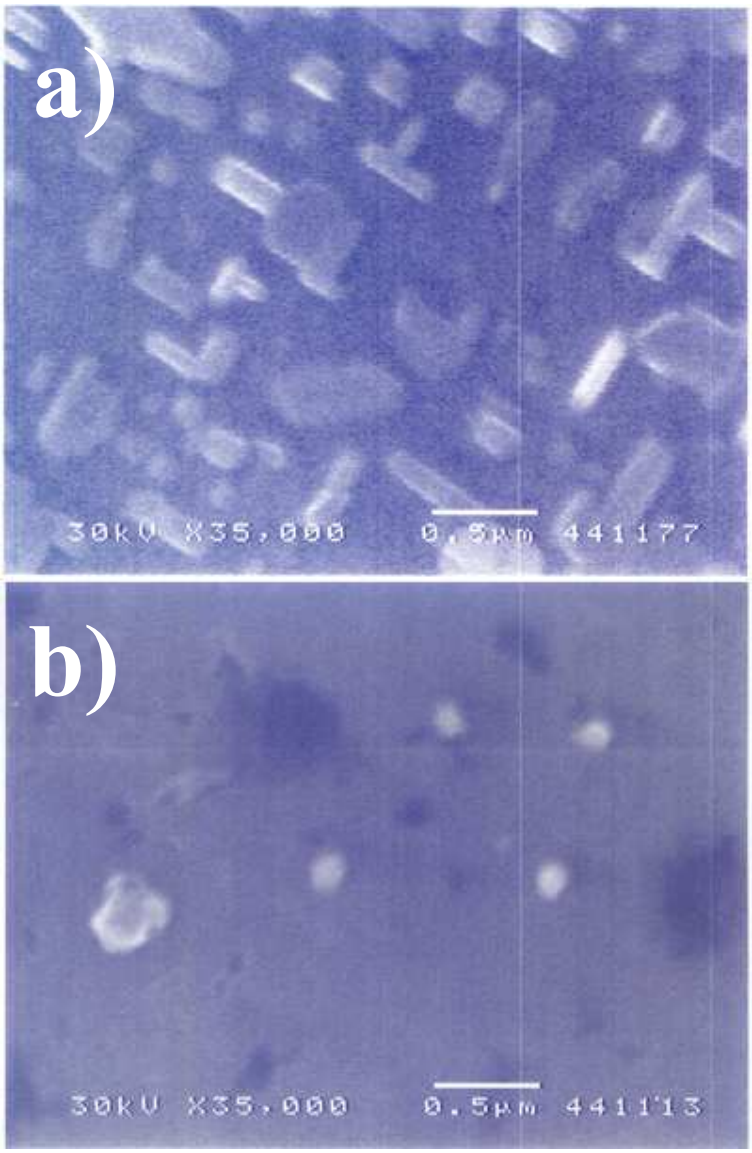

Figure 2.7: SEM images for a) mcs141, and b) mcs89. The a-axis growths are clearly identifiable on mcs141 as rectangles at 90° to one another. These structures are absent from mcs89. Films imaged by M. Lilly and D. Tobias.

ac susceptibility

X-ray diffraction is an excellent tool which allows us to determine the crystal structure of our films (and whether they are crystalline at all!). However, as mentioned in Sec. 2.1, YBCO is very sensitive to oxygen content, which the x-ray diffractometer cannot detect. To determine inhomogeneities in T_c, we use an ac susceptibility probe.

With ac susceptibility, the sample is placed in-between two coils. A small ac signal (typically 200 kHz) is applied to one coil. On the other side of the film, a voltage is created in the pickup coil via electromagnetic induction. The schematic is shown in Fig. 2.8. We use a lock-in amplifier to detect the signal at the pickup coil.

One of the unique properties of superconductors is that, below T_c, they expel magnetic field. Thus, as the temperature of the film goes below T_c, the amount of magnetic flux reaching the pickup coil will be reduced, and the voltage induced at the pickup coil will also be reduced. Because the flux flows through the bulk of the film, ac susceptibility is a good test of the film's homogeneity.

The signal measured from ac susceptibility has both real and imaginary parts. The real part always decreases going down through the transition, as the flux through the film decreases. The imaginary part shows a pronounced peak at the transition. From the imaginary part, we determine T_c as the maximum of the peak, and ΔT_c as the full-width at half maximum. For the best samples, T_c should be large and ΔT_c small. A good sample (mcs146) is shown in Fig. 2.9. In Fig. 2.9, the peak in the imaginary part (circles) gives $T_c \approx 90.4$ K, and the width gives $\Delta T_c \approx 0.2$ K.

Susceptibility measurements allow us to identify several common problems in films. In Fig. 2.10, we show four different ac susceptibility measurements. Fig. 2.10(a) is the same as Fig. 2.9, and is one of our best films. Fig. 2.10(b) shows

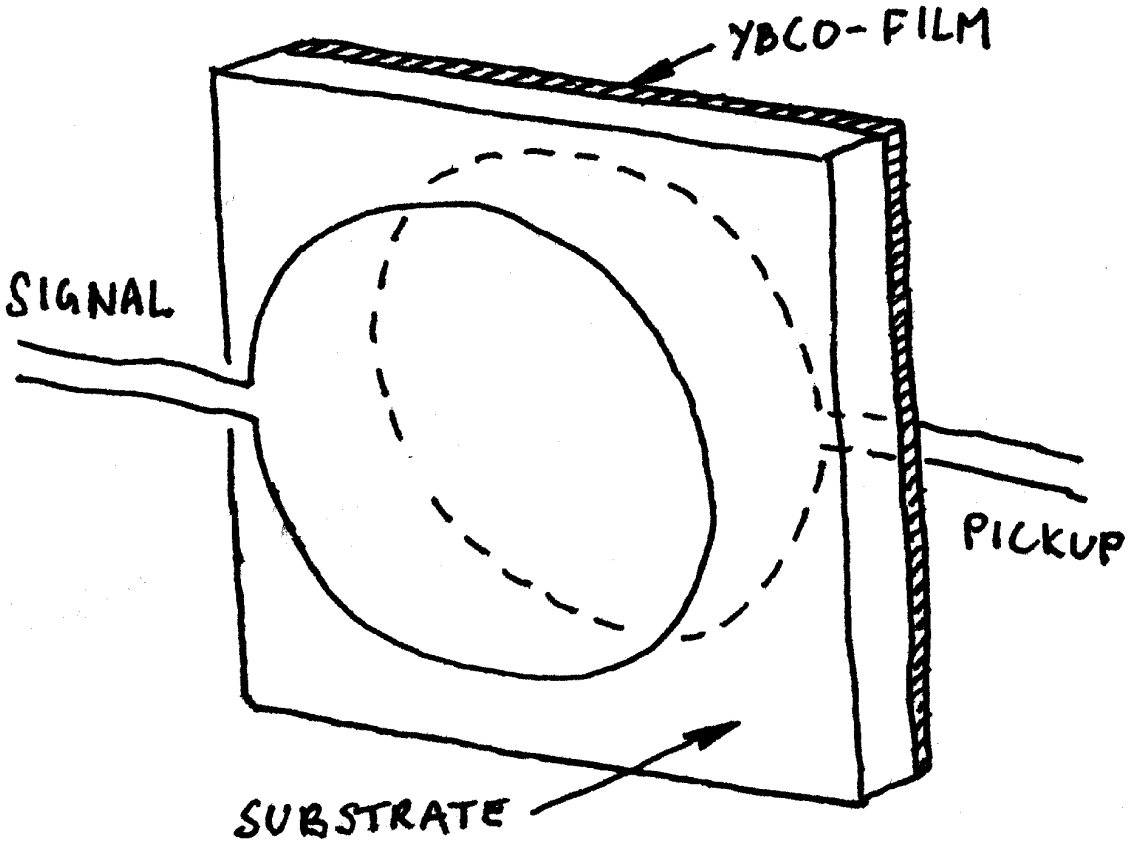

Figure 2.8: Schematic of ac susceptibility measurement. An ac signal is applied and picked up on the other side of the film. As the film becomes superconducting, it screens the magnetic field and changes the mutual inductance of the coils, reducing the signal at the pickup. Schematic drawn by T. Frederiksen.

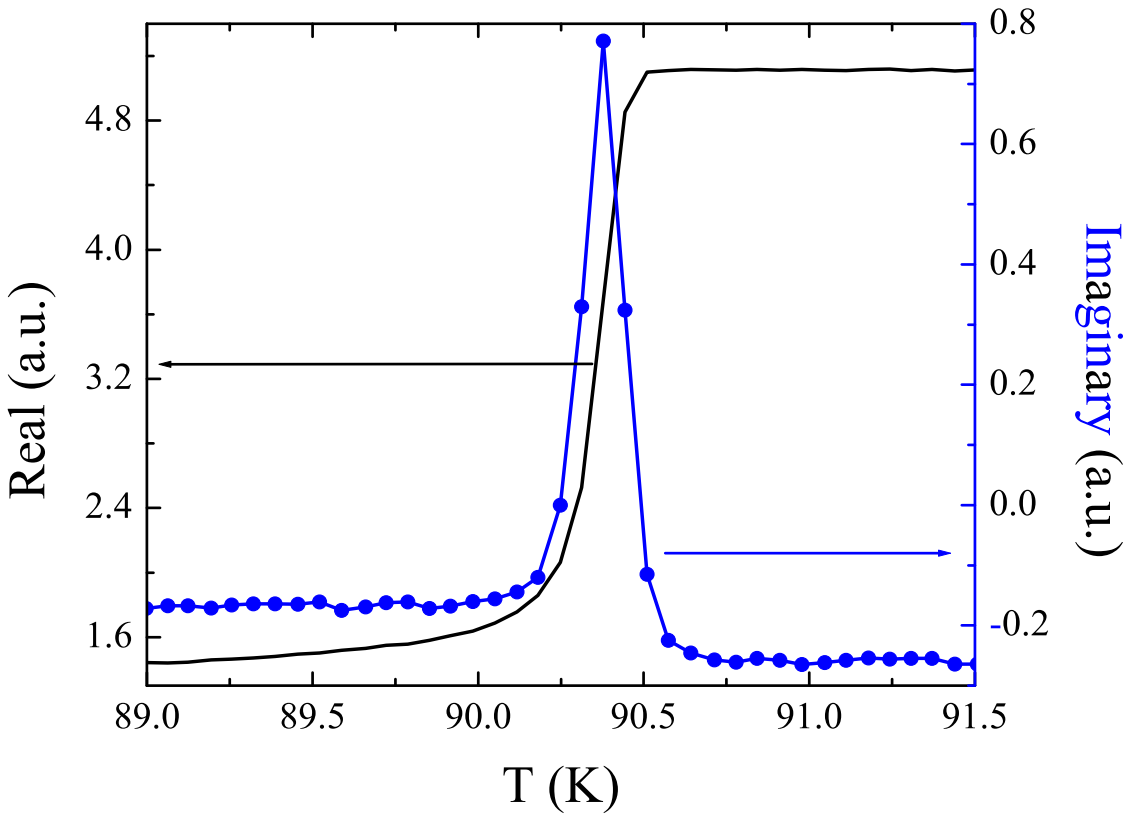

Figure 2.9: ac susceptibility of a good sample (mcs146), both real (solid) and imaginary (with circles) parts. Here, $T_c \approx 90.4$ K and $\Delta T_c \approx 0.2$ K.

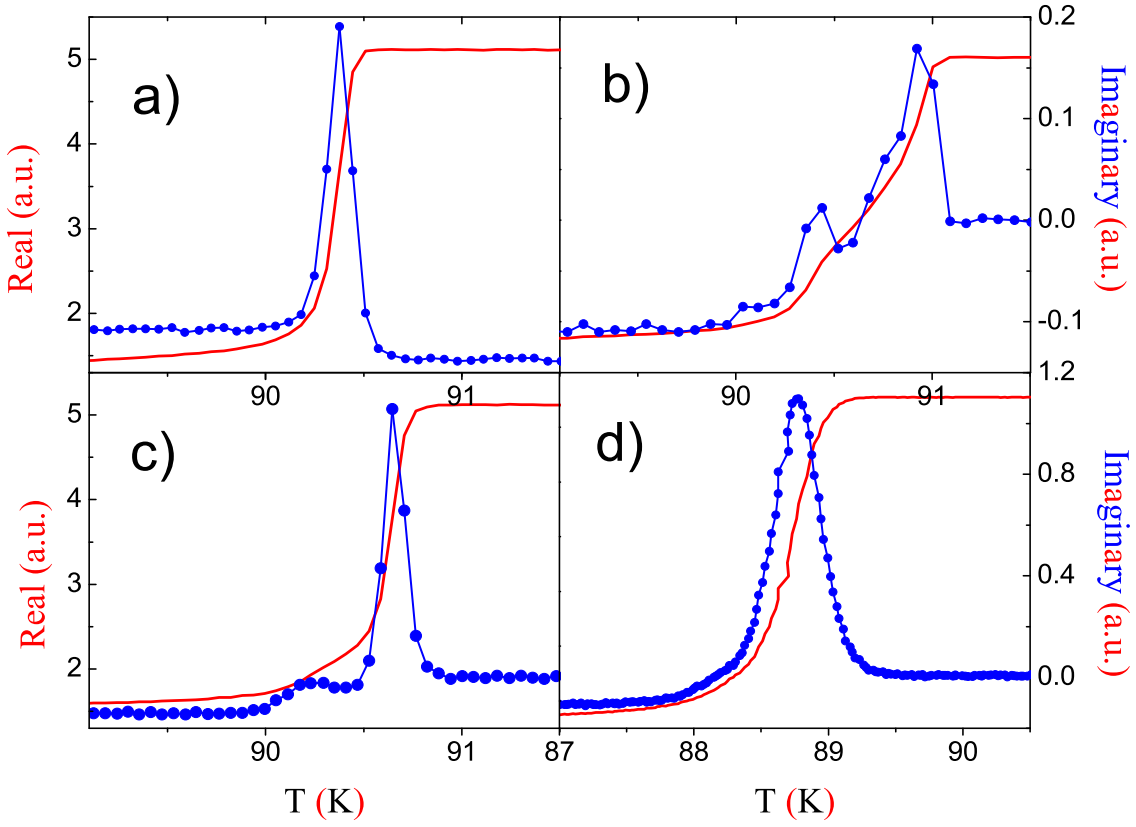

Figure 2.10: The ac susceptibility graphs of four different samples are shown: a) mcs146, b) mcs142, c) mcs144, and d) mcs140. Solid lines are the real part, lines with circles are the imaginary part. Panel (a) shows a good film, (b) a film with two transitions, (c) a film with a "shoulder", and (d) a generally poor film with a low T_c and wide transition.

a film with two transitions. This type of film is common when the substrate is poorly glued to the heater, and thus the temperature varies substantially over the substrate, leading to different oxygen concentrations. This is exactly what we hope to avoid in our films. Fig. 2.10(c) exhibits what we refer to as a "shoulder" below the main transition. We have found that the silver paint used to glue the substrate usually covers the sides of the substrate, making the extremities of the substrate slightly hotter than the middle. This gives the edges of the film a slightly different T_c than the center. We have tested this by scraping off the edges of the film and measuring it again, and the shoulder disappears. Because the center of the film is still uniform, it is possible to use these films. The film in the last panel, Fig. 2.10(d) has a wide transition and a low transition temperature. This film is not useful for our measurements.

Surface analysis

In order to ensure a uniform current flow, it is important that the surface of the film be as smooth as possible. To look at the surface roughness, we use an AFM. The AFM will also tell us whether we have unusual growth modes in our film. We have also used the AFM as a sensitive measure of the thickness of our films.

From an AFM image, we can calculate the roughness, given by:

$$R_a = \frac{1}{N}\sum_{i=1}^{N} |Z_i - \overline{Z}|, \tag{2.1}$$

where Z_i is the height of each of N points and $\overline{Z}$ the average height. Good films have a roughness somewhere between 50 Å and 100 Å, making the roughness at the surface 3-5% of the typical thickness.

A typical AFM picture for sample mcs172 is shown in Fig. 2.11. This film has a roughness of 130 Å. The main features in this picture are several pronounced peaks of height $>$ 100 nm. If we measure roughness in an area which does not include a peak, we find a roughness more similar to what we expect, $\approx$ 70 Å. These peaks

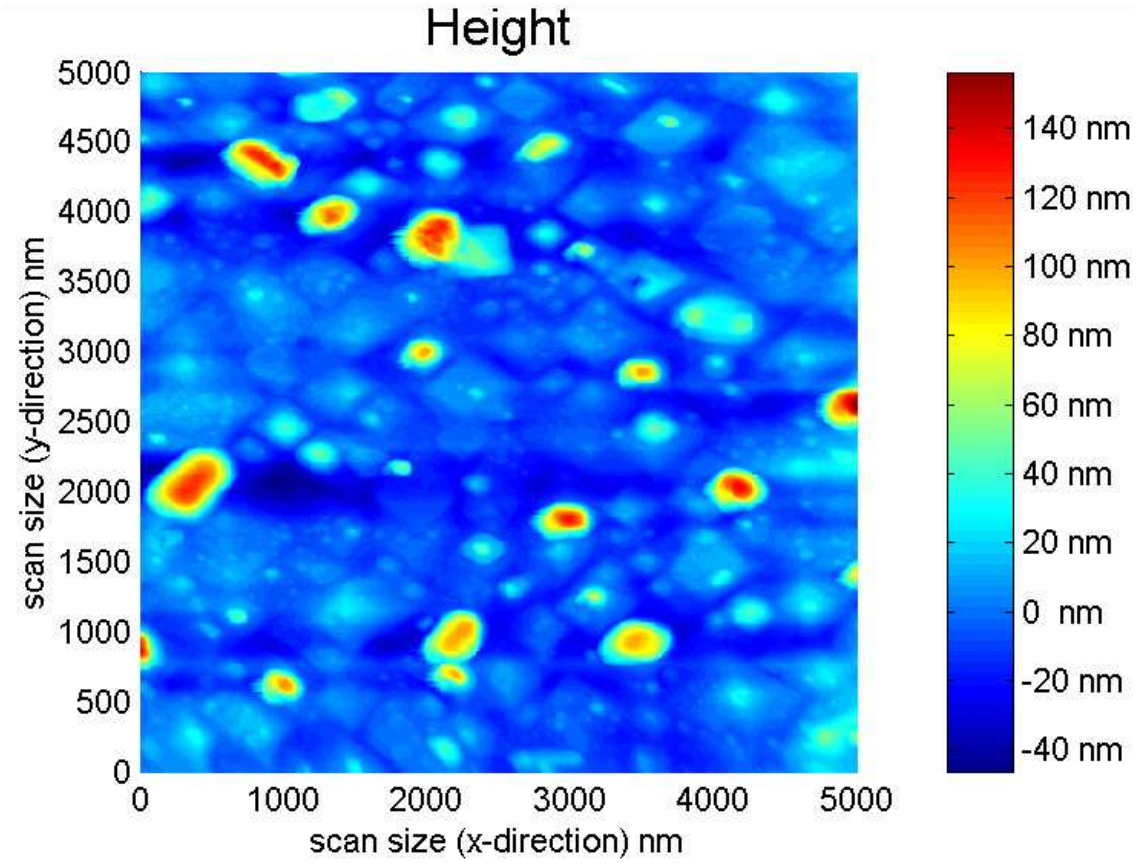

Figure 2.11: AFM image of a typical film (mcs172), with $R_a = 130$ Å. The large peaks (height > 100 nm) are a recurring feature in our films, but break off easily. Film imaged by M. Lilly.

are a recurring feature in our films, and tend to break off when cleaning the film or spinning photoresist.

We have also used the AFM to study the degradation of the film's surface as a function of time. It is well-known that an oxide layer forms on YBCO within a couple of hours after exposure to the atmosphere. To test whether this layer could be seen with the AFM, and also to determine if the surface degraded over time, we measured the roughness as a function of time. The results are shown in Fig. 2.12, in which we see no real change in roughness from 15 minutes to 75 days, and also no change after cleaning the film with acetone. Thus, we conclude that we

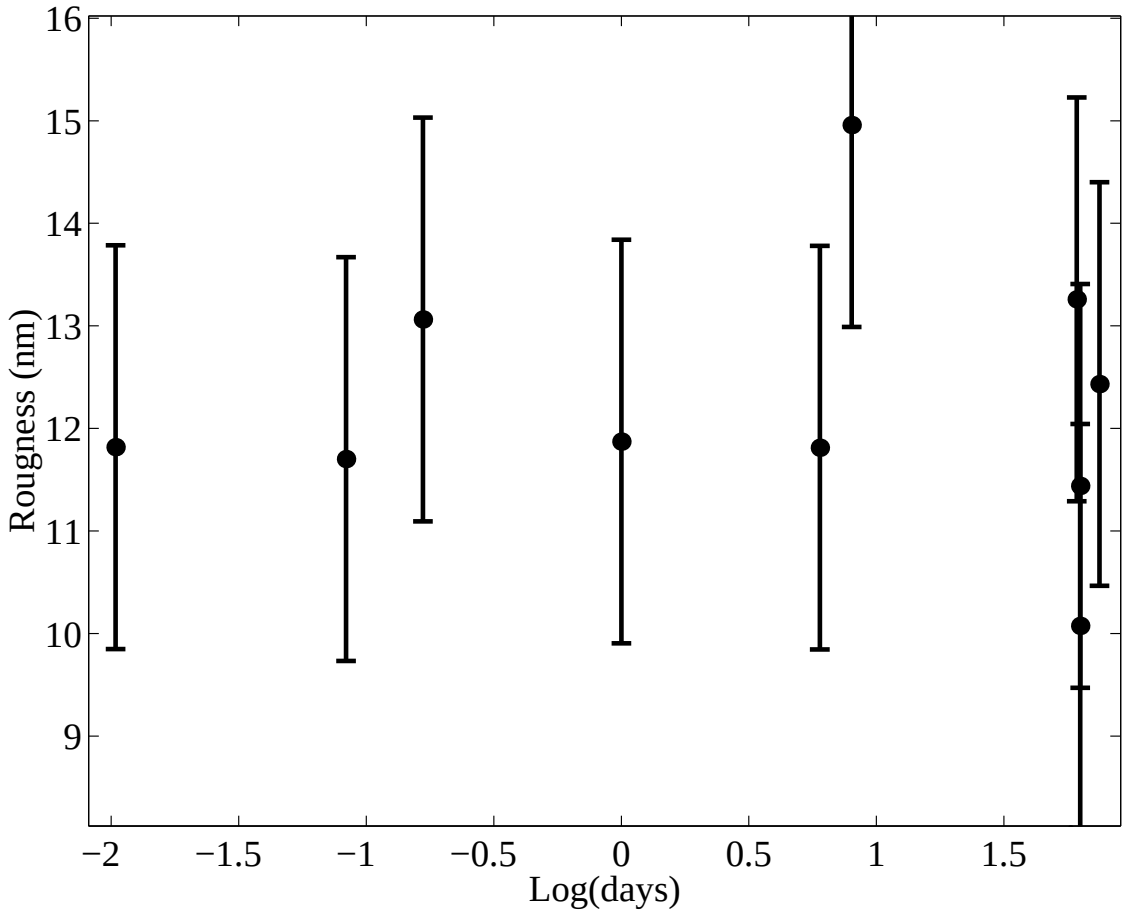

Figure 2.12: Surface roughness as a function of time, from 15 minutes after removing the film from the chamber to 75 days afterwards. The surface does not degrade with time, even when cleaned with acetone.

can measure roughness at any point in a film's lifetime, and still be assured of a meaningful measurement, and that the oxide layer is too thin to be measured with the AFM.

Critical current density

Recently we have begun to look at critical current density as a method of determining the quality of our films. Examining the critical current density will allow us to compare our films with others in the literature, and also to compare between our own films. We expect higher critical current densities for better quality films.

Resistance vs. temperature

The final step, and the final test, is a simple R vs. T graph. In an R vs. T graph, we are looking for a high T_c and a narrow transition width. Some typical films are shown in Fig. 2.13. In these graphs, ΔT_c is usually measured as 90% to 10% of the normal state value. We have taken T_c as the 10% point because we have found, empirically, that is it very close to T_c as determined from ac susceptibility and is also close to T_c as determined from our scaling analyses, which will be discussed later.[6] Fig. 2.14 shows the full range in temperature.

Sample mcs70a, the dashed-dotted line in Fig. 2.13, is one of our poorer samples, with a low transition temperature ($T_c \approx 90.4$ K) and a broad width ($\Delta T_c \approx 1.2$ K). Most of our samples are akin to the dashed line, sample mcs84a ($T_c \approx 91.5$ K and $\Delta T_c \approx 0.5$ K). Films with higher transitions and smaller widths are difficult to obtain. As a standard for improvement, we have included one of our best films, mcs118, the solid line in Fig. 2.13 has $T_c \approx 91.6$ K and $\Delta T_c \approx 0.4$ K. We see that the R vs. T plot gives a clear idea of the quality of the film.

These films have been measured with an applied current density of $J \approx 6 \times 10^6$ A/m^2. For most of the temperature range, the applied current level makes no difference, as the sample is ohmic. This is untrue in the transition region (as we will address in Chapter 5). Nonetheless, the difference between $J \sim 10^5$ A/m^2 and $J \sim 10^7$ A/m^2 on a linear R vs. T plot is hardly noticeable.

2.2.3 Film Patterning

For our measurements, we apply a current I and measure a voltage V. However, what we really wish to apply is current density J and measure electric field E. For that reason, we must control how and where the current flows. To to this, we

[6] Conventionally, researchers choose the 90% point for T_c as the onset of superconductivity or the 50% midpoint as an average.

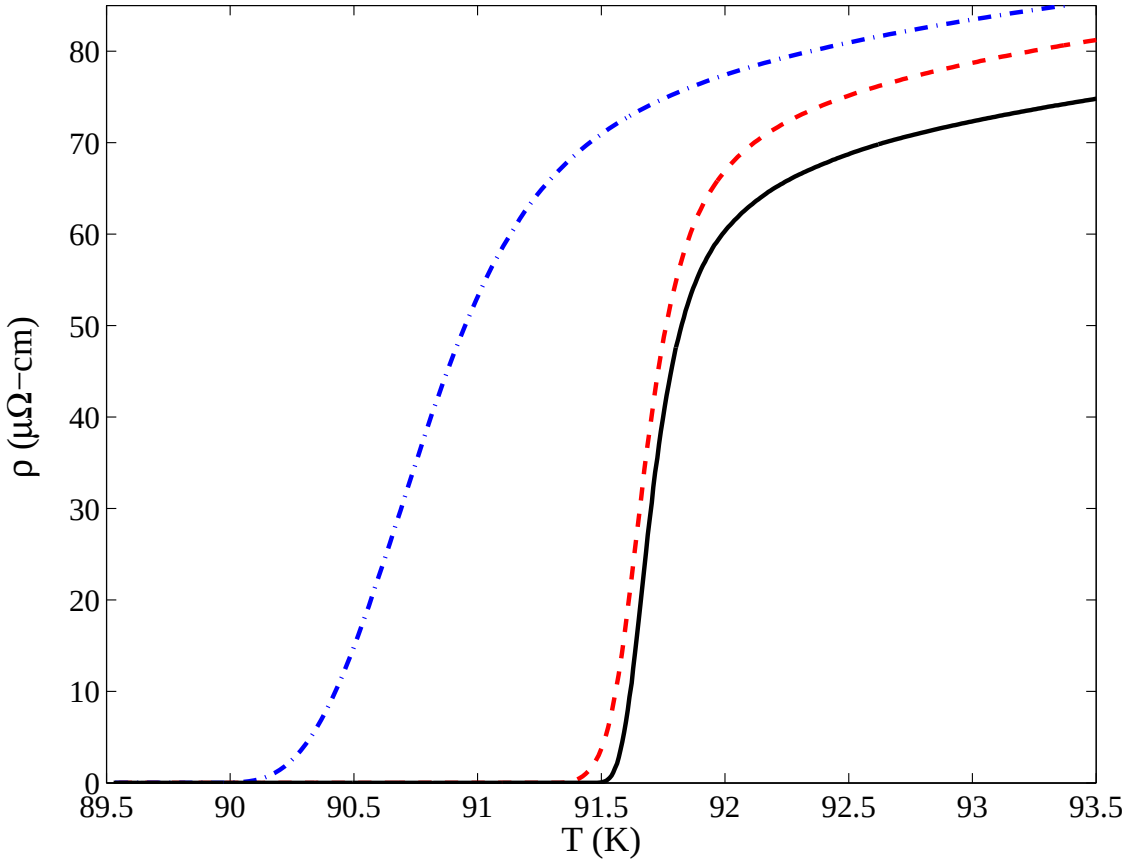

Figure 2.13: ρ vs. T near the transition for several films. The dashed-dotted line (sample mcs70a) is one of our poorer films, with a low transition and broad width. Most of our films are similar to the dashed line (sample mcs84a), while the solid line (sample mcs118) is one of our best films, with $T_c \approx 91.6$ K and $\Delta T_c \approx 0.4$ K. The full temperature range is shown in Fig. 2.14

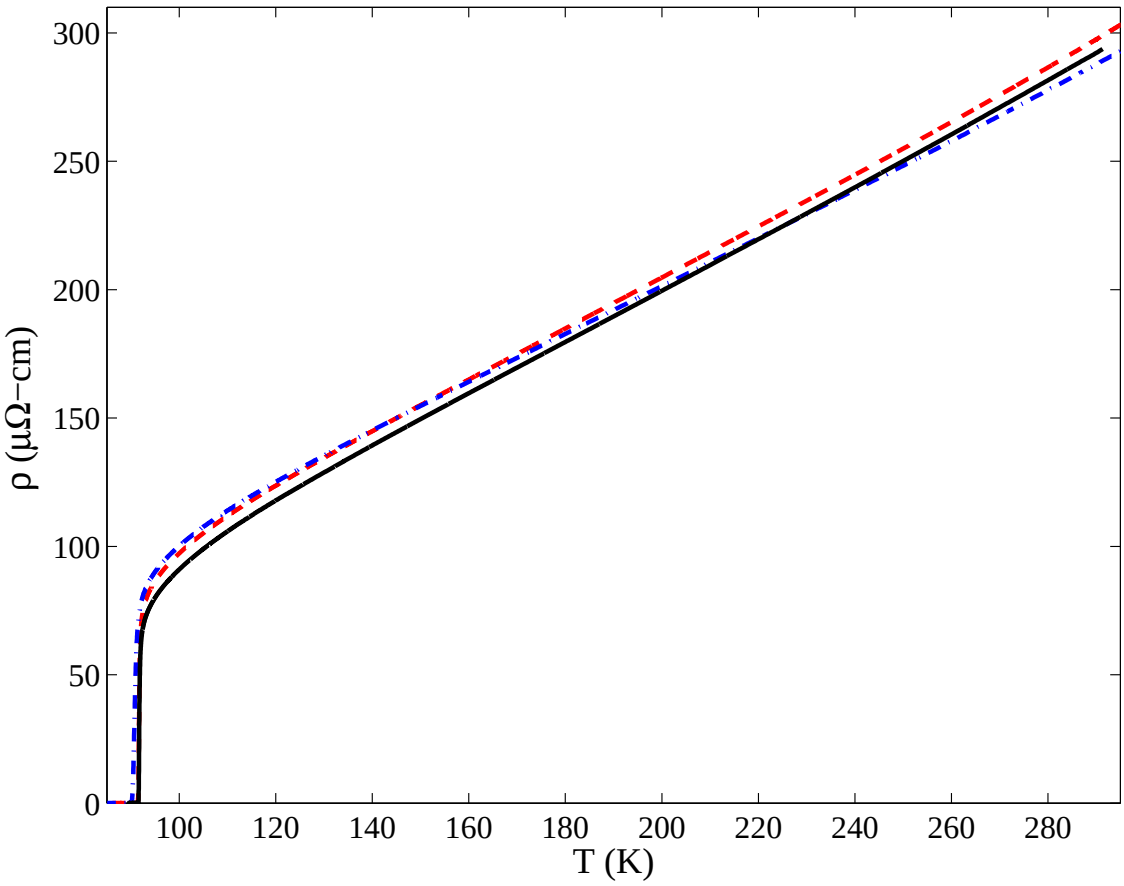

Figure 2.14: ρ vs. T near the transition for the same films as Fig. 2.13. The dashed-dotted line is sample mcs70a, the dashed line sample mcs84a, and the solid line sample mcs118.

pattern the film, essentially channelling the current to flow in a small, well-defined area. The details of the pattern will be discussed in Chapter 3. Here we will discuss how we make the pattern.

Photolithography

To make the pattern, we use a powerful tool which allows researchers to write sub-micrometer patterns on samples called *photolithography*. Photolithography uses a photoresist, a polymer which is sensitive to certain frequencies of light. When light shines on the photoresist, it breaks bonds in the polymer, making it easier to remove. Thus, any photoresist not exposed to light will remain as your pattern.[7]

We use Shipley S-1813 resist, and spin it on our samples at 5000 rpm for 45 s. This gives the photoresist about 1 μm thickness. Afterwards, we soft-bake our films by placing them on a hotplate for 1 minute at 90 °C. We place a chrome mask on top of the film to protect parts of the film from exposure. Then we expose the film to UV light ($\lambda = 365$ nm) at 8 mW/cm^2 for 12.5 s (this is a longer exposure than most, but is necessary because YBCO does not reflect the light back into the resist, as common samples, such as silicon or gold, do). The exposed photoresist is removed in developer. We develop the pattern in a 1:1 ratio of water and CD-30 (a Shipley developer) for 20 s. We can routinely develop patterns of 2 μm width and larger. The photoresist covered by the mask will not be removed by the developer, and will be the desired pattern.

Etching/Milling

Once the pattern is written on top of the film, we must remove the extra YBCO, leaving the desired pattern in the YBCO film itself. To do that, we have two choices: we can use an acid etch or an ion mill. Both methods have their advantages and

[7]This describes positive resist. Negative resist is hardened when light is shone upon it.

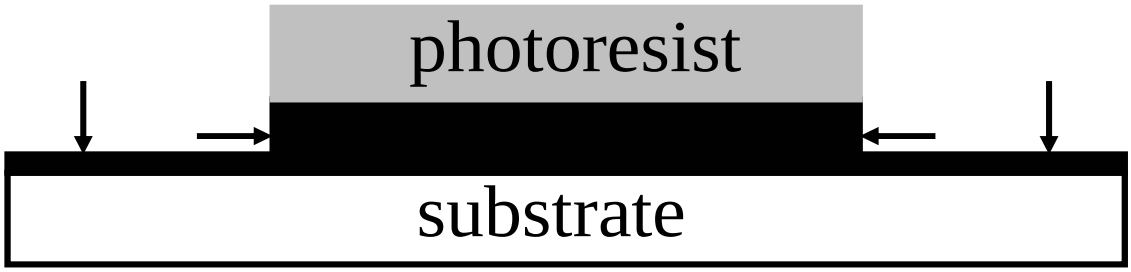

Figure 2.15: Schematic of the acid etch. The YBCO (black) is protected in places by the photoresist pattern. Etch directions are indicated by the arrows. Ideally, the acid only etches downward, etching the unpatterned areas, but in reality, some of the desired pattern is also etched.

disadvantages. Nearly all of our films were etched in acid.

We use 0.5% by volume phosphoric acid (H_3PO_4) in water to etch our YBCO films. To etch a film of thickness $\approx$ 2000 Å requires roughly 20 s in the acid etch.

The advantage of acid etch is that it does not affect the structure or composition of the unexposed film. However, as the acid attacks the unprotected film and etches it away, it exposes edges of film underneath the photoresist, and begins to etch in that direction as well. A schematic is shown in Fig. 2.15, where the black arrows indicate the etch directions. Phosphoric acid preferentially etches along the c-axis, thus it will etch faster into the film than it will into the sides of the pattern, nonetheless, some of the YBCO under the resist is etched away, thus our patterns are **always** narrower than we expect them to be. For this reason, it is difficult to etch patterns narrower than 4 μm.

This over-etch can be avoided with an ion mill. In an ion mill, argon atoms are stripped of their electrons and accelerated towards the sample. Before impact, they are neutralized with an electron beam. The argon atoms hit the sample with such force that atoms on the sample are knocked free. The photoresist is much thicker than the sample (1 μm compared to 2000 Å), and its mill rate is slower (typically half that of YBCO), so the exposed YBCO will be removed before the photoresist,

leaving the YBCO underneath the pattern of photoresist untouched.

The advantage of ion mill is that it can make very exact patterns and avoids any over-etch. However, it is more cumbersome because it involves placing the sample in a vacuum chamber and pumping down. Also, because the atoms hit the sample at high speeds, they impart a large amount of energy to the sample and can heat it. This heat can drive oxygen from the sample and change its superconducting properties. Most ion mills are water-cooled to avoid heating, but due to the relatively poor thermal conductivity of the substrate, heating can still be a problem.

Electrical contacts

Finally, in order to do any measurement, we must connect to the sample electrically. Connecting wires to the film is not an easy task, so special steps must be taken. We pattern large areas for contact pads, for both current and voltage leads. On top of those pads we deposit gold, and then connect wires to the gold contact pads.

We can deposit gold on the film via PLD or evaporation. Evaporation essentially heats the gold such that gold atoms evaporate from the source and fall on the sample. For the gold to stick well to the surface of the film, the film must be taken from the PLD chamber directly to the evaporation chamber, as the oxide layer that forms on YBCO films makes it hard for gold to stick.

In contrast, because PLD is such a violent deposition method, the gold atoms strike the film with enough energy to smash through the oxide layer and form a close bond with the film underneath. However, we have found that more than ≈ 500 Å of gold damages the YBCO underneath. For most of our measurements, this is not a problem, as our measurement is a 4-probe measurement of a section of YBCO protected by photoresist from gold. For this reason, usually we deposit gold via PLD.

We typically achieve contact resistances (gold pad to YBCO) of < 5 mΩ for pads of area 1.5×1.5 mm^2 ($R_{area} \approx 1.13 \times 10^{-8}\ \Omega - \text{m}^2$). To avoid heating which can

burn out the thin voltage leads, we do not solder the wires to the gold pads, but rather use a wire bonder.

2.3 Crystals

For the latter part of our research, we turned our attention to crystals. Like film-growing, crystal growth is one part science, one part art, and eight parts perseverance. W. N. Hardy, D. A. Bonn, and Ruxing Liang at the University of British Columbia in Vancouver, Canada have been persevering for more than 10 years in YBCO crystal growth, and consistently grow some of the best crystals in the world[14, 18]. Their crystals are untwinned (unlike our films, the a- and b-axes are **not** mixed), with high transition temperatures and small widths.

Through a generous collaboration, we obtained several crystals made by the UBC group, which we measured in our experiments.

2.3.1 Crystal Characterization

Because the crystals are delicate, there are fewer ways to test the quality of the crystals. Our main tools to test the samples were magnetic susceptibility and R vs. T.

Magnetic susceptibility

Similar to ac susceptibility, magnetic susceptibility examines the transition to the Meissner state, only this time in a constant magnetic field. In this experiment, a very sensitive SQUID magnetometer measures changes in magnetic flux as the sample's temperature is changed. This change can be fit to magnetic moment, which is linearly proportional to the susceptibility, $M = \chi m H$, where M is the magnetic moment, χ the susceptibility, m the mass, and H the applied magnetic field. Magnetic fields will broaden the transition, thus we want the applied magnetic

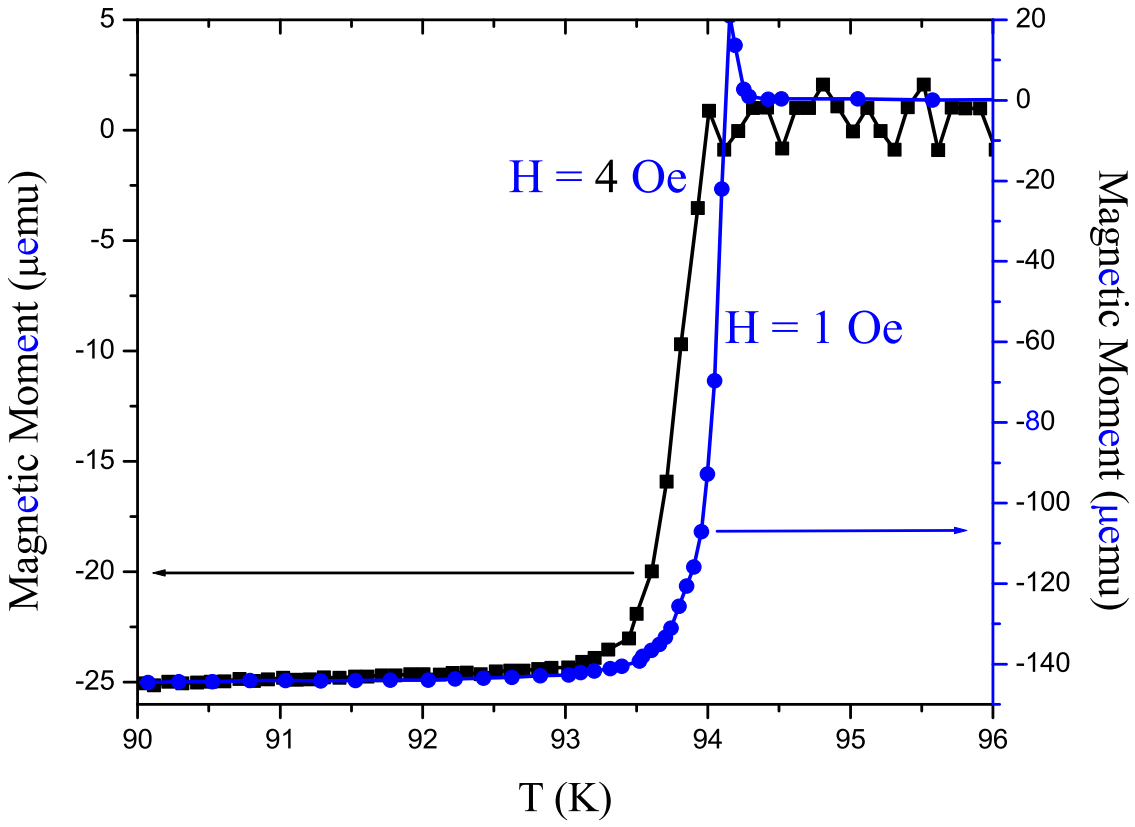

Figure 2.16: Magnetic moment vs. T for two crystals. The smaller crystal (squares) has a much smaller moment, and a lower transition due to the fact that the applied field is larger. The larger crystal (circles) crosses zero due to fitting errors in the measurement program. Both transitions have $T_c \approx 93.8$ K and $\Delta T_c \approx 0.4$ K.

field to be as small as possible. The moment is easier to read, however, when the applied field is large. The crystal is cooled in zero field, and then a field is applied, and the crystal is warmed slowly through the transition. The magnetic moment vs. temperature for two crystals from the UBC group are shown in Fig. 2.16.

The smaller of the two crystals shown in Fig. 2.16 (squares) appears to have a lower transition, but this is most likely due to the higher applied field which was necessary to obtain a reasonable signal from the crystal. Also, the larger crystal (circles) appears to change sign at T_c, but this is an artifact of errors in the fitting program (which determines the magnetic moment) as the signal becomes very

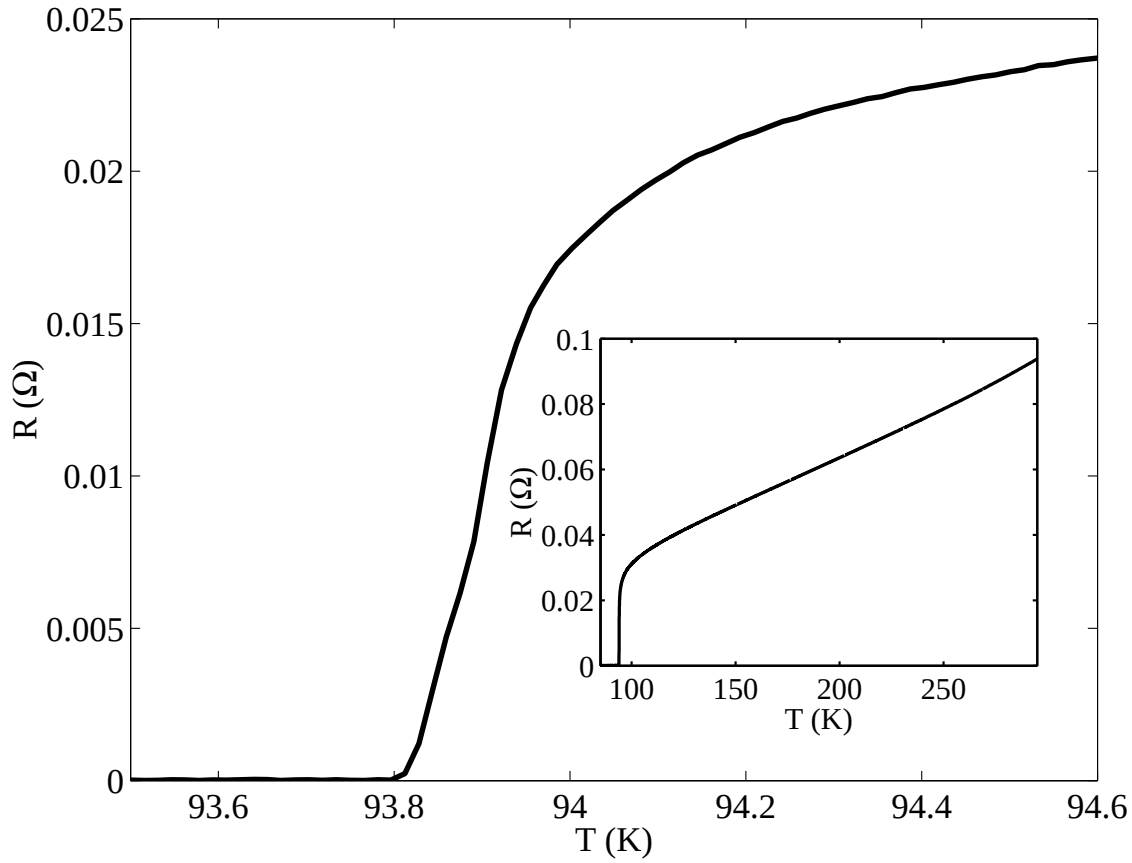

Figure 2.17: R vs. T for crystal ubc2, with the inset showing the full temperature range. In this graph, $T_c \approx 93.85$ K and $\Delta T_c \approx 0.25$ K.

small. From the graphs, we can determine $T_c \approx 93.8$ K and $\Delta T_c \approx 0.4$ K. A quick comparison with films would lead us to believe that the T_c is higher than the films, but ΔT_c is roughly the same. This quick comparison can be deceiving, as we are comparing measurements from two different experiments.

Resistance vs. temperature

Again as a last check, we will look at R vs. T. This is also an excellent way to compare the crystals with our films. The R vs. T for one crystal (ubc2) is shown in Fig. 2.17.

In this figure, the superior quality of the crystal over our films is clear. This

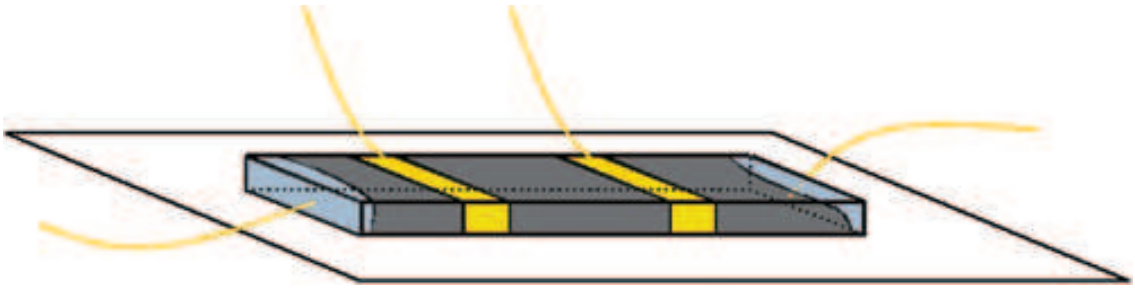

Figure 2.18: Crystal contacts. Silver paint is baked on the edges of the crystal for the current contacts in oxygen at 300 °C for 2 hours. Voltage contacts (toward the center) are PLD gold on the surface of the crystal.

crystal has $T_c \approx 93.85$ K and $\Delta T_c \approx 0.25$ K – thus a higher T_c by more than 2 K and a width smaller than our best widths by a factor of 2.

2.3.2 Electrical Contacts

Crystals are of much better quality than films. Unfortunately, there are a host of different problems which accompany crystals. They are much larger than films, and so to get the same current density in crystals as in the films, we must apply a much larger current. This, in turn, can lead to heating at the contacts, and so making good electrical contacts is a must. A schematic of the crystal contacts is shown in Fig. 2.18.

To make contacts, we use an oil-based silver paint. We cover the edges of the crystal where current will enter and bake the silver paint in oxygen at 300 °C for 2 hours. This will give us $R_{contact} \approx 1\Omega$ for an area of roughly 0.03 mm^2 ($R_{area} \approx 3 \times 10^{-8}\ \Omega - \mathrm{m}^2$), many orders of magnitude larger than for films, although the contact resistivity (R_{area}) is of the same order as for the films. In order to make small voltage contacts we cover the surface of the crystal except for two small bars and we deposit gold via PLD. Afterwards, silver paint is connected to the edge of the voltage contacts. Gold wires are then connected to the silver paint for all four

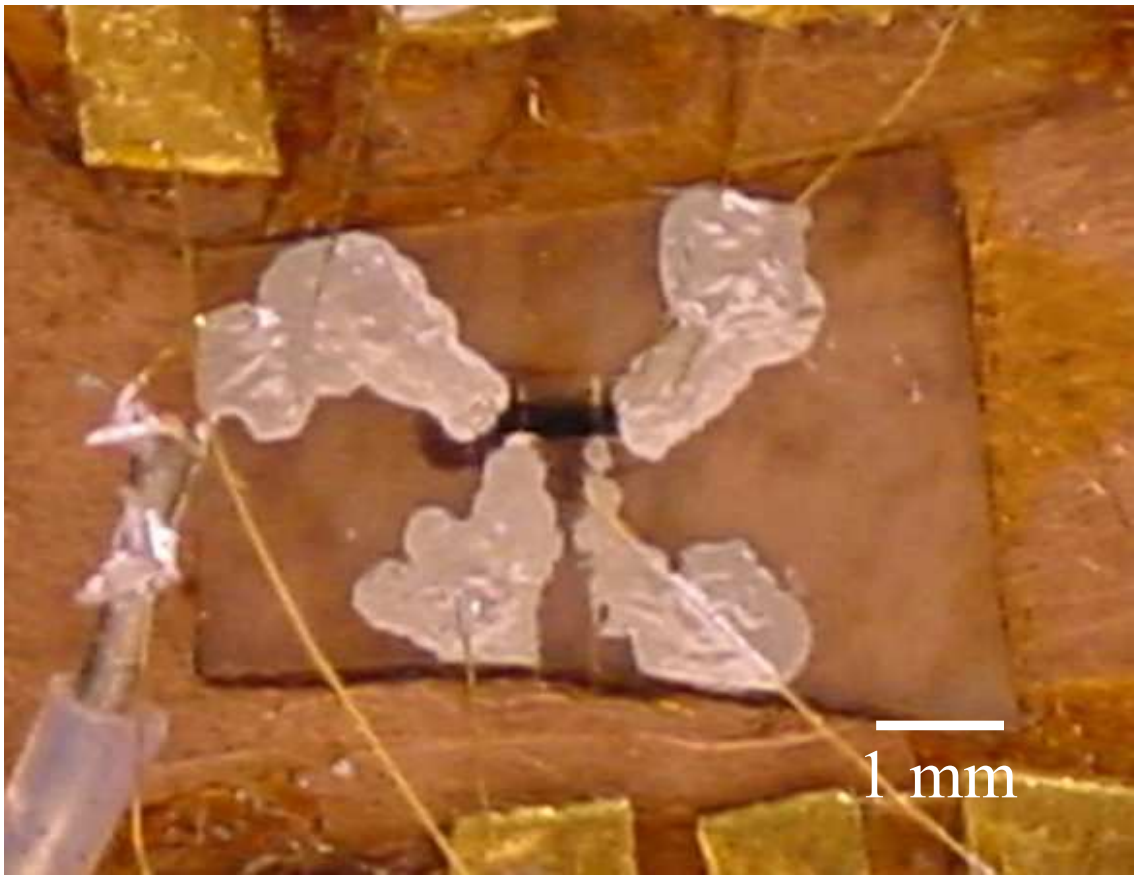

Figure 2.19: Crystal with contacts. The crystal is the small black area in the center of the photograph. Voltage contacts are gold on top, current contacts are silver paint on the edges.

contacts. A picture of a crystal with contacts is shown in Fig. 2.19.

Chapter 3

Experiment

In this dissertation, we will describe data from two different experiments. The majority of our data is dc and low-frequency (quasi-dc) voltage vs. current transport measurements on a variety of different samples. We also measured the specific heat of large single crystals of YBCO.

In this chapter, we will discuss the experiments, how they are designed and built, modifications we have made, and problems we have encountered during our research.

3.1 dc Transport

We performed very sensitive voltage vs. current ($I-V$) measurements at many different temperatures on a variety of different samples. Our measurements were all taken very close to T_c, where an $I-V$ curve can range over many decades of current and voltage. Moreover, an isotherm at any given temperature can have a very different shape from an $I-V$ curve only 0.2 K away from it. For these reasons, we need excellent temperature control, a low-noise environment, and a sensitive voltmeter and current source.

In this section we will describe how we take $I-V$ curves, the design of the probe we use, and some problems associated with our measurement.

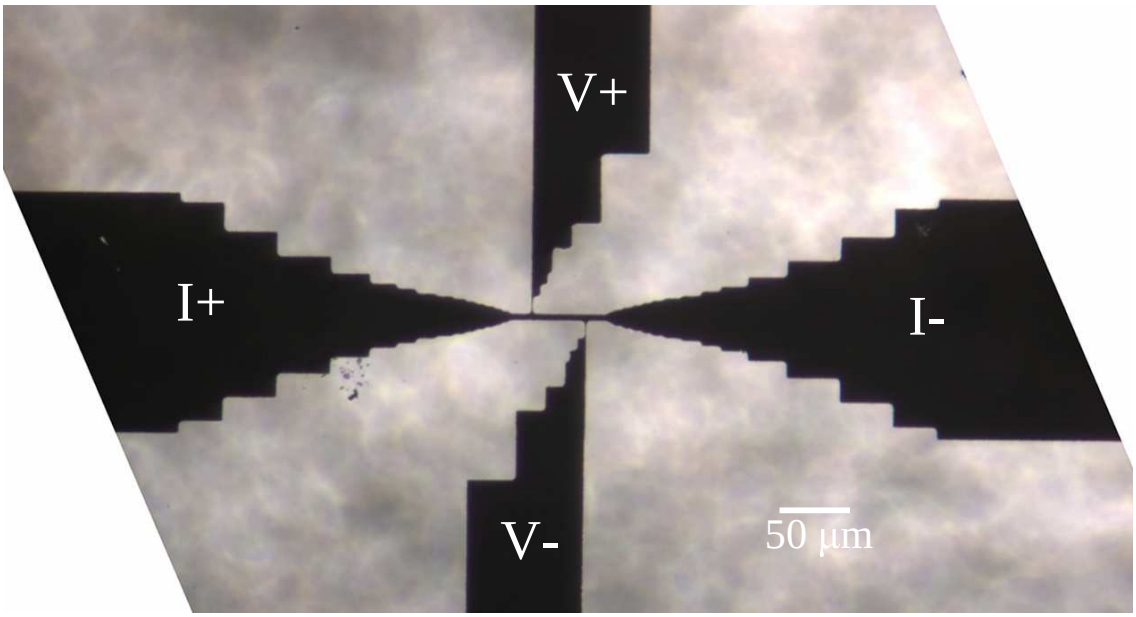

Figure 3.1: YBCO bridge pattern for sample ro68. The YBCO is black, the substrate gray. Current flows from $I+$ to $I-$ (left to right). The voltage is measured at $V+$ and $V-$, a 4-probe measurement. The bridge dimensions are $8 \times 40\mu\text{m}^2$. The gold contact pads cannot be seen on this scale.

3.1.1 Experimental Procedure

On the surface, this experiment is simple: we apply a current, and measure a voltage. However, there are some hidden steps to this deceptively simple measurement.

4-probe measurements

Because we are measuring small voltages (as is usually the case in superconductors), it is essential that we use a 4-probe measurement. This allows us to measure the voltage drop across the superconductor without interference from the leads or the contacts. We apply a current and channel it to flow in a small pattern which we call the $I - V$ bridge. This bridge has a variety of dimensions depending on the experiment, but it is always uniform, such that $I = J(wd)$, where w is the width of the bridge and d the thickness of the film. We attach the voltage leads directly to

the bridge, thus we measure the voltage drop across the bridge only.

A film (ro68) patterned into a typical 4-probe design is shown in Fig. 3.1. Current flows from left to right, from $I+$ to $I-$. The bridge is the narrow region in the center of the four leads. The voltage leads connect directly to the bridge and measure the voltage drop only across that section of YBCO.

The question now arises, if a 4-probe measurement essentially allows us to ignore the contacts and any resistance they might have, why did we want a small contact resistance, as mentioned in Sec. 2.2.3? A small contact resistance is necessary for two main reasons. First, current flows through the contacts and can dissipate a large power if the contact resistance is large, which in turn can heat the bridge above the set temperature. Secondly, a large contact resistance in the voltage leads can create a large common-mode voltage, which will be discussed in Sec. 3.1.3.

Thermal emfs

In an ideal world, connecting the voltage leads to the bridge as shown in Fig. 3.1 allows us to measure only the voltage generated in the bridge. In the real world, the voltage leads are connected to the top of the probe in various stages of wiring, with solder joints, copper wires, and gold wires. Whenever two different metals are joined, voltages can develop at the joints due to any one of several thermoelectric effects, all related to the mismatched Fermi energies of the two metals.[1] These are called thermal emfs, and any measurement we make includes these unwanted voltages. In our setup, generally $V_{th} \sim 1\ \mu$V, which is often several orders of magnitude larger than the signal we hope to measure. Moreover, thermal emfs are not constant in time (they tend to slowly drift) and are dependant on the temperature.

These emfs can be removed by a simple procedure. If we reverse the direction of current, the signal voltage will switch sign, while thermal emfs in the leads will

[1]For a discussion of thermoelectric effects see Ref. [13].

not switch sign. Thus, to measure a voltage V and remove the thermal emf V_{th}, across the sample, we take the difference of the voltages measured while switching the polarity of the current. Thus,

$$V = \frac{V(I+) - V(I-)}{2} = \frac{(V + V_{th}) - (-V + V_{th})}{2}. \tag{3.1}$$

V_{th} does not change appreciably in the time it takes for a reverse-polarity measurement (usually < 0.5 s).

Precision

A single reverse-polarity measurement of the voltage V is often not very precise. For precision, we measure V many times, and take the average of the measurements, $\overline{V}$, and also find the standard deviation, $\sigma_{\overline{V}}$. We continue our measurements until the standard deviation reaches our desired precision, generally $\overline{V}/\sigma_{\overline{V}} > 1000$. If the voltage is near the resolution of our voltmeter (≈ 1 nV), this is an impossible precision to reach, thus we stop our measurement when $\sigma_{\overline{V}} < 1$ nV.

In this way we can measure $I - V$ curves over many decades in current and voltage very precisely.

Low-frequency measurement

A slight variation on this experiment is a low-frequency measurement, first used by Koch *et al.*[19, 20]. Instead of discrete measurements, we apply current in a low-frequency ($\nu < 200$ Hz) sine wave. The voltage across the superconductor is amplified in a pre-amp and then imaged on an oscilloscope, averaged over many periods (generally > 1000), and recorded on computer. One period essentially yields 4 I-V curves. The thermal emfs can be removed by integrating over an entire period to find the offset in the signal, which is then subtracted from the data. At our lowest frequency ($\nu = 10$ Hz), the thermal emfs do not change in the time it takes to average the data (≈ 100 s).

This method has its advantages and disadvantages. Its major advantage is the fact that we can circumvent heating in the sample at higher applied currents, as will be discussed in Sec. 5.3.1. It is limited by the sensitivity of the pre-amps (roughly microvolts), though, which is worse than the dc nanovoltmeters we use, and thus is only useful at high currents and voltages.

3.1.2 Experimental Setup

Our experiment is simple to understand, and has already produced two Ph.D. dissertations. As such, the experiment has already been described in detail[21, 15]. We mention it here for completeness, and also to highlight any changes we have made.

Experimental schematic

A schematic diagram of the dc transport measurement experiment is given in Fig. 3.2. The workhorse of our system is the probe, explained in detail below. We place the probe into a cryostat filled with a liquid cryogen (usually nitrogen) to reach the temperatures required for our measurement. At the end of our probe is the vacuum can, which is continuously pumped by a turbo-pump outside the screened room. Because we are interested in zero field, we surround the cryostat with three layers of μ-metal shields which reduce the magnetic field inside to $< 2 \times 10^{-7}$ T, as measured with a calibrated Hall sensor.

To reduce noise, the cryostat is inside a screened room and low-pass π filters are placed at the top of the probe and also at the connection to the wall.[2] Connections between the top of the probe and the wall and from the wall to our instruments are made with shielded triax cables, again to prevent external noise from reaching our sample.

We apply a current with a Keithley model 224 current source and measure the

[2]These filters will be discussed in detail in Sec. 5.3.4.

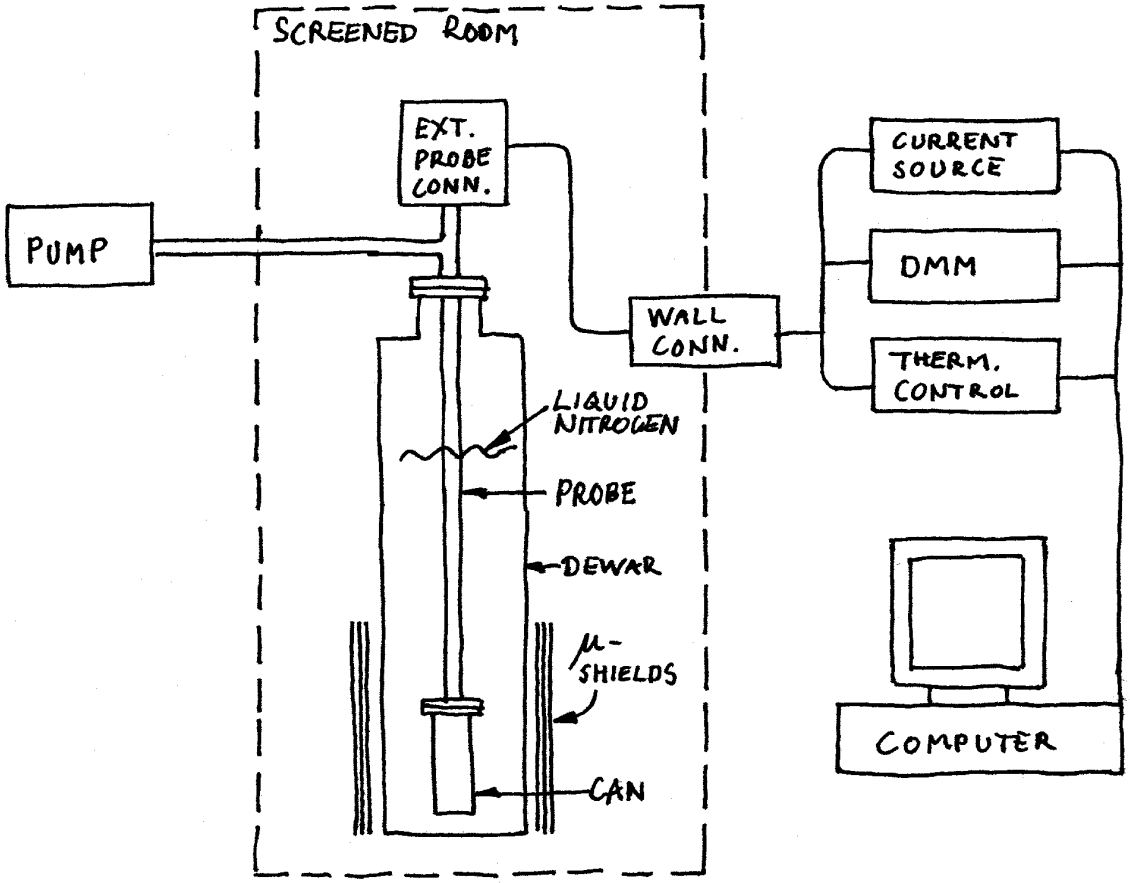

Figure 3.2: Schematic of the dc transport measurement. Schematic drawn by T. Frederiksen.

voltage with a Keithley model 182 digital nanovoltmeter. We regulate the temperature using a Conductus model LT-20 temperature controller. All of our instruments are controlled by computer via GPIB. Our data-taking programs are written in LabView.

dc transport probe

The probe we use was designed by J. M. Repaci[21] specifically for dc transport measurements. A diagram of the cold end of the probe is given in Fig. 3.3.

The probe has three separate thermal stages: the heat sink, the inner can, and the sample block. Each is only connected to the previous stage by stainless steel, effectively isolating each stage thermally. This design allows us to regulate the temperature of each stage independently. The heat sink is directly connected to the liquid cryogen. The sample block and inner can are connected to the heat sink via separate weakly thermally conducting links.

We regulate the temperature of the sample block using the heater and thermometer inside the sample block. The inner can can be regulated using the heater-thermometer pair either at the top or the bottom of the inner can. Usually the inner can and sample block are set to the same temperature, thus the inner can provides an excellent thermal shield for the sample, which sits at the end of the sample block. We can also fill the vacuum can with exchange gas, and then the inner can serves to regulate the temperature of the exchange gas. Unfortunately, there is no way to fill only the inner can with exchange gas. The addition of heaters and thermometers on the inner can is our most major modification.

The thermometry wires enter the vacuum can through one tube and then are thermally anchored to the heat sink. The sample wires come from the top of the probe in separate tubes (to reduce crosstalk and noise) and pass directly into the inner can. There the sample wires are thermally anchored to the inner can before going to the sample.

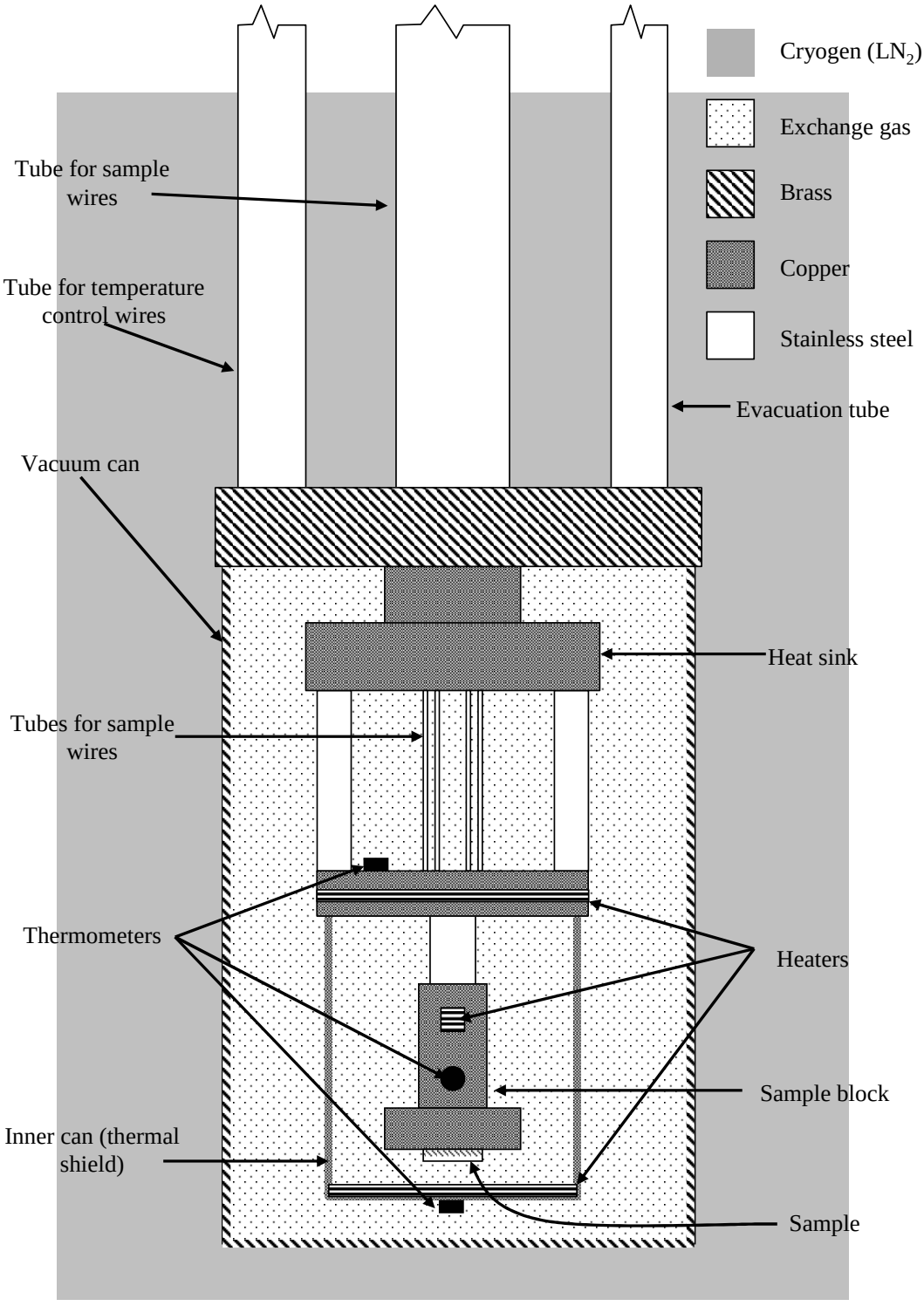

Figure 3.3: Diagram of the probe used in the dc transport experiments. The figure is not to scale. See the text for details.

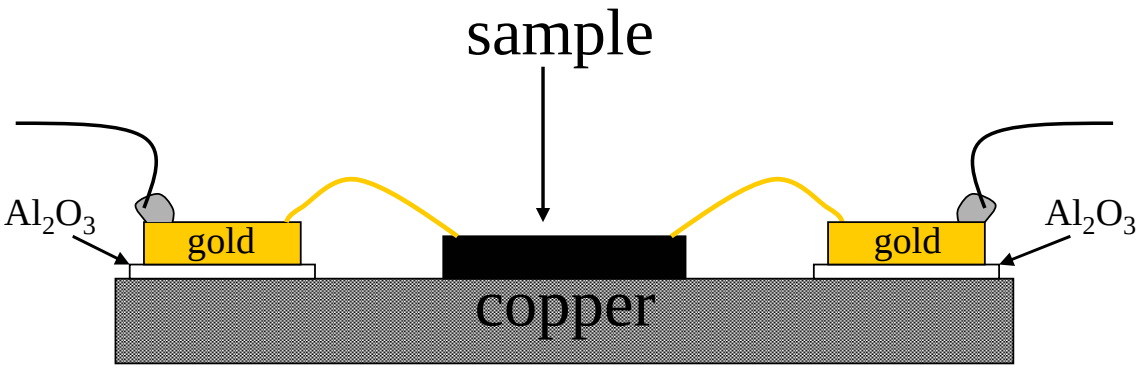

Figure 3.4: Schematic of the sample stage. The gold is glued to sapphire and then to the copper stage, ensuring a good thermal link.

The sample itself was glued, using GE varnish, to a thin copper plate called the stage. We glued bonding gold pads to sapphire and then glued the sapphire to the copper stage. The copper sample wires are soldered to one end of the gold pads, and the wirebonds connect the other end of the gold pads to the contact pads on the sample itself. A schematic is shown in Fig. 3.4. The gold/sapphire connected directly to the stage ensures excellent thermal contact, such that the wires to the sample are at the same temperature as the sample block. Finally, the stage is screwed on to the sample block with a thin layer of vacuum grease underneath.

Noise filtering

One of the major advantages of our probe is its excellent low-noise design. We will discuss the effect of noise on our data in detail in Sec. 5.3.4. Here we give a short description of the methods used to reduce noise.

Outside the cryostat, we have aggressively attempted to reduce noise. Our cryostat is placed inside a screened room to reduce outside electromagnetic noise. The wiring at the top of the probe passes through low-pass double-T filters (3 dB cutoff at 3 kHz) and at the screened room wall passes through low-pass π filters (3 dB cutoff at 5 kHz). The characteristics of these filters will be discussed in detail in

Sec. 5.3.4. All of our connections are made using triax cables to shield the signal wires from noise generated by the computer, current source and voltmeter, etc.

Inside the probe, the sample wires are always separated from the thermometer and heater wires, which can be electrically noisy. Each pair of sample wires is protected by a thin shielding tube until it enters the inner can. The heater and thermometer for the sample block are actually placed inside the sample block, and the thermometry wires enter the sample block through the stainless steel tube connecting the sample block to the inner can. In this way, the sample wires never "see" the noisy thermometry for the sample block.

For many measurements, low-pass filters were added inside the inner can, close to the sample (not pictured in Fig. 3.3).

3.1.3 Problems

Despite its apparent simplicity, there are many problems associated with the dc transport measurement. The most obvious include sample heating, the effects of electrical noise, magnetic field, and sample inhomogeneity. These are all major problems, but because of the effects they can have on the data, are discussed in Sec. 5.3. We discuss two other possible problems below.

Common mode

Common mode is not a problem most researchers encounter, and usually occurs only when the lead resistance to the sample is very large, or the voltage you wish to measure is very small. Because we are measuring the voltage drop across a superconductor, this can be a problem.

The only voltage we wish to measure is the voltage drop between the two voltage leads ($V+$ and $V-$ in Fig. 3.1), called the differential voltage, V_d. However, as current passes through the current leads (which are resistive), there are also voltage

drops in the current leads. The far end of the low current lead will be at ground. This means that the low voltage lead, $V-$, will not be at ground, but rather at an offset voltage, called the common voltage, V_c. Thus, the common voltage is a much larger voltage that the differential voltage rides upon. The ability of a voltmeter to reject this common voltage and measure only the differential voltage is called its common mode rejection. All voltmeters are rated for this ability, called the common mode rejection ratio (CMRR), given by:

$$\text{CMRR} = 20 \log_{10}(\frac{V_c}{V_d}). \tag{3.2}$$

This means that if $V_c > V_d \cdot 10^{\text{CMRR}/20}$, the voltmeter no longer reads the differential voltage properly. When this happens, the voltmeter will read only the common voltage multiplied by the common-mode gain.

Our Keithley 182 voltmeters have a rated CMRR of 160 (under certain conditions, which depend on integration time and load). We have measured the CMRR of the voltmeters in our system and found it to be closer to CMRR ≈ 120.

Luckily, the common-mode signals are easy to detect. Because our leads are ohmic, when the voltmeter fails to measure the differential voltage, we measure instead the resistance of the current lead multiplied by the common-mode gain, $G_c \approx 8 \times 10^{-7}$. Because our signals are usually non-linear at low voltages, this is easy to see. A typical plot of $I - V$ curves is shown in Fig. 3.5. Although the details of such a figure will be discussed (exhaustively) later, the important feature to notice in this plot is the peculiar behavior at low voltages. Each line in the plot is a different temperature, and at low voltages, the isotherms all fall on the same curve. We can calculate the resistance of this curve, and find that it is the lead resistance ($R_{lead} \approx 1000\ \Omega$ for this sample) times the common mode gain, indicating that the voltmeter is no longer reading the differential voltage. When we see different isotherms fall on the same ohmic curve, we usually suspect common-mode problems.

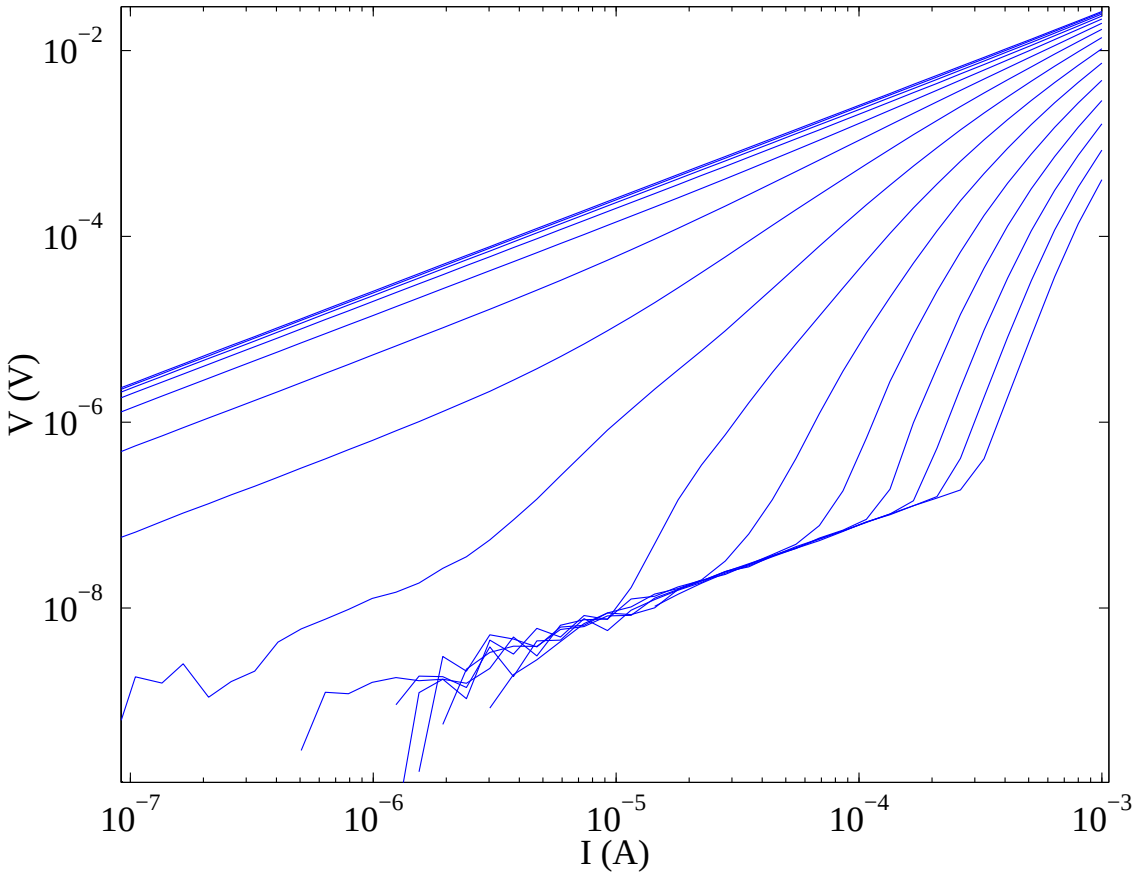

Figure 3.5: $I - V$ curves for sample mcs84a. Each line is a different temperature. The feature to notice here is that all the isotherms at very low voltages fall upon the same curve. This curve is just the lead resistance ($R_{lead} \approx 1000\ \Omega$ for this sample) times the common mode gain ($G_c \approx 8 \times 10^{-7}$), indicating that the voltmeter is no longer reading the differential voltage.

Non-uniform current flow

As mentioned in Sec. 2.2.3, we apply a current I and measure a voltage V – but what we really are interested in is applying a current density J and measuring an electric field E. We pattern our bridges such that $I = J(wd)$ and $V = EL$. This helps to insure that our current density is uniform throughout the sample. Things such as over-etch (as in Fig. 2.15) and surface roughness will cause non-uniform current flow. A roughness of 70 Å on a 2000 Å film gives an error of 4%, and an over-etch of 0.5 μm on an 8 μm bridge gives a 6% error.

In crystals, non-uniform current flow can be hard to avoid, as the crystals are never exactly rectangular. They are not much worse than the films, however, with deviations from rectilinearity usually less than 10%. More worrisome is ensuring that the current flows uniformly through the copper oxygen planes. For this reason, we attach the current contacts to the edges of the crystal.

3.2 Specific Heat

Specific heat is an important property of materials. In particular, specific heat undergoes drastic changes during a phase transition. Many researchers have looked at specific heat because not only are the theories for specific heat well understood, it is also a bulk measurement and is not very sensitive to damaged surface layers. Many experiments are surface experiments, and even dc transport (though it is a bulk measurement), can be affected by the small size of the films.

There are many methods to measure the specific heat of a sample, including adiabatic[22], modulation[23], and relaxation calorimetry[24, 25]. For samples of small mass, many researchers use relaxation or modulation calorimetry. Our lab uses relaxation calorimetry.

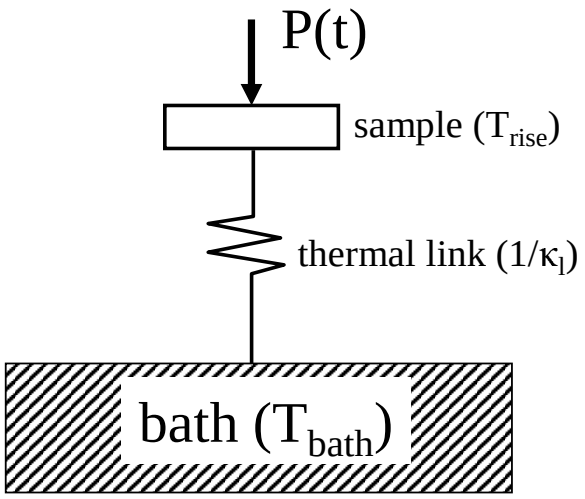

Figure 3.6: Schematic of relaxation calorimetry. A power $P(t)$ is applied to a sample with a thermal connection κ_l to a bath. When the power is suddenly turned off, the temperature of the sample decays to the bath temperature with a time constant $\tau = C/\kappa_l$.

3.2.1 Relaxation Calorimetry

The simplest way to measure the heat capacity is to apply a heat ΔQ and measure the temperature change ΔT. Then the heat capacity is given by

$$C = \frac{\Delta Q}{\Delta T}. \tag{3.3}$$

This requires the sample to be thermally isolated, which can present some difficulties. More significantly, for small samples, it is hard to measure the temperature change ΔT. We use relaxation calorimetry because of the small size of our samples.[3]

In this method, the sample is connected via a thermal link with a known thermal conductance κ_l to a thermal bath at a temperature T_{bath}. The sample is then heated with some power, $P(t)$, raising the temperature of the sample slightly to T_{rise}. If $\Delta T = T_{rise} - T_{bath}$, then from conservation of energy the power in the sample is

[3]Information on relaxation calorimetry was taken from Refs. [24, 26, 27].

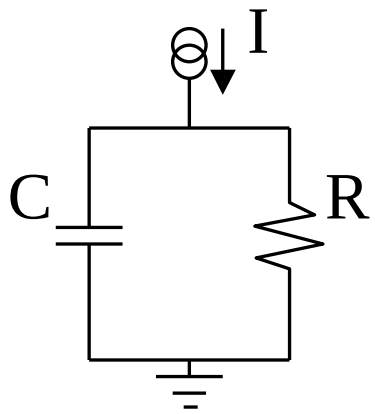

Figure 3.7: RC circuit, which is analogous to the relaxation calorimetry method.

given by

$$P(t) = \kappa_l \Delta T(t) + C\frac{d(\Delta T(t))}{dt}, \tag{3.4}$$

If $P(t)$ is constant, then eventually $d(\Delta T)/dt = 0$. This allows us to determine the thermal conductance κ of the link, $\kappa_l = P/\Delta T$. When the power is suddenly turned off,

$$\Delta T(t) = -\frac{C}{\kappa_l}\frac{d(\Delta T(t))}{dt}. \tag{3.5}$$

If the heat capacity $C(t)$ is constant over the temperature interval ΔT, this equation yields a familiar exponential decay. We recognize the time constant $\tau = C/\kappa_l$, giving the solution $\Delta T(t) = \Delta T(0)e^{-t/\tau}$, where we turn the power off at $t = 0$.

This system is analogous to an RC circuit (Fig. 3.7). In this analog, the voltage corresponds to the temperature, the capacitance corresponds to the heat capacity, and the resistance corresponds to $1/\kappa_l$.

Thus, to measure heat capacity, we connect a sample via a weak link to a thermal bath, heat it a small amount above the bath temperature, turn off the power, and measure the decay time constant. Specific heat is then heat capacity per mass.

3.2.2 Experimental Setup

To measure the heat capacity at different temperatures we use a simple probe[26]. The design is shown in Fig. 3.8.

Like the dc transport probe, a vacuum can is immersed in a cryogen, usually liquid nitrogen. The copper pot is connected with a weak thermal link to the heat sink. The pot is hollow, and can be filled with helium and then pumped on to reduce the temperature of the stage to less than 2 K. Because we are interested in temperatures well above that, we never used this feature, and kept the pot evacuated at all times. We used the heater and thermometer on the pot to regulate the temperature of the pot, and thus the stage. The stage is supported by small copper posts.

The stage is a home-made, designed and built by H. Balci[28]. A schematic is shown in Fig. 3.9. In this stage, a heater and thermometer are glued to a thin piece of sapphire (about 9 mm^2 $\times$ 100 μm). The sample is connected to the other side of the sapphire with thermally conducting grease. Gold wires are connected to the heater and thermometer using silver epoxy. The other end of those wires are glued to an anodized aluminum ring. This ring is screwed into the copper posts, thus the aluminum ring is at the same temperature as the pot.

In this experiment, the aluminum ring acts as the thermal bath, and the four gold wires are the thermal link between the sample and the bath. However, any measurement of heat capacity necessarily includes the heat capacities of the sapphire, heater, thermometer, and thermal grease. For this reason, every heat capacity measurement is actually two measurements. First, we apply grease to the stage and measure the heat capacities of the stage and grease, called the "addenda," $C_{addenda}$. Once we have measured $C_{addenda}$, we add the sample (note that the grease was applied earlier), and measure the heat capacity again. Then we subtract $C_{addenda}$ from the measured heat capacity to find C_{sample}.

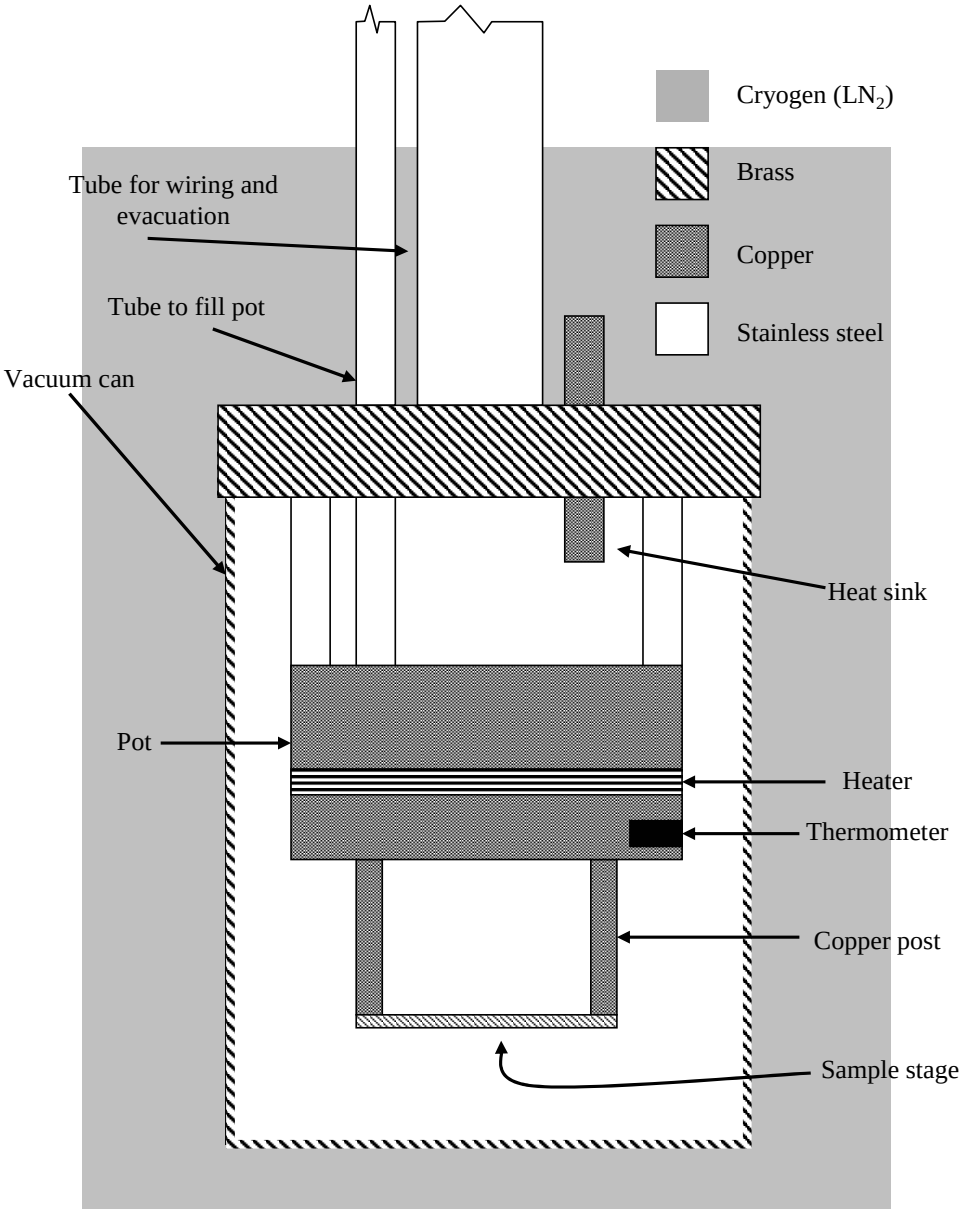

Figure 3.8: Schematic of the heat capacity probe. See the text for details. The drawing is not to scale.

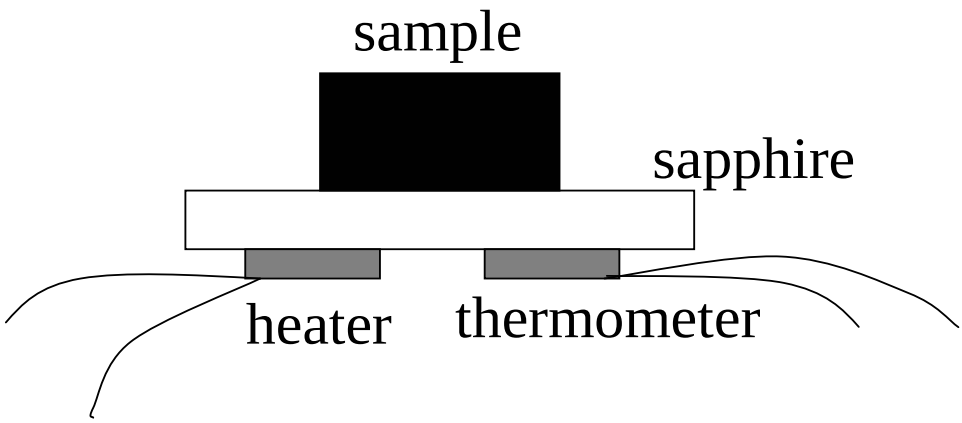

Figure 3.9: Schematic of the heat capacity stage. A heater and thermometer are glued to a 100 μm-thick piece of sapphire. The sample is connected with thermal grease to the other side.

3.2.3 Problems

This method is prone to several problems. If the samples are small, the addenda heat capacity can be larger than the sample. This is not a problem for us. First, our crystals are relatively large, and second, H. Balci has designed stages especially to reduce $C_{addenda}$. In our measurements, $C_{sample} > 3 \cdot C_{addenda}$.

At low temperatures, the time constant is very small, sometimes on the order of milliseconds (as κ is very big). This is also not a problem for us at $T \approx 90$ K. In fact, the opposite is usually true, the time constants are on the order of 10 s, which can lead to long measurement times. This is not an experimental difficulty, though it can be annoying.

Unfortunately, at $T \approx 90$ K we have major thermometry issues. We assume that C is constant over the small temperature rise ΔT. This is a good approximation over much of the temperature range. However, near T_c the heat capacity changes drastically in less than 100 mK, making that assumption invalid. For that reason, we would like to make ΔT as small as possible. However, measuring this small ΔT becomes quite difficult. Our thermometer has difficulty measuring $\Delta T < 25$ mK,

and in fact for $\Delta T < 200$ mK there is a large amount of noise in the measured decay. For this reason, we have used $\Delta T = 200$ mK for our measurements, which means that very close to T_c, C is an average over $\pm$ 100 mK.

Chapter 4

Theory

Our experiment is based on several different theoretical foundations: superconductivity, phase transitions, and (most recently) scaling in the critical regime of high-temperature superconductors. As such, the theoretical predictions for our measurements are well understood.

In this chapter we will present the basics for these theories. This is not intended to be an in-depth survey, but rather to serve as an introduction.

4.1 Ginzburg-Landau Theory

The Ginzburg-Landau (GL) theory to describe superconductors was first proposed in 1950[29] as a phenomenological theory which combined electrodynamics, quantum mechanics, and thermodynamics[3, 2, 4]. Bardeen, Cooper, and Schrieffer proposed a microscopic theory in 1957[30] which proved successful in accurately describing the origins of superconductivity. When it was shown in 1959 that the macroscopic GL theory was a direct consequence of the microscopic BCS theory, GL theory became a widely-accepted tool for understanding superconductors. GL theory looks at large, slowly varying populations of electrons, and for that reason is called a mean-field theory.

The mainstay of GL theory is a complex order parameter, given by $\psi(\mathbf{r}) =$

$|\psi(\mathbf{r})|e^{i\phi}$[3],[1] where the density of superconducting electrons is given by $n_s(\mathbf{r}) = |\psi(\mathbf{r})|^2$. This order parameter is assumed to go to zero at T_{c0}. T_{c0} is the mean-field transition temperature, which can be different from the actual transition temperature, T_c.

4.1.1 Static GL theory

When used by most researchers, GL theory is nearly static, that is, the order parameter may vary in space and in time, but these variations are presumed to be neither rapid nor over short distances. This is the essence of a mean-field theory: any electron sees (at worst) a slowly varying averaged (mean) background. In fact, this is not the case very close to T_c, where the fluctuations described in Sec. 1.1 cause the order parameter (and the density of superconducting electrons) to vary greatly over small distances and short times. Nonetheless, all discussions of superconductivity begin here.

In the absence of a magnetic field, GL theory assumes that the free energy density is given by[3, 2, 4]

$$f_s = f_n + \alpha|\psi|^2 + \frac{\beta}{2}|\psi|^4 + \frac{\hbar^2}{2m^*}|\nabla\psi|^2, \tag{4.1}$$

where f_n is the free energy density of the normal state, α and β are material parameters and m^* is the mass of the superconducting particles. Although the particles that contribute to superconductivity are known to be pairs of electrons, m^* is not precisely $2m_e$ due to metallic band structure and other effects. We have obtained the free energy density in Eq. 4.1 by simply expanding the free energy density in powers of $|\psi|^2$, thus α and β are the parameters that result from the Taylor expansion.

The system will be in equilibrium when the free energy is minimized. We will assume that $\beta > 0$. Then, in the absence of spatial variations ($|\nabla\psi| = 0$), two cases

[1] Although $\psi(\mathbf{r})$ is complex, for all the equations we will discuss (except Eq. 4.1) we can choose $\psi(\mathbf{r})$ to be real.

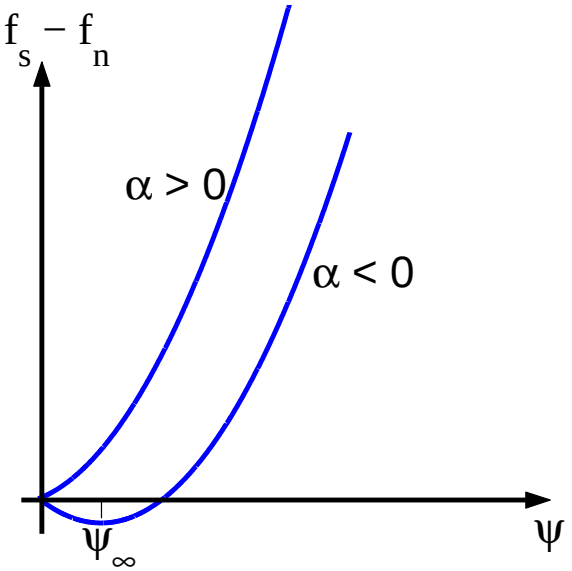

Figure 4.1: The free energy difference when $\alpha > 0$ and $\alpha < 0$. If $\alpha > 0$, then the equilibrium value is $|\psi|^2 = n_s = 0$ (the normal state). For $\alpha < 0$, $|\psi_\infty|^2 = -\frac{\alpha}{\beta}$ in the superconducting state.

arise: When α is greater than or less than zero. If $\alpha > 0$, then there is a minimum when $|\psi|^2 = n_s = 0$. Here $f_s = f_n$, which corresponds to the normal state, thus the density of superconducting electrons is zero.

On the other hand, if $\alpha < 0$, then the free energy has a minimum when

$$|\psi|^2 \equiv |\psi_\infty|^2 = -\frac{\alpha}{\beta}. \tag{4.2}$$

This equilibrium value is conventionally called ψ_∞ because that is the value for ψ deep inside the superconductor. This is sketched in Fig. 4.1.

Clearly, α must change sign about T_{c0} such that $|\psi|^2 = n_s$ goes to zero as $T \to T_{c0}$. If we Taylor expand α about T_{c0}, then to lowest order

$$\alpha(T) = \alpha_0 \frac{T - T_{c0}}{T_{c0}}. \tag{4.3}$$

This is strictly true only near T_{c0}.

We can put Eqs. 4.2 and 4.3 back into the equation for the free energy density

(Eq. 4.1) to obtain for $T \leq T_{c0}$

$$f_s = f_n - \frac{{\alpha_0}^2}{2\beta}\left(\frac{T - T_{c0}}{T_{c0}}\right)^2, \tag{4.4}$$

and for $T \geq T_{c0}$,

$$f_s = f_n. \tag{4.5}$$

We see that the superconducting state has a lower free energy density than the normal state for $T < T_{c0}$. The superconducting state has a free energy density[2]

$$f_s = f_n - \frac{1}{2}\mu_o H_c(T)^2, \tag{4.6}$$

which defines the thermodynamic critical field $H_c(T)$.[2] This is the same $H_c(T)$ as in Sec. 1.2, and thus is directly measurable (at least for type I superconductors). The difference in energy between the normal and superconducting states is called the condensation energy.[3] The condensation energy allows us to make the connection between the parameters α_0, β, and $H_c(T)$, as

$${\alpha_0}^2/\beta = \mu_o {H_c}^2(0). \tag{4.7}$$

We need another equation in order to relate both α_0 and β to measurable quantities.

Ginzburg-Landau coherence length

We return to Eq. 4.1 and consider when the order parameter varies in space (again in the absence of fields). For this case, $\psi(\mathbf{r})$ will change to minimize the free energy. We can use the variational method and find that the free energy will be a minimum when[3, 2, 4, 15]

$$-\frac{\hbar^2}{2m^*\alpha_0\frac{T-T_{c0}}{T_{c0}}}\nabla^2\psi + \frac{\beta}{\alpha_0\frac{T-T_{c0}}{T_{c0}}}|\psi|^2\psi + \psi = 0. \tag{4.8}$$

[2]Here we use mks units, following Ref. [2] rather than Refs. [3] and [4].

[3]The condensation energy and the source of this energy can be confusing. See Appendix B of Ref. [15] for a valiant attempt to sort out the various thermodynamic free energies, or Refs. [3] and [2].

This reduces to Eq. 4.2 for spatially homogenous order parameters, as expected.

Because every term in Eq. 4.8 has units of ψ, the coefficient of the gradient term must have units of length squared. We call this length $\Lambda^2 = \hbar^2/2m^*\alpha$. If we return to Eq. 4.8 and write it in terms of $f = \psi/\psi_\infty$, then we have

$$\Lambda^2 \frac{d^2 f}{dx^2} + f - f^3 = 0. \tag{4.9}$$

If we then set $f = 1 + g$, and solve Eq. 4.9 to first order in g, we find that[3]

$$g(x) \sim e^{-\sqrt{2}x/\Lambda}. \tag{4.10}$$

We can now identify the *coherence length*[3],[4] given by ξ:

$$\xi^2(T) = \frac{\Lambda^2}{2} = \frac{\hbar^2}{4m^*\alpha_0 \left|\frac{T-T_{c0}}{T_{c0}}\right|} \tag{4.11}$$

This is the characteristic length over which the order parameter ψ is uniform. We can rewrite Eq. 4.11 in a suggestive manner, namely:

$$\xi(T) \sim \left|\frac{T - T_{c0}}{T_{c0}}\right|^{-1/2}, \tag{4.12}$$

i.e., the coherence length varies as a power law close to T_{c0} depending on how far it is from T_{c0}. This type of power law dependence will prove to be pervasive later.

Penetration depth and type II superconductors

There is another important length in superconductors, called the *penetration depth* λ. Superconductors in a magnetic field below H_c (or H_{c1} for type II) expel the field from their bulk. This field does not drop to zero suddenly, but rather decays exponentially to zero inside the bulk. The decay constant gives the typical length fields can penetrate inside a superconductor (hence the name). The penetration depth is also related to α and β via[2]

$$\lambda^2 = -\frac{\beta}{\alpha}\frac{\mu_o m^*}{(q^*)^2}, \tag{4.13}$$

[4]This is below T_{c0}. Above T_{c0}, $\xi^2 = \Lambda^2$.

where q^* is the charge of the superconducting particles.

From the coherence length and the penetration depth, we can define the GL parameter κ[3, 2]

$$\kappa = \frac{\lambda}{\xi}. \tag{4.14}$$

It was Abrikosov who first noted that the GL parameter separates type I and type II superconductors. If $\kappa \ll 1$, then the coherence length is much greater than the penetration depth. This is the case for most conventional superconductors, and for all type I superconductors. On the other hand, when $\kappa \gg 1$, then the fields penetrate to distances larger than the coherence length. This leads to magnetic field penetrating in flux quanta, and type II superconductivity. The switch from type I to type II occurs at $\kappa = 1/\sqrt{2}$.

We can combine Eqs. 4.7, 4.11, and 4.13 to determine H_c in terms of measurable quantities ξ and λ[2]

$$H_c = \frac{\Phi_o}{2\sqrt{2}\pi\mu_o\lambda\xi}, \tag{4.15}$$

where we have set $q^* = 2e$. For type II superconductors, the above equation is not particularly useful, as nothing occurs at the thermodynamic critical field H_c. However, we can relate the thermodynamic critical field to the measured upper critical field in type II materials by $H_{c2} = \sqrt{2}\kappa H_c$[31, 3]. When combined with Eq. 4.15 this gives

$$H_{c2} = \frac{\Phi_o}{2\pi\mu_o\xi^2}. \tag{4.16}$$

Near T_{c0} we find that

$$H_{c2}(T) \sim \left|\frac{T - T_{c0}}{T_{c0}}\right|. \tag{4.17}$$

We now know how H_{c2} and ξ behave near T_{c0}, but GL theory can be used to predict other behavior as well[32]. For example, the thermodynamic definition of specific heat is $C = -T\frac{\partial^2 f}{\partial T^2}$. Below T_{c0}, $|\psi| = |\psi_\infty|$, and

$$C = -T\frac{\partial^2 f_n}{\partial T^2} + \frac{{\alpha_0}^2}{\beta {T_{c0}}^2}, \quad T < T_{c0} \tag{4.18}$$

whereas above T_{c0}, $|\psi| = 0$, so

$$C = -T\frac{\partial^2 f_n}{\partial T^2}, \quad T > T_{c0}. \tag{4.19}$$

Thus, as a material goes through the superconducting transition, GL theory predicts a discontinuous jump in the specific heat with magnitude ${\alpha_0}^2/\beta{T_{c0}}^2$ (which can be related to H_c or ξ and λ) . This jump and its magnitude has been well verified in many different conventional superconductors.

4.1.2 Fluctuations as Perturbations ("Gaussian" Fluctuations)

GL theory works well when the order parameter varies slowly or not at all. However, in any material there are always energy fluctuations of order $k_B T$. Near the T_c of a second-order phase transition, these energy fluctuations can cause local changes in the phase of the material, as there is no latent heat. These fluctuations can be both large and rapid. Basic GL theory ignores these fluctuations.

We can, however, incorporate fluctuations into GL theory as perturbations[3, 33, 32]. These perturbations are called "Gaussian" fluctuations. As one might expect, fluctuations can change the behavior of nearly every physical property of the superconductor, including diamagnetism, specific heat, and conductivity. Although the full derivation is beyond what we hope to do here, it is useful to quote some of the results.

Because we are treating the fluctuations as perturbations, the effects they have are additions to the usual GL results. For specific heat, from Eqs. 4.18 and 4.19, above T_{c0} we expect superconducting fluctuations to add to the specific heat.

It should not come as a surprise that fluctuation contribution to the specific heat (called ΔC) depends on its distance from T_{c0} by[33]

$$\Delta C \sim \left|\frac{T - T_{c0}}{T_{c0}}\right|^{\frac{D}{2}-2}. \tag{4.20}$$

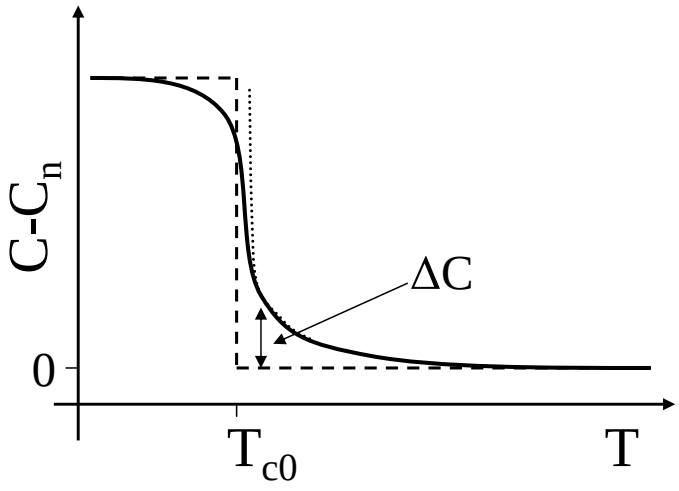

Figure 4.2: The dotted line shows the predicted specific heat with Gaussian fluctuations. The GL prediction for specific heat, a discontinuous jump, is shown by the dashed line. The fluctuation contribution is labelled ΔC. Experimental data from Ref. [34] (solid line) shows a rounded transition. The zero on the vertical axis is offset for clarity.

Thus, for a three-dimensional (3D) sample, $\Delta C \sim |T/T_{c0} - 1|^{-1/2}$. The fluctuation contribution is larger for two-dimensional (2D) samples, as $\Delta C \sim |T/T_{c0} - 1|^{-1}$. This enhancement to 2D specific heat has been verified in low-temperature superconductors[34], and is sketched in Fig. 4.2.

Fig. 4.2 plots the total specific heat minus the normal state specific heat. The dashed line represents the GL results, a discontinuous jump. The dotted line is the predicted results, which diverges as $T \to T_{c0}$. The solid line represents actual data, rounded about the transition. The rounding of the transition is explained in Ref. [34]. The fluctuation contribution is labelled ΔC.

Also of interest for us is the fluctuation-enhanced conductivity. Again, above T_{c0} we expect superconducting fluctuations to add to the conductivity. This is sketched in Fig. 4.3, where again the dashed line is the GL prediction and $\Delta\sigma$ the addition due to fluctuations.

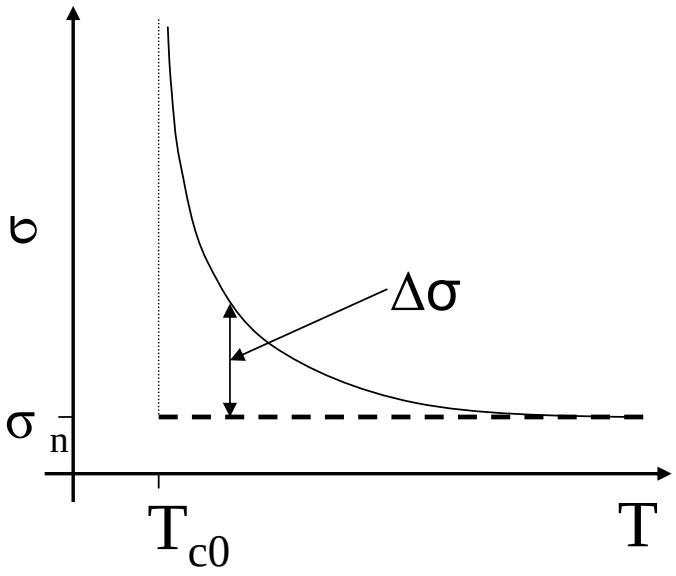

Figure 4.3: The solid line shows the predicted conductivity with Gaussian fluctuations. The GL prediction for conductivity is shown by the dotted line. The fluctuation contribution is labelled $\Delta\sigma$. σ_n refers to the normal-state conductivity.

Skipping directly to the results, we find that[33, 32]

$$\Delta\sigma \sim \left(\frac{T - T_{c0}}{T_{c0}}\right)^{\frac{D}{2}-2} \tag{4.21}$$

for $T \geq T_{c0}$. In 2D samples, the fluctuation contribution again is greater than for 3D samples. Measurements on 2D films have verified the fluctuation contribution[35, 33].

Ginzburg criterion

What happens when the fluctuations are so large that they cannot be treated as perturbations? When that occurs, GL theory breaks down and can no longer be used – we must use a completely different theory. First, however, we shall ask a simpler question: when does this occur? The answer to this question is the *Ginzburg criterion.*

We can answer this quickly (but approximately) by the following argument. A fluctuation of size ξ near T_{c0} will carry with it an approximate energy den-

sity of $k_B T_{c0}/\frac{4}{3}\pi\xi^3$. When this energy becomes greater than the condensation energy, $\frac{1}{2}\mu_o {H_c}^2$, we can expect GL theory to break down. Rewriting Eq. 4.12 as $\xi = \xi(0)|T/T_{c0} - 1|^{-1/2}$ and Eq. 4.17 as $H_c = H_c(0)|T/T_{c0} - 1|$, and using Eq. 4.16, we find that this occurs when

$$|T - T_{c0}| < 72\frac{\pi\mu_o\kappa^4}{\Phi_o^3 H_{c2}(0)}k_B^2 T_{c0}^3, \tag{4.22}$$

where again we have used the fact that $H_{c2} = \sqrt{2}\kappa H_c$.

To answer this question more exactly we must introduce the correlation function $\Gamma(r)$. $\Gamma(r)$ is given by

$$\Gamma(r) = \langle(\psi(r) - \psi_\infty)(\psi(0) - \psi_\infty)\rangle. \tag{4.23}$$

For fluctuations, $\Gamma(r)$ will tell us how well correlated two regions a distance r apart are. $\Gamma(r)$ can be evaluated for the fluctuating regions, and is given by[3]

$$\Gamma(r) = \frac{k_B T}{4\pi\frac{\hbar^2}{2m^*}}\frac{e^{-r/\xi}}{r} \tag{4.24}$$

for $D = 3$. If there is no correlation, $\Gamma(r) = 0$, and the more correlation, the larger the value for $\Gamma(r)$. $\Gamma(r)$ is not valid for $r \to 0$ as it has an unphysical divergence[3].

This form for the correlation function (Eq. 4.24) assumes equipartition for two modes from the complex order parameter. If, instead, we assume a real order parameter with only one mode, then we have $\frac{1}{2}k_B T$ in place of $k_B T$, and the correlation function has the form (still not valid as $r \to 0$)[4, 15]

$$\Gamma(r) = \frac{k_B T}{8\pi\frac{\hbar^2}{2m^*}}\frac{e^{-r/\xi}}{r}. \tag{4.25}$$

We will use Eq. 4.24 because, although we can usually choose the order parameter to be real, in general, it is complex.

GL theory will fail when the fluctuations become more ordered than the superconductor itself. In other words, it fails when the correlation function for fluctuations a distance ξ apart given by $\Gamma(\xi)$ becomes larger than the squared order parameter

given by GL theory, or[36, 31]

$$\Gamma(\xi) > |\psi_\infty|^2. \tag{4.26}$$

Combining Eqs. 4.2, 4.3, 4.11, and 4.24, we find that GL theory fails when[5]

$$\left|\frac{T - T_{c0}}{T_{c0}}\right| < \frac{1}{8\pi^2 e^2}\frac{\beta^2}{\alpha_0}\left(\frac{2m^*}{\hbar^2}\right)^3 (k_B T_{c0})^2, \tag{4.27}$$

which assumes $T \approx T_{c0}$ in Eq. 4.24. Here e is the base of the natural logarithm, not the charge on an electron. Eq. 4.27 can be rewritten in terms of measurable parameters using Eqs. 4.7 and 4.16, and the fact that $\xi^2(0) = \hbar^2/4m^*\alpha_0$ from Eq. 4.11. After some algebra, this gives

$$|T - T_{c0}| < \frac{\pi\mu_o\kappa^4}{2e^2{\Phi_o}^3 H_{c2}(0)}{k_B}^2 T_{c0}^3. \tag{4.28}$$

Plugging in for the known parameters, we have

$$|T - T_{c0}| < 5.7 \times 10^{-9}\frac{\kappa^4 T_{c0}^3}{H_{c2}(0)}. \tag{4.29}$$

Here, $\mu_o H_{c2}(0)$ is measured in tesla and T_{c0} in kelvin. Eq. 4.29 is one form of the Ginzburg criterion.

We are now in a position to answer: when does GL theory fail? For conventional superconductors, $\kappa \approx 10$, $T_{c0} \approx 10$ K, and $\mu_o H_{c2}(0) \approx 1$ T[31]. Thus, GL theory breaks down only when $|T - T_{c0}| < 1 \times 10^{-7}$ K – impossible to access experimentally. This helps explain why GL theory works so well for conventional superconductors.

But for the new high-temperature superconductors, the situation is very different[31]. It is somewhat complicated by the fact that these superconductors are anisotropic. Eq. 4.28 is modified to become[10]

$$|T - T_{c0}| < \frac{1}{\gamma^2}\frac{\pi\mu_o\kappa^4}{2e^2{\Phi_o}^3 H_{c2}(0)}{k_B}^2 T_{c0}^3, \tag{4.30}$$

[5]This differs from Ref. [31] by a factor of $\frac{1}{4e^2}$. Ref. [31] assumes equipartition for one mode as opposed to two, leading to a factor of $\frac{1}{4}$; and also uses the small-r form for $\Gamma(r)$, when $e^{-r/\xi} \approx 1$. To our knowledge, Eq. 4.27 is the correct equation.

or

$$|T - T_{c0}| < 5.7 \times 10^{-9} \frac{\kappa^4 T_{c0}^3}{\gamma^2 H_{c2}(0)}, \tag{4.31}$$

where $\gamma = \xi_c/\xi_{ab}$; i.e., the ratio of the coherence lengths along the c and a and b axes, respectively. For YBCO, $\kappa \approx 120$, $\gamma \approx 0.2$, $T_{c0} \approx 90$ K, and $\mu_o H_{c2}(0) \approx 90$ T[15]. This gives $|T - T_{c0}| < 0.32$ K. Thus, GL theory fails within a 0.6 K window centered about T_{c0}, which is easily accessed experimentally.

4.2 Critical Regime

The Ginzburg criterion tells us when mean-field theory breaks down. We find this occurs in a region very close to the critical temperature. This is called the *critical regime* or critical region. In this regime, the fluctuations can no longer be treated as perturbations to mean-field theory. In fact, we can see from Eq. 4.12 that we expect that the typical size of a superconducting fluctuation above T_{c0} will become infinite at T_{c0}. Clearly, to analyze the critical regime, we must move away from considering fluctuations to be small. In this section, we will follow the derivation in Ref. [4] (a highly readable and highly recommended book).

If the fluctuations are not perturbations, let us move to the other side of the spectrum and state the hypothesis that in the critical regime, fluctuations **dominate** the behavior. This simple statement is perhaps somewhat radical, but from it we can derive a set of equations which, it will turn out, are obeyed remarkably well in a variety of different systems.

4.2.1 Scaling

Empirically, it was found that as $T \to T_c$,[6] the physical parameters of a system (be it liquid-vapor, ferromagnetic, or others) diverged as power laws similar to Eq. 4.12. This leads us to state empirically that the size ξ of a fluctuation goes as

$$\xi \sim \left| \frac{T - T_c}{T_c} \right|^{-\nu} = |t|^{-\nu}, \tag{4.32}$$

where for convenience we have defined $t \equiv T/T_c - 1$.[7] The size of ξ diverges at T_c, so it certainly seems as though fluctuations should play a large role in the behavior of the material near the phase transition. Additionally, researchers have found near T_c that the specific heat C goes as

$$C \sim |t|^{-\alpha}, \tag{4.33}$$

where we have already defined two *critical exponents*, ν and α.[8] But this only dips the spoon into the alphabet soup, as empirically, nearly every physical parameter varies as a power law near T_c. For example, magnetization M in a ferromagnet or density difference in the liquid-vapor transition go as

$$M \text{ or } \rho_L - \rho_{critical} \text{ or } \rho_{critical} - \rho_V \ \sim |t|^{\beta}, \tag{4.34}$$

or magnetic susceptibility $\chi = \frac{\partial M}{\partial H}$ in a ferromagnet and compressibility $K = \frac{\partial \rho}{\partial P}$ in liquid-vapor,

$$\chi \text{ or } K \ \sim |t|^{-\gamma}. \tag{4.35}$$

[6] We now refer to T_c, the true critical temperature, as opposed to the mean-field transition temperature, T_{c0}.

[7] Older references universally define $\varepsilon \equiv T/T_c - 1$. We have adopted the more modern convention of t, which unfortunately is easily confused with thickness. For this reason we use d to indicate thickness – which is unfortunate, as older references use this for dimension. We will use D to indicate dimension.

[8] The critical exponents α and later β have nothing in common with the GL theory parameters α and β (besides having the same name). Although this will undoubtedly cause confusion, we wanted to keep the symbols the same as those used in the literature.

There are more formulae and more exponents; in addition to α, β, γ, and ν, there are δ, η, μ, and ζ (see Ref. [4] or [32]). All these formulae and critical exponents have been seen experimentally, and they can all be boiled down to some function of ξ – i.e., scaled to ξ. This is the essence of scaling, to wit:

Everything depends on ξ.

This certainly agrees with our assumption that fluctuations dominate the behavior.

These critical exponents are interesting, but they lead us to wonder what, exactly, they mean. Moreover, are they related, and can we predict them?

4.2.2 Critical Exponents

To find some theory that will explain the empirical results above, we start, as before, by writing down a free energy. Suppose we have a system of size L. Because we assume a priori that fluctuations dominate the behavior, it makes sense to expand the free energy in terms of the dimensionless parameter, L/ξ. Then we have[4]

$$F = F_o + C_1 \left(\frac{L}{\xi}\right)^n + \frac{C_2}{2}\left(\frac{L}{\xi}\right)^{2n} + \cdots, \tag{4.36}$$

which is highly reminiscent of Eq. 4.1. Because we know ξ diverges close to T_c, we will keep only the first term in the expansion.

If we consider a free energy density $f = (F - F_o)/L^D$ in D dimensions, then if $n = D$ the free energy density is independent of the size of the system, which is a reasonable thing to expect. This means

$$f \sim \xi^{-D} \tag{4.37}$$

or

$$f \sim |t|^{D\nu}. \tag{4.38}$$

This allows us to begin to write other properties, such as:

$$C = -T\frac{\partial^2 f}{\partial T^2} = -\frac{T}{T_c}\frac{\partial^2 f}{\partial t^2} \sim |t|^{D\nu - 2}, \tag{4.39}$$

where we have used one of the most powerful weapons of scaling: throwing away quantities that do not diverge. We could set $T = T_c$, but because T does not diverge as $T \to T_c$, it does not dominate the behavior as the singular $|t|^{D\nu-2}$ does – thus we hide it in the $\sim$ symbol, essentially throwing it away. In a similar manner we have discarded the factors $D\nu$ and $(D\nu - 1)$.

However, this simple derivation has already given an important result, namely

$$\alpha = 2 - D\nu, \tag{4.40}$$

which means, at the very least, α and ν are **not** independent of one another.[9]

In a similar manner, we can derive relations between all of the critical exponents, and find that the alphabet soup of α, β, γ, etc. can be reduced to just two exponents, x and y, and the dimension D. The first exponent we've already met in another guise, it is just

$$\xi \sim |t|^{-x}, \tag{4.41}$$

another way for saying ν, and clearly comes from the temperature dependence. The other exponent comes from the second parameter which governs the phase transition (magnetic field in superconductors and ferromagnets, pressure in liquid-vapor).[10] Very close to T_c,

$$\xi \sim |H|^{-y} \text{ or } \xi \sim |P - P_c|^{-y}. \tag{4.42}$$

We have not (and will not) discuss this second parameter because our measurements are in zero field. We will refer the reader again to Ref. [4] for a full discussion. In fact, we have already derived the only relation we will need later (Eq. 4.40).

---

[9]Relations that involve the dimension D, such as Eq. 4.40, technically fall under the heading of *hyperscaling*[37] (as opposed to regular scaling). The difference is not of great significance for our purposes, and we will continue to refer to it as scaling.

[10]The magnetic field plays a different role in ferromagnets, where it causes order, and superconductors, where it destroys order. Nonetheless, magnetic field and temperature are the parameters which govern both phase transitions.

Essentially, the critical exponents are derived from a sort of dimensional analysis, where we have scaled all the equations in terms of quantities that either diverge or go to zero at the phase transition. This dimensional analysis will give us the equations we need to describe the normal-superconducting phase transition in Sec. 4.3.

The question now remains: if these divergences have been seen experimentally, then values for α, β, γ, etc. must be known experimentally for different phase transitions. The scaling laws predict how α is related to β and γ, how ν is related to α, etc. And indeed, the relations between exponents are obeyed in a variety of very different phase transitions[38, 39]. Thus, despite the apparent naïvité of the derivation, it seems to agree with experiment quite well. In fact, the relations between the exponents (like Eq. 4.40) are so robust, they even work for exponents derived from GL theory – if $D = 4$.[11]

We now have predictions that tell us how fluctuations behave near a second-order phase transition, and clear power-law behavior for the measurable physical parameters of the system. But if we don't want to use the values for the exponents predicted by GL theory (which would be strange, considering inside the critical regime we know GL theory breaks down), we need a theory which **can** predict the exponents. For this, we use the 3D-XY model.

4.2.3 3D-XY Model

We begin by looking at a collection of spins in a lattice as an approximation for a ferromagnet. These spins have an interaction energy given by[39]

$$H_{int} = -J\mathbf{s}_i \cdot \mathbf{s}_j, \tag{4.43}$$

where we assume $J = 0$ unless the spins $\mathbf{s}_i$ and $\mathbf{s}_j$ are nearest neighbors. If the spins are confined to move in only one dimension (up or down), then we have the Ising

[11] For a discussion of the *upper critical dimension* (which for GL theory is $D = 4$), see Refs. [39] or [37].

model, if they can rotate in all three, the Heisenberg model, and if they can only rotate in a plane, we have the XY model.

It is simple enough to write down the partition function Z in the presence of a magnetic field $\mathbf{B}$[39],

$$Z = \sum_{s_i} \exp[\frac{\mathbf{B} \cdot \sum_i \mathbf{s}_i + \frac{1}{2} \sum_{ij} J \mathbf{s}_i \cdot \mathbf{s}_j}{k_B T}], \tag{4.44}$$

where the sum is over all i and j and the factor of $\frac{1}{2}$ corrects for double counting.

Given the partition function, anyone can (in theory) calculate the physical properties of the system – for example heat capacity $C = k_B T^2 \frac{\partial^2 \log Z}{\partial T^2}$. In reality, this is not so easy. For one thing, it is hard to imagine Eq. 4.44 giving divergences. This only happens, in fact, when then number of spins summed over goes to infinity[40]. In general, the solution to this model is actually quite difficult, and our current understanding of the problem comes from renormalization-group theory.[12]

In this framework, the physical properties of the system can be evaluated for a three-dimensional lattice of spins using numerical simulations, series expansions, and other techniques[37]. Most recent estimates for two of the exponents in 3D-XY theory are[41, 42]

$$\nu = 0.672 \pm 0.002 \tag{4.45}$$

and

$$\alpha = -0.007 \pm 0.006. \tag{4.46}$$

Not surprisingly, these predictions agree very well with Eq. 4.40, as well as agreeing within the error bars of experimental data[38].

These numbers come from the XY model in three dimensions, a model that describes a 3D lattice of spins that can only rotate in a plane. The question now arises, why do these values work for other phase transitions, and why would the 3D-XY model be useful for a superconductor? The answer is one of the important ideas of critical phenomena: *Universality*.

[12]For an introduction to renormalization-group theory, see Refs. [39], [40], or [37].

The important feature of the XY model which extends its usefulness beyond ferromagnets is the degrees of freedom of the spin. Because, in the XY model, the spin is confined to a plane, the spin is a 2D vector, and requires two numbers to describe it. A spin that can rotate in three dimensions requires three numbers to describe it, up or down spin needs only one. In this manner, we can see that for the spin model, there are two important parameters, the dimension in space, D, and the dimension of the order parameter, usually called n. Thus the Ising model has $n = 1$, the Heisenberg $n = 3$, and the XY model $n = 2$.

Researchers have shown that phase transitions with order parameters of the same dimensions and samples with the same spatial dimensions belong to the same universality class. Within each class, the behavior near the critical point is expected to be the same, regardless of the material. Thus a ferromagnetic transition can be identical in behavior to that of water if they belong to the same universality class. In the liquid-vapor transition, the density difference $\rho_L - \rho_{critical}$ or $\rho_{critical} - \rho_V$ is a scalar, putting it in the same universality class as the Ising model.

Superconductors have an order parameter which is complex – described by magnitude and phase – so $n = 2$ for superconductors. Therefore, superconductors belong to the same universality class as the 3D-XY model, and exponents derived for the 3D-XY model should hold for the normal-superconducting phase transition in three-dimensional samples.

Dynamic scaling

There is one final exponent and its experimental consequences that we must discuss. The majority of our measurements will be conductivity measurements near T_c. However, in order to discuss the fluctuation conductivity $\Delta\sigma$ we must introduce the fluctuation lifetime, τ. Unlike specific heat, conductance measures dissipation, and any dissipative measurement depends not only on the size of the fluctuations, but also on their lifetime. Following our assertion that everything depends on ξ, we

write:

$$\tau \sim \xi^z, \tag{4.47}$$

where the exponent z is called the dynamic critical exponent. This makes all the other exponents static critical exponents.

The simplest arguments suggest that the fluctuations decay diffusively. In diffusion, length $\sim$ time$^{1/2}$[43, 37], thus we expect $z = 2$. If $z > 2$ the fluctuations decay more slowly than diffusively, which is not so hard to imagine (fluctuations stuck on defects or the like). If $z < 2$, the fluctuations decay faster than diffusively, which is harder to imagine. The result $z = 2$ is found in a more exhaustive manner in Ref. [44].

4.3 The Superconducting Phase Transition

We are now in a position to derive the equations we will use to describe the normal-superconducting phase transition. The derivation relies heavily on dimensional analysis and the fact that ξ dominates the behavior. In this section, we will closely follow the derivation in Ref. [45].

4.3.1 Scaling Relations in Superconductors

We already know that $\xi \sim |t|^{-\nu}$ and $\tau \sim \xi^z$. From Eq. 4.16 we know that $H_{c2} \sim \Phi_o \xi^{-2}$, which leads us to postulate

$$B \sim \Phi_o \xi^{-2} \sim \xi^{-2}, \tag{4.48}$$

keeping only terms which diverge. We know from Maxwell's equations that $\nabla \times \mathbf{E} = -\partial \mathbf{B}/\partial t$. We can make the derivatives dimensionless if we introduce $\tilde{x} = x/\xi$ and $\tilde{t} = t/\tau$, then

$$\frac{1}{\xi}\frac{\partial E}{\partial \tilde{x}} = -\frac{1}{\tau}\frac{\partial B}{\partial \tilde{t}} \tag{4.49}$$

which suggests that

$$\frac{E}{\xi} \sim \frac{B}{\tau}. \tag{4.50}$$

Combining Eqs. 4.47, 4.48, and 4.50 we find

$$E \sim \xi^{-1-z}. \tag{4.51}$$

We can apply a simple argument to determine how the current density J scales with ξ. We know that the power dissipated in a fluctuation will be $\sim JE\xi^D$. We also know the thermal fluctuations will have an energy k_BT (this has been one of the staples of our argument). If the fluctuation has a lifetime τ, then we can say

$$JE\xi^D \sim \frac{k_BT}{\tau} \tag{4.52}$$

or

$$J \sim \frac{k_BT}{E\xi^D\tau} \sim T\xi^{1-D}, \tag{4.53}$$

where J is now the D-dimensional current density. Eq. 4.53 also determines how the critical current scales near T_c.

This allows us to determine the fluctuation conductivity, $\Delta\sigma \equiv \sigma_{fl}$:

$$\sigma_{fl} = \frac{E}{J} = \frac{1}{T}\xi^{D-2-z}. \tag{4.54}$$

From Eq. 4.54 we can see that the fluctuation conductivity is ohmic ($E \propto J$). However, below T_c, the superconductor is not expected to respond linearly at all. Additionally, above T_c, we expect non-linear effects at high J. Eq. 4.54 is clearly not valid in these cases. We can extend the validity of Eq. 4.54 and include non-linear effects as a function of J, and write

$$\frac{E}{J} = \frac{\xi^{D-2-z}}{T} F_{\pm}\left(\frac{J\xi^{D-1}}{T}\right), \tag{4.55}$$

where $F_{\pm}$ are unknown functions above and below T_c. The argument of $F_{\pm}$ is chosen to be dimensionless (from Eq. 4.53), and thus obey scaling. In the limit as $J \to 0$,

above T_c the function in Eq. 4.55 becomes $F_+(0)$, a constant, and we recover Eq. 4.54.

Additionally, if $E \propto V$ and $J \propto I$ via simple geometric factors, then we can absorb the geometrical factors into the unknown functions and write[9, 10]

$$\frac{V}{I} = \xi^{D-2-z} \chi_{\pm} \left(\frac{I\xi^{D-1}}{T} \right), \tag{4.56}$$

where $\chi_{\pm}$ are two new unknown functions. We have also dropped the first factor of $1/T$, following convention[10]. Exactly why the first factor of $1/T$ is dropped – but not the factor in the argument of $\chi_{\pm}$ – is unclear, but because the temperature T does not change appreciably in the critical regime, Eqs. 4.55 and 4.56 are equivalent.

Eq. 4.56 is the major theoretical prediction that researchers have tried to verify for more than ten years. This result, and the predictions for the exponents given by 3D-XY theory, will be the theoretical foundations for our measurements.

Useful limits

Eq. 4.56 has two useful limits. Above T_c as $I \to 0$, the function χ_+ approaches a constant. Thus, in the limit of low currents,

$$\frac{V}{I} \equiv R_L = \xi^{D-2-z} \chi_+(0) \sim |t|^{\nu(2+z-D)}. \tag{4.57}$$

There is another interesting limit when $T = T_c$. At T_c, ξ is infinite. However, we know that the conductivity remains finite. The only way for the conductivity to remain finite while ξ diverges is if the function χ is a power law such that all powers of ξ exactly cancel.[13] This implies

$$\frac{V}{I} \sim \xi^{D-2-z} \left(\frac{I\xi^{D-1}}{T} \right)^{\frac{2+z-D}{D-1}} \sim I^{\frac{2+z-D}{D-1}} \tag{4.58}$$

or

$$V \sim I^{\frac{z+1}{D-1}}, \tag{4.59}$$

[13]This is what is known in physics as "a neat trick."

in other words, V is a power law in I **exactly** and **only** at T_c. We will use this fact extensively in the next chapter.

4.3.2 Theoretical Predictions

Theoretical predictions, especially in the vortex-glass transition, are complicated by the fact that the exponents are not well-known theoretically[10, 19, 46, 47]. Moreover, there is still debate whether the vortex-glass transition exists at all[48, 49, 50, 51]! For a normal-superconducting phase transition to occur, the superconductor must go from a resistive state to a state with zero resistance[52]. In practice, it is hard to distinguish between zero resistance (phase transition) and immeasurably small resistance (no phase transition). We circumvent this difficulty by looking at zero field, where the existence of a phase transition is not in doubt and we expect to see 3D-XY exponents.

It is useful to show exactly what a normal-superconducting transition is expected to look like (be it zero field or the vortex-glass transition). Here we show theoretical predictions, to be compared with experimental data later.

$I - V$ isotherms

Most of our data are voltage vs. current ($I - V$) curves, each taken at a different temperature. Our data is taken typically over many decades of current and voltage, so we plot it on a log-log scale. We expect to see $I - V$ curves as shown in Fig. 4.4.

One of the major advantages of a log-log plot is the fact that, from Eq. 4.59, we expect the isotherm at T_c to be a straight line. The slope of the isotherm will then give us z, as the slope $= \frac{z+1}{D-1}$. We can also identify ohmic behavior (slope $= 1$ on a log-log plot). This is marked with a dashed line in Fig. 4.4. The isotherm at the highest temperature in the figure is ohmic over the whole range of currents, thus we conclude that the isotherm is in the normal state. Isotherms above T_c but

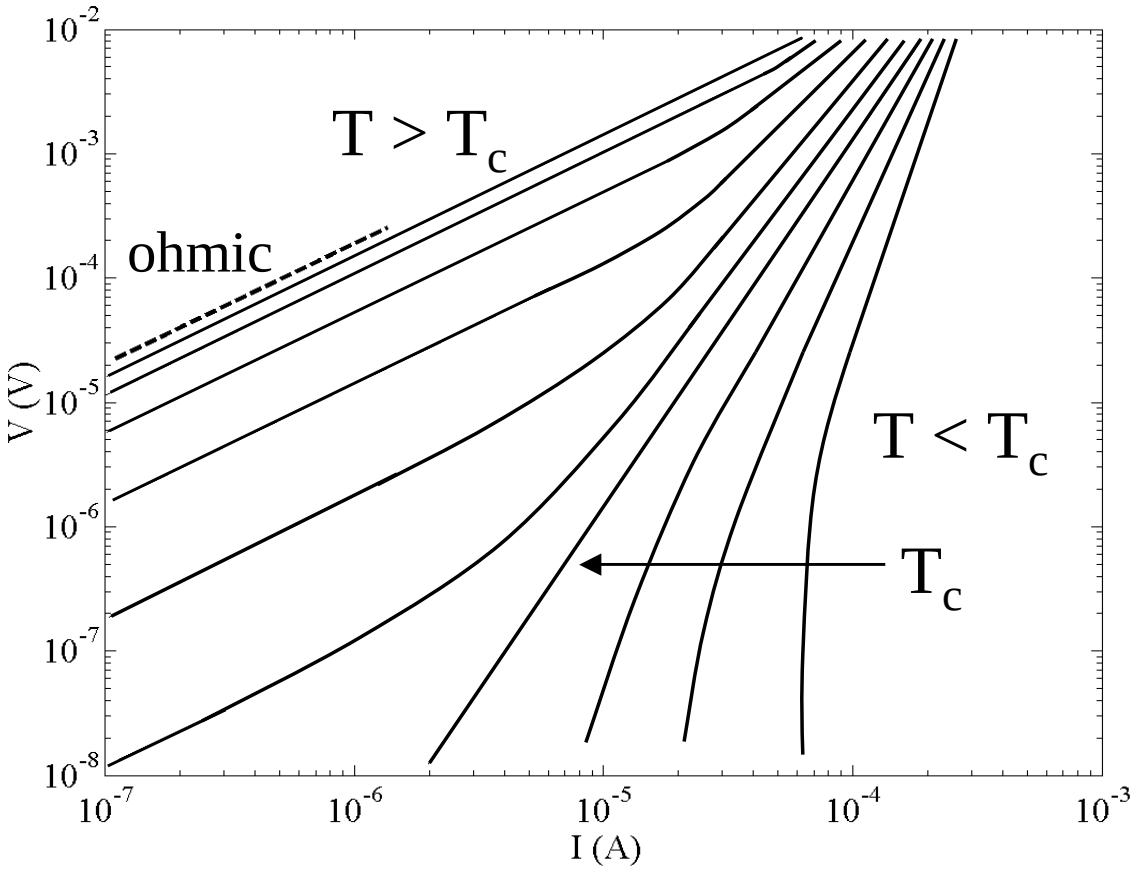

Figure 4.4: Schematic of expected $I - V$ curves from Eq. 4.56. The dashed line indicates a slope of 1, or ohmic. The isotherm at T_c is clearly identifiable as a power law (straight line with slope $\neq 1$ on the log-log plot). Above T_c for low currents, the isotherms bend towards ohmic behavior. Below T_c, the isotherms increase in slope as current decreases.

close enough to T_c to be affected by fluctuations are non-linear at high currents and become linear at lower currents, as predicted by Eq. 4.57. Below T_c, we see the isotherms drop rapidly in voltage, indicating a transition to a zero voltage state.

Using Eq. 4.59, we can get z from the isotherm at T_c. By analyzing the ohmic behavior at low currents (usually called ohmic "tails"), if we know T_c and z, we can find ν from Eq. 4.57.

Derivative plot

Sometimes finding T_c is not as simple as it seems from Fig. 4.4. We can employ another method to find T_c and z. If we take the logarithmic derivative, $\partial \log V / \partial \log I$, at T_c we have:

$$\frac{\partial \log V}{\partial \log I} = \frac{z+1}{D-1}, \tag{4.60}$$

i.e., a horizontal line whose intercept should give us a value for z. In fact, T_c will be the *only* horizontal isotherm in the derivative plot. The expected derivative plot is sketched in Fig. 4.5.

Here, T_c is easily identified as the horizontal isotherm. Moreover, it is easy to see another prediction, called the *opposite concavity criterion*[12]. We have predicted that isotherms equal distances from T_c at the same current level should have opposite concavities. These opposite concavities translate to increasing or decreasing slope on the derivative plot, and thus the criterion is easy to identify. Finally, we can see for $T > T_c$ the isotherms tend to $\partial \log V / \partial \log I = 1$ (ohmic behavior), again as predicted by Eq. 4.57.

Data collapse

The final prediction is what is called the *data collapse*. We can re-write Eq. 4.56 in a suggestive manner, namely,

$$\frac{V}{I}\left|\frac{T-T_c}{T_c}\right|^{\nu(1-z)} = \chi_{\pm}\left(\frac{I}{T}\left|\frac{T-T_c}{T_c}\right|^{-2\nu}\right), \tag{4.61}$$

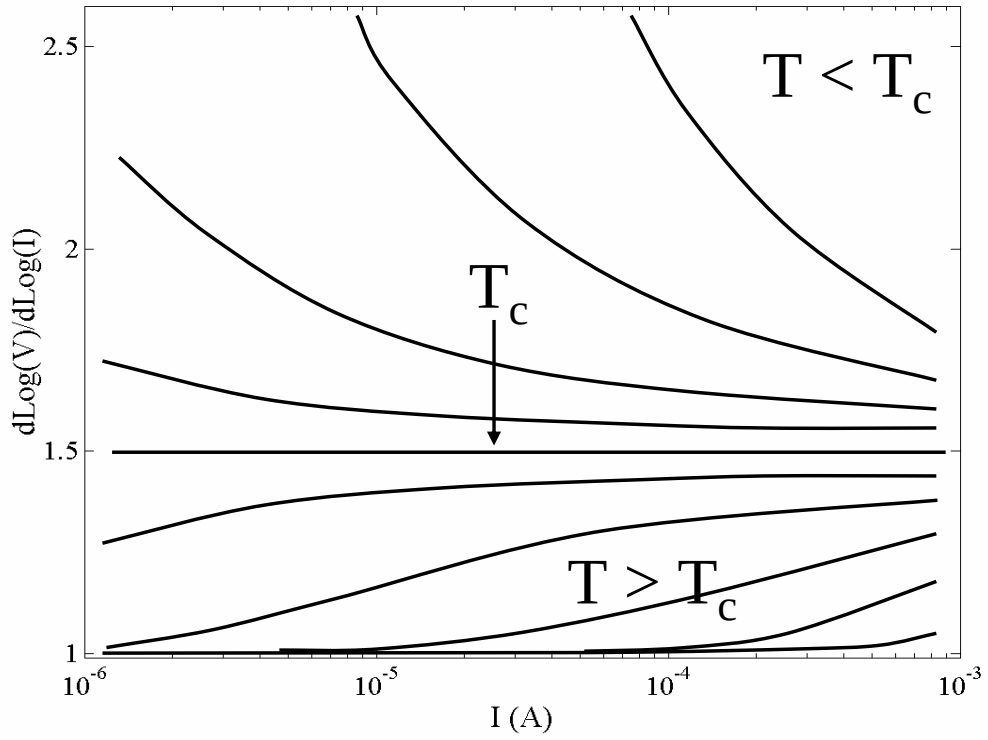

Figure 4.5: Schematic of expected $\partial \log V / \partial \log I$ vs I. T_c is identified as the horizontal isotherm. Isotherms above and below T_c display opposite concavity about T_c[12]. $\partial \log V / \partial \log I = 1$ indicates ohmic behavior.

where we have explicitly plugged in $D = 3$ for the dimension. We can see that if we plot the left-hand side of Eq. 4.61 vs. the arguments of the unknown functions $\chi_\pm$ from the right-hand side, then the isotherms will fall upon two curves, χ_+ for above T_c, and χ_- below T_c. Thus, if we are looking at a true phase transition where Eq. 4.61 applies, then all of the isotherms from Fig. 4.4 will collapse onto two distinct curves. A data collapse is sketched in Fig. 4.6. Data collapse is seen as the "icing on the cake" and the final proof that a phase transition does indeed exist. Moreover, because the data collapse depends on the values for T_c, z, and ν, a good data collapse is evidence of the correct choices for the critical parameters.

Derivative scaling

Another clever trick is to use derivative scaling. Starting with Eq. 4.56, we can take $\partial \log V / \partial \log I$ to find[15, 45]

$$\frac{\partial \log V}{\partial \log I} = \frac{I\xi^{D-1}}{T} \frac{\chi'_\pm \left(\frac{I\xi^{D-1}}{T} \right)}{\chi_\pm \left(\frac{I\xi^{D-1}}{T} \right)}. \tag{4.62}$$

The right-hand side of this equation is just another function of the variable $\frac{I\xi^{D-1}}{T}$, thus Eq. 4.62 can be rewritten as

$$\frac{\partial \log V}{\partial \log I} = \Lambda_\pm \left(\frac{I\xi^{D-1}}{T} \right), \tag{4.63}$$

where $\Lambda_\pm$ are new unknown functions.

In other words, we can plot $\partial \log V / \partial \log I$ vs. $\frac{I\xi^{D-1}}{T}$ and all the isotherms should scale in a similar manner to the regular $I - V$ scaling collapse. This is yet a further test of the phase transition.

This test is particularly useful for the following reason. Instead of using the low-current data (Eq. 4.57) to find ν, you can use the scaling form for J itself, Eq. 4.53. Because $J \sim |t|^{\nu(1-D)}$, we can pick a current density J such that we get the same value of $\partial \log E / \partial \log J$ for different isotherms. If we plot these values of J vs. $|t|$, then the slope on a log-log plot should give $\nu(1 - D)$[19].

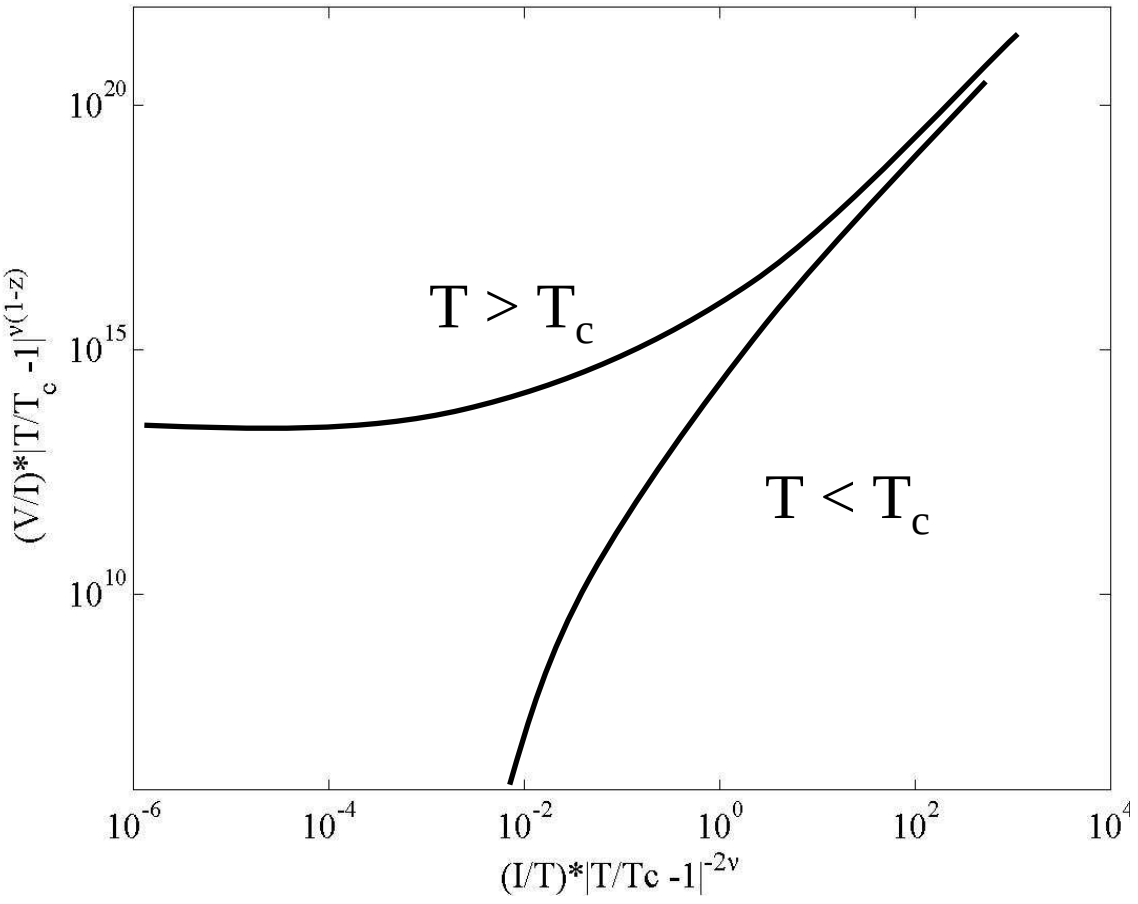

Figure 4.6: Schematic of expected data collapse. The left-hand side of Eq. 4.61 vs. the argument of the unknown functions $\chi_{\pm}$. All the isotherms from Fig. 4.4 fall on one of two curves for above and below T_c. A good data collapse is viewed as strong evidence for a phase transition as well as confirmation of the correct choices for T_c, z, and ν.

Strachan has shown that derivative scaling does this exact procedure, except not for one arbitrary value of $\partial \log E/\partial \log J$, but for all values of $\partial \log E/\partial \log J$ at the same time[53]. Thus, derivative scaling is more exacting than conventional tests to find ν.

Specific heat

For good measure, we will show a schematic of what is expected from specific heat. Critical behavior in specific heat has been well verified in ^{4}He[54, 55], and we expect specific heat in the critical regime of superconductors to look the same. The specific heat is expected to go as:[54, 55]

$$C = \frac{A^{\pm}}{\alpha}|t|^{-\alpha} + B^{\pm}, \tag{4.64}$$

where $B^{\pm}$ are first-order corrections to the scaling form[55]. The exponent α and the ratio A^+/A^- are known from theory and experiment. It is predicted that $B^+ = B^-$. The most recent (and careful) experiment on specific heat in ^{4}He gives[55]:

$$\alpha = -0.0129 \pm 0.0004 \tag{4.65}$$

and

$$A^+/A^- = 1.054 \pm 0.001. \tag{4.66}$$

In the limit as α goes to zero,[14]

$$\lim_{\alpha\to 0} \int \frac{1}{t^{\alpha+1}}\, dt = \lim_{\alpha\to 0} -\frac{1}{\alpha} t^{-\alpha} = \ln(t). \tag{4.67}$$

So, because $\alpha \approx 0$, we expect

$$C \approx -A^{\pm} \ln(t) + B^{\pm}. \tag{4.68}$$

Thus, on a semi-log plot, the specific heat will be two nearly parallel lines with slightly different slopes A^+ and A^-. Over the limited range of accessible temperatures, this plot looks like parallel lines with different intercepts, as sketched in Fig. 4.7.

[14] What follows is another neat trick.

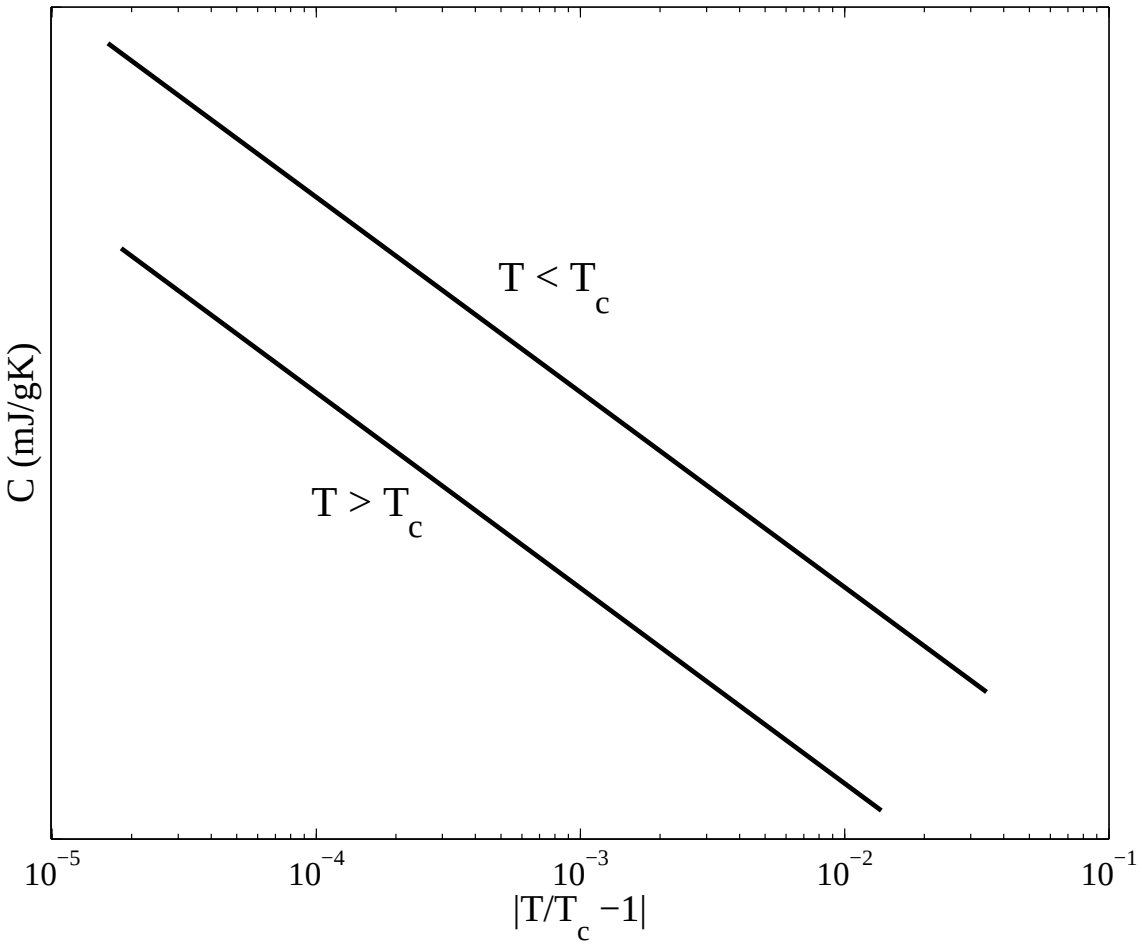

Figure 4.7: Expected specific heat in the critical regime. On a semi-log plot, we expect two nearly parallel lines. The apparent different intercepts are due to A^+ and A^-.

Chapter 5

Transport Measurements in Films

Our work builds on previous dc transport measurements on superconductors. For more than ten years, researchers have looked at $I - V$ measurements for evidence of phase transitions, both in field and in zero field. Many researchers have claimed to see the phase transition and have quoted critical exponents, but our recent work has cast doubt on the methods used to find T_c, ν, and z.

In this chapter, we will examine the conventional method of data analysis and its pitfalls. In an attempt to overcome these pitfalls, we will introduce a more sensitive tool for finding T_c and z, the derivative plot. This tool uncovers new problems in the form of unexpected ohmic behavior at low currents, the so-called "ohmic tails". These ohmic tails and their possible sources are the main focus of this dissertation.

5.1 Conventional Analysis

The predictions made by Fisher, Fisher, and Huse outlined in Ch. 4 [9, 10, 11] led to a large body of experimental and theoretical work on the superconducting phase transition in field and in zero field. Using $I - V$ curves, a consensus has emerged the vortex-glass transition exists in YBCO[19, 56, 57, 58, 59, 60, 61, 62, 63, 64, 65, 66, 67], as well as in other materials[68, 69, 70], although the reported exponents range from $z = 1.25$ to 6 and $\nu = 0.63$ to 2[71, 72]. Researchers have also used

$I - V$ curves to examine the normal-superconducting transition of YBCO in zero field[46, 73, 71, 72], where even here there are disagreements in the exponents.

Nonetheless, this general consensus has led $I - V$ curves to become the favorite tool to look at the superconducting phase transition, especially in field. This is despite arguments that agreement with scaling is misleading[48, 74] and arguments that there is actually no phase transition at all in a field[49, 50, 51]. There are also problems within the framework of scaling, such as the range of validity in voltage[75, 76], and finite size effects[46, 20].

Our current work builds upon previous work in our group. However, to understand the context for our current (and previous) work, we must first discuss the conventional method of analyzing $I - V$ curves.

5.1.1 The Data: dc $I - V$ Curves

We begin with the conventional analysis of sample mcs146. This is one of our best films. X-ray diffraction shows clear c-axis orientation and no evidence for impurity phases, and ac susceptibility gives $\Delta T_c = 0.15$ K. We patterned this film into a bridge with dimensions 20×100 μm^2. The R vs. T in the transition region is shown in Fig. 5.1. Here, $T_c = 91.5$ K (according to our definition of T_c) and $\Delta T_c = 0.5$ K. We measured the thickness of mcs146 with an AFM and found that $d = 2100$ Å.

We measure the voltage V across the bridge as a function of applied current I.[1] This is akin to the total conductance, $\Sigma = I/V$. However, what we wish to examine is the fluctuation conductivity, $\Delta\sigma$ (see Fig. 4.3). To do this, we must separate the voltage generated by the fluctuations, V_{fl}, from the voltage generated by the electrons in the normal state, V_n. In the two-fluid model, the fluctuations and the normal electrons are two different parallel channels for the current to flow through.

[1]Each voltage V consists of many reverse-polarity measurements, as described in Sec. 3.1.1.

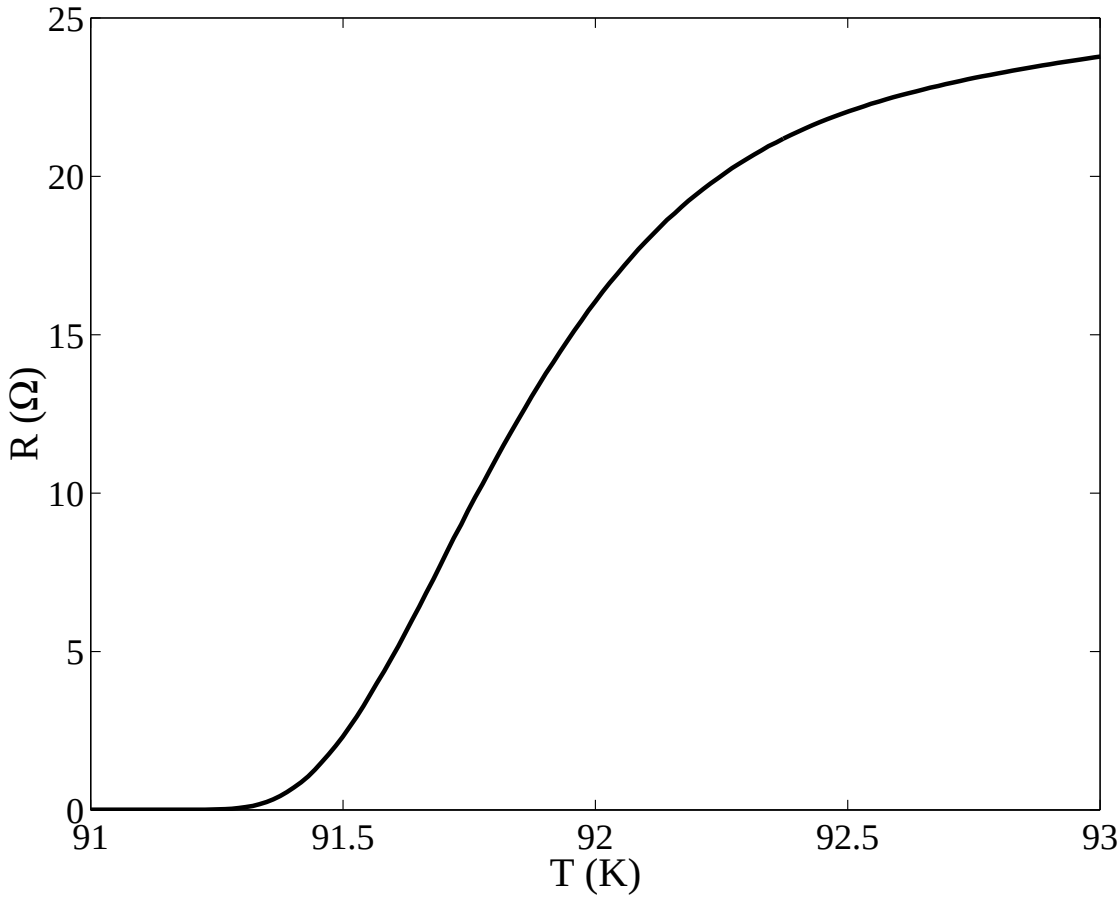

Figure 5.1: R vs. T for sample mcs146 near the transition. By our definition from Ch. 2, $T_c = 91.5$ K and $\Delta T_c = 0.5$ K. The bridge dimensions for this sample are 20×100 μm^2. The film is 2100 Å thick.

Thus,

$$V = V_n = V_{fl} \text{ and } I = I_n + I_{fl}, \tag{5.1}$$

i.e., a simple parallel circuit. But the normal channel is a simple resistor, $V_n = I_n \cdot R_n$, so

$$I_{fl} = I - \frac{V_n}{R_n}. \tag{5.2}$$

How can we know R_n when we are in the middle of the superconducting transition? We cannot measure it, but we can extrapolate the value of R_n into the transition region. The full R vs. T is shown in Fig. 5.2. The dotted line in Fig. 5.2 is the fit to the normal-state resistance, $R_n(T) = aT + b$. We extrapolate this resistance into the transition region to find

$$I_{fl} = I - \frac{V}{aT + b}, \tag{5.3}$$

and

$$V_{fl} = V, \tag{5.4}$$

where V is the measured voltage and I is the applied current. Following convention, we will drop the subscripts on V_{fl} and I_{fl}, however, it is important to remember that we have subtracted out the normal channel.

We then take $I - V$ curves in the transition region. These curves are shown in Fig. 5.3. These $I - V$ curves, and the $I - V$ curves we will usually show, will be only the fluctuation channel. We find many similarities between Fig. 5.3 and the expected $I - V$ curves from Fig. 4.4. At high temperatures, the $I - V$ curves are parallel to each other, and parallel to the dotted line which has a slope of 1. This means $V \sim I$, or ohmic. At intermediate temperatures, we see non-linear behavior at high currents and ohmic behavior at low currents. At the lowest temperatures, we see the isotherms increase in slope as I decreases, also as expected. Only a few tenths of a kelvin below the lowest temperature pictured in Fig. 5.3, the voltage becomes too small to measure with our nanovoltmeter. All this agrees qualitatively with what we expected (Fig. 4.4).

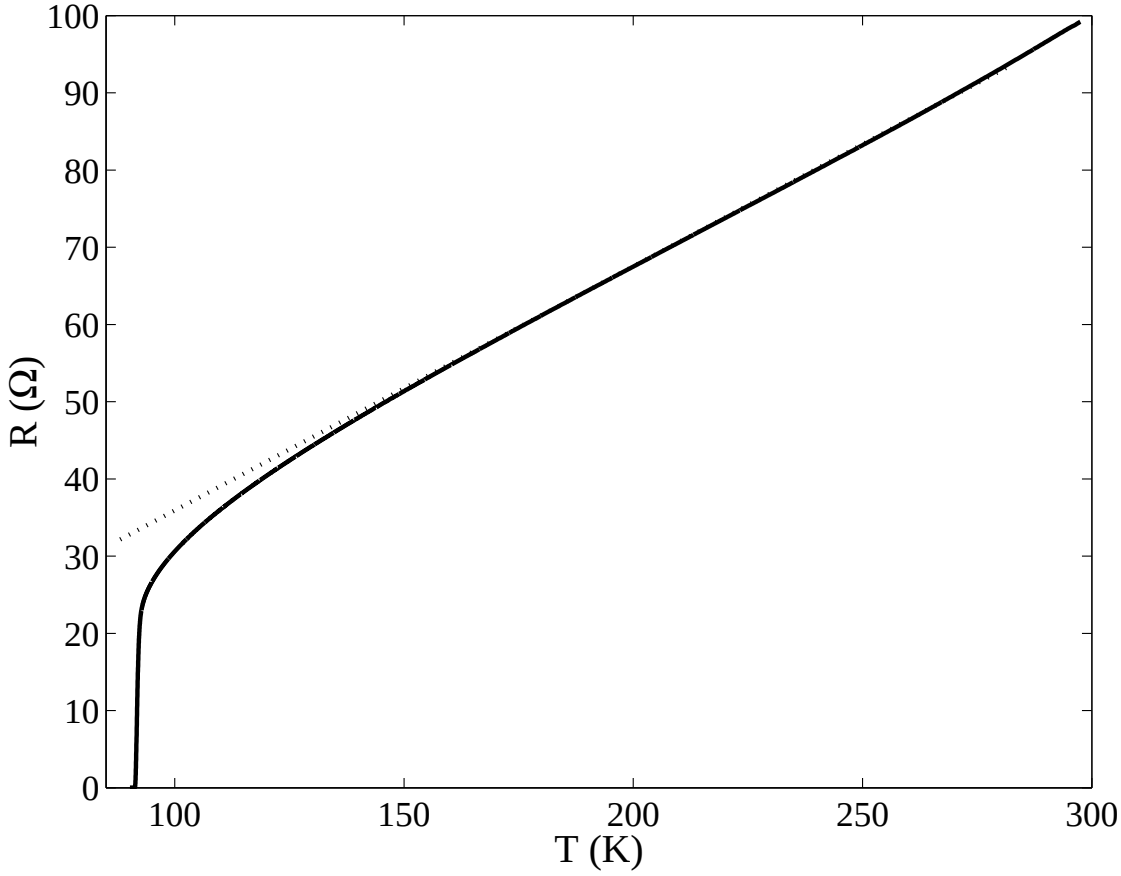

Figure 5.2: R vs. T for sample mcs146 from 77K to room temperature. The dotted line is the fit, $R_n(T) = aT + b$, to the temperature dependence of the normal-state resistance.

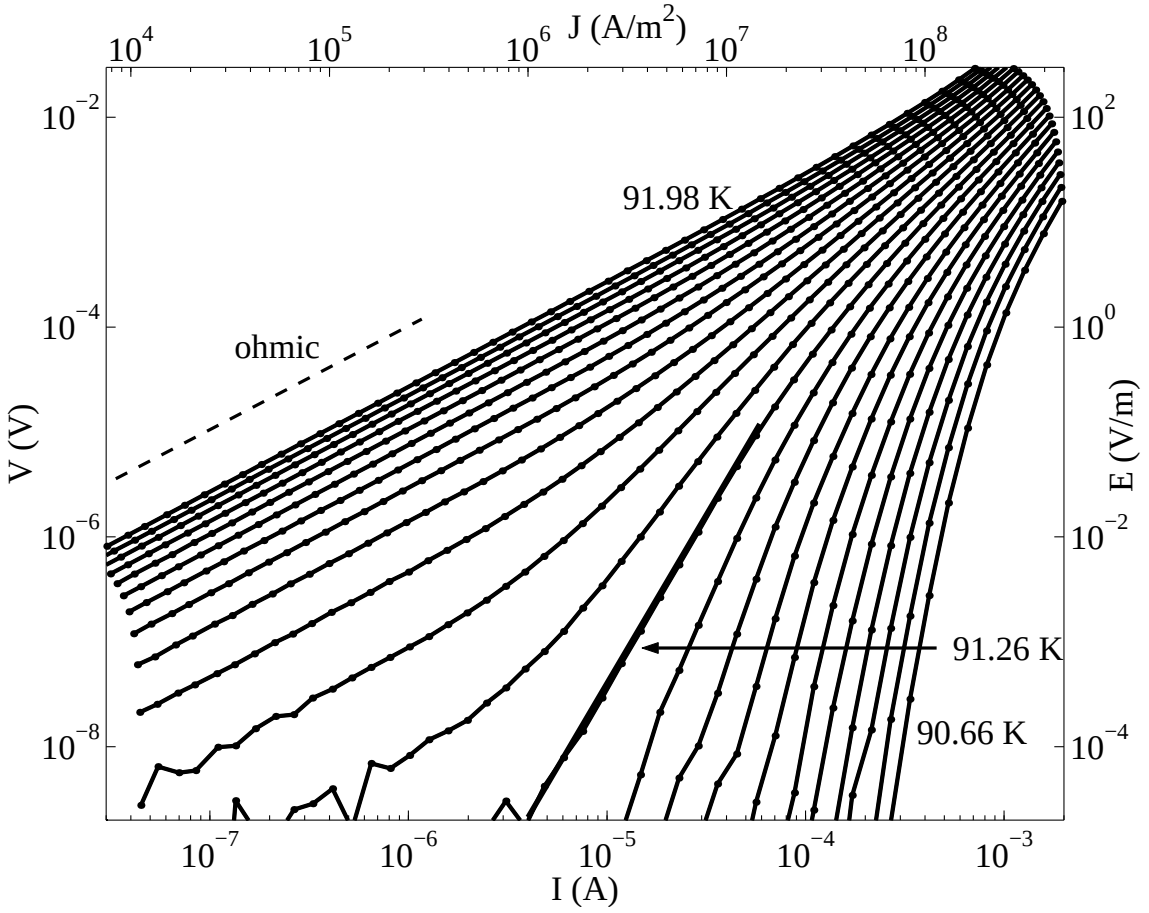

Figure 5.3: $I - V$ curves for sample mcs146 (2100 Å thick). The dashed line has a slope of one (ohmic). The solid line at 91.26 K is a power-law fit at lower voltages. Isotherms are separated by 60 mK. Note that the normal channel has been subtracted, as described in the text.

5.1.2 Finding the Critical Parameters

Now that we have the fluctuation channel $I - V$ data, we must find the critical parameters for the transition: T_c, ν, and z. To determine these parameters, we will follow the outline given in Sec. 4.3.2.

Power law: T_c and z

There are some aspects of our experimental $I - V$ curves which do not conform to expectations. Most striking is the fact that there is no isotherm which is a straight line on the log-log plot over all decades in current and voltage. If we exclude the data above $\approx 10^{-5}$ V, the curve at 91.26 K (marked by the solid line in Fig. 5.3) appears to be straight. The conventional justification for excluding this high-voltage data is that the critical regime is not only bounded in temperature, but also in current and voltage, and at high voltages, the sample is driven out of the critical regime[75, 20].

If we exclude this data, then we can identify $T_c = 91.26$ K. We can fit this isotherm to the form $V \sim I^{(z+1)/2}$ and extract a value for z. The solid line in Fig. 5.3 has a slope of 3.19, which gives $z = 5.35$ (slope $= (z + 1)/2$). This is very similar to the z values reported for the vortex-glass transition (oddly enough)[71], and at odds with some exponents reported for zero field, $z = 1.25$[72], $z = 2$[46], and $z = 3$[73]. We expect $z = 2$ for diffusive dynamics.

Low-current ohmic tails: ν

Strange value for z notwithstanding, we have identified the critical temperature T_c and the dynamic critical exponent z. All that remains is to find the static exponent ν. To do this, we use Eq. 4.57. We find the resistance of the low-current ohmic tails and plot the resistance $\log(R_L)$ vs. $\log(|T/T_c - 1|)$. Because $R_L \sim |T/T_c - 1|^{\nu(z-1)}$ (for $D = 3$), the slope of the graph will give us a value for ν, provided we know z. This is graphed in Fig. 5.4.

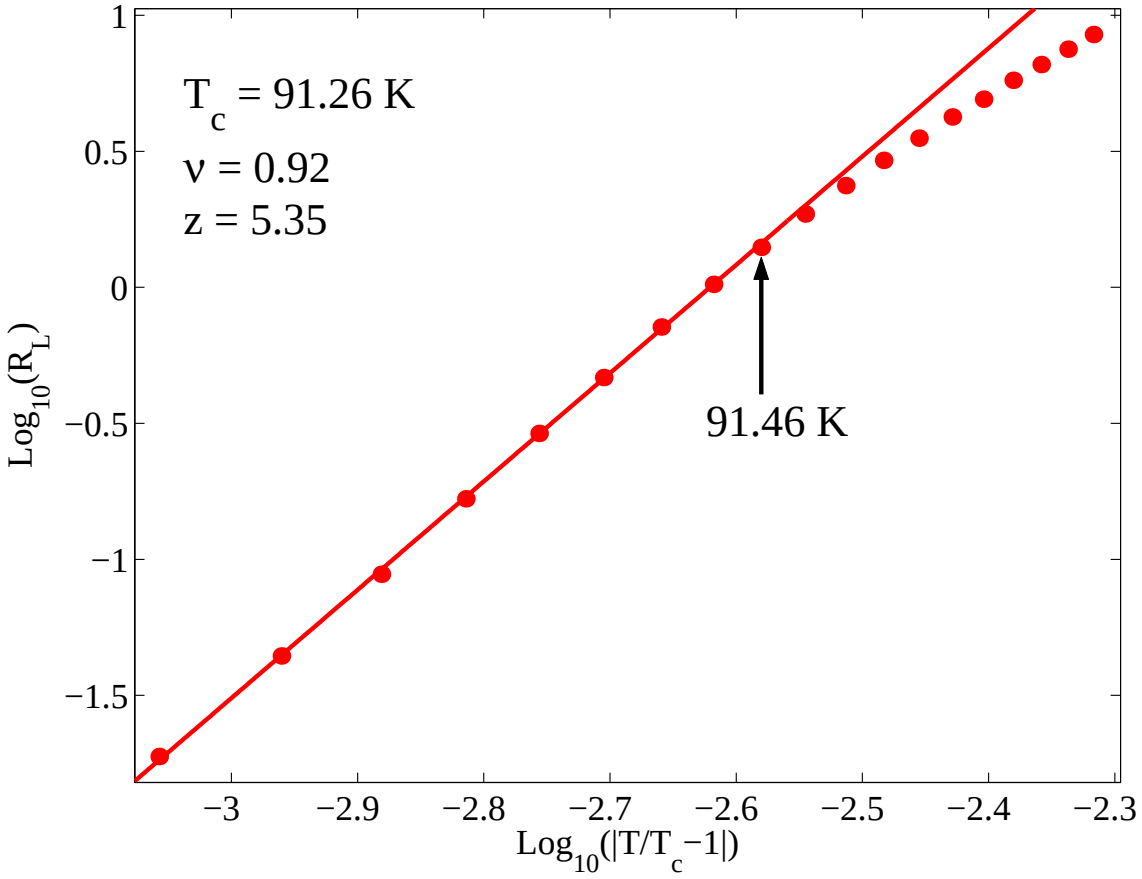

Figure 5.4: R_L vs. $\log(|T/T_c - 1|)$ for sample mcs146. The straight line is a fit for the expected power-law behavior, $R_L \sim |T/T_c - 1|^{\nu(z-1)}$. Where the isotherms begin to deviate, at about 91.46 K, is conventionally labelled the extent of the critical regime. Each point is separated by 20 mK.

Again we find deviations from the expected behavior. Instead of a straight line on a log-log plot, Fig. 5.4 shows systematic deviations beginning about 91.46 K and becoming more pronounced at higher temperatures. However, we do not expect Eq. 4.57 to be valid at all temperatures, rather only in the critical regime. Thus, the isotherms above 91.46 K which deviate from linearity are conventionally considered outside the critical regime. The last temperature which agrees with the fit, 91.46 K, determines the size of the critical regime. In this case, $|T - T_c| = |91.26\text{K} - 91.46\text{K}| = 0.2$ K, not far from the estimated size of the critical regime from Eq. 4.31. Because we expect the transition to be symmetric, 91.06 K should be the lowest temperature in the critical regime.

Now we have T_c, ν, z, and the isotherms expected to agree to scaling – all the relevant parameters for the transition.

Data collapse

Now that we have the necessary ingredients, we can test to see if we can, indeed, ice the cake (to continue the metaphor from Ch. 4). We recall Eq. 4.61,

$$\frac{V}{I}\left|\frac{T-T_c}{T_c}\right|^{\nu(1-z)} = \chi_{\pm}\left(\frac{I}{T}\left|\frac{T-T_c}{T_c}\right|^{-2\nu}\right), \tag{5.5}$$

and plot the left-hand-side of Eq. 4.61 vs. the arguments of the unknown functions $\chi_{\pm}$. If we have found the correct critical parameters, and if there is indeed a second-order phase transition, then all the isotherms should fall on two curves, for above and below T_c (the functions χ_+ and χ_-). The collapse of isotherms from Fig. 5.3 is shown in Fig. 5.5.

Although there appear to be systematic deviations (shown in Fig. 5.6) from the collapse, one cannot reasonably expect a perfect collapse from experimental data, and this collapse is not worse than others in the literature[73]. This type of collapse is what has been offered in hundreds of papers as proof of a phase transition, especially the vortex-glass transition; and it is these hundreds of papers which have created a

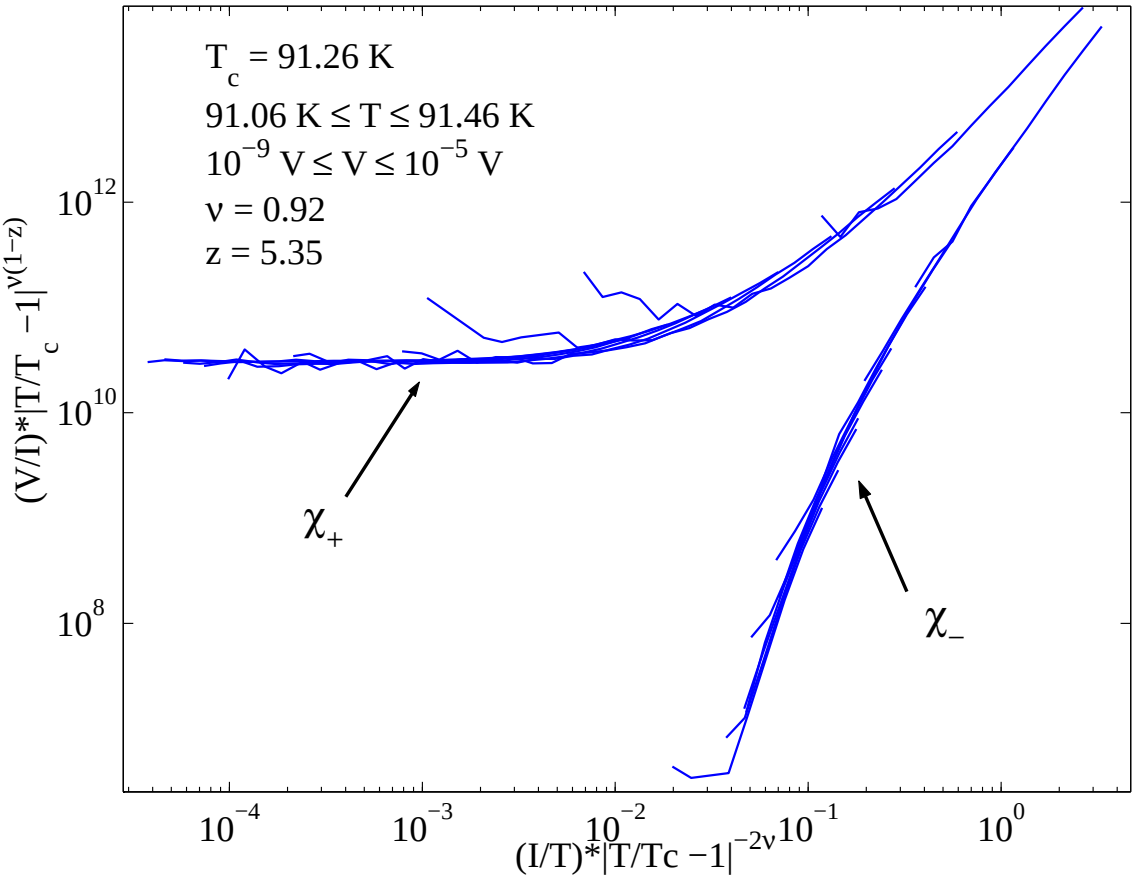

Figure 5.5: Conventional data collapse for sample mcs146. The critical parameters are listed in the figure. There are systematic deviations, nonetheless, the collapse is not unconvincing.

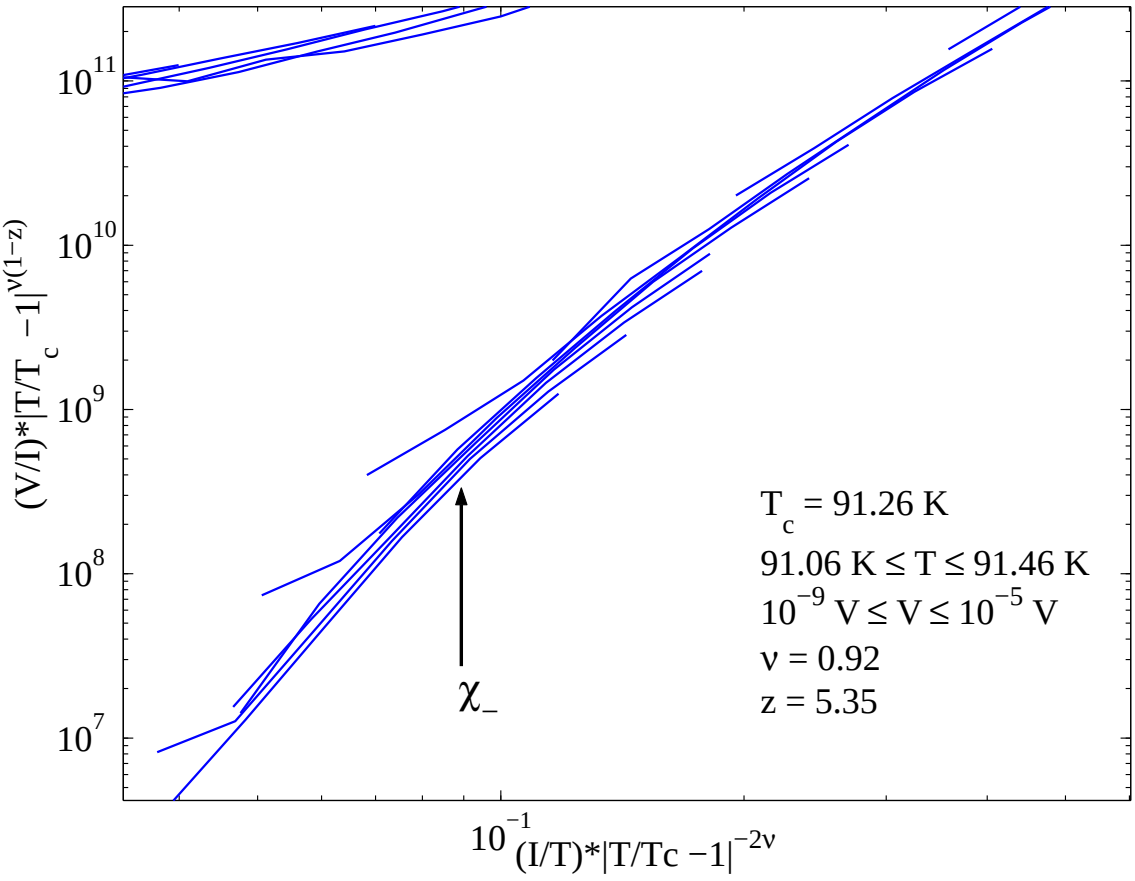

Figure 5.6: Conventional data collapse for sample mcs146, showing a zoom of the χ_- branch. The critical parameters are listed in the figure. In this figure, the systematic deviations are obvious.

consensus that the vortex-glass transition exists.

5.1.3 Results of the Conventional Analysis

There are several doubts that should occur to any reasonable scientists upon explanation of the conventional data analysis. One of these doubts comes from a quick survey of the literature. As mentioned earlier, there is a wide range of reported values for the critical exponents, especially in the vortex-glass transition.[2] These

[2]See the table in Ref. [72] and Ref. [71] and [75] for a quick look at the wide variety of critical exponents for the vortex-glass transition.

exponents all come from similar samples in similar magnetic fields, and all use a data analysis similar to the analysis outlined here – and yet the measured dynamic exponents range from $z = 1.25$ to $z = 6$!

Other doubts come from removing data at higher voltages. In the vortex-glass transition, data at higher voltages are attributed to "free flux flow"[75, 20] and are summarily removed. But the electric field (and hence the voltage) at which this free flux flow occurs is ill-defined, and most researchers define it as the voltage where deviations from scaling occur. This means data which disagrees with scaling is thrown away (although a somewhat reasonable explanation is given for discarding the data). This selective omission of data is more difficult to justify in zero field (there are no vortices to flow freely), and perhaps for this reason, data collapses in low fields are considered "uncontrolled"[72].

In addition to the selective omission of data, there is a serious problem with the exponents derived from the conventional data analysis. It is indeed compelling that data at $\mu_o H = 2$ T, 3 T, and 4 T all fall upon the same curves in a data collapse using the same exponents[3, 56], implying that the phase transitions in these fields are just one phase transition – the vortex-glass transition. But this same compelling evidence becomes worrisome when data in very low and zero magnetic fields *also* yield the same exponents[71]. No one expects the zero-field and the vortex-glass transitions to give the same exponents. If the vortex-glass exponents are similar to zero-field exponents, they are expected to be 3D-XY exponents, not the consensus values of $\nu \approx 1.2$, $z \approx 5$.

These drawbacks prompted us to take another look at the vortex-glass transition to see if we could determine why so many people got so many different exponents, and why the exponents, even in low fields, seemed to be very different from 3D-XY exponents.

5.2 A More Critical Look at the Transition

The problems listed above led our previous group member, D. R. Strachan, to re-examine the vortex-glass transition. Surprisingly, he found that he could arbitrarily choose an isotherm for the transition temperature, provided that isotherm did not have an ohmic tail (in Fig. 5.3, we could choose any isotherm below 91.26 K). With that isotherm as the transition temperature, he was able to carry through the data analysis outlined above, and demonstrated three data collapses for the same experimental data. Each collapse had different values for the transition temperature, ν, and z[12]. Of course, for each data collapse, Strachan chose a different range of allowable voltages, and a different range of temperatures, as dictated by the $\log(R_L)$ vs. $\log(|T/T_c - 1|)$ plots. Strachan's three data collapses are shown in Fig. 5.7.

The end result is very upsetting: using the conventional data analysis as it is used in hundreds of papers, Strachan was able to show not one, but *three* reasonable data collapses, each with its own set of critical parameters. If there is a vortex-glass transition, it seems unlikely that $z = 5.46$ *and* $z = 10.1$ *and* $z = 13.1$, as implied by Strachan's work[12].

Strachan reasoned that what was needed was a better method for determining whether a transition had occurred. It was not that scaling didn't work, but the opposite – scaling seemed to work too well.

5.2.1 Derivative Plot

To determine the transition temperature (in the vortex-glass or zero-field transitions), you must look carefully at the curvature of the isotherms. Again, as shown in Fig. 4.4, we expect $I - V$ curves above T_c to have positive curvature, those below T_c to have negative curvature[19, 75]. Conventionally, researchers choose an isotherm which looks linear on a log-log plot over the largest number of decades. This isotherm separates positive curvature from negative curvature, at least in the-

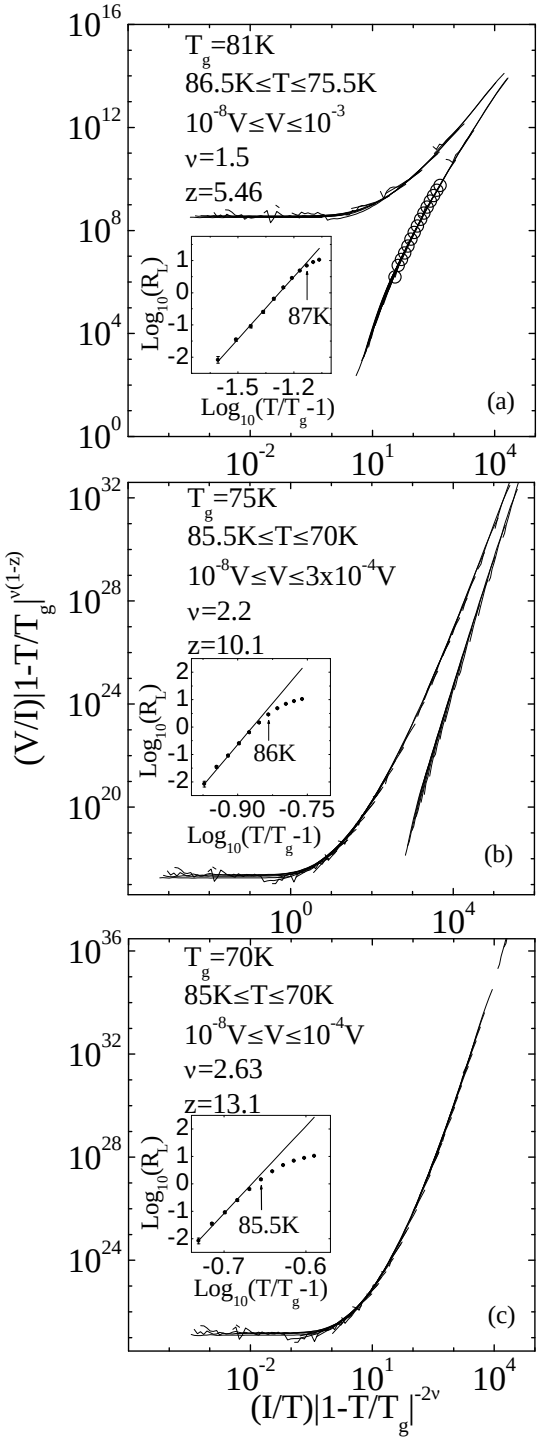

Figure 5.7: By changing T_c, z, and ν, Strachan was able to demonstrate three different data collapses for the same set of experimental data. This showed that a data collapse was not conclusive evidence for a phase transition. Figure from Ref. [12].

ory.

There are better ways to find the isotherm which is a straight line. There is a simple method of differentiating a straight line from other nearly straight lines: take the derivative. If the curve in question really is a straight line, then its derivative should be obvious as a horizontal line. Following J. M. Repaci[77], we plot the derivatives of $\log(V)$ vs. $\log(I)$ isotherms. We expect a figure similar to that of Fig. 4.5. The plot of $\partial \log V/\partial \log I$ vs. I for the isotherms in Fig. 5.3 is shown in Fig. 5.8.

The isotherms at the extreme temperatures in Fig. 5.8 agree with expectations. The highest temperatures are slightly nonlinear ($\partial \log V/\partial \log I > 1$) at high currents and rapidly become ohmic ($\partial \log V/\partial \log I = 1$) at lower currents. The lowest temperatures are non-linear, and increase in slope as current decreases.

The intermediate temperatures do not agree with our expectations (Fig. 4.5). Most striking is the fact that the conventional choice for T_c, 91.26 K, is not horizontal at all! In fact, what we thought was a straight line in Fig. 5.3 was merely a peak in $\partial \log V/\partial \log I$. This peak in $\partial \log V/\partial \log I$ occurs at other temperatures as well, both above and below 91.26 K. Below 91.26 K, the isotherms are quickly limited by our voltage sensitivity, nonetheless, we can see the isotherms begin to decrease in slope as current decreases.

It seems as though there is nothing special about the isotherm at 91.26 K, except that it does not have a pronounced ohmic tail. The fact that it does not have an ohmic tail is due solely to the fact that the data reach the voltage sensitivity limit, although given enough voltage sensitivity, the derivative plot suggests that the isotherm at 91.26 K would have an ohmic tail, as would the isotherms at lower temperatures.

Finally, when looking at the derivative plot, we can find **no** isotherm which is horizontal over a wide range of current. This seems to imply that there is no T_c, and thus no phase transition! The apparent lack of a transition is a cause for concern.

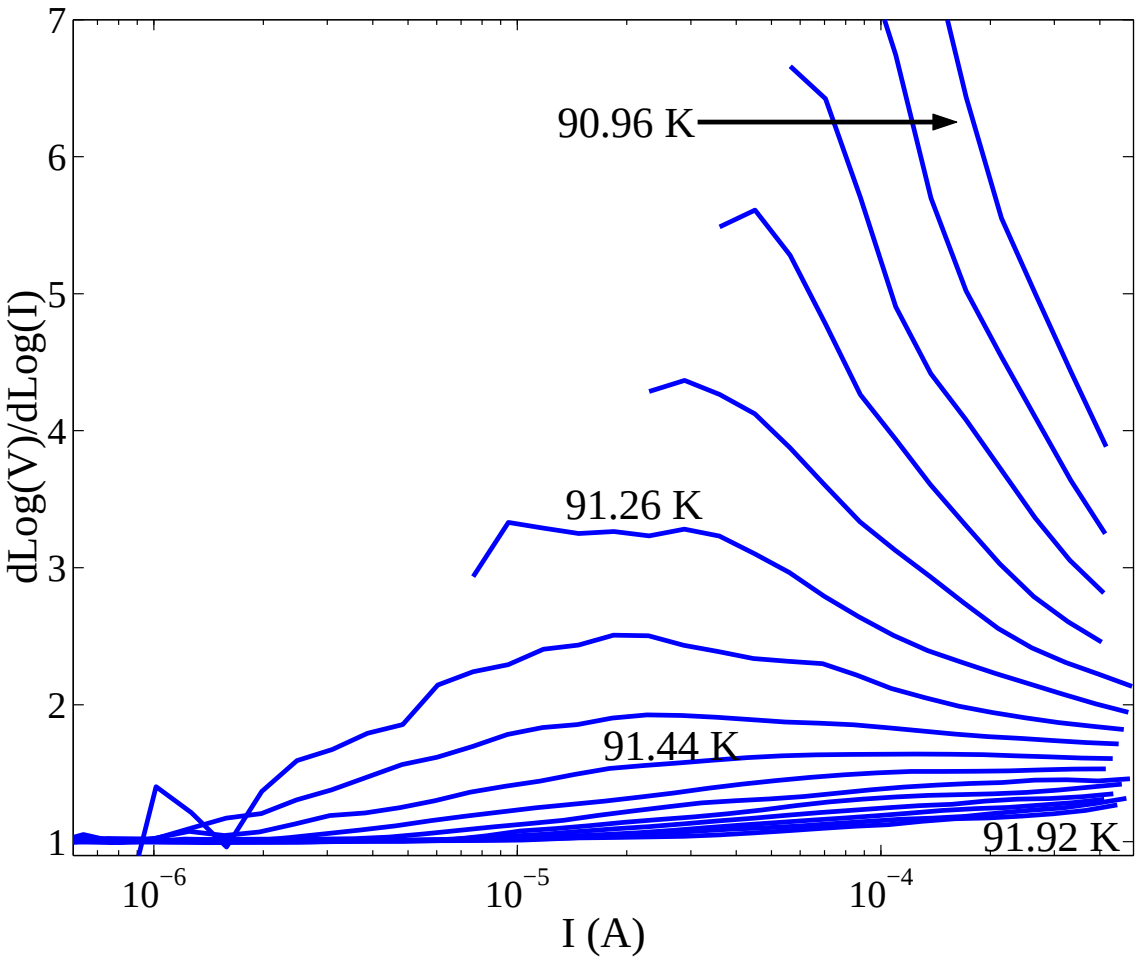

Figure 5.8: $\partial \log V / \partial \log I$ vs. I for mcs146. The conventional choice for T_c, 91.26 K, is clearly not a horizontal line, and cannot be T_c. Surprisingly, there is no isotherm horizontal over a wide range of current, as theory requires at $T = T_c$. Isotherms are separated by 60 mK.

There is no reason that there should not be a phase transition in zero field, and other experiments strongly support a phase transition with 3D-XY exponents[78, 79]. Moreover, the appearance of the peak in the derivative plot is unexpected, and in fact cannot be explained within the theoretical framework described in Sec. 4.3.

The opposite concavity criterion

Upon closer inspection of the derivative plot, there appears to be a region of data that agrees with expectations. The isotherm at 91.44 K in Fig. 5.8 has a pronounced ohmic tail at lower currents, clearly visible in the figure. At higher currents, however, it appears to be horizontal. Fig. 5.9 magnifies the higher currents.

In Fig. 5.9, we can see that the isotherms above and below 91.44 K have slopes with opposite signs at higher currents, and that the isotherm exactly at 91.44 K is nearly horizontal at the high currents. Ignoring the lower currents, this graph agrees with our expectations from Fig. 4.5. From this graph, we would take $T_c \approx 91.44$ K. Then the slopes of the isotherms about T_c have opposite signs, leading to opposite concavities in the $I - V$ curves.

This is, in essence, the *opposite concavity criterion*[12]. We have proposed that isotherms at equal temperatures away from T_c (i.e. $|T/T_c - 1|$), the isotherms should display opposite concavities at the same current level. The opposite concavity criterion is a more stringent test for the existence of a phase transition.

The opposite concavity criterion allows us to find an unambiguous choice for T_c, which then eliminates much of the flexibility in scaling that Strachan found. From our own data, we find clear evidence of a phase transition – at least at the higher currents.

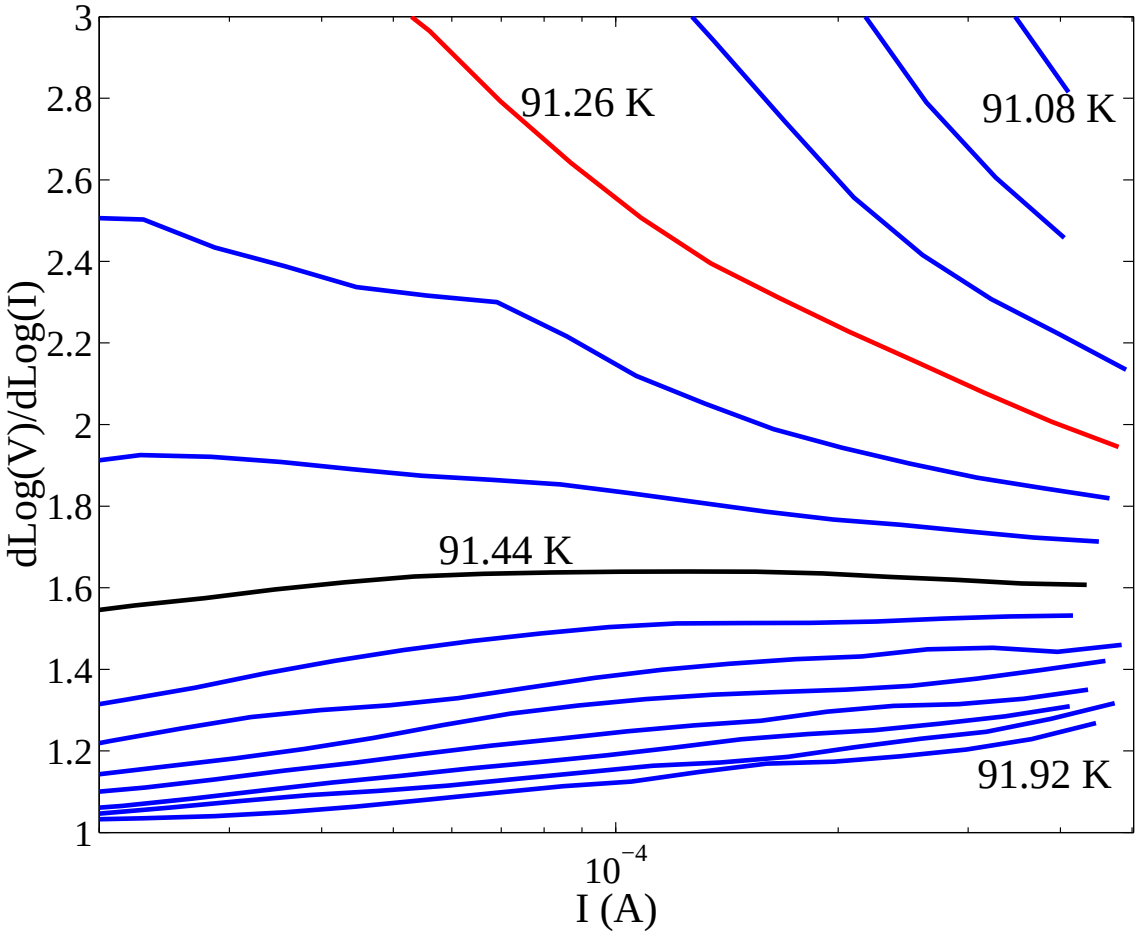

Figure 5.9: $\partial \log(V)/\partial \log(I)$ vs. I, showing the higher currents only. The isotherm 91.44 K is very nearly horizontal, and isotherms above and below it in temperature display opposite concavities, satisfying our opposite concavity criterion[12]. Isotherms are separated by 60 mK.

5.2.2 High-Current Data

The agreement with the opposite concavity criterion is tantalizing, but not without pitfalls. The major pitfall, of course, is the fact that we must ignore the data at the lower currents. We are also stymied by the fact that the separation between "low" and "high" currents is not clear. In fact, in Fig. 5.9, we would label the separation at the point where the 91.44 K isotherm begins to drop towards ohmic behavior – a cutoff at least as arbitrary as the free flux flow cutoff conventionally used in the vortex-glass transition.

Nonetheless, it is instructive to see where the analysis will take us, and whether it offers any better results than the conventional analysis. The question remains: "What do we do about the low-current ohmic tails?" We will assume, for the time being, that the tails are an artifact in the data, created from something not under our control, but that we are allowed to discard from the data. In short, we are going to ignore some of the ohmic tails – simply close our eyes and pretend they do not exist. The source of these ohmic tails will be discussed in detail in Sec. 5.3.

Critical parameters

If we wish to analyze the data, we must find the critical parameters. Using the derivative plot in Fig. 5.9 and the opposite concavity criterion, we can find T_c, which is slightly greater than 91.44 K (the isotherm at 91.44 K has a positive, but very small, slope). Other isotherms not shown in Fig. 5.9 can narrow the range to $T_c = 91.46 \pm 0.04$ K.

Having found T_c, we can now find z. Because $V \sim I^{(z+1)/2}$, the isotherm at T_c in the derivative plot should be a horizontal line with intercept $(z+1)/2$. From Fig. 5.9, we can see that the intercept of the critical isotherm would be ≈ 1.55, which gives $z = 2.1$. Due to uncertainty in the choice for T_c, the error in the intercept gives $z = 2.1 \pm 0.15$.

Already the high-current analysis yields better results than the conventional analysis. We have unambiguously found T_c, and the derivative plot gives a value for z which agrees with the theoretical prediction to within experimental error.

To find ν, we must again use Eq. 4.57. The problem with using Eq. 4.57, though, is that it assumes a value for T_c. Although using the derivative plot to find T_c is certainly better than eyeballing $I-V$ curves, it would be best to determine a method for finding ν without *a priori* assuming a value for T_c. Moreover, to analyze the high-current data, we must jettison much of the low-current data. However, to find R_L, we must use **some** of the ohmic tails at low currents – but which ones? We propose a method of finding $\nu(z-1)$ without assuming a value for T_c. This method is also not without problems, but perhaps the problems are fewer than the conventional method.

At low currents above T_c, we know from Eq. 4.57 that

$$R_L \sim \left(\frac{T-T_c}{T_c}\right)^{\nu(z-1)} \tag{5.6}$$

for $D = 3$. On a log-log plot, this will be a straight line. Following the same line of reasoning which led us to the derivative plot, from Eq. 5.6 we can see that $\partial \log(R_L)/\partial \log(T-T_c) = \nu(z-1)$, i.e., a constant. Thus a plot of $\partial \log(R_L)/\partial \log(T-T_c)$ vs. T will be a horizontal line, with intercept $\nu(z-1)$. Although this seems like extra, unnecessary data analysis, using this method, we can test *different* values for T_c. Whichever value for T_c gives a horizontal line must be the correct value for T_c. In this way, we can find $\nu(z-1)$ and T_c by a second method.

The plot of $\partial \log(R_L)/\partial \log(T-T_c)$ vs. T is shown in Fig. 5.10. Each curve represents a different choice for the critical temperature. We do not expect $\partial \log(R_L)/\partial \log(T-T_c)$ at high temperatures (e.g., $T = 92$ K) to give the same constant value as temperatures in the critical regime. Hence, all the curves at high temperatures look similar, and tend to slope downwards, indicating that they are outside the critical regime. All of the curves also have strong deviations downward at temperatures

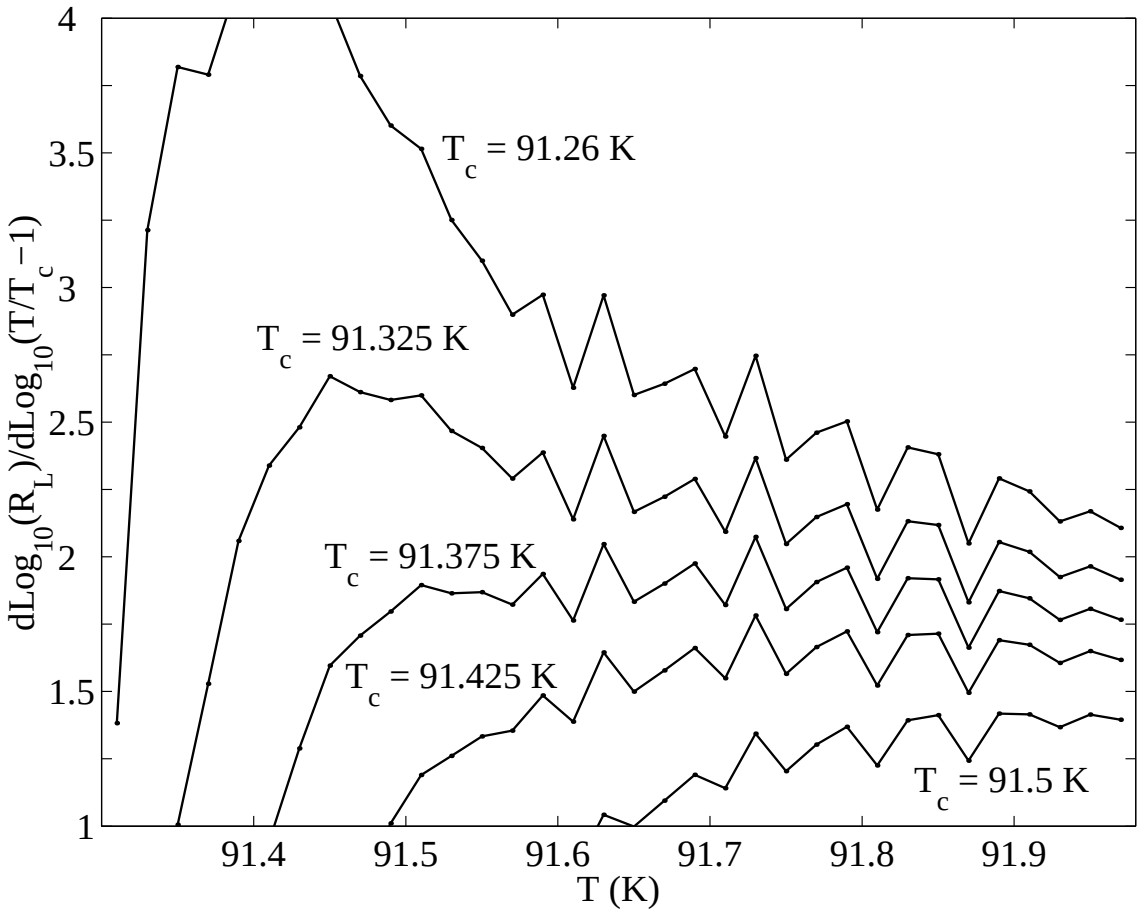

Figure 5.10: $\partial \log(R_L)/\partial \log(T - T_c)$ vs. T. Each curve represents a different choice for T_c. The correct choice of T_c should give a constant as a function of T. Above the low-current ohmic tails, but below the high temperatures, the $\partial \log(R_L)/\partial \log(T - T_c)$ is constant at ≈ 91.4 K.

near T_c. Again, in this analysis, we will discard the low-current ohmic tails near (and at) T_c, so these downward deviations we ignore.

In this limited range of temperatures, we compare the curves. In particular, the conventional choice for T_c, 91.26 K, is not constant at all, contrary to expectations. In fact, $\partial \log(R_L)/\partial \log(T - T_c)$ seems constant (above the drop close to T_c, but below the highest temperatures) at about $T_c \approx 91.4$ K. From this graph, we estimate $T_c = 91.4 \pm 0.05$ K. We see that this T_c, and the T_c found from the derivative plot (Fig. 5.9), $T_c = 91.46$ K $\pm$ 0.04 K agree within experimental errors. Finally,

from Fig. 5.10 we can find an intercept of 1.75 ± 0.2. These values give a value of $\nu = 1.6 \pm 0.4$ (assuming $z = 2.1 \pm 0.15$).

This method is certainly not without its drawbacks, most notably choosing such a limited range in temperature and calling ten data points or so constant. Nonetheless, the critical temperatures from the $I-V$ curve derivative plot and the R_L vs. $|T/T_c - 1|$ derivative plot agree with one another to within experimental error, and in both cases, the conventional choice for T_c is clearly incorrect. Moreover, the analysis implies that we can trust low-current data from 91.5 K to about 91.7 K.

This method has yielded an unexpected value for ν, $\nu = 1.6$. We can try, nonetheless, to ice the cake, and attempt a data collapse, now discarding only the low current data for temperatures below 91.5 K. The resulting collapse is shown in Fig. 5.11.

This data collapse also has systematic deviations, most notably in the low-current ohmic tails, which do not fall on top of one another. Nonetheless, this collapse is not less convincing than the conventional collapse in Fig. 5.5. The major advantage of this data collapse is the fact that the method we have used to find the critical parameters is more exacting than the conventional method.

Derivative scaling

As a final step, we can compare the derivative scaling plots for given the conventional analysis and the high-current analysis. Using Eq. 4.63, we can scale the same data using the conventional-analysis critical parameters, or the high-current critical parameters. The results are shown in Figs. 5.12 and 5.13.

Strachan[15] showed that the derivative scaling collapse was better for the high-current analysis than for the conventional analysis. In Fig. 5.12, the predicted data collapse does not occur at all, whereas in Fig. 5.13, we can see a much better collapse. These results confirm Strachan's claim. However, this success must be taken with a grain of salt: from the high-current analysis only one decade of data in current

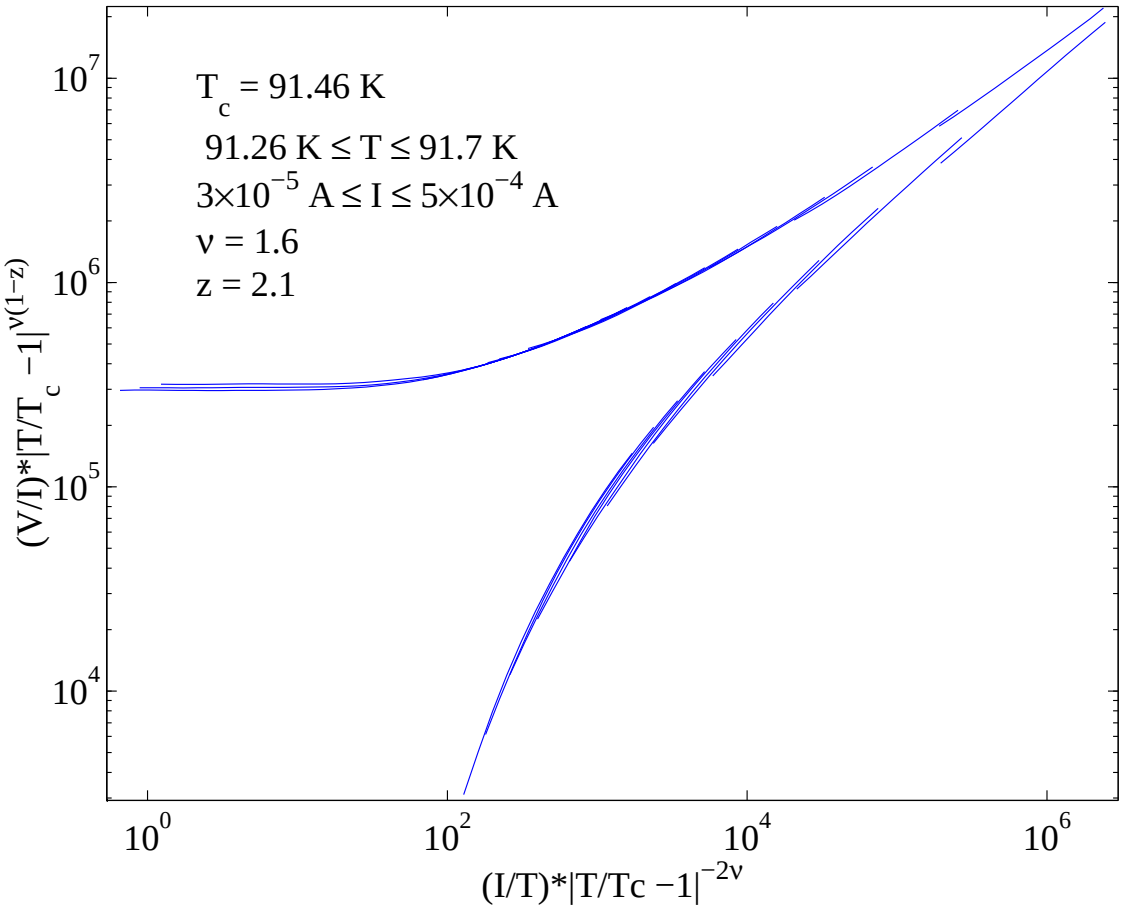

Figure 5.11: High-current data collapse, using parameters found from the less ambiguous method of determining the critical parameters. There are still systematic deviations. Note that the data below 4×10^{-5} A for $T < 91.5$ K have been discarded.

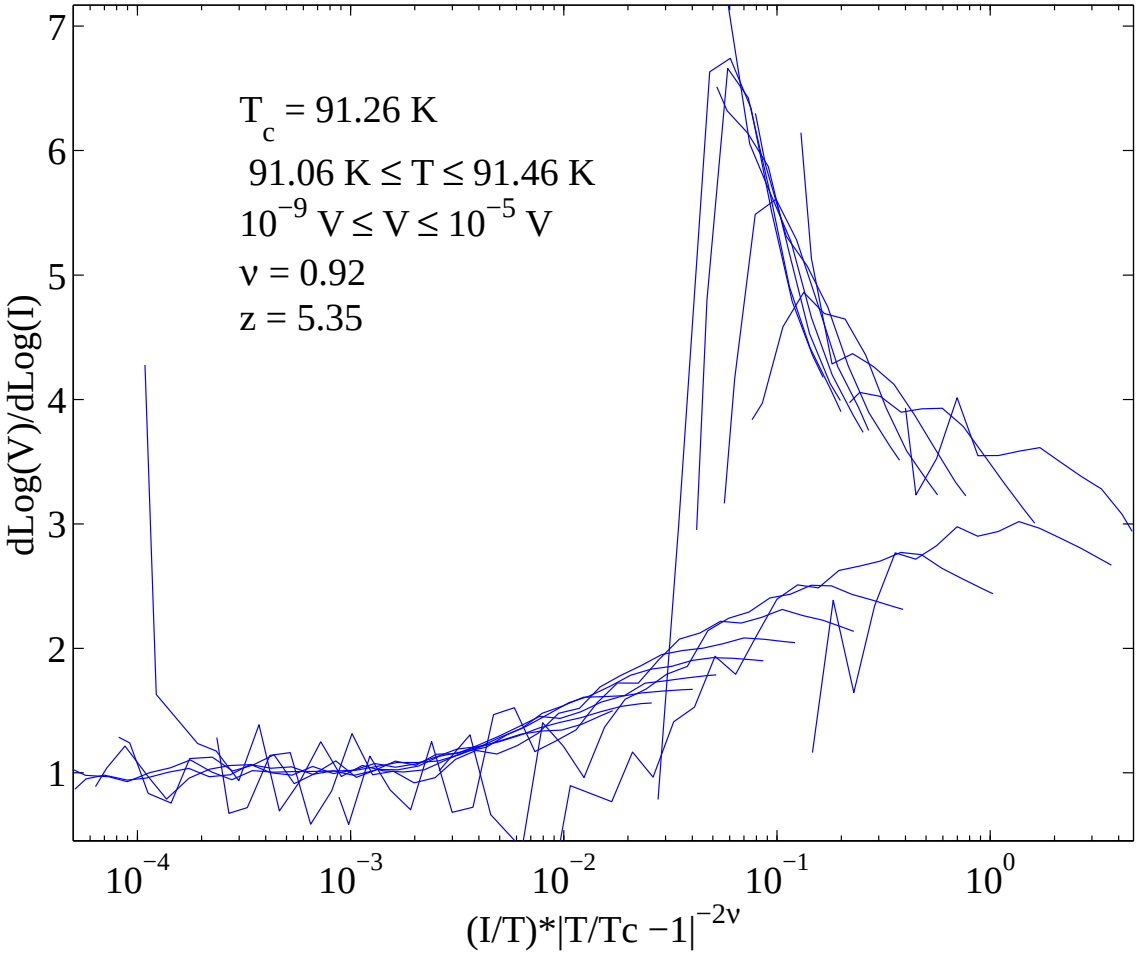

Figure 5.12: Derivative scaling plot using the conventional-analysis critical parameters. From this plot, it is clear that the apparent agreement with scaling is misleading, as the predicted data collapse does not occur.

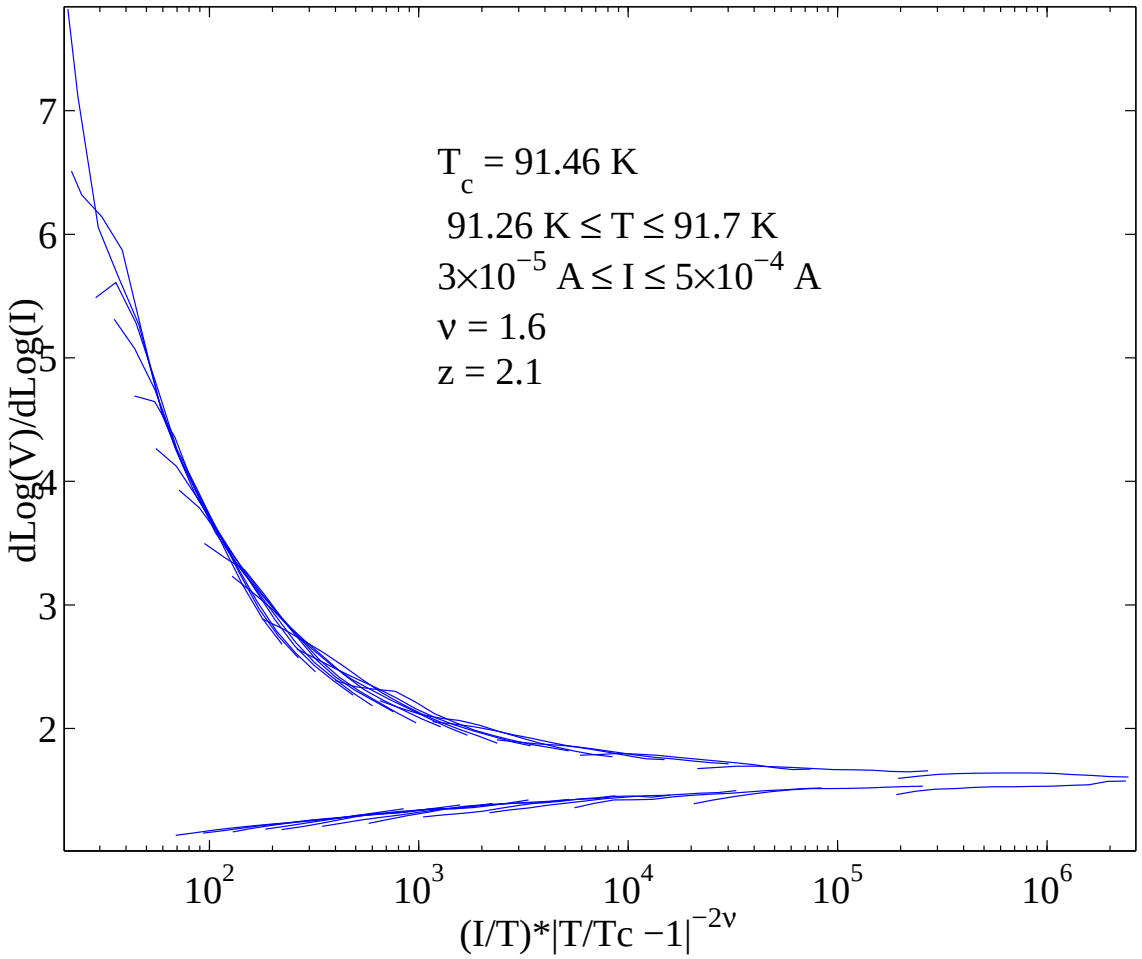

Figure 5.13: Derivative scaling collapse using the high-current critical parameters. This collapse seems to indicate a better agreement with scaling and a better choice for the critical parameters.

survives, perhaps giving a misleadingly good data collapse.

5.2.3 Results of Our Analysis

It is useful here to summarize the results of our high-current analysis. We began by looking for a method to determine T_c unambiguously. By examining the derivative plot, we found that data at the higher currents agreed with the opposite concavity criterion and indicated a true phase transition.

From that derivative plot, we were able to find T_c and z. Plotting $\partial \log(R_L)/\partial \log(T - T_c)$ vs. T, we were able to determine ν and also T_c by a second method. The two values for T_c agreed with each other within experimental error. With these values for T_c, z, and ν, we demonstrated a data collapse as good as the conventional data collapse. Lastly, we showed that the derivative scaling collapse was markedly better for the high-current analysis than for the conventional analysis. Clearly, the high-current analysis offers a better and more systematic method of analyzing the data.

Throughout the analysis, however, we have doggedly ignored the data at lower currents, for the simple reason that, from the derivative plot, the data at lower currents just don't *look* like a phase transition! Because we know in zero field that there is a phase transition, we are forced to attribute this low-current data to something we don't, as yet, understand. This is the major drawback of the high-current analysis: it forces us to ignore what turns out to be most of the data. Moreover, we don't even have a reason to discard the data half as reasonable as the "free flux flow" argument used in the conventional analysis to discard data at higher voltages. In an effort to save the high-current analysis from this failing, we will discuss the ohmic tails and their possible sources in detail in the next section.

Finally, we must discuss the exponents derived from the high-current analysis. The dynamic critical exponent z agrees with the theoretical predictions to within

experimental error. This result we find comforting and a sign that we are on the right track with the high-current analysis. This value for z is robust, and we have seen it in more than 20 different films.

The value for ν is less exciting. It is, in fact, further from the expected value of $\nu \approx 0.67$ than the conventional analysis! Is this just wrong, or are the predictions wrong? Some transport measurements in low fields demonstrate $\nu > 1$[71], and others find $\nu \approx 0.67$[46]. Are there other experiments (i.e., not transport measurements) which can confirm the high value for the static exponent?

The short answer is no. Although some specific heat and penetration depth measurements support mean-field exponents for the transition ($\nu \approx 0.5$)[80, 81, 82], more recent experiments and a re-analysis of previously published data support 3D-XY exponents ($\nu \approx 0.67$) [79, 83, 84, 85], and recent thermal expansivity data are consistent with 3D-XY exponents[78]. None of these experiments find anything approaching $\nu > 1$.

Nonetheless, the high currents agree with a phase transition as predicted by scaling and give a reasonable value for z, leading us to think that we are on the right track. Perhaps if we can find an explanation for the low-current ohmic tails, we can find a reason for our strange value for ν.

5.3 Possible Sources of Low-Current Ohmic Tails

In the previous section, we discussed the high-current analysis and the fact that, in order to proceed with the analysis, we were forced to ignore the low-current ohmic behavior, the "tails," and discard all the low-current data. At that point, it was unjustified, although it yielded some promising results.

In this section, we will work from the assumption that the high-current data represent the true phase transition, and that low-current ohmic tails are an artifact obscuring the transition. What we would like to do is identify the phenomenon

creating the ohmic tails and correct it, if possible. If not, the identification of its source might allow us to justify discarding the low-current data, or, even better, understand how it affects the high-current data.

This section could have been included in Sec. 3.1.3, as it consists of a series of problems associated with the dc transport measurement. They are included here because of the effect they can have on the isotherms. Every problem listed here has the unusual and extremely deleterious effect of creating or mimicking the low-current ohmic tails. In the end, every problem in this section is ruled out as a possible culprit for the ohmic tails in our zero-field data, although getting to that end is a long and arduous experimental road.

5.3.1 Heating

In our measurements, the temperature measured by the thermometer in the sample block is kept constant using feedback. If, however, we somehow heat the bridge during the course of a measurement, the $I - V$ curve we have will be meaningless. Because we have been careful to heat sink our wires at several stages before they reach the sample, any heat from the wires at 300 K at the top of the probe dissipates in the heat sinks at the bottom of the probe and not into the sample. This leaves the applied current as the most probable source of heating. Any applied current will dissipate energy and create heat. In the worst-case scenario, we can imagine that the ohmic tails are actually the *true* isotherm, and as the current increases, so does the heat created, and actually the non-linear portion of the isotherm is merely the sample marching upwards in temperature as the current increases.

Short of putting a thermometer on the bridge (no small feat), there is no way we can measure the temperature of the bridge directly. We can, however, try to find the source of heating, and can make estimates as to the amount of heating, and the expected temperature change in the bridge.

Leads and contacts or bridge?

If we are inadvertently heating the sample by applying a current, we would like to know what the source of that heating is. It can come from two places: the leads and contacts (i.e., everything leading up to the bridge) or the bridge itself. If the leads and contacts have a large resistance, then they will create a large amount of Joule heating, which will flow directly into the bridge. On the other hand, the bridge may be heating on its own, unavoidably.[3]

It is a simple task to determine the power dissipated by the sample, $P = I \cdot V$. From the $I - V$ curves in Fig. 5.3, we can determine the power dissipated by the current at any temperature and current. We can see in the figure that at the highest temperature shown, the maximum power dissipated is $P \approx 2 \times 10^{-5}$ W when the current is $I \approx 1 \times 10^{-3}$ A.

The last heat sinks are the gold pads glued directly to the stage (see Fig. 3.4). From the gold heat sink, there is a short gold wire connected to the sample. This wire is in vacuum, and thus any heat generated in the wire can only sink to the sample or the gold pad it came from, and is a potential problem. The wire is roughly 1 cm long and 3.2×10^{-3} cm (0.00125 in.) in diameter. If the resistivity of gold at 77 K is $\rho \approx 0.5$ $\mu\Omega$-cm[13], then each wire has a resistance of $R \approx 60$ mΩ. The contacts, as discussed, are approximately 5 mΩ each. At 1 mA, the leads and contacts dissipate a power of 6.5×10^{-8} W, three orders of magnitude less than the power generated in the bridge, and so of little concern.

Of greater concern is the YBCO pattern leading up to the bridge. Each $I - V$ bridge is only a small portion of the entire YBCO sample pattern. The YBCO leads before the bridge can also dissipate energy. From the dimensions of the pattern, we can determine the resistance ratio $R_{YBCO-lead}/R_{bridge} \approx 2.6$, which implies the

[3]We could avoid this heating easily, actually, by not applying a current, but it's hard to measure $I - V$ curves if $I = 0$.

YBCO pattern on the substrate dissipates almost three times the power that the bridge dissipates. This is true only when the sample is resistive. In the critical regime, the wider leads dissipate less power because $E \sim J^A$, where A is greater than 1. If $E \sim J^{3/2}$ ($z = 2$), then the powers dissipated in the bridge and the leads are roughly equal. If $E \sim J^2$, then the leads dissipate 0.7 times the power dissipated in the bridge, and the higher the exponent, the less power dissipated. This is important because A increases as the temperature decreases. Thus, precisely where the shape of the $I-V$ curve changes radically for a small temperature change, the leads will always generate less heat than the bridge itself. Moreover, because the YBCO leads are directly connected to a heat sink – the substrate – we expect most of the heat generated in these leads to dissipate into the substrate.

From these numbers we can see that the gold leads and contacts generate far less heat than the YBCO bridge. We also see that the YBCO leads on the substrate can generate more heat than the YBCO bridge itself, but if the $I-V$ curve is non-linear, they will generate less heat than the YBCO bridge; moreover, the YBCO leads are always connected to a heat sink (the substrate). For this reason we have concentrated our effort on looking at the self-heating of the bridge.

Heating in the bridge

We would like to estimate the temperature as a function of position in a bridge of dimensions $L \times w \times d$ carrying a current I. We assume that the temperature is uniform along the width of the bridge, so we only need to solve for the temperature along one dimension, the length of the bridge.

Following Skocpol *et al.*[86], we can estimate the heating in a our bridge. Heat is generated by the power, $I \cdot V$, and can flow out through the edges of the bridge or into the substrate. Writing the heat-flow equation in terms of E and J, we have:

$$-\kappa \frac{d^2T}{dx^2} + \frac{\alpha}{d}(T - T_b) = E \cdot J, \tag{5.7}$$

where κ is the thermal conductivity of the bridge material, T_b is the base temperature (i.e., the temperature of the substrate), $E \cdot J$ is the source term generated by the applied current, d is the film thickness, and α is the heat transfer coefficient from the bridge to the substrate per unit area of the film. This equation describes the heat flow in our bridge in one dimension, x, position along the length of the bridge.

This heat flow equation is difficult to solve unless we make some assumptions. Because we know the leads dissipate less heat than the bridge, we will assume that heating only occurs in the bridge, and that the edges of the bridge are at the base temperature, T_b. This gives us boundary conditions. The source term, $E \cdot J$, is also a strongly varying function of temperature, as any increase in temperature locally also strongly changes the $E - J$ curve. The actual functional forms for E and J are unknown. We will assume E is linear in J (ohmic), as well as linear in T, and write $E \cdot J = (aT + b)J$. Assuming E is linear in J and T is untrue over much of the temperatures we are interested in, but it will serve as a good first approximation.

With these assumptions, and some algebra, we can re-write Eq. 5.7 as

$$-\kappa \frac{d^2T}{dx^2} + \left(\frac{\alpha}{d} - Ja\right) T = Jb + \frac{\alpha}{d} T_b. \tag{5.8}$$

With a re-definition of the parameters, $\left(\frac{\alpha}{d} - Ja\right) = B$ and $Jb + \frac{\alpha}{d} T_b = K$,[4] we can solve Eq. 5.8 subject to the boundary conditions $T(L/2) = T(-L/2) = T_b$, and find

$$T(x) = \frac{K}{B} + \left(T_b - \frac{K}{B}\right) \frac{\cosh(\sqrt{\frac{B}{\kappa}} x)}{\cosh(\sqrt{\frac{B}{\kappa}} \frac{L}{2})}, \tag{5.9}$$

and the average temperature in the bridge, T_{ave}, is

$$T_{ave} = \frac{K}{B} + \frac{2}{L} \left(T_b - \frac{K}{B}\right) \sqrt{\frac{\kappa}{B}} \tanh(\sqrt{\frac{B}{\kappa}} \frac{L}{2}). \tag{5.10}$$

We can make these equations nearly illegible by plugging back in the original

[4]Be careful not to confuse K (which is really just a temporary placeholder) for κ, the thermal conductivity of the bridge.

parameters for K and B,

$$T(x) = \frac{\frac{\alpha}{d}T_b + Jb}{\frac{\alpha}{d} - Ja} + \left(\frac{J(aT_b + b)}{\frac{\alpha}{d} - Ja}\right) \frac{\cosh(\sqrt{\frac{\frac{\alpha}{d} - Ja}{\kappa}}x)}{\cosh(\sqrt{\frac{\frac{\alpha}{d} - Ja}{\kappa}}\frac{L}{2})}, \tag{5.11}$$

and

$$T_{ave} = \frac{\frac{\alpha}{d}T_b + Jb}{\frac{\alpha}{d} - Ja} + \left(\frac{J(aT_b + b)}{\frac{\alpha}{d} - Ja}\right) \frac{\tanh(\sqrt{\frac{\frac{\alpha}{d} - Ja}{\kappa}}\frac{L}{2})}{\sqrt{\frac{\frac{\alpha}{d} - Ja}{\kappa}}\frac{L}{2}}. \tag{5.12}$$

Although we have made some assumptions to arrive at these equations, they have the distinct advantage of being analytic and easy to solve. From experiments[87, 88, 89], we find that the thermal conductivity of YBCO is $\kappa \approx 5$ W/K-m. Although κ is different for the a- and b-axes vs. the c-axis, these differences do not change the results very much. Given our previous assumptions (E is linear in J and T), we can estimate a and b for $E = aT + b$ from an R vs. T plot such as Fig. 5.1.

The parameter α is the most important, and the most difficult to quantify. Most of the heat leaves the bridge into the substrate, if the sample is in vacuum, thus the rate at which heat leaves the bridge into the substrate severely limits the cooling. We cannot find any experiments which measure α for YBCO-STO. From Ref. [86], we know the tin-sapphire interface gives $\alpha \approx 2\times10^4$ W/K-m^2. Because the YBCO-STO lattices are matched whereas the tin-sapphire lattices are not, phonons should pass easier through the YBCO-STO interface than through the tin-sapphire interface. This leads us to expect α to be greater for YBCO-STO than for tin-sapphire. We will use $\alpha \approx 1 \times 10^5$ W/K-m^2.

Our calculations are for a bridge of dimensions 8×40 μm^2 and 2000 Å thick.[5] For $E = aT + b$, we will use the steep slope from the R vs. T curve (between 91.5 K and 92 K in Fig. 5.1). With these numbers, we can plot $\Delta T = T(x) - T_b$ as a function of position. This will depend on the current through the bridge and also the base temperature. We choose a point on the R vs. T curve near the largest

[5]These are our typical bridge dimensions. Sample mcs146 is 20×100 μm^2 because it was used in another experiment, described in the next section.

slope to get an idea of what the most heating possible looks like. This is shown in Fig. 5.14.

Fig. 5.14 shows heating in the bridge at an applied current of 100 μA at $T_b = 91.6$ K. Here we can see that ΔT goes to zero at the edges of the 40 μm long bridge, as per our boundary conditions. The bridge is hottest at the center, reaching $\Delta T \approx 5$ mK. A temperature rise of 5 mK is still very small compared to most intervals between isotherms (usually 50 mK or more). However, ΔT depends strongly on the applied current I. For this reason, it is more useful to plot $T_{ave} - T_b$ as a function of current. This is shown in Fig. 5.15.

Fig. 5.15 shows $T_{ave} - T_b$ as a function of current for two different base temperatures. At the lower base temperature, 91.4 K, the R vs. T curve has a smaller slope than at 91.6 K, which leads to less heating at all applied currents. We can see that there is no significant heating at either base temperature until $I > 10^{-4}$ A.

The results of these estimates lead us to doubt the worst-case scenario described at the beginning of this section. We expect no heating from any of the leads or the contacts, and expect self-heating in the bridge to occur at $I \approx 10^{-3}$ A. This means that any applied current less than 1 mA safely probes the sample without unduly heating it.

These results lead us to ask: if we expect heating at ≈ 1 mA, what does this look like in the data? And can we get rid of it?

I-V curves with heating

In fact, heating in the $I - V$ curves leaves an obvious signal. As we would expect, the $I - V$ curves begin to deviate upwards towards the higher-temperature isotherms, finally falling on the highest-temperature isotherm, i.e., becoming fully normal. Isotherms with heating are shown in Fig. 5.16.

In this figure we can see $I - V$ curves for sample mcs153. As expected, the isotherms at the highest currents deviate upwards and eventually all go to the

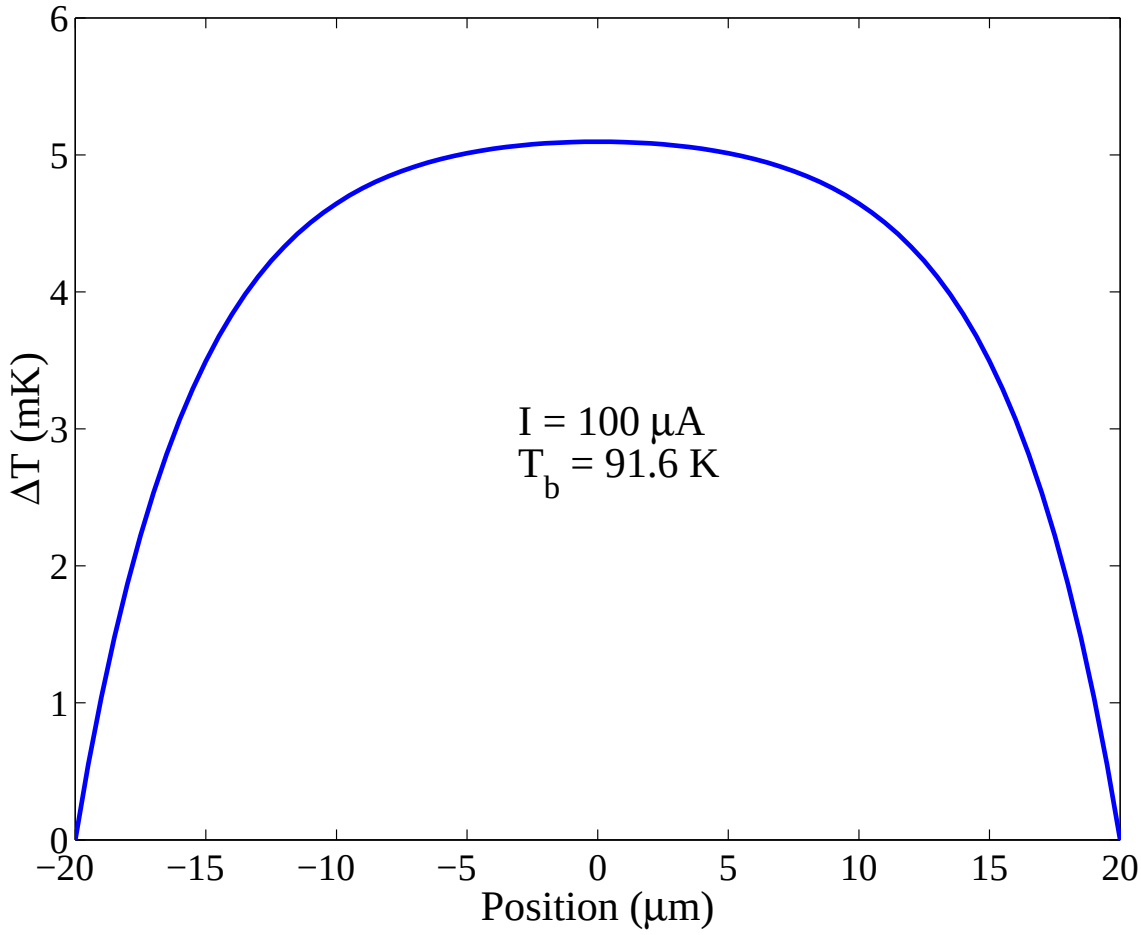

Figure 5.14: $\Delta T = T(x) - T_b$ as a function of position in a 8×40 μm^2, 2100 Å thick bridge, with an applied current of 100 μA. The base temperature is 91.6 K and we have taken $E = aT + b$ from the range 91.5 K to 92 K in Fig. 5.1. At its max, $\Delta T \approx 5$ mK.

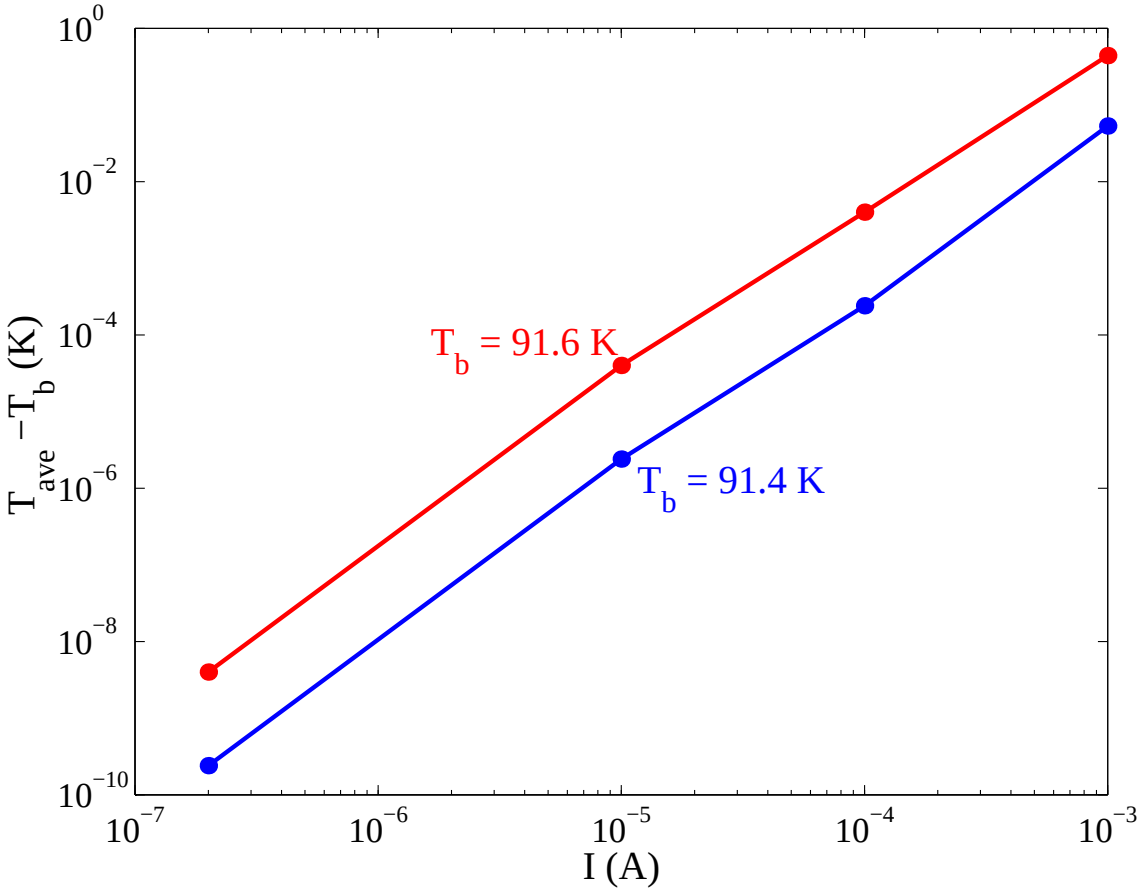

Figure 5.15: $T_{ave} - T_b$ as a function of current. Each curve is for a different base temperature. The lower base temperature, 91.4 K, has a smaller slope in the $E = aT + b$ curve, as compared to $T_b = 91.6$ K. Nonetheless, we expect no significant heating until about 10^{-3} A.

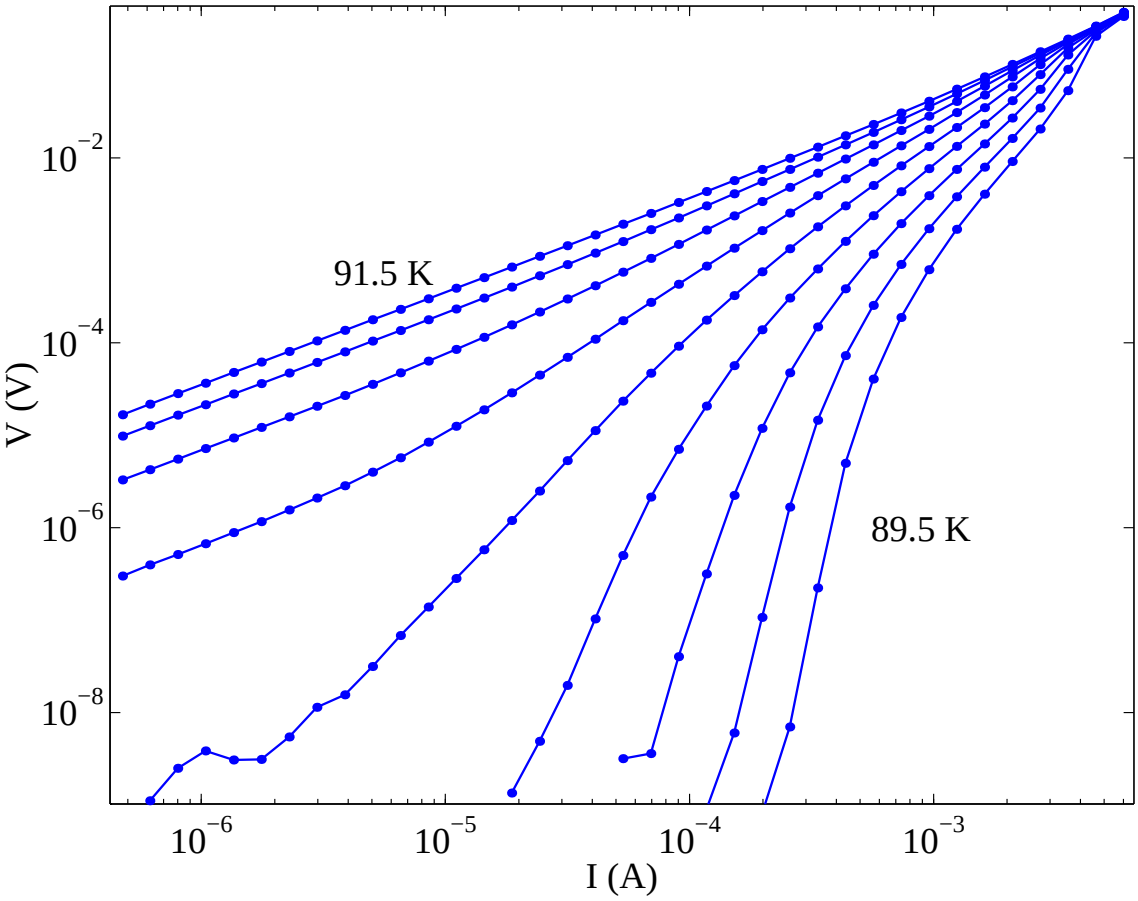

Figure 5.16: $I-V$ curves for sample mcs153 which have heating at higher currents. The heating is obvious as the isotherms deviate upwards as current increases, finally falling upon the highest temperature curve in the normal state. As expected from our estimates, heating occurs at about 1 mA.

highest-temperature isotherm. This is significant because this isotherm is in the normal state, thus we have heated sample out of the critical regime and into the normal state. Most striking is that this heating occurs at about 1 mA, very close to our estimates.

Low frequency measurements

In Sec. 3.1.1, we described a low-frequency experiment[19, 20] as a variation of the standard discrete dc transport measurement. In this experiment, we apply a low-frequency sine wave ($\nu < 200$ Hz) to the sample and capture the voltage across the sample on an oscilloscope. The major drawback of this method is that it is impossible to achieve the sensitivity offered by our nanovoltmeter.

The low-frequency measurement has an advantage at very high currents, however. If we apply a sine wave with a maximum current of 10 mA, for example, then we know at the maxima of the wave we are heating the bridge. If the period of the applied signal is shorter than the time it takes the heat to decay from the bridge into the substrate, then by the time the applied current goes to zero, the bridge has not cooled off. Typically, the time constant of the bridge is on the order of seconds, and our applied signals have periods ≈ 0.1 s. Thus, because the heat cannot escape into the substrate before the next maximum in the applied current, the bridge comes to an averaged temperature higher than the base temperature. What is significant is the fact that this temperature is constant from high to low currents, so we know high and low currents are at the same temperature. In effect, we have circumvented the heating problem by heating the sample a uniform amount.[6]

This can make determination of the temperature of the isotherm somewhat difficult. However, we can match up the low-frequency isotherm with a discrete-measurement isotherm without heating to find the temperature of the low-frequency

[6]Similar to its cousin the neat trick, this is what physicists refer to as a "clever trick."

isotherm, in effect using the sample itself as a thermometer.

In Fig. 5.17 we show $I-V$ curves for sample ds81d which have both discrete and low-frequency measurements. The discrete measurement covers 10^{-7} A $\leq I \leq 10^{-3}$ A, i.e., most of the data. The low frequency data is shown only at the upper right-hand corner, 10^{-3} A $\leq I \leq 6 \times 10^{-3}$ A. Unfortunately, due to the sensitivity of the pre-amps, our low-frequency data are very noisy below the voltages shown in the figure. This limits the usefulness of the low-frequency measurement at low currents.

However, the story is very different at high currents. In Fig. 5.18, we magnify the highest currents. Here we can see the discrete $I-V$ curves all bend upwards at the highest currents, whereas the low-frequency measurements meet with the discrete measurements at about 1 mA and then continue without heating as current increases. Moreover, we can see that in order to make the isotherms agree, we must lower the base temperature for the low-frequency isotherms, indicating that the bridge is heated during the low-frequency measurement, as expected.

At the highest currents in Fig. 5.18, the low-frequency isotherms also begin to bend upwards slightly. Although we might attribute this to heating also, it is more likely coming from driving the sample out of the critical regime. We can estimate the maximum current necessary to drive the sample out of the critical regime from Eq. 4.53 (assuming $D = 3$) as[90]

$$J_{max} = \left| \frac{T_{max} - T_c}{T_c} \right|^{2\nu} \cdot \frac{c k_B T_{max}}{\xi_o^2 \Phi_o}, \tag{5.13}$$

where c is an undetermined constant expected to be of the same order as the YBCO anisotropy parameter, $\gamma = 0.2$, ξ_o is the size of the coherence length at $T = 0$, and T_{max} is the maximum temperature where the critical regime is expected to be valid. From our estimates in Ch. 4, $T_{max} = T_c + 0.32$ K. For sample ds81d (50 μm wide and 2500 Å thick), we estimate $I_{max} \approx 3$ mA, which agrees with where we see the upturn in the low frequency measurements.[7]

[7]We will encounter J_{max}'s little brother, J_{min}, in the next section.

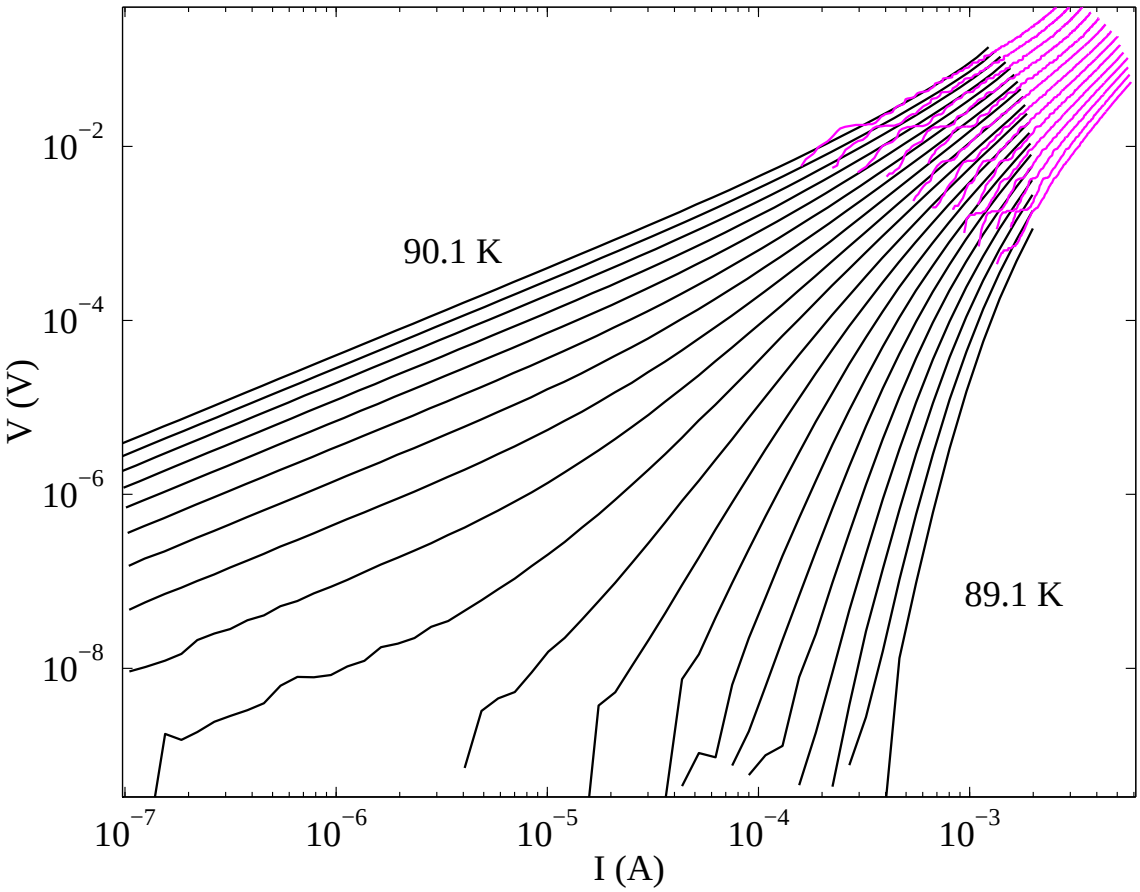

Figure 5.17: Discrete and low-frequency $I-V$ curves for sample ds81d. The discrete measurement covers 10^{-7} A $\leq I \leq 10^{-3}$ A, the low frequency measurement, in the upper right corner, 10^{-3} A $\leq I \leq 6 \times 10^{-3}$ A. In this way, we can extend the useful data approximately one decade in voltage and current. The discrete measurement isotherms are separated by 100 mK, the low-frequency measurement isotherms by 50 mK.

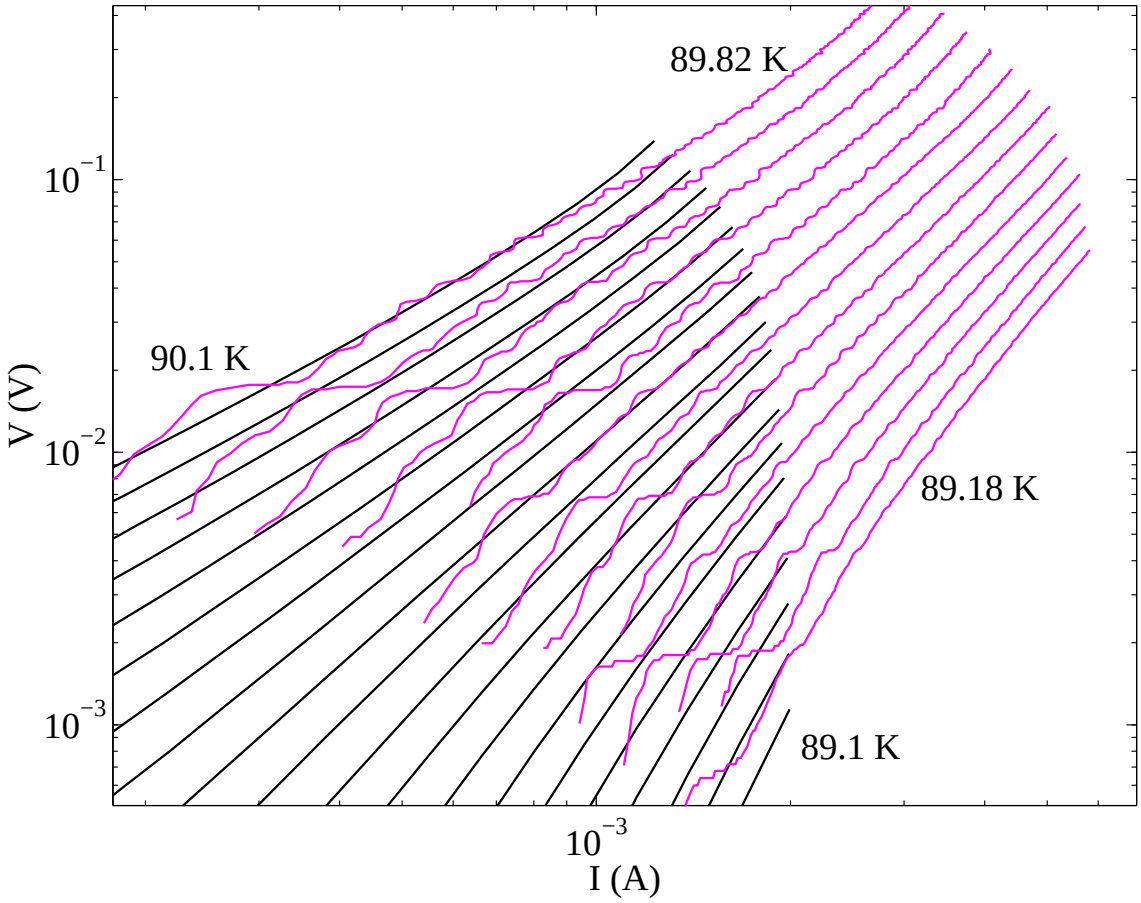

Figure 5.18: Highest current $I - V$ curves, showing discrete and low-frequency $I - V$ curves. The discrete and low-frequency measurements agree at about 1 mA. Above that, the discrete measurements bend upwards, indicating heating, whereas the low-frequency measurements do not show any heating, as expected. The base temperature for the low-frequency measurements is lower than for the discrete measurements, also as expected. The discrete measurement isotherms are separated by 100 mK, the low-frequency measurement isotherms by 50 mK.

This method is useful for extending the range of useful data roughly a decade in current and voltage. It circumvents the heating at higher currents, although very high currents drive the sample out of the critical regime, and it is less useful for the lower currents.

Summary

Heating can be a major problem, drastically changing the shape of the $I-V$ curves. However, our estimates show that any heating should take place in the bridge as opposed to the leads or contacts. Our calculations suggest that this heating will occur in a typical bridge at an applied current of about 1 mA. This is indeed what we see in Fig. 5.16. Finally, using the low-frequency measurement[19, 20], we can extend the range of useful data beyond where the $I-V$ curves from the discrete measurement show deviations, demonstrating experimentally that these deviations are due to heating.

However, our work rules out heating as a source for the low-current ohmic tails. We now know data at currents less than 1 mA show no effects from heating, so we must look elsewhere for a cause.

5.3.2 Magnetic Field

The application of a magnetic field is expected to radically change the $I-V$ curves. In particular, as discussed at length above, a magnetic field is expected to change the zero-field transition into the vortex-glass transition.

We would like to un-complicate our measurement as much as possible, and for this reason, we use three layers of μ-metal shields to screen the magnetic field from our sample. We have measured the magnetic field inside our dewar using a calibrated Hall sensor and found it to be $\mu_o H_{residual} = 0.18\ \mu\text{T} \pm 0.1\ \mu\text{T}$. This is more than

250 times smaller than the Earth's ambient field.[8]

Once we have set the field as close to zero as we can, it is interesting to see what effect small magnetic fields have on the sample. Do we even need to be worried about fields as small as the Earth's ambient field, $B_{Earth} \approx 50$ μT?

Effects of low magnetic fields on I-V curves

We can look at the effect of small fields by attaching a solenoid to the outside of the vacuum can. In this way, we can apply a magnetic field directly to the sample. We cannot apply a field greater than ≈ 15 mT, but then, we are not trying to look at the vortex-glass transition. The effect of magnetic fields on sample mcs156 is shown in Fig. 5.19. In this figure and in our measurements, the field is applied perpendicular to the substrate (meaning parallel to the c-axis of the film).

The result is sobering. The first thing to notice is that at high currents, the $I-V$ curves in different fields all agree, i.e., the field as no effect. The magnetic field has a pronounced effect at lower currents, however. In particular, we can see that a field of $\mu_o H = 1000$ μT creates ohmic tails in $I - V$ curves which were non-linear in 0.2 μT. And fields as small as the Earth's field, 50 μT, can change the shape of $I - V$ curves. Below 50 μT, there seems to be little change in the $I - V$ curves in the range of experimentally accessible voltages.

These results indicate that we were right to place our experiment inside μ-metal shields. But Fig. 5.19 also shows us that we can create ohmic tails in a previously non-ohmic $I - V$ curve simply by turning up the field – although the high-current data seems immune to the effects of magnetic fields. This seems to support our argument that the high-current data represents the true phase transition. But the

[8]We have chosen to stick to our guns and use SI units – if only for the reason that we measure current in amperes, not esu/s. This makes some familiar numbers, like the Earth's field in cgs units (0.5 gauss), look rather odd in SI (50 μT). The simple conversion to remember is 10^4 G = 1 T.

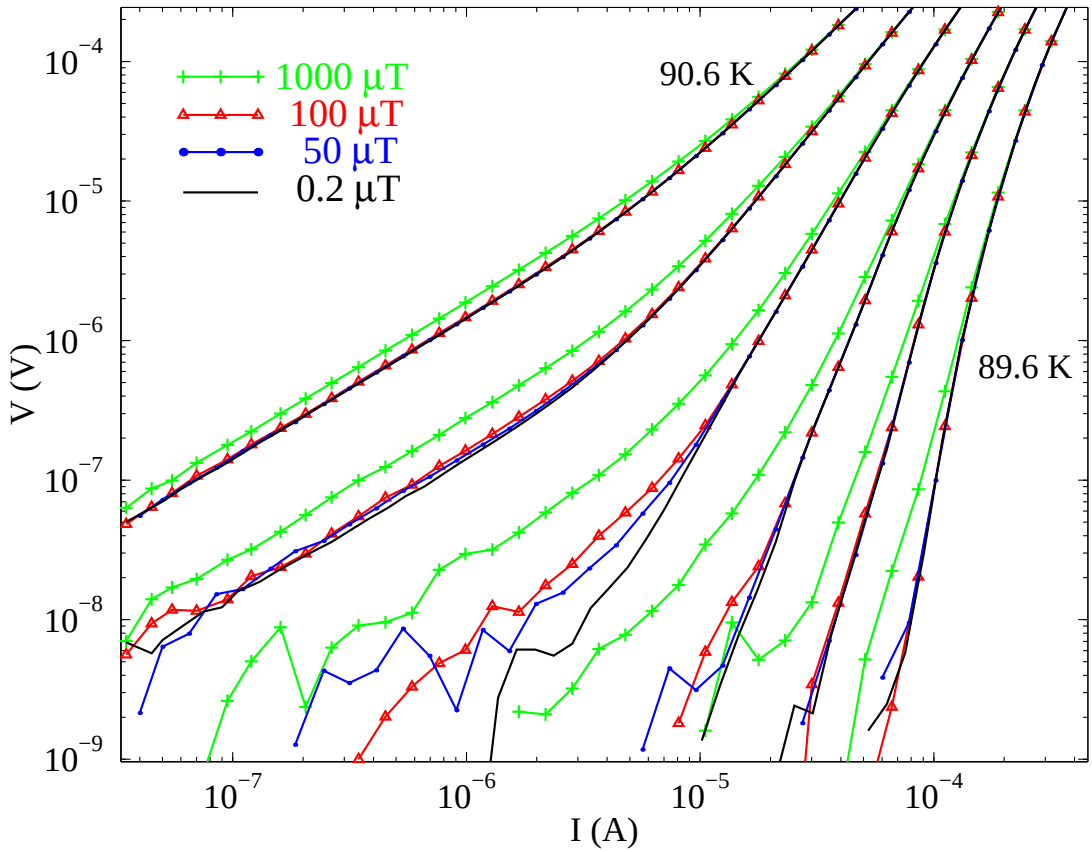

Figure 5.19: The effect of small magnetic field on $I-V$ curves for sample mcs156. The solid line shows the $I-V$ curves for the residual field inside the dewar, $\mu_o H = 0.2$ μT. We can see that even fields as small as 50 μT can alter the shape of the $I-V$ curves. At fields of 1000 μT, we can see ohmic tails in the data that did not exist in the data taken in 0.2 μT. The data in all the fields seem to agree at high currents.

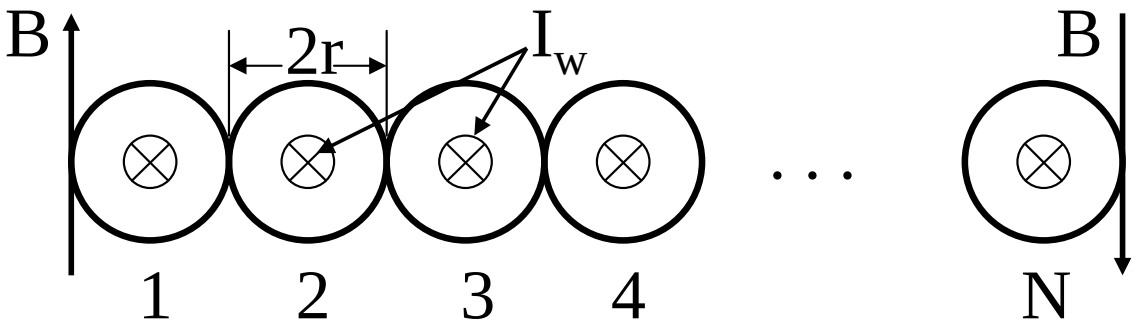

Figure 5.20: Schematic of the $I - V$ bridge as a collection of wires radius r, each carrying current I_w. The current is flowing into the page. The strongest fields occur at the edges of the collection of wires, denoted by **B** in the figure.

fact that magnetic field can make ohmic tails immediately raises the question: Can this be the cause for the ohmic tails in our zero-field data?

In our standard dc transport experiment, we have reduced the ambient field as much as we can, so where would the magnetic field come from to create the ohmic tails? We can eliminate all other sources of magnetic field, but, like heating, we cannot eliminate the bridge itself. The bridge carries a current which creates a magnetic field. Could the self-field created by the bridge be so large as to create an ohmic tail?

Self-field estimates

To see whether or not the bridge has a self-field large enough to create the ohmic tails, we need to estimate the self-field. We can consider the bridge as a collection of wires, all of radius r, each carrying a current I_w. This schematic is sketched in Fig. 5.20, where the current is flowing into the paper.

The strongest fields will be at the edges of the collection of wires, denoted by **B**, and point in the directions indicated in the figure. Between the wires, the magnetic fields will tend to cancel, and the net field will be smaller than at the edges. Of course, above and below the wires, there will also be a net field. However,

experiments have shown that field directed along the copper-oxygen planes in YBCO have much less effect on the superconductivity than fields directed along the c-axis[91]. For this reason, we concentrate on the field at the sides.

Using Ampere's law, we can calculate the field at the edges exactly as

$$B = \frac{\mu_o I_w}{2\pi r} + \frac{\mu_o I_w}{2\pi(3r)} + \frac{\mu_o I_w}{2\pi(5r)} + \cdots, \tag{5.14}$$

or, more simply,

$$B = \frac{\mu_o I_w}{2\pi r} \sum_{i=1}^{N} \frac{1}{2i-1}. \tag{5.15}$$

If our bridge is 8 μm wide and 2000 Å thick, then we can approximate our bridge by 40 wires each with a radius of 1000 Å. Moreover, if the bridge carries a current I, then $I_w = I/40$. The sum we can evaluate and find $\sum_{i=1}^{40} \frac{1}{2i-1} \approx 2.83$. Thus, we have

$$B = \frac{\mu_o I_w}{2\pi r} \sum_{i=1}^{40} \frac{1}{2i-1} = \frac{4\pi \times 10^{-7}(\mathrm{Tm/A})(I/40)}{2\pi \cdot 1 \times 10^{-7}\mathrm{m}} \cdot 2.83 = 2.83\frac{I}{20}\ \mathrm{T/A} \tag{5.16}$$

for a typical bridge. We can now plot self-field as a function of current. This is shown in Fig. 5.21.

In Fig. 5.21, we can see that for small currents, the self-field generated is $\lesssim 1\ \mu$T. However, when $I \approx 1$ mA, then $B_{self} \approx 100\ \mu$T, large enough to generate an ohmic tail. This large field would be cause for worry – if not for the fact that this only occurs at **high** currents. Our experimental data suggests even 1000 μT is not enough to alter the data at high currents. Similarly, the self-field at low currents is many orders of magnitude smaller than what is required to create the ohmic tails. Thus, although the self-field generated can be large, it is never large at low currents.

Cancellation of self-field

Calculations are nice and comforting, but they cannot take the place of cold, hard, experimental data. To assuage any remaining doubts, we designed an experiment to cancel the self-field based on earlier experiments[92].

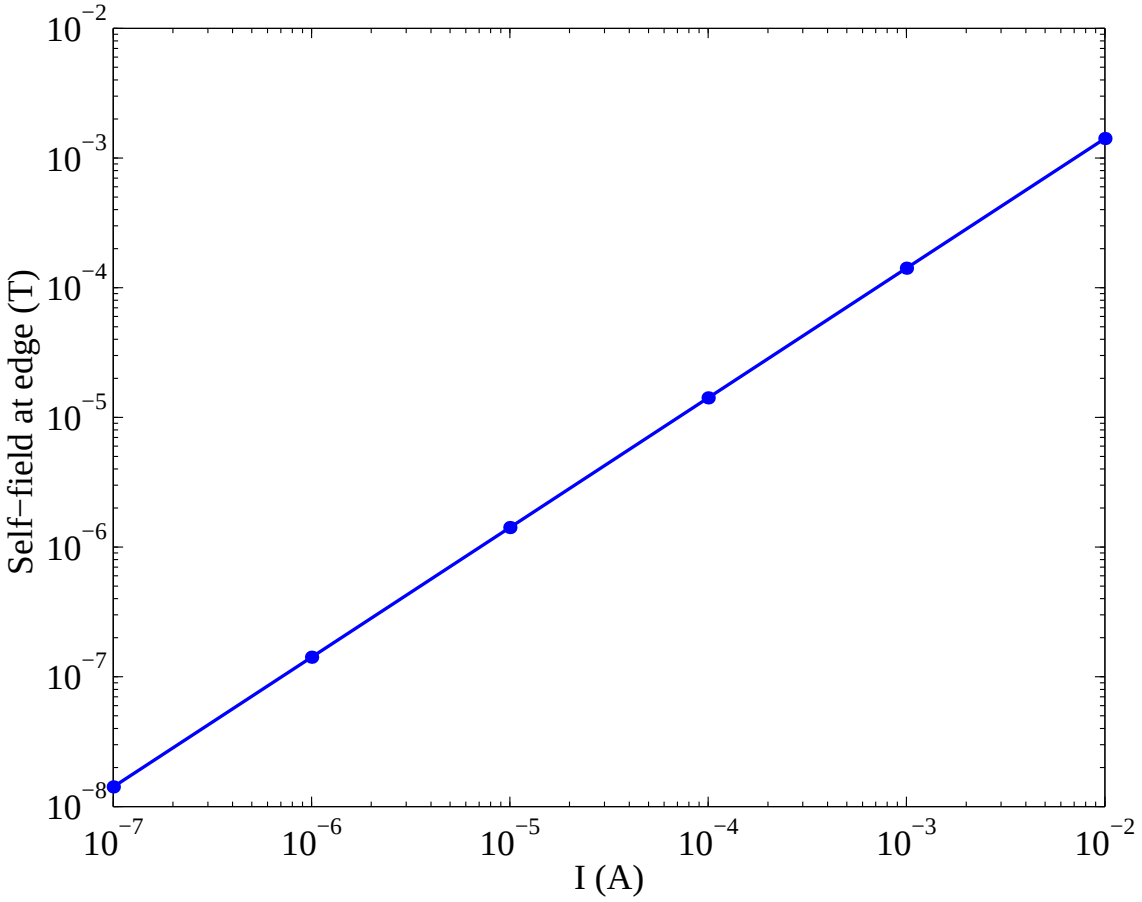

Figure 5.21: Self-field as a function of applied current for a bridge 8 μm wide and 2000 Å thick. We know fields as small as 50 μT can change the $I - V$ curves, and our self-field estimates suggest that these fields can be generated if $I \gtrsim 1$ mA.

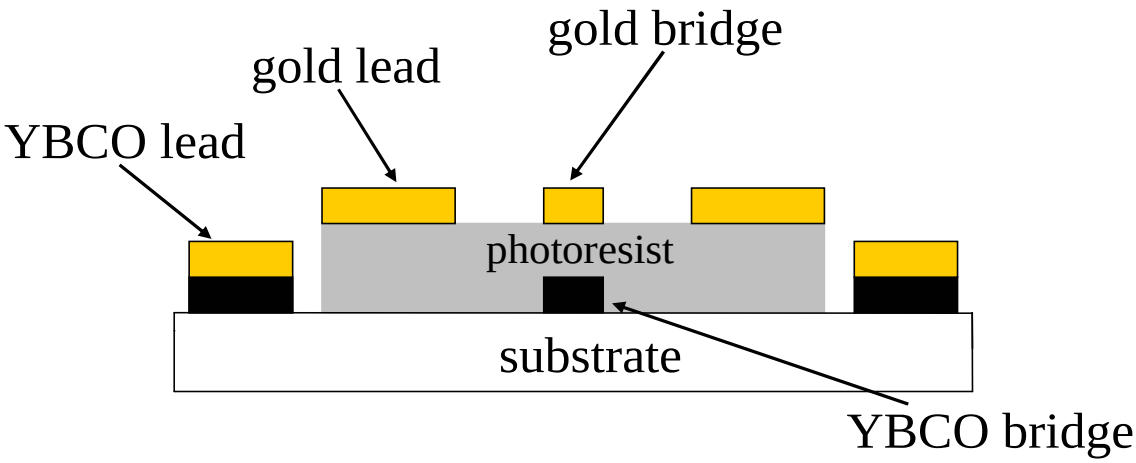

Figure 5.22: Cross-sectional view of experimental schematic to cancel self-field. A gold layer is deposited directly above the YBCO (black) and etched into a similar bridge design, with separate leads (connections between the leads and the bridges not shown). Note that the gold on the YBCO leads is not connected to the gold bridge. This figure is not to scale.

To cancel the self-field exactly, we should pass a current in the opposite direction in the bridge to create a field in the opposite direction, which will then cancel the self-field exactly. In practical terms, we can place a second bridge directly above the first bridge and pass a current in the opposite direction. While this won't cancel the self-field exactly, it should at least reduce the field at the edges of the bridge. The schematic is shown in Fig. 5.22.

Here we see a cross-section of the experimental set-up. The YBCO bridge is covered by a layer of photoresist. On top of that layer, we deposit a layer of gold of the same thickness as the YBCO (about 2000 Å). This gold is then etched into a bridge pattern similar to that of the YBCO underneath.[9] This means that the bridges are separated only by the thickness of the photoresist, about 1 μm. In this design, we can apply a current in one direction in the YBCO bridge (say, into the

[9]The gold on the YBCO leads is to ensure a low contact resistance, and is not connected to the gold bridge.

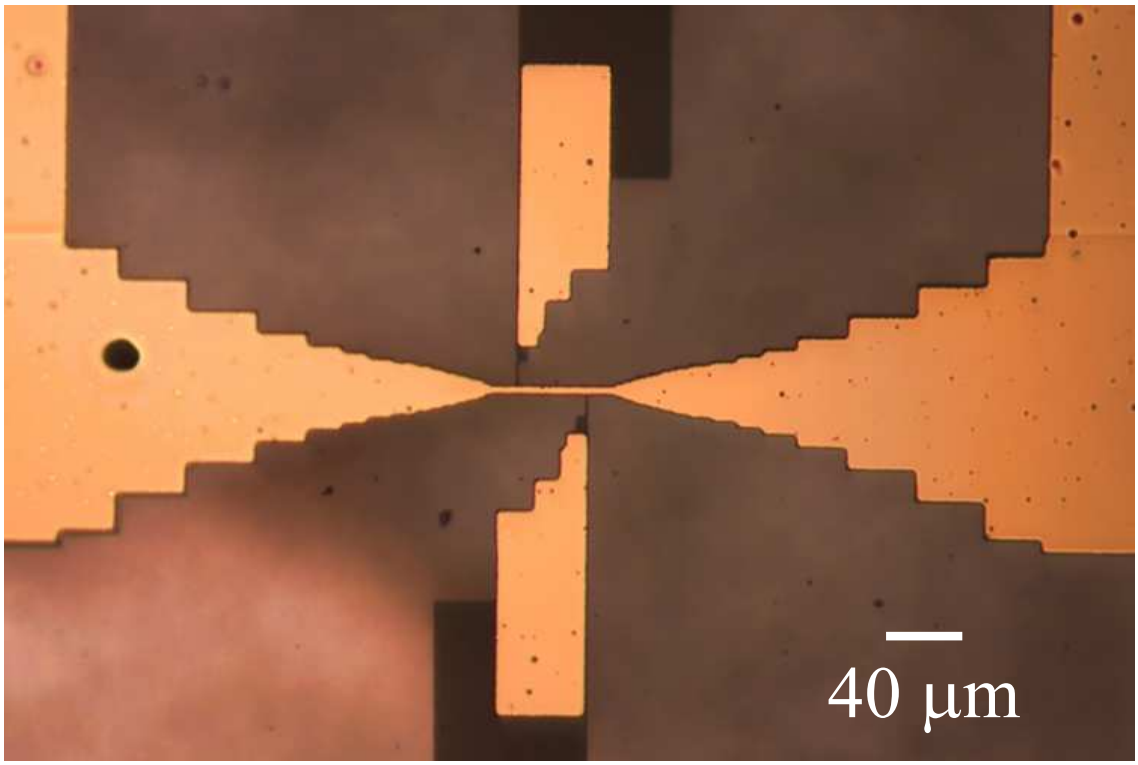

Figure 5.23: Sample mcs120, with gold bridge. Because the gold bridge is of exactly the same pattern as the YBCO bridge, the YBCO bridge cannot be seen. Parts of the YBCO voltage leads can be seen. The gold above and below the gold bridge is the same shape as the YBCO voltage leads, but it does not connect to the gold bridge. They were used to help align the mask. The contacts (for the gold bridge and for the YBCO bridge) are not shown in the figure.

paper) and in the opposite direction in the gold bridge above it (out of the paper). Thus, the field created by the current in the gold bridge should reduce the field at the edges of the YBCO bridge. A picture of the sample is shown in Fig. 5.23.

In this figure, we can see mostly gold. This is because the gold bridge pattern is the same size as the YBCO pattern, and so completely covers the YBCO bridge. Some of the YBCO voltage leads can be seen above and below the bridge. The gold above and below the bridge is the same shape as the YBCO voltage leads, but does not connect to the gold bridge. These patterns were used to help align the mask

onto the sample such that the gold bridge lay directly on top of the YBCO bridge.

With both bridges in place, we can apply a current in the YBCO bridge and the same current in the opposite direction in the gold bridge. We can also apply the same current in the **same** direction, which should also increase the ohmic tail (if they are created from self-field). The $I-V$ curves and data points taken with current in the gold bridge are shown in Fig. 5.24.

The $I-V$ curves measured without current flowing in the gold bridge are shown as black solid lines in Fig. 5.24. To streamline the figure, we have shown the tests with the gold bridge at only two measured temperatures, 92.0 K and 91.8 K. The $I-V$ points measured with current flowing in the gold bridge are represented as triangles. The points with the current in the gold bridge (I_{gb}) flowing in the same direction as the current in the YBCO bridge (I) ("with") are represented as $\triangledown$ symbols. The points measured with I_{gb} flowing in the opposite direction as I ("against") are marked with $\triangle$ symbols. When I_{gb} flows in the opposite direction as I, it will reduce the field at the edges of the YBCO bridge, thus if the self-field is creating the ohmic tails, we expect the $\triangle$ symbols to lie below the solid lines. Similarly, when I_{gb} flows with I, it should exacerbate the ohmic tails, thus we expect the $\triangledown$ symbols to lie above the solid lines. Finally, we can test not only when the magnitudes $I_{gb} = I$, but also when $I_{gb} > I$, in an effort to compensate for the fact that the gold bridge is not directly on top of the YBCO bridge, but rather lies 1 μm above it. The various levels of current in the gold bridge are represented as different colors.

We can see that nearly any level of current in the gold bridge has no effect on the $I-V$ point measured in the YBCO bridge, and that the $\triangledown$ and $\triangle$ symbols often lie directly on top of one another, indicating that the YBCO bridge is insensitive to the direction of current flowing in the gold bridge. There is no difference in the $I-V$ points until $I_{gb} = 10$ mA, at which point there is a systematic deviation upwards, for I_{gb} flowing both with and against I. From our previous estimates with heating

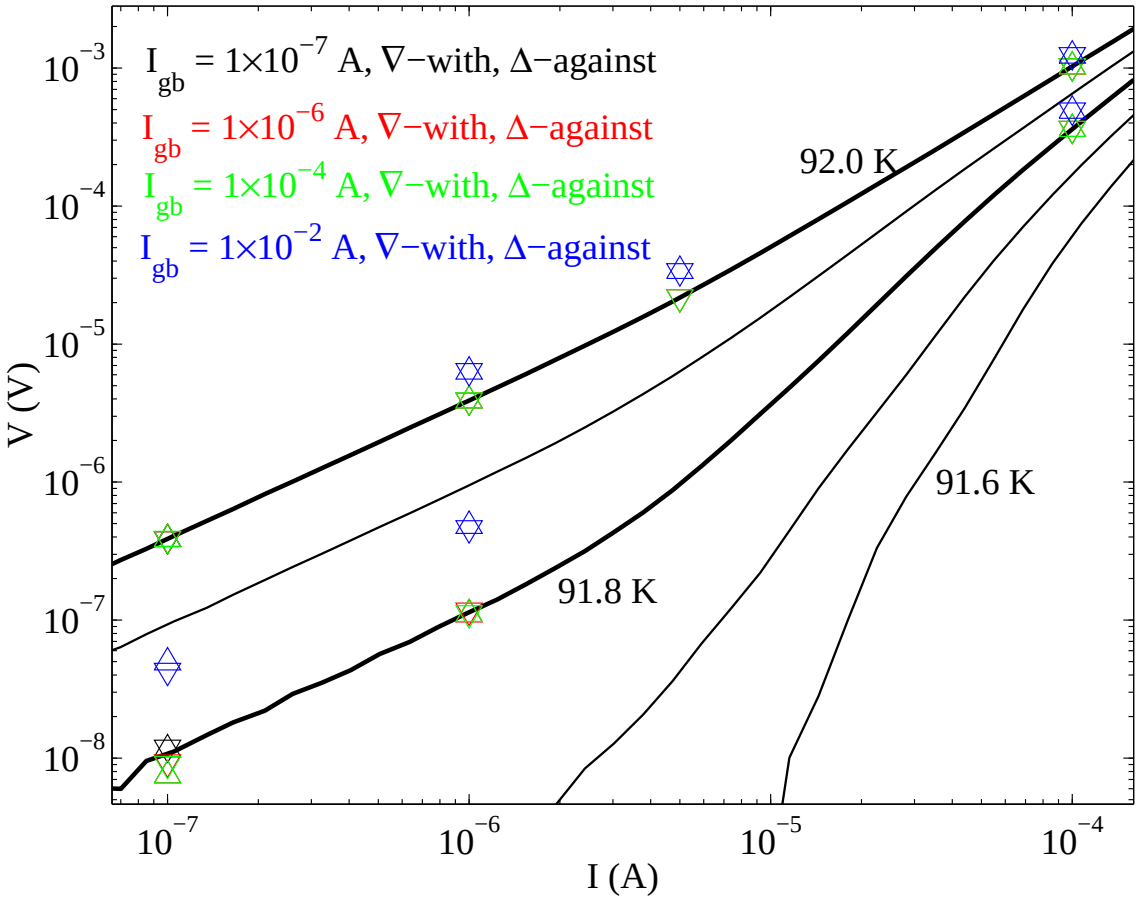

Figure 5.24: Results of the experiment to cancel the self-field. Shown are gold bridge tests at 92.0 K and 91.8 K. The $I-V$ curves for no current in the gold bridge are shown as solid lines. The $I-V$ points measured with current flowing in the gold bridge are represented as triangles (flowing with the current in the YBCO bridge, ∇ symbols, against, Δ symbols). Each color represents a different applied current in the gold bridge. The colors are meaningless, however, as there is no deviation in the $I-V$ curves until the current in the gold bridge reaches 10 mA, when there are systematic deviations at all currents in the YBCO bridge. At this level of current in the gold bridge, we can see that the gold bridge is heating the YBCO bridge underneath, causing the measured voltage to rise. The error in the points is the size of the points.

in thin bridges, we can see that the gold bridge is generating large amounts of heat at this high current level, and that heat is being transferred directly to the YBCO bridge, heating the bridge to a higher temperature.

Summary

We have shown experimentally that fields as low as 50 μT can alter the shape of zero-field $I-V$ curves at low currents, while the high-current data is unaffected by fields as high as 1000 μT. This led us to wonder whether the self-field generated by the current in the YBCO bridge might be the source for the low-current ohmic tails.

We estimated the self-field the YBCO bridge could produce at the edges of the bridge, and found it to be > 100 μT, but only when $I \approx 1$ mA. Our estimates implied that the bridge, at low currents, could not produce a self-field large enough to create the zero-field ohmic tails.

To test this hypothesis, we designed an experiment to cancel the self-field of the YBCO bridge. We photolithographically patterned a second bridge of gold directly above the YBCO bridge, the two separated only by ≈ 1 μm of photoresist. We applied current in the gold bridge, designed to reduce the ohmic tails, and to increase them (depending on the direction of current flow in the gold bridge) – however, we saw that the current flowing in the gold bridge had no effect on the $I-V$ curves, until heat generated in the gold bridge raised the temperature of the YBCO bridge.

Thus, we have reached the same conclusion as with heating: although it can be a serious problem, a magnetic field is not the source of the zero-field ohmic tails.

5.3.3 Sample Inhomogeneity

Sample inhomogeneity is an insidious problem that every physicist who studies a material grapples with. In our case, it is hard to predict what will happen if T_c is

not the same throughout the material. At a given temperature, some of the sample would be below T_c and behave non-linearly, but another part would be above its T_c and act as a resistor – not exactly the results we are looking for.

Inhomogeneous samples

Let us reduce the problem. Suppose the bridge is composed of two regions, one with $T_c = 90$ K and the other $T_c = 91$ K. If we measure the sample at $T = 91$ K, then half the sample will be at T_c, ($V \sim I^{3/2}$, if $z = 2$) and the other half will be normal ($V \sim I$). The $I - V$ curves for the two regions are the straight lines in Fig. 5.25.

Suppose the two regions are connected in series. Then the current **must** flow through both regions. This makes the total voltage across the bridge the sum of the two voltages. This is the curve above the straight lines in Fig. 5.25. We can see that this looks remarkably like our ohmic tails. The $I - V$ curve is non-linear at high currents and ohmic at low currents.

If, however, the two regions are in parallel, then we have a markedly different situation, shown in Fig. 5.26. In parallel, the total voltage will always be less than the smallest voltage. This is the line below the straight lines in Fig. 5.26. This is the opposite of what we see in our zero-field data – it is ohmic at high currents, and non-linear at low currents.

Is it more likely for regions with different transition temperatures to be in series or parallel in our samples? We can imagine that as we deposit the sample, the substrate is at different temperatures. For example, we know the sides of the substrate are hotter than the middle of the substrate (discussed earlier). Because the deposition temperature determines the oxygen content of the film, and hence the transition temperature, this can lead the transition temperatures changing radially from the center of the film. Any bridge we pattern would contain regions of different transition temperatures connected in series.

On the other hand, we know that the YBCO lattice, although similar, is not

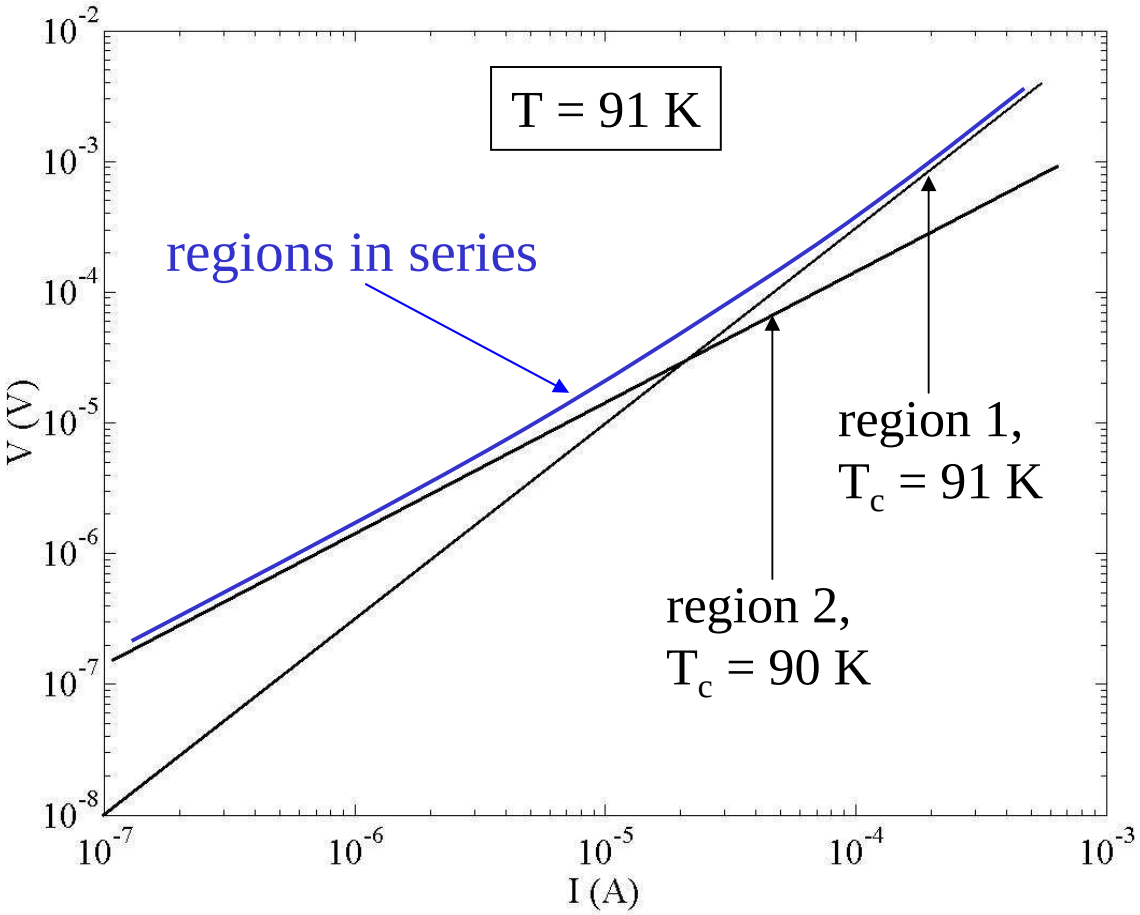

Figure 5.25: The $I-V$ curves for two regions with different transition temperatures are shown as straight lines. If the regions are connected in series, the total $I-V$ curve is the curve above the straight lines. This looks like our low-current ohmic tails.

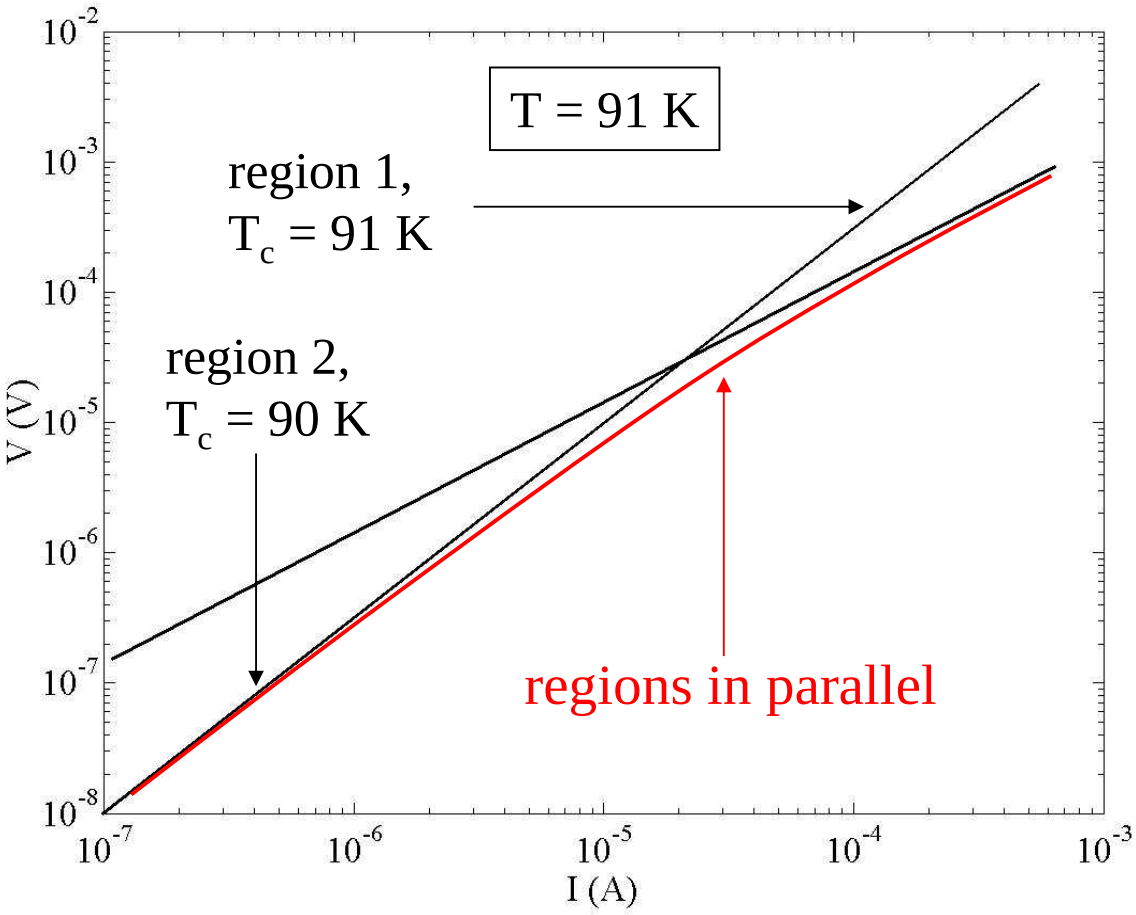

Figure 5.26: The $I-V$ curves for two regions with different transition temperatures are shown as straight lines. If the regions are connected in parallel, the composite $I-V$ curve is the curve below the straight lines. This is the opposite of what we see in our zero-field $I-V$ curves.

the same as the STO lattice. This creates strain on the lowest layers of the YBCO films, as they are forced to conform to the STO lattice. The YBCO film, as it grows thicker, will relax to the bulk value for the lattice parameters. Different lattices will create different transition temperatures, thus any bridge would contain layers connected in parallel. Thus it seems likely we have inhomogeneities in series **and** parallel.

This question can be answered by looking at the ac-susceptibility graphs. The signal received at the pickup coil depends on the amount of magnetic field penetrating the sample. Thus, if the sample contains two layers in parallel (i.e., the top of the film and the bottom), it is possible that the pickup coil might only see one of the regions. When the top becomes superconducting, it will screen the magnetic field, and so the superconducting transition of the bottom will not be seen – the magnetic field is already being screened.

However, if the sample contains regions in parallel (i.e., the center and the sides), when the center becomes superconducting it will only screen magnetic field from the center. Thus, when the sides also go through the transition, we should see a second region become superconducting, as the magnetic field is forced out of the remaining area.

We have seen these types of two-transition samples, shown in Fig. 2.10. Our best films, however, have very narrow widths and only one transition. This seems to rule out regions of different transition temperatures. We cannot rule out layers with different transition temperatures, but our $I - V$ data does not seem to agree with what we would expect from layers with different transition temperatures. These facts indicate our samples are free from large-scale inhomogeneities.

Of course, there is the third possibility, that the regions are small and randomly mixed together. This particular scenario is a nightmare. We can see that many small regions with many different T_cs will broaden the transition in the ac susceptibility measurement, and for this reason, we have reduced the width of the transition as

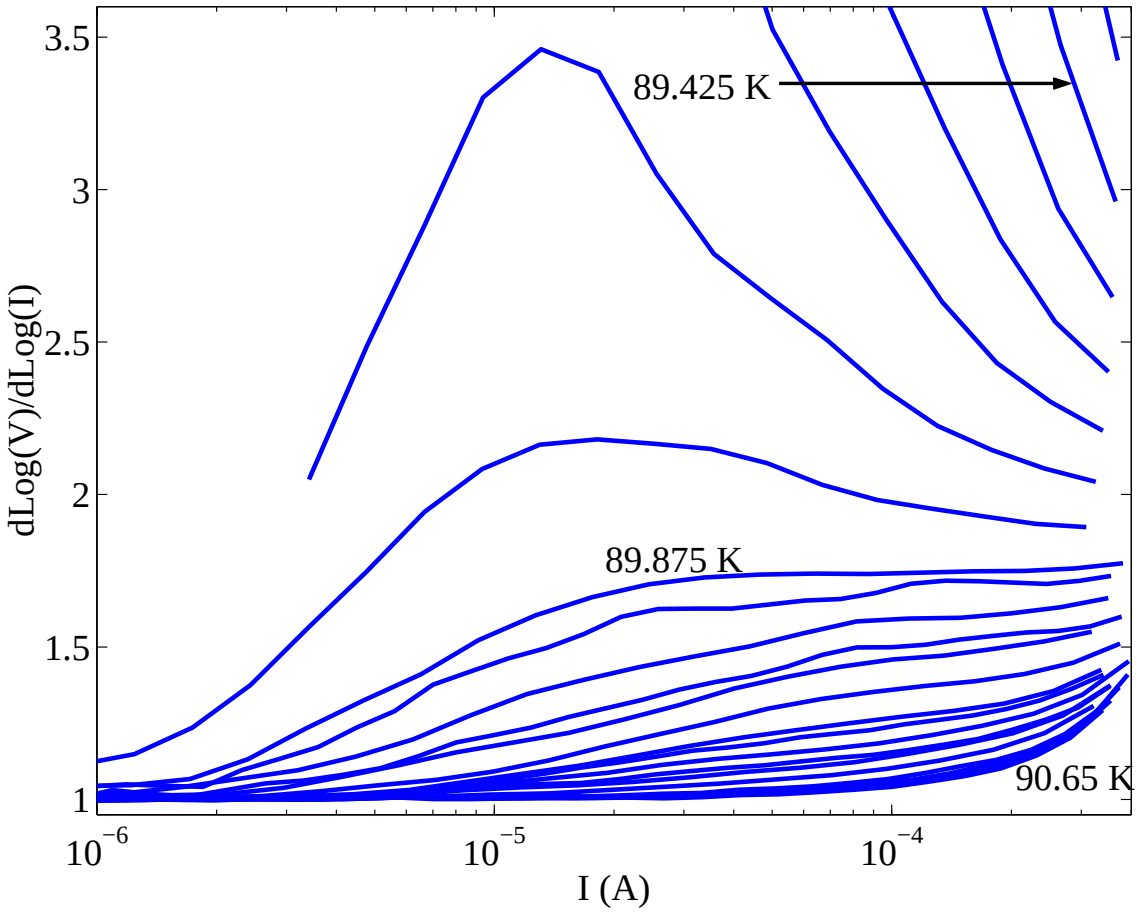

Figure 5.27: Derivative plot for sputtered film N. We can see that the isotherms still have pronounced ohmic tails, and that the high-current T_c, 89.875 K, gives $z \approx 2.5$, similar to our measurements on PLD films.

much as possible.

Films grown via other methods

Film growth with PLD is known to be fast and simple. It is also well-known that films grown via PLD can be some of the worst quality films compared with other growth methods. To see if growth method made a difference in our data, we tested a 2500 Å thick film grown via sputtering by Roy Beck at the Tel-Aviv University. Sputtered films are generally considered to be more homogenous than PLD films[17].

We cut to the chase and show the derivative plot for sample N in Fig. 5.27. In

this plot, we can see that the $I-V$ curves still have pronounced ohmic tails. From this plot, we would say $T_c \approx 89.875$ K. This value for T_c gives $z \approx 2.5$, similar to our measurements on PLD-grown films. Thus it seems as though growth mechanism is not a factor on the low-current ohmic tails.

Summary

It is impossible to rule out sample inhomogeneity as the cause of our ohmic tails. In particular, the simple model of two regions in series reproduces our ohmic tails. However, our ac susceptibility data implies that there are no regions connected in series, and our $I-V$ curves themselves are inconsistent with layers of the film having different transition temperatures. Moreover, films grown by sputtering show nearly identical traits to our films grown by PLD. This implies growth method does not determine the data we see.

Although a possible source, we have optimized our films to the best of our ability (although better films and crystals will always exist), and our data indicates that sample inhomogeneity is not the cause of our ohmic tails. We must look elsewhere.

5.3.4 Noise

An experimenter's first instincts when faced with noise is to: 1) add filters, 2) average, and 3) forget about it. Noise is another intractable, endemic problem (like sample inhomogeneity), but with computers that can take data overnight, why worry?

For many situations these are the correct steps to take. However, previous work done in our group[21, 15] has demonstrated theoretically and experimentally that noise in a non-linear sample can actually generate ohmic tails similar to those found in our zero-field data. This is not an effect we can simply average away and forget.

Effect of current noise on non-linear I-V curves

The current we set on our current source is not really what the sample sees. Let us call the applied current I_{app}, and the current the sample sees I_{samp}. Then,[10]

$$I_{samp} = \int_{-\infty}^{\infty} P(I)dI, \tag{5.17}$$

where $P(I)$ is the probability density function for the current. Ideally, we would like $P(I) = \delta(I - I_{app})$, such that $I_{samp} = I_{app}$, but noise will complicate $P(I)$ and broaden the distribution from the delta function, giving it a width σ_I. The expectation value of $P(I)$ is I_{app}, and we expect the distribution to be symmetric about this mean. This is reasonable, as we expect current noise not to have a preferred direction.

Now suppose the bridge has a response $V = f(I)$, where $f(I) = -f(-I)$ (i.e., anti-symmetric), as we expect the voltage to change signs if we reverse the direction of current. Any measured voltage $\langle V \rangle$ will be

$$\langle V \rangle = \int_{-\infty}^{\infty} f(I)P(I)dI. \tag{5.18}$$

If $I_{app} = 0$, then $\langle V \rangle = 0$ from the symmetry of $P(I)$ and the anti-symmetry of $f(I)$. This is the same result independent of noise.

For non-zero applied currents, there are two very different situations. If I_{app} is large, such that $I_{app} \gg \sigma_I$, then the mean of $P(I)$ is much greater than its width. This implies that $P(I) \approx \delta(I - I_{app})$, and

$$\langle V \rangle = \int_{-\infty}^{\infty} f(I)P(I)dI \approx \int_{-\infty}^{\infty} f(I)\delta(I - I_{app})dI = f(I_{app}), \tag{5.19}$$

again the same voltage with and without noise.

On the other hand, if I_{app} is very small, then it makes sense to expand the distribution about $I = 0$. If $P(I) = g(I - I_{app})$, where $g(I)$ is some symmetric

[10]For the following equations, we follow the outline in Ref. [15].

distribution function like a Gaussian, then to first order in I_{app},

$$P(I) = g(I - I_{app}) \approx g(I) + \frac{\partial g(I)}{\partial I}(-I_{app}). \tag{5.20}$$

Inserting this back into Eq. 5.18, we find

$$\begin{aligned} \langle V \rangle &= \int_{-\infty}^{\infty} f(I)P(I)dI \\ &\approx \int_{-\infty}^{\infty} f(I)g(I)dI + (-I_{app})\int_{-\infty}^{\infty} f(I)\frac{\partial g(I)}{\partial I}dI \\ &\approx 0 + I_{app}R_{eff}, \end{aligned} \tag{5.21}$$

where

$$R_{eff} = -\int_{-\infty}^{\infty} f(I)\frac{\partial g(I)}{\partial I}dI. \tag{5.22}$$

The first term in Eq. 5.21 is zero from the symmetry of $g(I)$ and the antisymmetry of $f(I)$.

This is a startling result. This implies that, independent of the form of $f(I)$, with noise, the voltage measured will always be linear in the applied current! Thus even a highly non-linear $f(I)$ will give $\langle V \rangle \sim I_{app}$ for low currents, whereas for high currents, $\langle V \rangle = f(I_{app})$. This is precisely the effect we have seen in our data, and noise offers the most appealing explanation for the low-current ohmic tails yet.

Before continuing, let us make the above equations more concrete.[11] We assume that $P(I)$ is a Gaussian distribution, such that

$$P(I) = \frac{1}{\sigma_I\sqrt{2\pi}}e^{-(I-I_{app})^2/2\sigma_I^2}, \tag{5.23}$$

where again σ_I is the width of the distribution. The measured voltage can be written as

$$\begin{aligned} \langle V \rangle &= \int_{-\infty}^{\infty} f(I)P(I)dI \\ &= \int_{-\infty}^{0} f(I)P(I)dI + \int_{-\infty}^{0} f(-I)P(I)dI \\ &= \int_{0}^{\infty} f(I)[P(I) - P(-I)]dI. \end{aligned} \tag{5.24}$$

[11] Here we follow Ref. [21].

Plugging Eq. 5.23 into Eq. 5.24, we find

$$\langle V\rangle = \frac{1}{\sigma_I}\sqrt{\frac{2}{\pi}}e^{-I_{app}^2/2\sigma_I^2}\int_0^\infty f(I)e^{-I^2/2\sigma_I^2}\sinh(\frac{II_{app}}{\sigma_I^2})dI. \tag{5.25}$$

We can further simplify the equation under the same conditions as those for which we arrived at Eq. 5.21, namely, I_{app} is small and $I_{app} \ll \sigma_I$. With the substitution $x = I/\sigma_I$, we find to first order in I_{app},

$$\begin{aligned}\langle V\rangle &\approx \sqrt{\frac{2}{\pi}}\int_0^\infty f(x\sigma_I)e^{-x^2/2}\sinh(xI_{app}/\sigma_I)dx \\ &\approx \frac{I_{app}}{\sigma_I}\sqrt{\frac{2}{\pi}}\int_0^\infty xf(x\sigma_I)e^{-x^2/2}dx \\ &= I_{app}R(\sigma_I),\end{aligned} \tag{5.26}$$

where

$$R(\sigma_I) = \frac{1}{\sigma_I}\sqrt{\frac{2}{\pi}}\int_0^\infty xf(x\sigma_I)e^{-x^2/2}dx. \tag{5.27}$$

Again, V is linear in the applied current, as expected.

In general, the form of the $I-V$ curve $V = f(I)$ is unknown, and is, in fact, what we are searching for. However, there are two special cases when we know the shape of the $I-V$ curve. We know for $T > T_c$ and $I_{app} \to 0$, $V = R_0 I$ (Eq. 4.57). In this case,[12]

$$\begin{aligned}\langle V\rangle &= \frac{I_{app}}{\sigma_I}\sqrt{\frac{2}{\pi}}\int_0^\infty x\cdot R_0\cdot(xI)e^{-x^2/2}dx \\ &= I_{app}R_0\sqrt{\frac{2}{\pi}}\int_0^\infty x^2e^{-x^2/2}dx \\ &= I_{app}R_0\sqrt{\frac{2}{\pi}}\cdot\frac{\Gamma(3/2)}{2(\frac{1}{2})^{3/2}} \\ &= I_{app}R_0.\end{aligned} \tag{5.28}$$

This justifies experimenters' knee-jerk reactions to average: For a linear signal, there is no change when you add noise, except to require more averages to get a more precise signal. Thus, low-current ohmic tails which result from the phase transition (Eq. 4.57) should be unaffected by noise. We will return to this fact later.

[12]In the following, Γ refers to the Gamma function, not the correlation function.

Of course, we also know $f(I)$ when $T = T_c$. At T_c, $V = bI^a$, i.e. a power law. We can plug this form for $f(I)$ into Eq. 5.27 and find

$$\begin{aligned} R(\sigma_I) &= \frac{1}{\sigma_I}\sqrt{\frac{2}{\pi}}\int_0^\infty x \cdot b(x\sigma_I)^a e^{-x^2/2}dx \\ &= b\sigma_I^{a-1}\sqrt{\frac{2}{\pi}}\int_0^\infty x^{a+1}e^{-x^2/2}dx \\ &= b\sigma_I^{a-1}\sqrt{\frac{2^{a+1}}{\pi}}\cdot\Gamma(\frac{a}{2}+1). \end{aligned} \tag{5.29}$$

We will use this result later.

Now that we have demonstrated mathematically that noise can create low-current ohmic tails, we would like to know if these same ohmic tails can be seen experimentally. As discussed in Sec. 3.1.2, we filter our lines to reduce noise (characterization of our filters follows in just a few pages). Experimentally, reducing the noise further is not easy. On the other hand, it is a relatively simple thing to *increase* the noise in the system by removing the filters.[13] If our equations are correct, increasing the noise should create ohmic responses in the sample that were not there before.

Exactly this experiment is shown in Fig. 5.28. In this figure, the solid lines are the typical $I - V$ measurement for sample mcs84a, a 2200 Å thick film with a bridge of dimensions 8×40 μm^2. Our typical measurement has π filters at the screen room wall and double-T filters at the top of the probe. The dashed lines show the measurement taken without any filters at all. At high currents, both measurements agree, as expected. However, as the current decreases, we can see ohmic tails in the isotherms taken without filtering not present in the isotherms taken with filtering. Thus, we see the result exactly as expected: by adding noise, we can create ohmic behavior in a previously non-ohmic $I - V$ curve.

This effect cannot be averaged away, as the noise changes the behavior of the sample. The sample, in effect, is averaging the noise for us. In order to eliminate

[13]This is the "make things worse first" trick passed down to us by F.C. Wellstood.

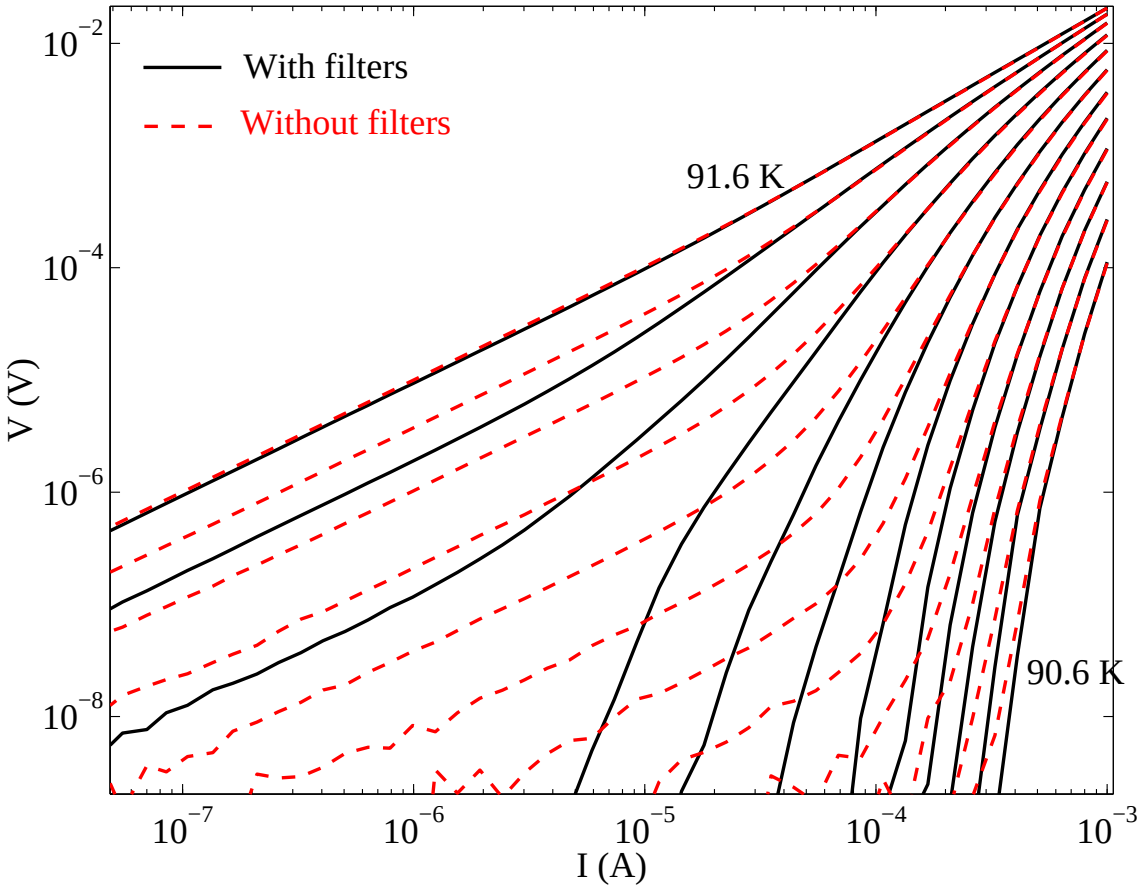

Figure 5.28: $I - V$ curves for mcs84a with and without filtering. The solid lines show typical filtering (π filters on the screen room wall and double-T filters on top of the probe). The dashed lines show the measurement with no filters. We can see both sets agree at high currents, as expected. At lower currents, we can see ohmic behavior in the isotherms without filtering absent in the filtered isotherms, indicating noise can create ohmic tails. The isotherms are separated by 200 mK.

ohmic tails created by noise, we must reduce the noise reaching the sample.

Estimates of noise

We are now in the position where we suspect that our low-current ohmic tails are due to noise reaching the sample, despite our attempts to filter it.

The first question we can answer is: How much noise do we need? If the ohmic tails are due to noise, then we can use the above equations to determine σ_I.

Let us take the isotherm that, in the high currents, appears to be T_c. We would suspect that the high-current behavior is the true critical behavior, and the low-current behavior is created by noise. If this is so, then we can fit the high currents of the isotherm at T_c to a power law $V = bI^a$. We can also fit the low currents to $V = R_0 I$, as we expect an ohmic response due to noise. We can now use Eq. 5.29 and find

$$\sigma_I = \left[\frac{R_0 \sqrt{\frac{\pi}{2^{a+1}}}}{b\Gamma(\frac{a}{2}+1)} \right]^{\frac{1}{a-1}}. \tag{5.30}$$

For the isotherm that looks like T_c in Fig. 5.28 (91.4 K, the second-hottest isotherm), we can fit the high-current regime and find $a = 1.55$ and $b = 10^{2.8}$. We can also fit the ohmic tails for the filtered and unfiltered isotherm, and find $R_0 = 0.7\ \Omega$ for the filtered isotherm and $R_0 = 2.2\ \Omega$ for the unfiltered isotherm. Plugging back into Eq. 5.30, we find that

$$\sigma_I \approx 11\ \mu\text{A},\ \text{unfiltered}, \tag{5.31}$$

and

$$\sigma_I \approx 1.3\ \mu\text{A},\ \text{filtered}. \tag{5.32}$$

This strikes us as an unusually large amount of current noise. Is it possible to create this? The unfiltered isotherm is open to the elements, so to speak, and is susceptible to all the noise created in the electronics, computers, and the environment, and perhaps 11 μA of current noise is not unusual. For the isotherms which are filtered, however, where would the noise come from?

Our low-pass filters have 3 dB cutoffs at 3 kHz, effectively screening noise from outside sources. This only leaves internal sources for noise – namely Johnson noise[93, 94]. This thermal noise is white noise created by the electrons in a resistor. This creates a voltage

$$V_{noise} = \sqrt{4k_B T R B}, \tag{5.33}$$

where B is the bandwidth of the system. Let us consider the leads after the last filter on the top of the probe to the sample. These leads have a resistance $R_{leads} \approx 10\ \Omega$. They are heat sunk only at the bottom of the probe, so as a worst-case for noise, we can say the whole length is at $T = 300$ K. The twisted-pair in our probe cannot transmit frequencies much above 1 GHz[95], which – again as a worst case – we take to be our bandwidth. Then the leads themselves can create a voltage of $V_{noise} = \sqrt{4 \cdot 1.4 \times 10^{-23}\ \text{J/K} \cdot 300\ \text{K} \cdot 10\ \Omega \cdot 1\ \text{GHz}} = 13\ \mu\text{V}$. At the top of the probe, the filters are connected to ground. This creates a circuit for the noise to flow, where the current will flow through the sample and the leads to ground. Because the sample is usually tiny, the resistance of the circuit will be R_{leads}, which means the sample sees a current $I_{noise} = 1.3\ \mu$A! This is, in fact, precisely the current required to create the ohmic tails!

Of course, even at frequencies much lower than 1 GHz, the twisted pair and connectors of our probe are not optimized for high frequencies and attenuate the signal starting at roughly 1 MHz. If, instead of 1 GHz, we assume a more realistic bandwidth of 20 MHz, and also assume that our leads are at an average temperature of $T = 200$ K, we find that this will create a current $I_{noise} = 0.15\ \mu$A, ten times smaller than our worst-case estimate. Moreover, although the lead resistance at dc is 10 Ω, because the top of our probe is filtered using T filters, the high frequencies will see higher impedance than 10 Ω due to the inductors in the circuit, further reducing I_{noise}.

Nonetheless, the fact that we could find estimates even to within an order of

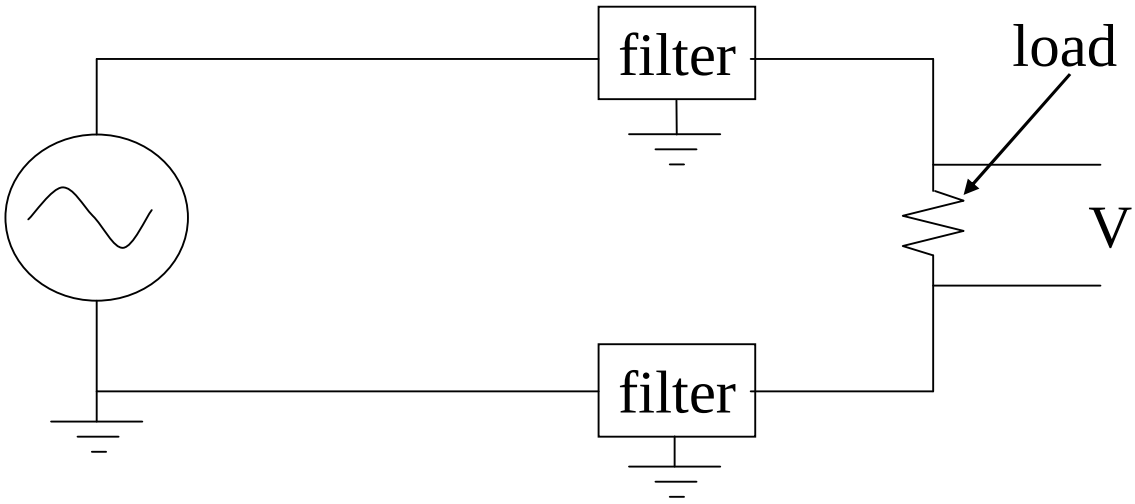

Figure 5.29: Schematic of the insertion loss measurement. A signal is applied from a function generator. The resulting voltage across a 50 Ω load is measured both with and without the filters.

magnitude caused us to worry, and led us to further filter our probe in an attempt to reduce the noise reaching the sample.

Attempted filtering in the dc transport probe

Following the lead of another group, we decided to place filters on the cold end of our probe[95]. With a 3 dB cutoff of 3 kHz, this should reduce the noise at the sample even in the worst-case scenario estimates to $I_{noise} = 2$ nA, three orders of magnitude lower.

Before adding filters willy-nilly, however, it is useful to know exactly how these filters behave. For this reason, we characterized our filters, both when warm at 300 K and cold at 77 K. To measure the filters, we tested their insertion loss in dB. The schematic for the measurement is shown in Fig. 5.29.

The voltage from a function generator is placed in a circuit with a 50 Ω load. Without the filters in the circuit, the voltage V_1 across the load is measured. The filters are placed in the circuit, and the voltage V_2 across the load is measured again.

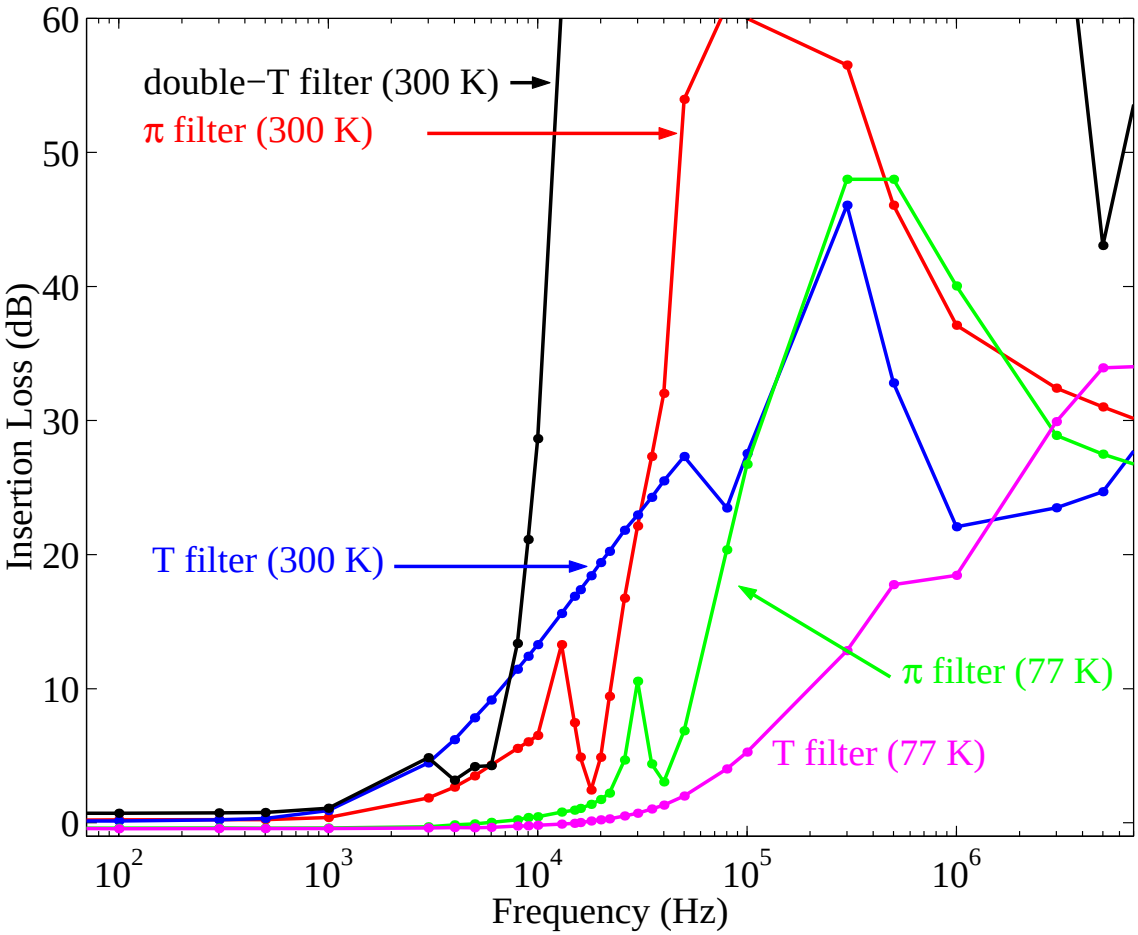

Figure 5.30: Insertion loss of our filters at 300 K and 77 K. The 3 dB point shifts upwards in frequency as the temperature decreases.

The insertion loss is given by:

$$\text{Insertion Loss (dB)} = 20 \cdot \log(\frac{V_1}{V_2}). \tag{5.34}$$

We used commercial π, T, and double-T low-pass filters in our experiment. In addition, we made low-pass Cu-powder filters. These filters have been shown to filter very high frequencies.[14]

In Fig. 5.30 we show some of our characterization. At higher frequencies, the filters seem to be less effective, as the insertion loss decreases. Actually, the signal

[14]The details of these filters can be found in Ref. [95].

from the function generator bypasses the circuit completely and passes through the air to the oscilloscope, because free space has a lower impedance than our circuit. Thus, the decrease at high frequencies is an artifact of our measurement. When the source is separated from the measurement (as when we measured the response of the probe, which is inside the screen room), the insertion loss at high frequencies does not decrease.

We can see that the different filters have different 3 dB points, and that the 3 dB point shifts to higher frequencies when the filters are cold. Nonetheless, the cold filters should reduce the noise substantially, low enough to reduce the ohmic tails (if noise is the cause of our ohmic tails). Our Cu-powder filters were characterized by T. Frederiksen, who showed that they had an insertion loss of greater than 60 dB for $\nu > 10$ GHz[96].

Now that we are certain the filters will function, let us examine the $I-V$ curves taken with various filtering schemes. The first we would like to compare is our typical filtering scheme, π and double-T filters at the top of the probe, to a fully-filtered scheme: warm filters at the top of the probe and the screen room wall, and cold T and Cu-powder filters at the cold end. This is shown in Fig. 5.31.

Contrary to expectations, the two filtering schemes are identical! The addition of filters to the cold end of the probe has no effect on the data. We must now wonder what, exactly, are the cold filters doing? We would like to compare just the cold filters vs. just the warm filters.

In Fig. 5.32, the solid lines indicate warm filters (π and double-T at 300 K), and the dashed-dotted lines indicate cold filters (T and Cu-powder at 90 K). It is not surprising that the cold filters do not work as well as the warm filters. We know from Fig. 5.30 that the 3 dB point of the T filters moves up in frequency as they become cold, thus the cold filters alone should not function as well as the warm filters. However, the cold filters do still filter the data substantially over no filters at all. All three filter combinations are shown in Fig. 5.33.

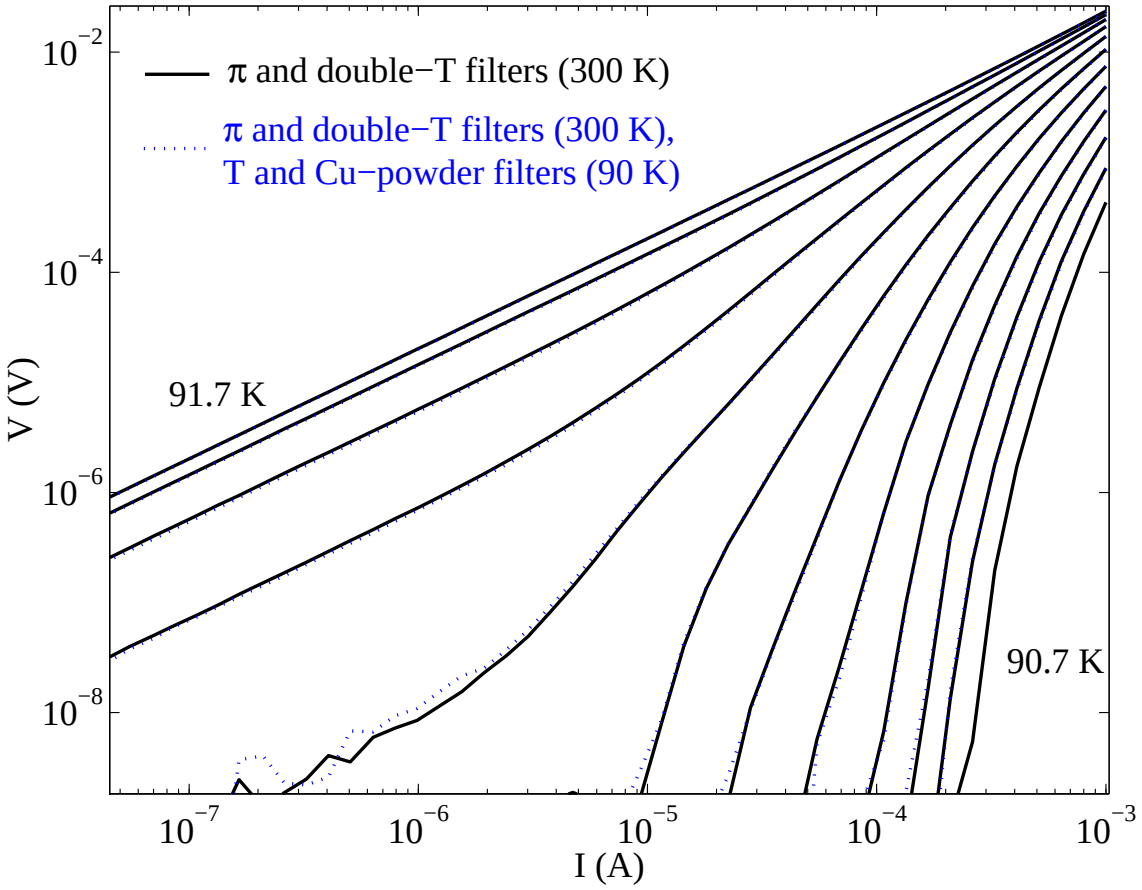

Figure 5.31: Two different filtering schemes for mcs84a. Solid lines show the typical filtering (π and double-T at 300 K). The dotted lines show the addition of T and Cu-powder filters at the cold end of the probe. Surprisingly, additional filtering has no effect on the data.

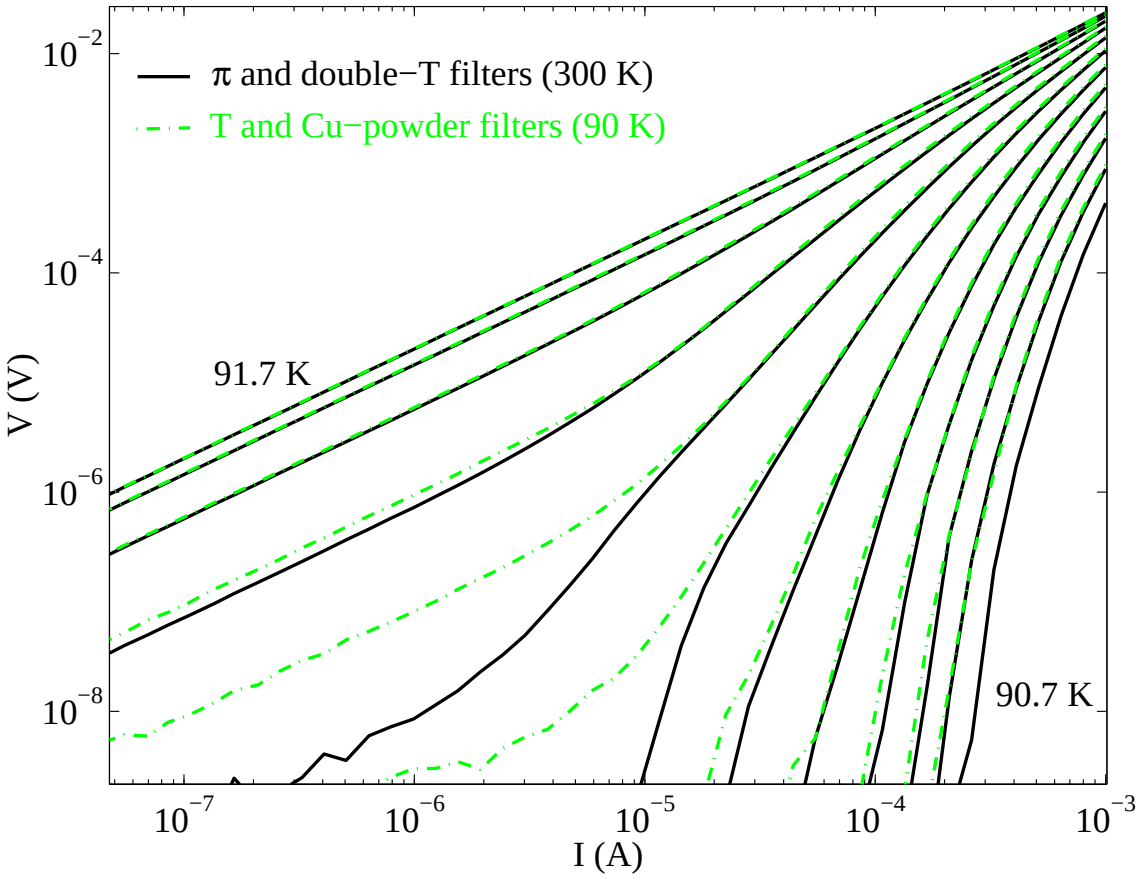

Figure 5.32: Two different filtering schemes for mcs84a. Solid lines show the typical filtering (π and double-T at 300 K). The dashed-dotted lines show cold filtering only (T and Cu-powder at 90 K). Cold filters alone are worse than warm filters alone, but still reduce the noise over no filtering.

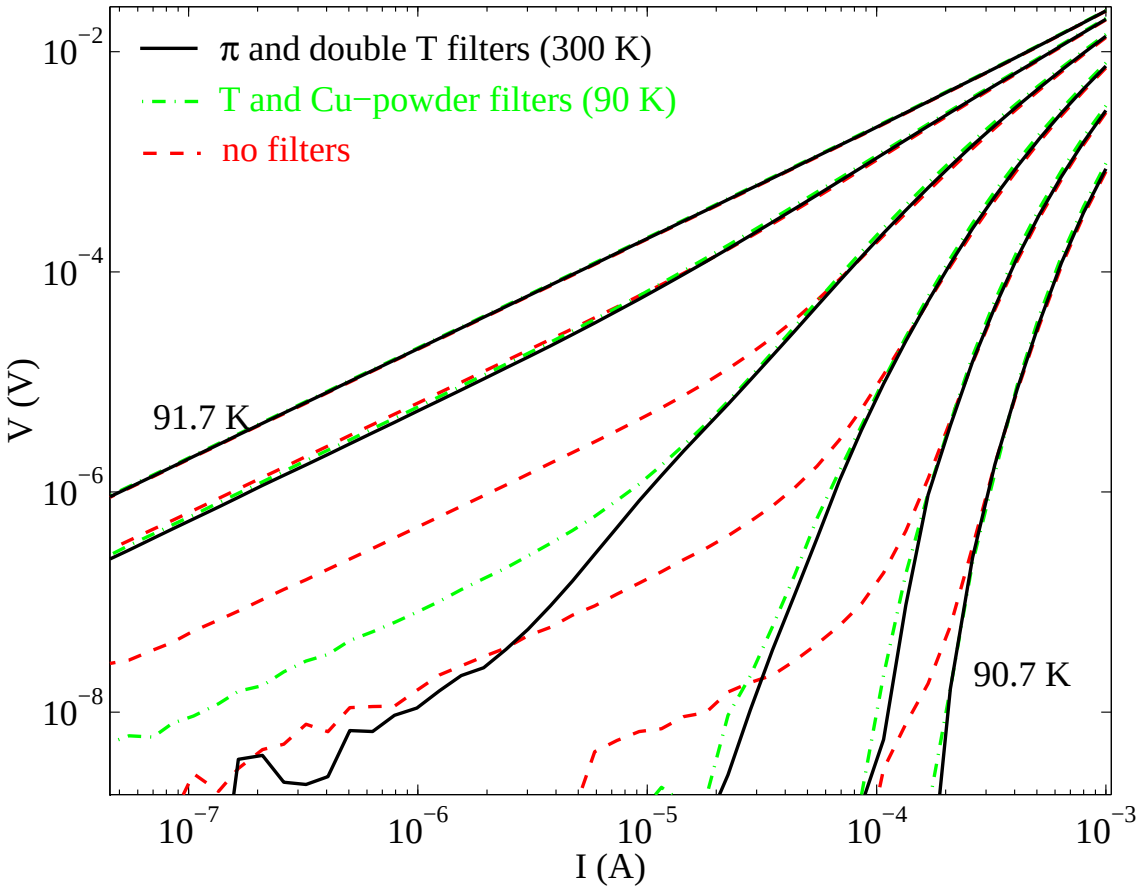

Figure 5.33: All three filtering schemes for mcs84a: warm only (same as warm & cold), cold only, and no filtering. The results indicate that we cannot improve upon our typical filtering at the top of the probe and in the screen room wall.

Our results indicate that we cannot filter better than the warm filters – that luckily, our predecessors hit upon the correct amount of filtering. In desperation, we experimented with various noise reduction schemes beyond filtering. We placed large inductors (1 μH - 1 mH) and large resistors (100 Ω - 1 kΩ) close to the sample in hopes that the larger line impedance would reduce the current noise (larger impedance for the same voltage noise). These did not change the data. We disconnected the sample from all outside noise: computer, current source, and voltmeter, and used a battery as a current source and measured the voltage on a battery-powered voltmeter, again with no improvement over our typical filtering.

In the end, we connected our probe up to a spectrum analyzer, but were unable to measure anything above the noise floor of the pre-amps, about 1 nV/$\sqrt{\text{Hz}}$. With a bandwidth of 3 kHz, even 1 nV/$\sqrt{\text{Hz}}$ is far too small to create the 1 μA of noise necessary to explain our data. Our worst-case scenario of $I_{noise} = 1.3$ μA was clearly an overestimate. We are forced to conclude that noise, although a likely culprit, is not the cause for the ohmic tails in our data.

Current or current density?

It is interesting to note that the estimates of noise all consider an amount of *current*. Of course, what really matters to the sample is current *density*. If we have a fixed amount of noise current, applying that same amount of noise to a wider sample will create a much smaller noise current density. If the sample is wide enough, noise that is a problem in a narrow bridge (read: high noise current density) might not be a problem in a wide bridge (read: low noise current density).

In fact, this is what we see. In mcs101, a 2200 Å sample with a bridge 20 times the length and 20 times the width of our typical bridges (160×800 μm^2), we see no difference between warm filters only and cold filters only. This disagrees with Fig. 5.32. But if cold filtering has a certain noise current associated with it, the noise current density will be twenty times smaller in mcs101 than in mcs84a.

In this way, we are tempted to want to use wider bridges than our typical width (8 μm), to reduce the noise current density. We have, in fact, measured $I - V$ curves on the same sample on bridges of several different widths (discussed in the next section), all of which show identical characteristics, implying that for our typical filtering and typical bridge width, the noise current density is already too low to affect our data.

Using noise to test non-linearity of I-V curves

One would think we've done just about all we can with noise. However, there is one last thing to note about noise in our system. When looking at the previous figures, we can see that the addition of noise, as noted, can create ohmic tails where the isotherm with less noise was non-linear. This agrees with the theory we noted before.

But if we look closer at the isotherms, we notice that the addition of noise can also *change the resistance* of some of the low-current ohmic tails. "So what?", you may ask. Consider an ohmic tail resulting from the phase transition (Eq. 4.57). We know if we add noise to an ohmic sample, it does not change the resistance of the sample (Eq. 5.28).

But when we add noise, we *do* change the resistance of the low-current ohmic tails! This implies that the underlying $I - V$ curve ***must*** be non-linear! If the ohmic tails are caused by some averaging effect (it will be argued in the following section that this occurs due to finite size effects), then the underlying behavior of the sample is still non-linear. This is the first direct evidence that our original assertion – that the ohmic tails are artifacts – is correct. If these ohmic tails were a result of the true phase transition as predicted by Eq. 4.57, their resistance would not change with additional noise. This is a fantastic result, and one that is very comforting.

Summary

Given the fact that we have demonstrated theoretically and experimentally that noise can create ohmic behavior in a non-ohmic sample, it is a natural choice for the source of our ohmic-tail woes. However, numerous filtering schemes cannot make the ohmic tails disappear (much to our chagrin). Our measurement of the noise in the system is orders of magnitude too small to account for the ohmic tails. Moreover, bridges with larger widths – and hence lower noise current densities – show identical behavior to narrower width bridges, implying that we have filtered out all the noise, even in our narrow bridges.

Out of this investigation, however, comes our first proof of our original assertion, that the ohmic tails are an artifact, and that the high-current behavior is the true phase transition. The addition of noise to a linear sample will not change its behavior. However, the addition of noise in our samples actually changes the resistance of the low-current ohmic tails – implying that the underlying $I - V$ curve *must* be non-linear!

This is comforting, and with this small success, we turn to look elsewhere for the cause of the ohmic tails.

5.4 Finite Size Effects in Films

Finite size effects are often a likely candidate to blame when things go wrong. This is because the effects that a finite-size sample can have on the data (which, of course, assumes an infinite sample) are not easy to quantify. I know what a magnetic field is and can calculate it, but a finite size effect?

This is not to say that finite size effects are intractable. In this section we will discuss finite size effects, their impact on the data, and demonstrate that the limited thickness of our sample can create the ohmic tails we see.

5.4.1 Length Scales

When do we need to worry about the size of our sample? This is the fundamental question that arises when working with finite size effects. To answer this, we must look into the length scales of the problem.

The fundamental length scale of the problem is, of course, the size of the fluctuations, ξ. We recall that

$$\xi = \xi_o \left| \frac{T - T_c}{T_c} \right|^{-\nu}, \tag{5.35}$$

which tells us the typical size of a fluctuation as a function of temperature. Of course, there are a few more important lengths (especially out here in the real world), namely the length L, width w, and thickness d of our sample. The thickness is the limiting length as it is so much smaller than either of the other two lengths.

There is a third length of significance. We apply a current (or current density, really) in order to probe the sample. We know from Eq. 4.53 that

$$J \sim k_B T \xi^{-2}, \tag{5.36}$$

for $D = 3$. This equation can be turned around, and indicates that a given applied current density J probes fluctuations of a size L_J[10, 9, 19, 20, 46]

$$L_J = \sqrt{\frac{c k_B T}{\Phi_o J}}, \tag{5.37}$$

where we have added the constants back in such that the units agree. The undetermined constant c in Eq. 5.37 is expected to be of the same order as the YBCO anisotropy parameter, $\gamma = 0.2$[10, 20, 97].

3D regime

We can see right away that there are certain inequalities that must hold in order for our data to be a true investigation of the 3-D phase transition. The first two are $d > \xi$ and $d > L_J$. The first inequality implies the typical fluctuation, smaller

than the smallest length in the bridge, doesn't realize that the sample is finite; the second inequality says that we are looking at only the fluctuations smaller than the thickness of the film.

Given that the thickness is larger than ξ or L_J, what happens when $\xi > L_J$ or $L_J > \xi$? These two limits describe markedly different behavior.

When $L_J > \xi$ (which implies J is small), we are probing a length much larger than the typical fluctuation. This means that we are averaging over many smaller fluctuations. This averaging is expected to produce an ohmic signal for $T > T_c$, precisely the signature predicted by Eq. 4.57[10]. Below T_c, the $I-V$ curves in this region are expected to behave exponentially[10].

If $\xi > L_J$, then the fluctuations are, on average, much larger than the length scale we are looking at. Now we are no longer looking at many fluctuations, and it is in this regime, both above and below T_c, that we expect to see power-law behavior[10].

What will happen if $\xi > d$ or $L_J > d$? In the first case, the fluctuations are limited by the thickness of the film, and can no longer grow along the c-axis. They become 2D fluctuations, fluctuating in the a-b planes, but not along the c-axis. This, needless to say, is not what we are looking for. In the second case, our current attempts to probe only fluctuations that are larger than the thickness of the film. This means that we see only the fluctuations that are limited in size along the c-axis, and again we probe 2D fluctuations. Interestingly enough, the $I-V$ curves of these 2D fluctuations are expected to look ohmic[10, 20, 97], although the underlying behavior is non-linear, as there are fluctuations smaller than the thickness of the film which we are not probing. This is precisely the situation described at the end of the previous section. This ohmic behavior is treacherous, as it can mimic the true phase transition.

$I - V$ curve "maps"

We have just defined a regime, bounded in length, were we can expect 3D data. These lengths, though, can be turned into currents and temperatures. It is instructive to ask: in terms of current and temperature, where is the region of 3D data in a typical $I - V$ curve plot?

This (rather confusing) graph is shown in Fig. 5.34. In order to make this map, we were forced to make several assumptions. We took $T_c = 91.44$ K, the value found from the derivative plot. We also assumed $c = 0.2$, and $\nu = 0.67$. Lastly, we took $\xi_o = 20$ Å, that is, slightly larger than the spacing between copper-oxygen planes.

With these assumptions, the solid lines indicate equalities, namely where $L_J = d$, $L_J = \xi$, and $\xi = d$. The thick isotherms indicate a region very close to T_c where $\xi > d$. Outside these isotherms, and at currents higher than the $L_J = d$ line, we find four regions of 3D data, as described above. These regions correspond to where we found evidence of a 3D phase transition in the derivative plot.

However, all of the data at lower currents than the $L_J = d$ line is 2D data, and is not useful for our experiment. More interesting still, this occurs at almost exactly the current where the low-current ohmic tails set in – and 2D fluctuations are expected to be ohmic! Is this yet another lucky coincidence, or evidence that the finite size of the sample is creating the ohmic tails?

Before moving on it is instructive to show how the map would look if $\nu = 1$, closer to the value we found in our high-current data collapse. This is shown in Fig. 5.35

There is no region on this map which contains 3D data – it is all 2D data, and maps with $\nu > 1$ make the map even worse. This is a further indication that $\nu \geq 1$ is incorrect, despite its apparent agreement with the high-current scaling.

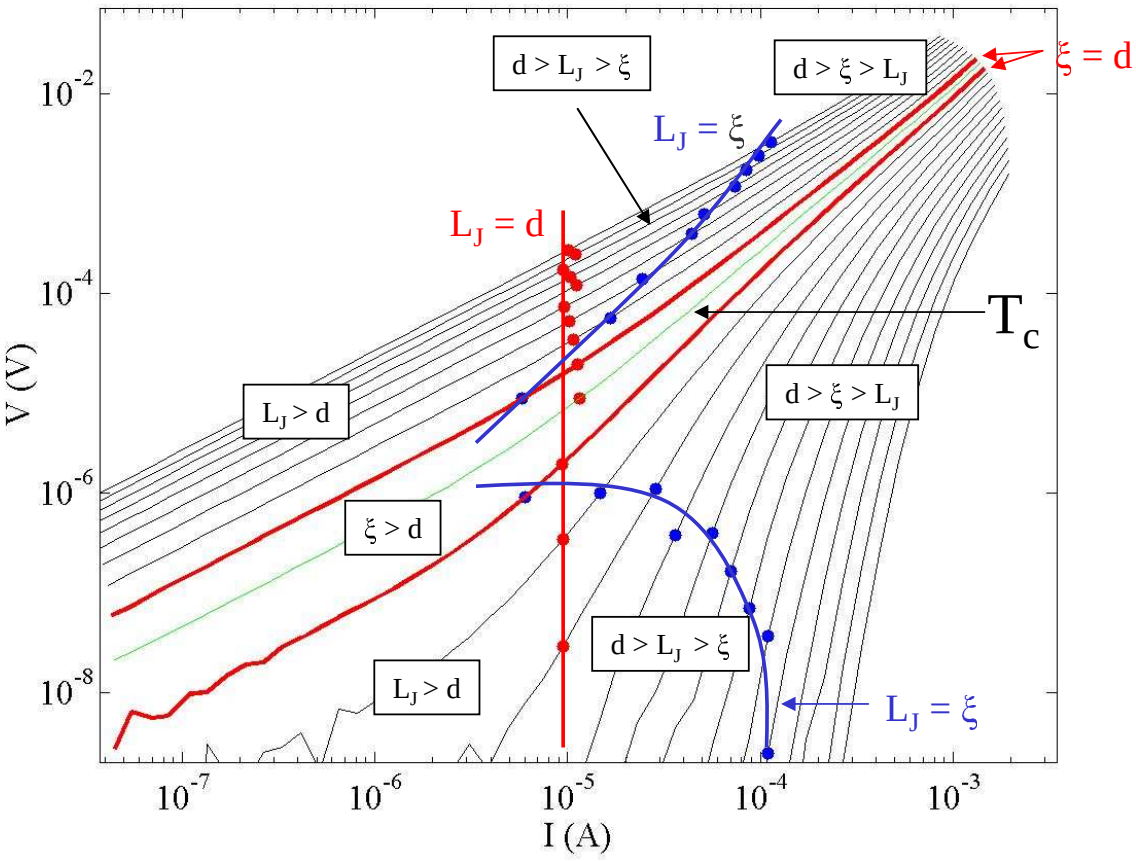

Figure 5.34: $I - V$ curve map for mcs146. This assumes $\nu = 0.67$, $T_c = 91.44$ K, and $c = 0.2$. The solid lines indicate where $L_J = d$, $L_J = \xi$, and $\xi = d$. The data to the left of the line indicating $L_J = d$ is 2D, and cannot be used. The four regions where d is the largest size indicate 3D data.

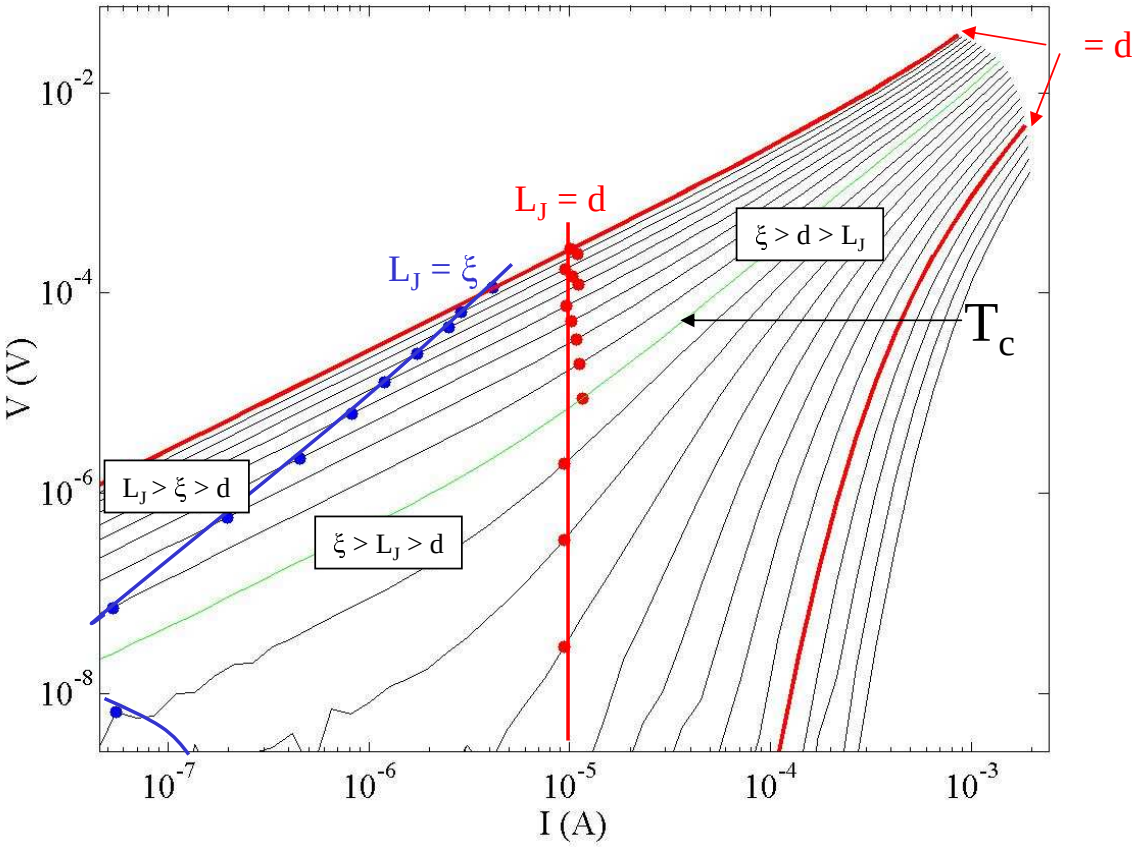

Figure 5.35: $I - V$ curve map for mcs146. This assumes $\nu = 1$, $T_c = 91.44$ K, and $c = 0.2$. The solid lines indicate where $L_J = d$, $L_J = \xi$, and $\xi = d$. There are no data on this plot which are 3D.

5.4.2 Previous Work

Of course, we are not working in a vacuum, and we are not the first ones to propose that finite size effects obscure the 3D transition. Much of the previous work was done in a field, examining the vortex-glass transition, but the equations are identical, and as L_J does not depend on ν, the work done in field directly relates to our work in zero field.

Dekker *et al.* [97] found $z = 2.2 \pm 0.4$ from high-current data in a 500 Å thick YBCO film in zero field, and saw ohmic tails at low currents. Using Eq. 5.37, they noted that the fluctuation size along the c-axis saturated at ≈ 470 Å, indicating the fluctuations had reached the thickness of the film. However, Dekker *et al.* made no predictions as to ν nor attempted a data collapse.

Wöltgens *et al.* [20] measured films of different thicknesses in a magnetic field. They found deviations from 3D-scaling which appeared as ohmic tails in films with $d \leq 500$ Å, as compared to a 3000 Å film. However, they *assume* that the finite-size effects in thin films do not extend to the 3000 Å film because the $I-V$ curves for the 3000 Å film scale with typical vortex-glass exponents. This assumption is doubtful given the ease with which $I - V$ curves can be scaled using different choices of T_g, ν, and z[12]. This makes the data collapse of the 3000 Å film inconclusive evidence that the thicker film is unaffected by the finite-size effects they see in thinner films. A quick analysis shows that they included data in their collapse of the thick film below the current where $L_J = d$, indicating 2D data were included in a 3D analysis.

Similarly, Yeh *et al.* [46] found grain boundaries in their crystals limited the size of their fluctuations, and created a finite size effect. However, they analyzed their data in a manner identical to that of Wöltgens *et al.*, namely, as ohmic deviations from the 3D scaling collapse. Again as shown by Strachan[12], assuming a data collapse to prove the existence of a transition is treacherous at best (foolhardy at worst, at least after the publication of Ref. [12] in 2001).

Finally, Sawa *et al.* [98] showed data collapses for films as thin as 180 Å and as thick as 10,000 Å in a 2 T applied field. To collapse the data, they were forced to systematically change T_c, ν and z. They cited this as evidence for the need for an anisotropic 3D-XY model. On the other hand, all of their collapses included data at currents below the $L_J = d$ line, indicating that perhaps as that line shifted in current for the different thicknesses, they were required to change their critical parameters to force a data collapse.

Those who found 2D ohmic behavior at low currents found it as deviations from a 3D scaling collapse. They assumed the collapse worked first and explained deviations second. Those who had no trouble with even very thin films found that z and ν varied for every thickness of film (as well as finding very odd values of z and ν).

Perhaps there is a way we can look for finite size effects without looking for deviations from a scaling collapse.

5.4.3 Finding J_{min}

The $I-V$ curve map in Fig. 5.34 suggests that the ohmic tails occur at $L_J = d$ and are due to finite size effects. In order to make the map, we converted the L_J into a current, despite the fact that equations like Eq. 5.37 indicate that it is current density which matters, not current.

We would like to know if the ohmic tails occur at a given current or current density. For example, ohmic tails due to noise would occur at a certain current, whereas ohmic tails from finite size effects should occur at a certain current density.

Current or current density?

To test this question, we modified our experiment. Instead of one bridge, we patterned three bridges in series, each bridge with its own set of voltage leads. In

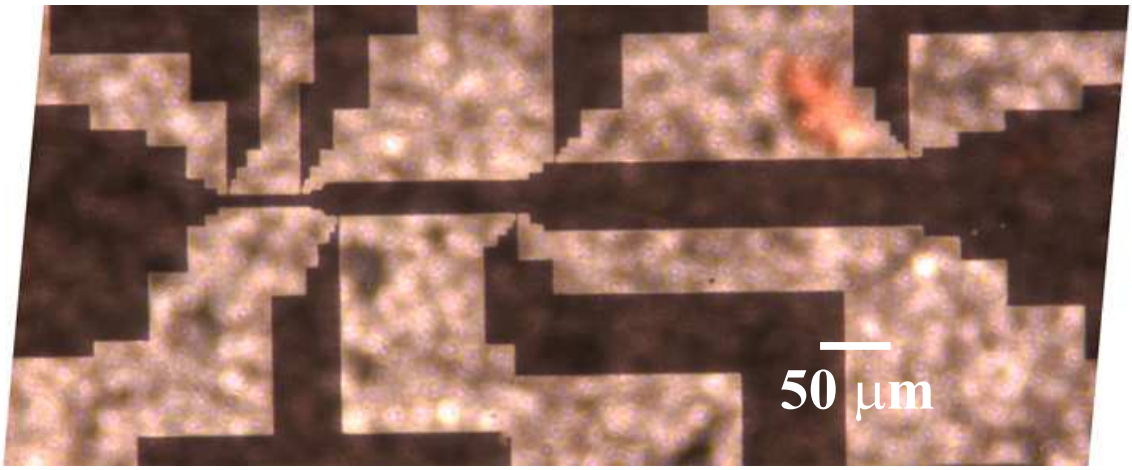

Figure 5.36: Picture of mcs146, showing all three bridges, each with its own set of voltage leads. The YBCO is black. The voltage lead on the far right is broken.

this way, we tested bridges of different widths, under identical conditions, and each bridge had identical material properties, because it was made from the same film. One of the films with three bridges was mcs146. A picture of mcs146 is shown in Fig. 5.36. In this figure, the film is substantially thinner than 2100 Å. We ion milled the sample in an attempt to measure different thicknesses on the same film. Unfortunately, the ion mill damaged the sample. The sample was ion milled after we took the data we will present here.

We have already seen the derivative plot for mcs146 for a 20×100 μm^2 bridge (Fig. 5.8). Let us skip the $I - V$ curves and focus on the derivative plot. The derivative plot as a function of I is shown for three bridges (20×100 μm^2, 50×250 μm^2, and 100×500 μm^2) at 91.26 K in Fig. 5.37.[15] It is clear why we have chosen to display only one temperature in this figure, because more than one would clutter the graph hopelessly – the isotherms do not agree at all!

The situation is radically different in a derivative plot as a function of current density J. This is shown in Fig. 5.38. In this figure, we can see that the isotherms for

[15]We have switched and now refer to it as $\partial \log E / \partial \log J$ as opposed to $\partial \log V / \partial \log I$. Because of the magic of logarithms, the two are identical.

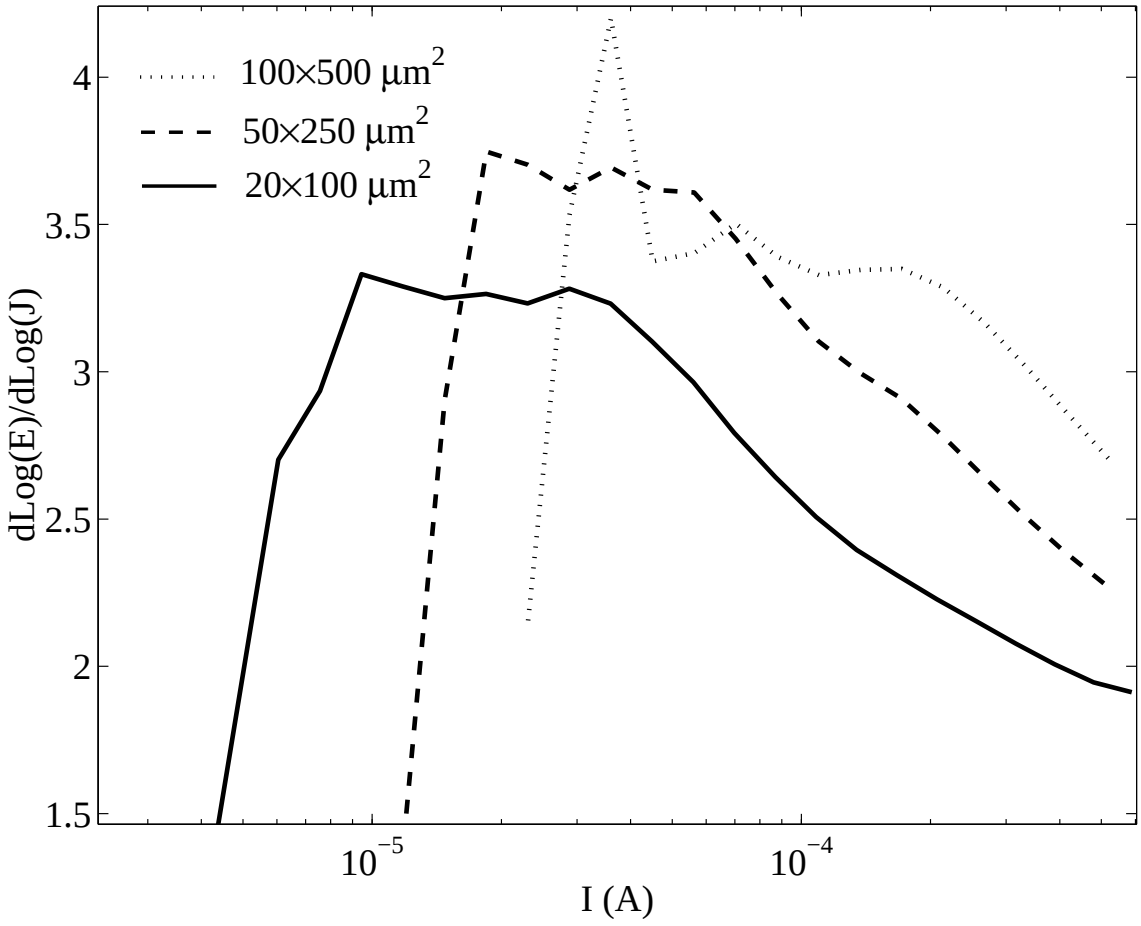

Figure 5.37: Derivative plot for three bridges on mcs146 as a function of current I. The temperature for all three curves is 91.26 K. The bridge dimensions are 20×100 μm^2, 50×250 μm^2, and 100×500 μm^2. The isotherms clearly do not overlap.

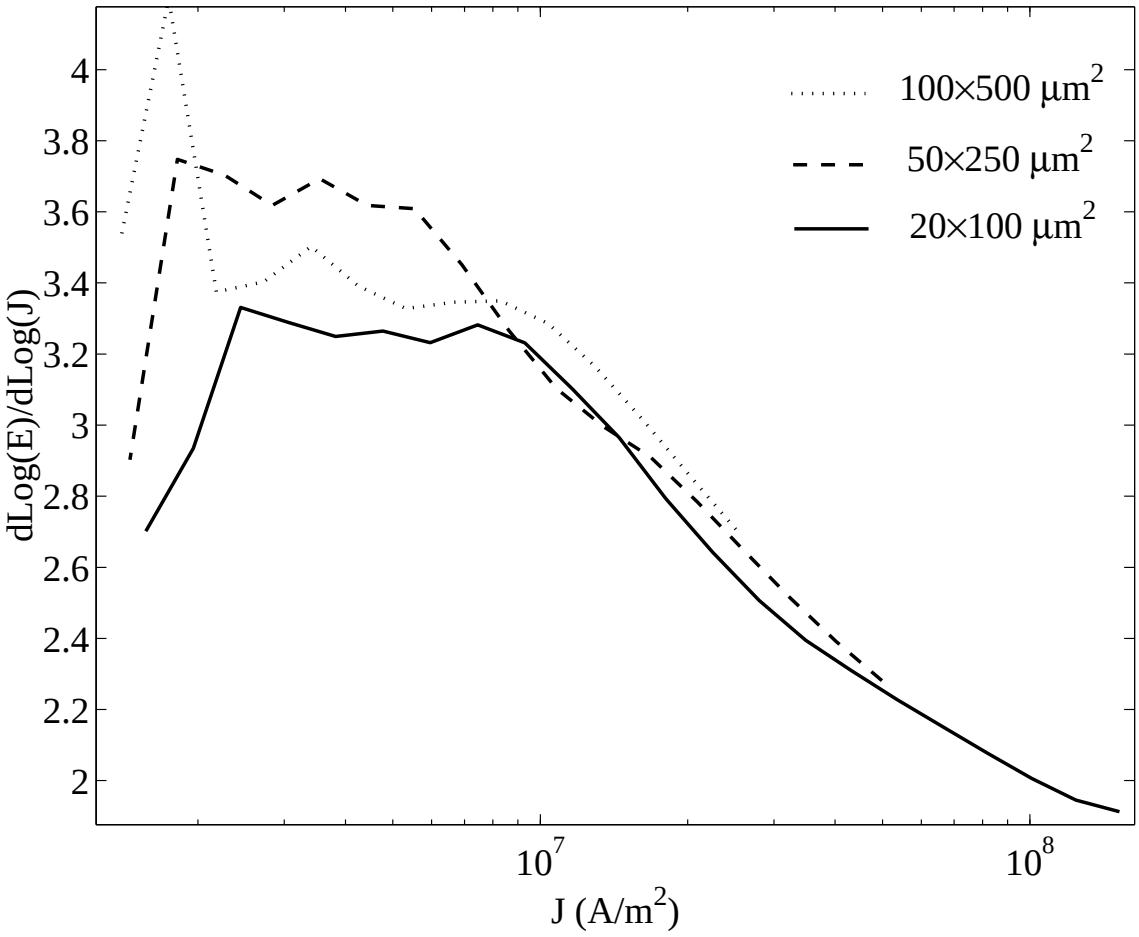

Figure 5.38: Derivative plot for three bridges on mcs146 as a function of current density J for 91.26 K. These isotherms overlap, indicating the ohmic tails occur at a certain current density rather than current.

the three different bridges all lie on top of one another and display nearly identical behavior. Thus we see that the bridge responds as a function of current density rather than current, and demonstrates that the ohmic tails occur at a certain current density.[16]

We can now plot all of the isotherms as a function of J. This is shown in Fig. 5.39. In this figure it is clear that the agreement of the 91.26 K isotherm was not a

[16]It is also evidence that the current flows through the bulk of our bridge, as opposed to flowing on the edges as seen in Ref. [99].

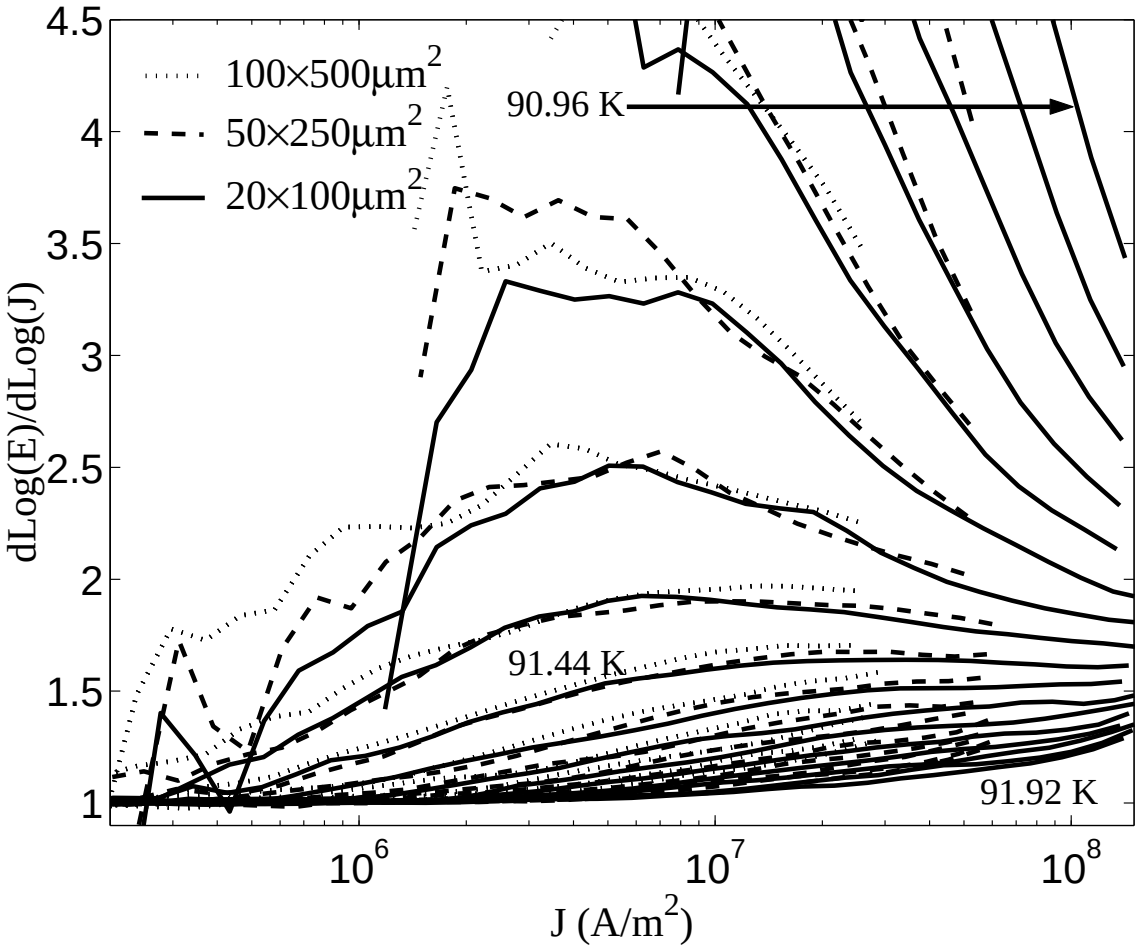

Figure 5.39: Derivative plot for three bridges on mcs146 as a function of current density J. Here we can see all isotherms in the derivative plot overlap as a function of J.

coincidence, as all the isotherms fall on top of one another as a function of J.

Choosing J_{min}

We can see that the ohmic tails occur at a certain current density. Moreover, from the maps, we see that the ohmic tails begin at where $L_J = d$. This leads us to define a minimum current density, such that smaller current densities probe 2D fluctuations. From Eq. 5.37, we set $L_J = d$ to find

$$J_{min} = ck_BT/\Phi_o d^2. \tag{5.38}$$

Now we know how to find J_{min} theoretically, but how do we find it in our data?

The high currents appear to exhibit 3D behavior, and the very low currents, ohmic behavior. J_{min} must be in the transition between the two. Unfortunately, this leaves a large range in current (usually a decade or more). We will use the same criterion used by Dekker *et al.*, when $\partial \log E / \partial \log J = 1.2$. This choice is arbitrary, and other values of $\partial \log E / \partial \log J$ would work as well.

5.4.4 J_{min} in Films of Different Thicknesses

Now that we know the ohmic behavior occurs at a certain current density, and we have a method of finding J_{min}, we want to examine J_{min} in films of different thicknesses. If the ohmic tails really are caused by finite-size effects, then we expect $1/\sqrt{J_{min}}$ vs. d to be a line with slope $(\Phi_o / c k_B T)^{1/2}$. This slope will give a value for the undetermined constant c.

The only question remains, at what temperature T? To choose $I - V$ curves to compare between films, we have taken the isotherm which, from high-current data, most seems like T_c, that is, horizontal on a derivative plot. The films do not all have identical values for T_c, but they vary only from 91.4 K - 92.5 K, a total change of about 1%.

The results are plotted in Figure 5.40. Each value for $1/\sqrt{J_{min}}$ incorporates error in I_{min}, bridge width and thickness, leading to error bars of about $\pm 22\%$. Nonetheless, the trend is clear: as d increases, J_{min} decreases. The solid line in Fig. 5.40 is a weighted least-squares linear fit to the data with a reduced chi-squared of $\tilde{\chi}^2 = 0.41$. From the slope we determine $c = 0.60 \pm 0.17$, the same order of magnitude as $\gamma \approx 0.2$, as expected.

The line fit in Fig. 5.40 does not have a zero intercept, as one would expect from Eq. 5.38. This most likely results from a low choice of J_{min}. The transition from a power law to ohmic occurs over more than a decade, and $d\log E / d\log J = 1.2$ is

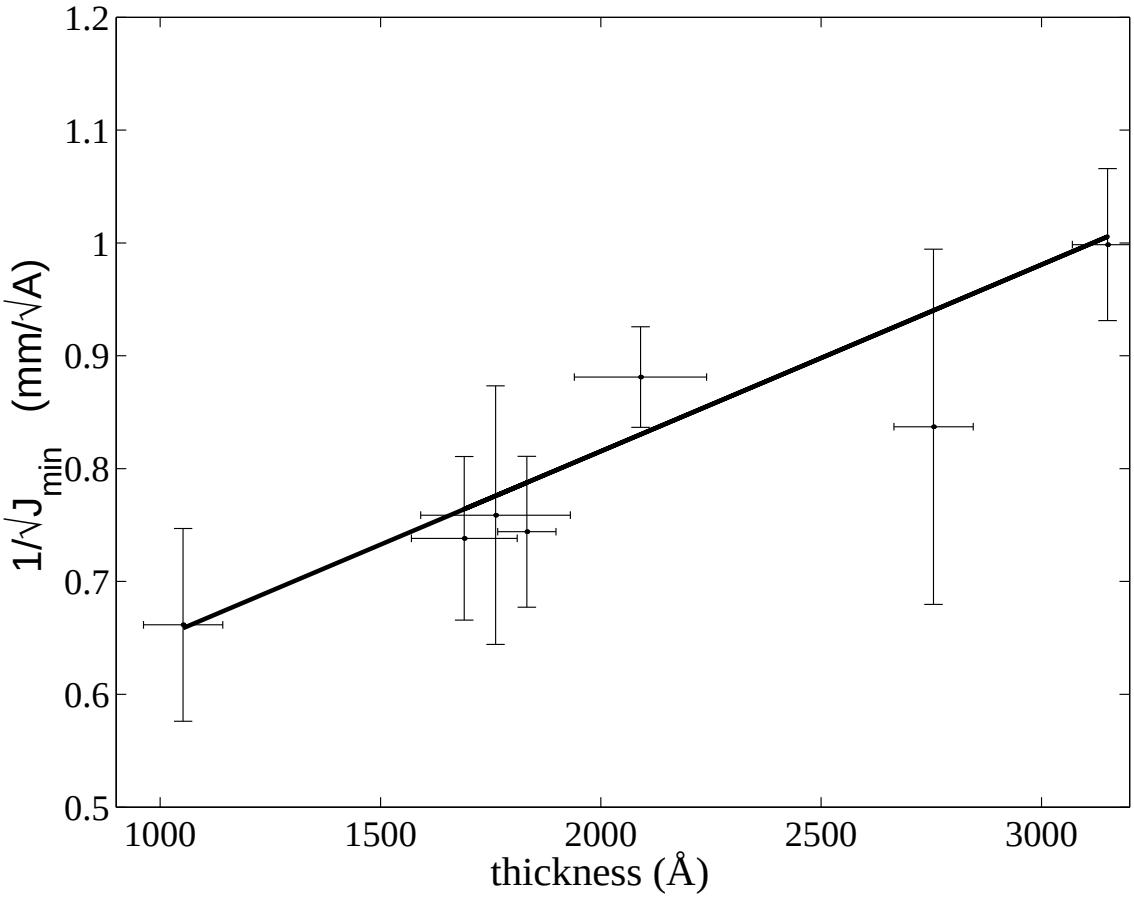

Figure 5.40: $1/\sqrt{J_{min}}$ vs. thickness for eight different films. The solid line is a weighted least-squares linear fit to the data, with a reduced chi-squared $\tilde{\chi}^2 = 0.41$. The slope of the line gives $c = 0.60 \pm 0.17$, of the same order as $\gamma \approx 0.2$, as expected.

towards the lower end of this transition. It is difficult to choose values closer to the high currents, as each film has different values for $\partial \log E / \partial \log J$ in the high-current data. However, the non-zero intercept in the figure does not significantly change the value of J_{min}.

It seems as though we may have found our villain in the end. We have shown that the ohmic behavior occurs as a function of current density and not current, and that J_{min} obeys an inverse-square relationship with the thickness d, and found experimentally that $c = 0.6 \pm 0.17$, of the same order as $\gamma \approx 0.2$, as expected.

Implications of finite size effects

Our results indicate that finite size effects obscure the normal-superconducting phase transition, especially for applied current densities less than J_{min}. On the other hand, this seems to imply that analyzing the high current data is legitimate, implying that the exponents we derive from the high current analysis ($z \approx 2.1$ and $\nu \approx 1.2$ in most of our samples) are the correct values.

On the one hand, at T_c, the fluctuation size diverges, so the size of the fluctuation will always be larger than L_J. This implies that varying L_J (by changing J) won't change the fluctuations we are looking at. Moreover, the power-law relationship we use to find T_c and z is expected to obey at all currents. Thus, we expect to find reasonable values for T_c and z from the high-current analysis.

On the other hand, it is more difficult to find ν. Finding ν requires us to use the low-current ohmic tails – and now we know that these ohmic tails are artifacts of the finite size of our sample. This means that we can no longer use them for data analysis – leaving a data collapse (or the derivative plot collapse) to find ν. While the data collapse has been often used to find critical exponents, we have shown that it must be used with caution. This leaves our value for ν in limbo: a method without the pitfalls of the data collapse must be found before we can state with certainty the value for ν.

Before we discard our value for ν entirely, it is interesting to note that recent theoretical work which incorporates finite size effects in the transition finds values for ν similar to those we have found in our data, $\nu \approx 1.2$[47, 100]. These results indicate that finite size effects may extend beyond $J = J_{min}$ to change the behavior at even higher currents.

5.5 Summary

Because this chapter was so long, it behooves us here to provide a short summary.

We found that the conventional analysis of $I - V$ curves had certain problems. It was irksome that the critical parameters were so far from the expected values, and that so much of the high-voltage data were discarded. When Strachan showed that many different data collapses could be achieved by simply changing T_c, z, and ν (and also the amount of data thrown away), we began to look for another method to determine the critical parameters.

We found a better method in the derivative plot. From the high currents, we found unambiguous choices for T_c and z, choices which agreed with theory. This was promising – only the derivative plot unearthed new problems, and showed unexplained ohmic behavior at low currents.

After discarding heating, sample inhomogeneity, magnetic field, and noise as likely causes of the ohmic tails, we lit upon finite size effects. We were able to show that there is a current density, J_{min}, such that lower currents probe 2D fluctuations. These 2D fluctuations look ohmic. By looking at J_{min} in films of different thickness, we showed that $1/\sqrt{J_{min}}$ vs. d was linear as expected, and from the slope got a value for the constant $c = 0.6 \pm 0.17$, which is of the same order as the YBCO anisotropy parameter $\gamma \approx 0.2$, as expected.

Chapter 6

Measurements in Crystals

Given the ease with which we can grow, pattern, and measure films, many would consider branching out into the world of crystals foolish. Crystals are notoriously difficult to grow, and once grown, it is nigh-impossible to attach contacts, thermally anchor, etc. Considering these problems, why bother?

There are many different experiments which can measure the critical behavior of YBCO and extract exponents. One of the other ideas our group has been working on is trying to conduct **two** experiments on the same sample. This will give us two independent measurements of T_c and the critical exponents (and hopefully, the two will agree!). This idea is not new, and has been attempted before[101]. Previously, Strachan attempted to measure the dc transport and the microwave conductivity $\sigma(\omega)$ on the same film, with limited success[15]. With crystals, we could measure specific heat and dc transport on the same sample (the microwave measurement is ill-suited to crystals).

The advantage of specific heat over the microwave measurement is that it requires only a small amount of data analysis to extract C from the measurement, where the microwave measurement requires significant (and difficult) data analysis to extract $\sigma(\omega)$ from the output of the network analyzer. Moreover, we know instantly whether we are measuring C properly, because many experimenters have already measured the specific heat of YBCO, although few have combined it with another experiment.

There is yet another advantage to crystals. If indeed finite size effects are obscuring the transition in films, as we have argued in the previous chapter, then by using a crystal, the smallest length in the sample grows by 2 orders of magnitude or more! We can test to see if crystals are immune to these finite size effects, as we expect them to be. If they are, then they should demonstrate the transition with 3D-XY exponents.

6.1 Specific Heat

We measured the specific heat of an 8.1 mg YBCO single crystal grown by the UBC group[14, 18]. As expected, the data show a jump at T_c (recall in GL theory, at T_c there is a discontinuity in specific heat [Eqs. 4.18 and 4.19]).

Unfortunately, our data is not precise enough to weigh in on the current debate in the specific heat community, namely, does $\alpha = 0.5$ (GL plus Gaussian fluctuations, Sec. 4.1.2) or does $\alpha \approx 0$ (3D-XY, Sec. 4.2.3)? Reasonable fits can be obtained for either value of α.

Perhaps, though, we can contribute in another way. Our own analysis of the high-current of $I - V$ curves indicates that $\nu > 1$. Using specific heat, we can see if we can fit our data using this value for ν.

6.1.1 Specific Heat Data

Our data is taken using the relaxation method described in Ch. 3. Any specific heat measurement consists of two parts: the addenda, called $C_{addenda}$, and the sample, called C. First we measure $C_{addenda}$, then we add the sample and measure $C_{tot} = C + C_{addenda}$.

Technically, everything we measure is a heat capacity, and not a specific heat. In particular, because $C_{addenda}$ is the combined heat capacities of several different things (heater, thermometer, grease, etc.), it cannot be turned into a specific heat.

When we discuss the sample, however, we divide C by the mass of the sample, making it a specific heat. However, following the literature, this is *also* given the symbol C (as opposed to c, the symbol used in most textbooks). As a rule of thumb, when we are talking about $C_{addenda}$, it is a heat capacity, C, a specific heat. When completely confused, be sure to check the units.

The addenda

The addenda consists of everything that is not the sample: the sapphire stage, heater, thermometer, and also the thermal grease used to connect the sample to the stage. After measuring $C_{addenda}$, the sample is placed on the stage and the measurement is run again, this time measuring $C_{tot} = C + C_{addenda}$. For this reason it is important to make $C_{addenda}$ as small as possible, such that the signal from the addenda does not obscure the signal from the sample. Our stages have been home-made by H. Balci, especially designed to reduce $C_{addenda}$. For our measurements, $C \approx 3 \cdot C_{addenda}$.

In Fig. 6.1 we show a typical addenda measurement. Because the majority of $C_{addenda}$ comes from the grease, each time we measure $C_{addenda}$ it is different (but similar). The error bars in the plot indicate the statistical error after 20 measurements. Each data point is actually an average of specific heat $\pm$ 50 mK about each point (on the scale shown, roughly twice the size of the points), as the rise temperature was 100 mK above the bath temperature. As expected, $C_{addenda}$ is a smooth function through the transition region.

The line is a weighted cubic fit to the data. It is this fit that we will subtract from our measurement of C_{tot} to find C.

Specific heat of YBCO

Once we have measured the addenda, we can subtract it from the total heat capacity to find the specific heat of the sample. The procedure seems straightforward, and

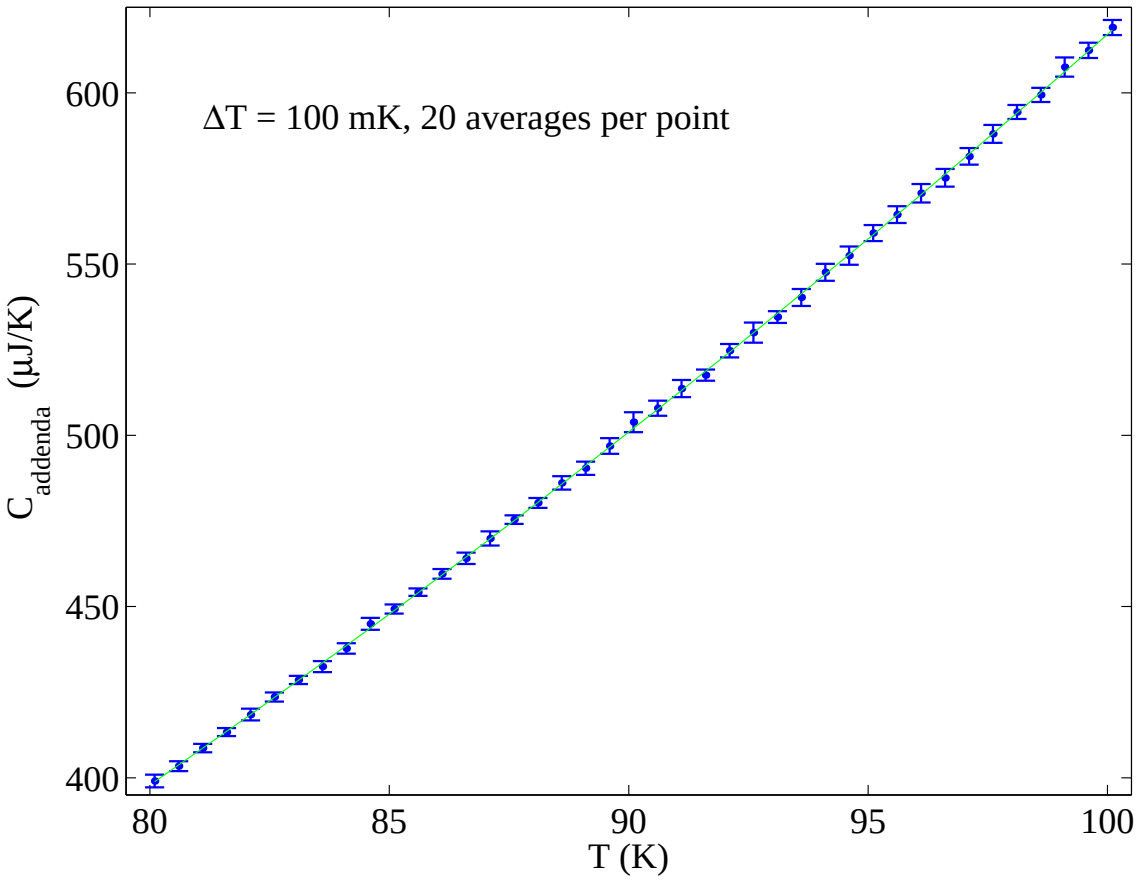

Figure 6.1: A typical measurement of $C_{addenda}$. In this plot, the error bars indicate the statistical error after 20 measurements. The rise above the bath temperature was 100 mK (refer to Sec. 3.2.1). The line is a weighted cubic fit to the data.

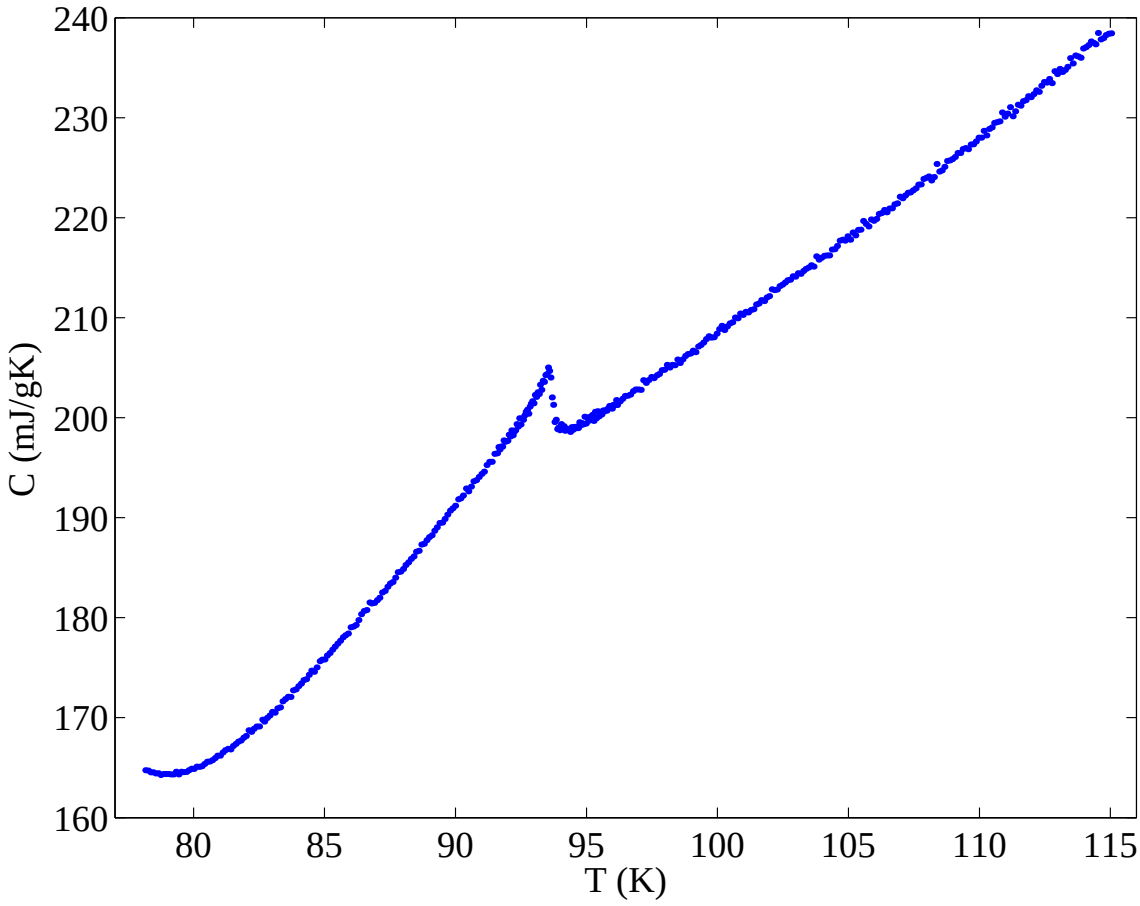

Figure 6.2: Specific heat of a YBCO single crystal, from 78 K to 115 K. The superconducting transition is obvious at about 94 K. The upturn at $T \approx 82$ K is unexpected. The data were taken as twenty averages per point, and $\Delta T = 200$ mK.

the results are shown in Fig. 6.2.[1] Each point was averaged 20 times, and $\Delta T = 200$ mK.

In this figure, we can immediately recognize the superconducting transition as the jump in specific heat at about 94 K. This occurs at the same temperature as the transition we measured in our magnetization measurements (Fig. 2.16). These data leave no doubt as to the existence of a phase transition in YBCO.

[1]In this figure, we have given up and used non-SI units. We have a legitimate reason, however, as the unit used most often in the literature is mJ/gK, making our results easy to compare with those of other researchers. For purists, however, 1 mJ/gK = 1 J/kg-K.

These data also show some unexpected results. First, there is an upturn beginning about 82 K. Because we did not measure the addenda below 80 K, we might attribute this upturn to errors from extending the addenda fit below the measured addenda. However, this upturn is present in the raw data (C_{tot}). Moreover, the upturn begins at 82 K, where we do have data for $C_{addenda}$.

This upturn is most likely nitrogen condensing on our sample. The crystal offers a much larger area for nitrogen gas to condense upon than the stage, and as we get closer to the boiling point of nitrogen (about 77.6 K in our dewar, which is slightly under pressure), more and more should condense on our crystal. Nitrogen has a very large specific heat, and so even an atomic layer on the surface of our crystal (roughly 1 mm^3 in size) will be measurable. Helium condensation near 4.2 K has corrupted data in other measurements in our lab.

Another unexpected result becomes obvious when we zoom in to the transition. In Fig. 6.3, we notice that the data are not a smooth curve. Each data point contains an error of roughly ± 0.6 mJ/gK, quite significant on the scale of the graph. In fact, the error bars were not included in the figure because they tended to obscure the data. This is the major drawback of our experiment – our thermometer is not very sensitive. For a ΔT of 100 mK, our thermometer has a change of about $\Delta V \approx 1$ μV (depending on the temperature and the current in the thermometer). Of course, 1 μV is easy to read, however, this 1 μV change is riding on a 1 mV signal. This leads to noisy data, which are clearly visible in Fig. 6.3.

This noise is especially harmful when we look at the magnitude of the specific heat jump ΔC.[2] We can see that $\Delta C \approx 6$ mJ/gK, only about 3 % of the total signal. In other words, we are looking for a small signal with an inaccurate thermometer – not the best of experimental worlds.

Nonetheless, our measured specific heat is nearly identical to that for other

[2]Be careful not to confuse this with the fluctuation contribution to specific heat, also called (of course) ΔC (see Ch. 4).

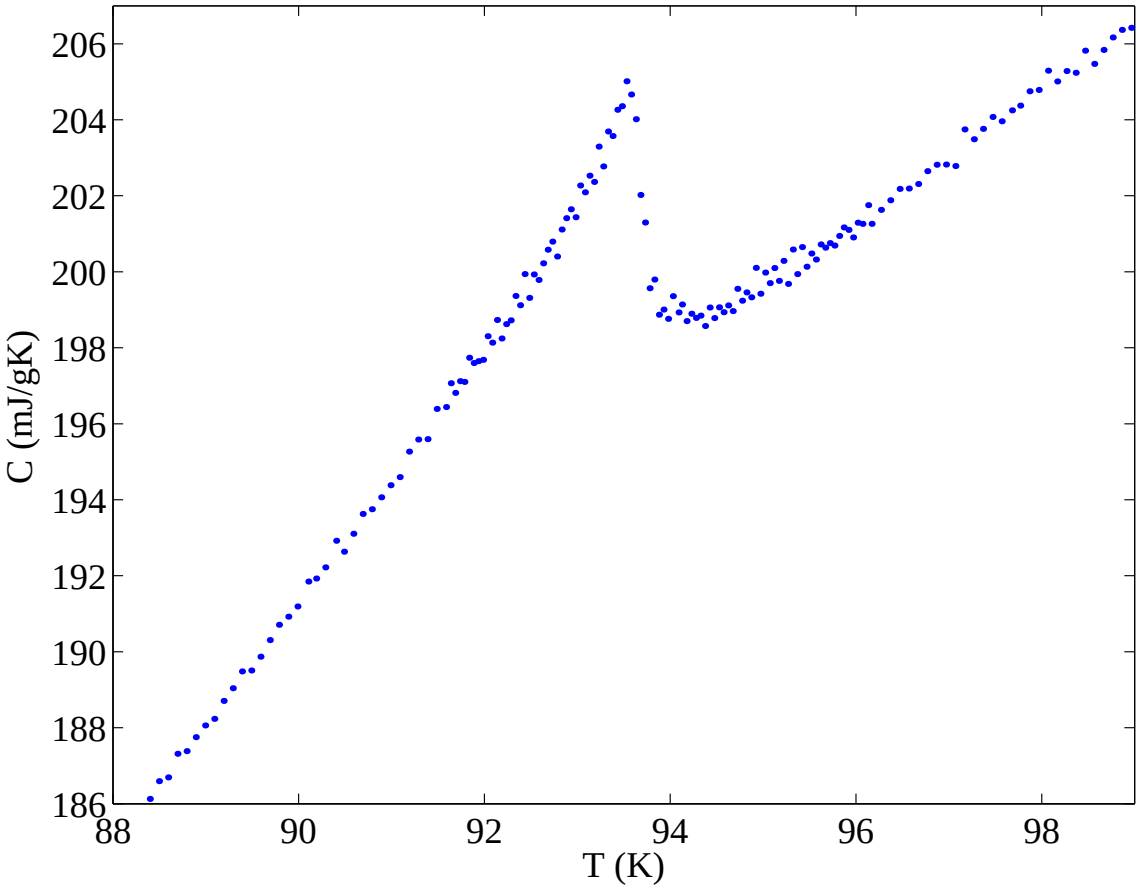

Figure 6.3: Specific heat of a YBCO single crystal, from 88 K to 99 K. In this figure, it is clear that the curve is not smooth. Each point contains sizable errors of ±0.6 mJ/gK – so large, in fact, that the error bars were omitted because they obstruct the graph. The jump in specific heat, $\Delta C \approx 6$ mJ/gK, is only about 3 % of the signal.

crystals made by the UBC group and measured by other experimentalists[18, 102]; thus, despite the shortcomings of our apparatus, our data is reliable.

6.1.2 Analysis of Specific Heat Data

The problems in the data notwithstanding, we can now try to analyze the data. Recall that in Ch. 4, we claimed the specific heat followed the equation

$$C = \frac{A^{\pm}}{\alpha} \left| \frac{T - T_c}{T_c} \right|^{-\alpha} + B^{\pm}, \tag{6.1}$$

which, in fact, looks almost nothing like the data presented in Fig. 6.3.

Of course, when we proposed Eq. 6.1, we failed to mention that this equation, like most equations, is only valid under certain circumstances. Eq. 6.1 describes how specific heat behaves near the superconducting second-order phase transition. This, of course, is a phase transition that only the electrons undergo, thus we do not expect the phonons to play a significant role in this transition, although at such high temperatures, we do expect the phonons to contribute significantly to the specific heat.

Moreover, Eq. 6.1 describes the behavior in the critical regime only. Outside the critical regime, we expect the transition to look like GL theory (perhaps with fluctuations as perturbations), and beyond that, we expect it to look like regular electronic specific heat ($C_{el} = \gamma T$). These are yet further wrinkles that complicate the data analysis.

C_{el} and C_{ph}

Let us consider the specific heat outside the critical regime. To first order, we can approximate this specific heat as linear in temperature. Although the fit will depend on the temperature range we choose, for the following argument the exact range we choose does not matter.

We first ask, what effect does the electronic specific heat have? We expect it to be large in the critical regime, and outside the critical regime we expect it to go as $C_{el} = \gamma T$. Outside the critical regime, is C_{el} significant? The electronic specific heat has been measured[103], and $\gamma < 0.04$ mJ/gK^2 ($\gamma T \lesssim 4$ mJ/gK) outside the critical regime, and $\gamma < 0.12$ mJ/gK^2 ($\gamma T \lesssim 12$ mJ/gK)for all temperatures. If we fit the data from 105 K to 110 K, we find a slope of ≈ 2.1 mJ/gK^2. Thus, we see that we can ignore the electronic specific heat outside the transition region.

This leaves us to worry about the phonon contribution, C_{ph}. The lattice contribution to the specific heat has been measured, and the Debye temperature has been found to be $\Theta_D \approx 450$ K[104, 105]. This puts the region of interest (near 90 K) directly in-between the low- and high-temperature limits of lattice specific heat. As a result, many different methods have been used to fit the region of interest, including (but not limited to): linear, quadratic, cubic, quartic, and two or three Einstein modes[84].

This is another debate we do not wish to wade into. Over a small enough range in temperature, C_{ph} *must* be linear, and so we will fit the phonon contribution to $C_{ph} = C_{ph1}T + C_{ph0}$. This also agrees with other experimenters who note little difference between the linear and quadratic fits for C_{ph} near the critical regime[79, 102].

Two possible fits for C_{ph} are shown in Fig. 6.4, each with its own advantages and disadvantages. The solid line seems to fit specific heat data both above and below the transition. On the other hand, the dashed line fits a wider range of temperatures, and also fits closer to the transition. In practice, both fits are so similar that we can use either fit without changing the data analysis much. Each fit is a weighted least-squares fit for the given regions in temperature.

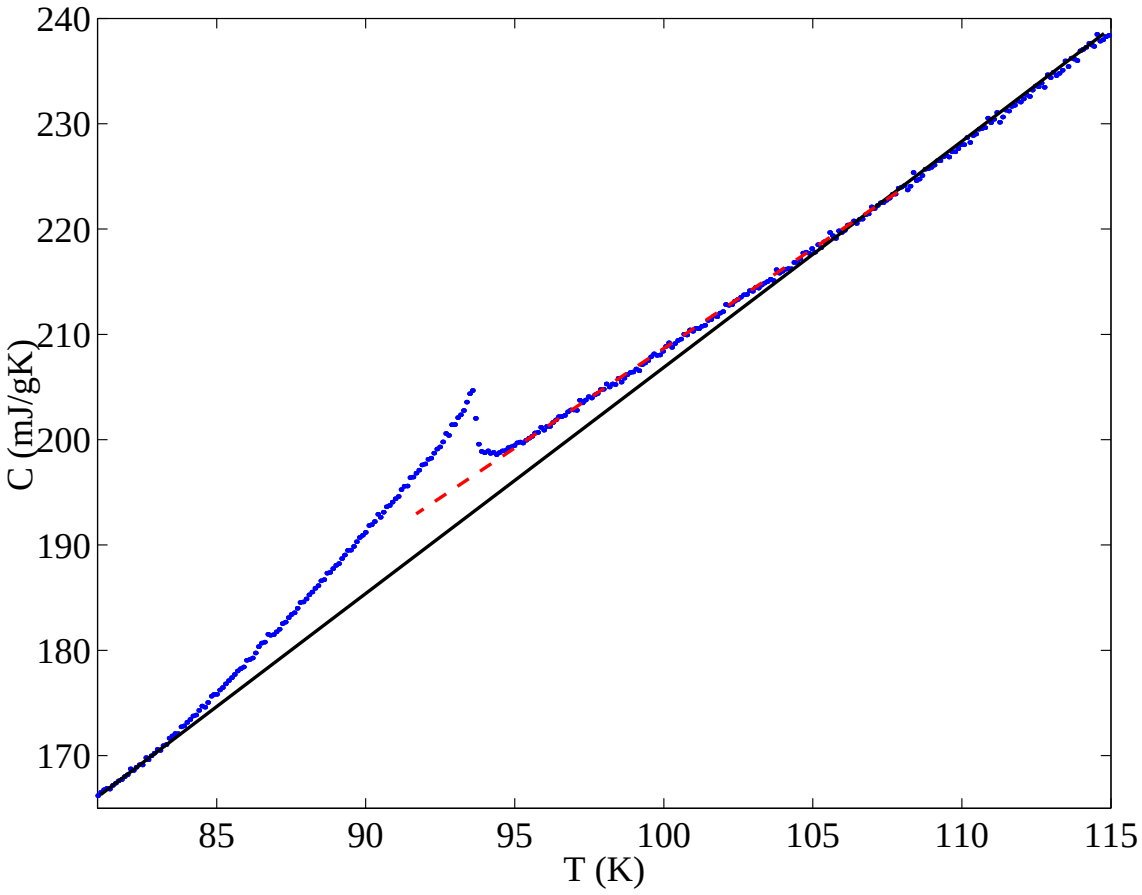

Figure 6.4: Specific heat of a YBCO single crystal, with two possible fits for C_{ph}. The solid line is a good choice as it connects on both sides of the critical region. The dashed line fits over a larger range of temperature, and closer to the transition.

Data analysis

We now see that, with the simplest fit for the phonon contribution, the measured specific heat in the critical region goes as

$$C = \frac{A^{\pm}}{\alpha}\left|\frac{T-T_c}{T_c}\right|^{-\alpha} + B^{\pm} + C_{ph1}T + C_{ph0}. \tag{6.2}$$

Ideally, we would like to take the derivative, dC/dt, where $t = (T/T_c - 1)$, to find

$$\frac{dC}{dt} = A^{\pm}|t|^{-(\alpha+1)} + C_{ph1}T_c, \tag{6.3}$$

which eliminates many of the fit parameters, leaving only C_{ph1} from the phonon contribution. After subtracting $C_{ph1}T_c$ from $\frac{dC}{dt}$, the value of the exponent α should be obvious on a log-log plot.

Unfortunately, as mentioned earlier, our data simply aren't precise enough to allow us to take the derivative. We must resort to the brute-force method – subtraction. The specific heat without the lattice contribution is often called C_{sing}, as it is expected to be singular at T_c, and is given by

$$C_{sing} = C - (C_{ph1}T + C_{ph0}). \tag{6.4}$$

This subtraction is shown in Fig. 6.5, using the solid line fit in Fig. 6.4 for C_{ph}.

Fits

Now that we have found the singular part of the specific heat, we will attempt to fit the data. Recall from Ch. 4 (Eq. 4.67) that

$$\frac{A^{\pm}}{\alpha}|t|^{-\alpha} \approx -A^{\pm}\ln(|t|), \tag{6.5}$$

if α is very small. This implies that the specific heat on a semi-log plot will look like two nearly parallel lines. This is shown in Fig. 6.6. To make this plot, we have chosen $T_c = 93.58$ K, the point at the peak in Fig. 6.3. Although there is some error

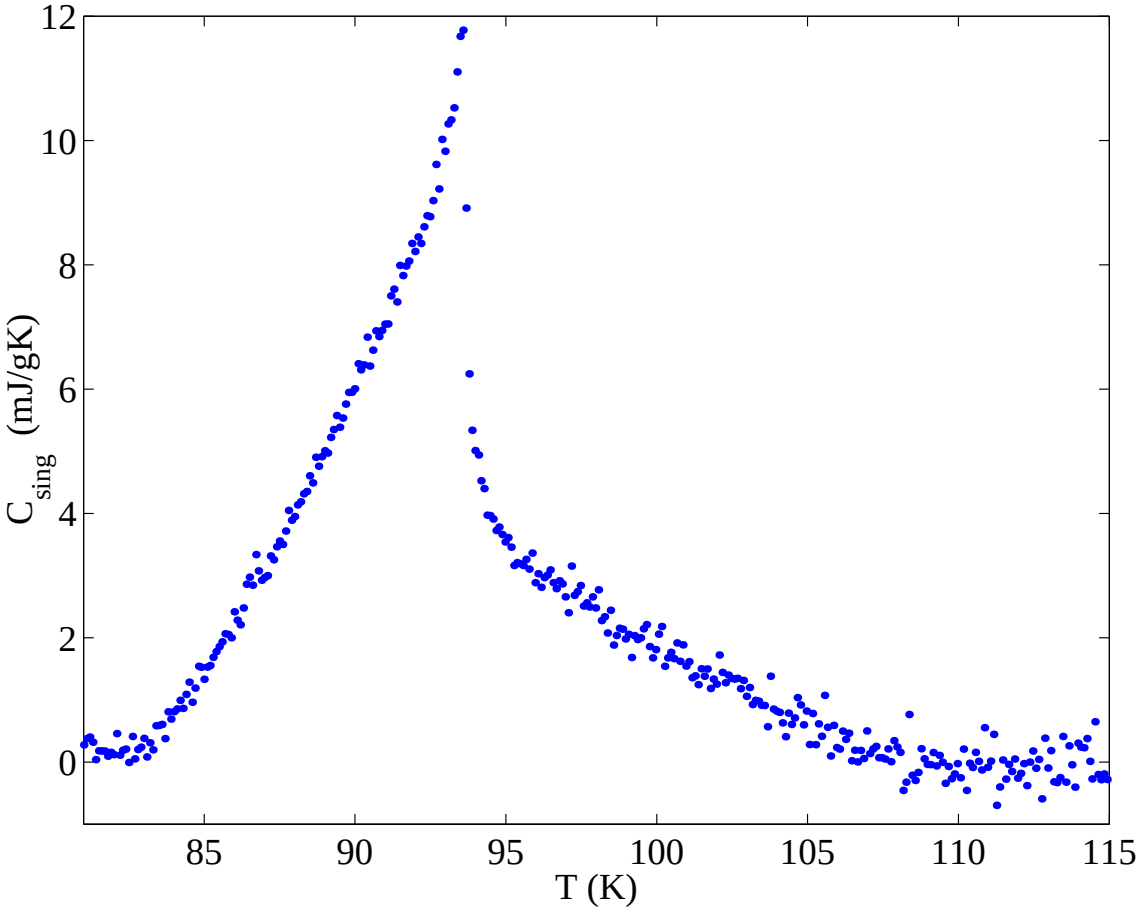

Figure 6.5: Singular part of the specific heat of a YBCO single crystal, after subtracting out C_{ph}. C_{ph} was chosen as the solid line fit from Fig. 6.4.

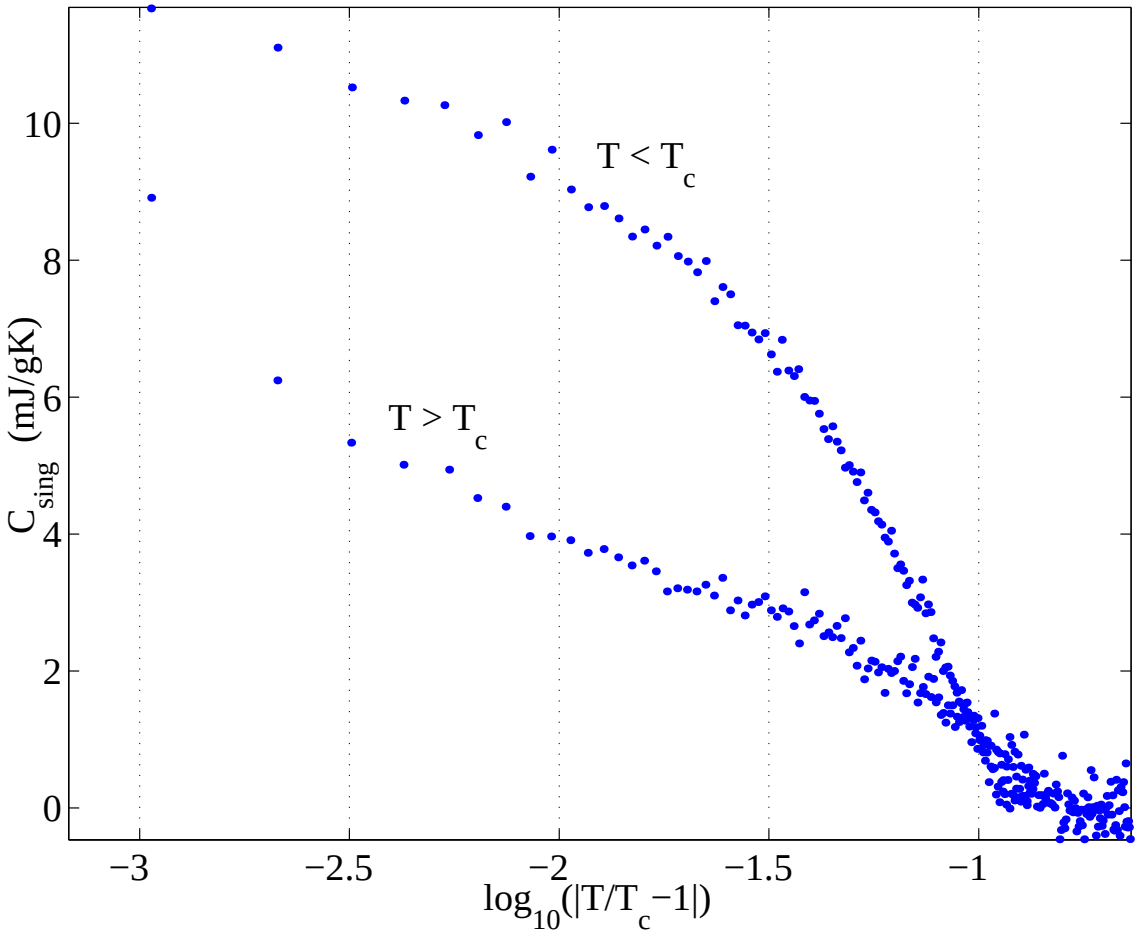

Figure 6.6: Semi-log plot of the singular part of the specific heat of YBCO. When $\log(T/T_c - 1) = -2$, this corresponds to $T_c \pm 1$ K. The data close to T_c look like two parallel lines, as expected, indicating α is very small. Here $T_c = 93.58$ K.

in choosing T_c (at least ± 100 mK, the separation between data points), values from 93.4 K to 93.8 K do not change the following data analysis significantly.

As expected, for temperatures up to about 1 K away from T_c (where $\log(T/T_c - 1) = -2$), the data look like two parallel lines.[3] From this we can infer that α is very small. We recall that $\alpha = 2 - D\nu$ (Eq. 4.40), therefore if $\alpha \approx 0$, then $\nu \approx 0.67$. Already we have general agreement with 3D-XY theory, as seen by other measurements on specific heat[79, 83, 84, 102].

Let us see if we can now fit our data to 3D-XY theory. We recall that the exponent α and the ratio A^+/A^- are well known theoretically and experimentally. Theory predicts[106]

$$\alpha = -0.007 \pm 0.006 \quad \text{and} \quad A^+/A^- = 1.029 \pm 0.013, \tag{6.6}$$

while from experiments on ^{4}He, we expect[55]

$$\alpha = -0.0129 \pm 0.0004 \quad \text{and} \quad A^+/A^- = 1.054 \pm 0.001. \tag{6.7}$$

In our fit, there are many adjustable parameters: α, A^+, A^-, B^+, and B^-. What we would really like to know, however, is if our data agrees with 3D-XY theory, not whether we can fit any number of theories to the data. For this reason, we set $\alpha = -0.013$ and $B^+ = B^-$ as expected from 3D-XY theory. This leaves only three adjustable parameters, A^+, A^-, and B^+. The resulting fit is shown in Fig. 6.7.

In the figure we can see a reasonable fit for $|T - T_c| < 1$ K. This is much wider than predicted[31], but similar to other measurements[79, 78]. In this fit, we constrained $\alpha = -0.013$, but put no restrictions on A^+ and A^-. From the fit in Fig. 6.7 and other fits for different values of T_c and C_{ph}, we find that $A^+/A^- = 1.06 \pm 0.02$, very close to the predicted value, again in agreement with 3D-XY theory. The downturn

[3]Two points very near T_c for $T > T_c$ deviate from these parallel lines. We can see from Fig. 6.5 that these two points correspond to the greatest value of dC/dT, meaning these points are averaged over 200 mK when C varies the most in T, making these points unreliable.

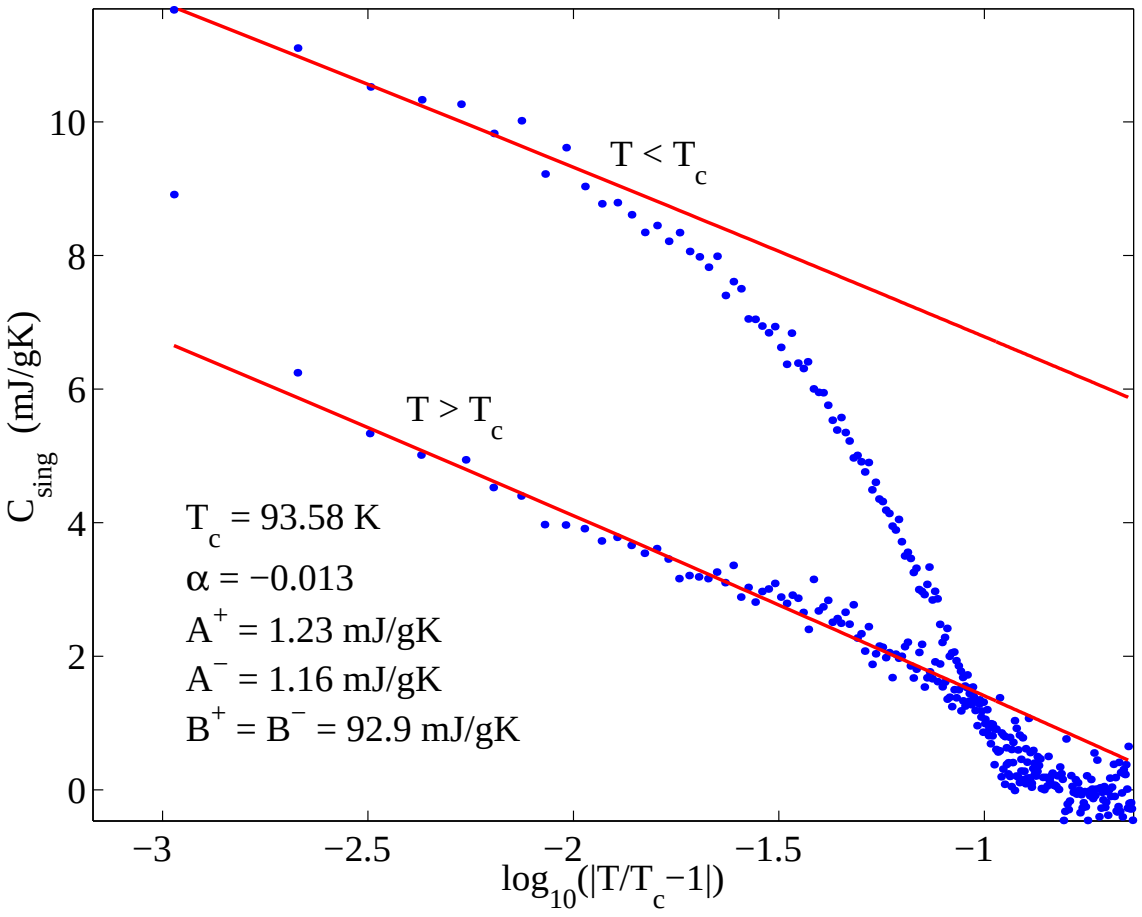

Figure 6.7: Fit of C_{sing} to 3D-XY theory. We have fixed $\alpha = -0.013$, the exponent expected from experiments in ^{4}He[55], and $B^+ = B^-$. The resulting fit parameters are shown in the figure. We see that the ratio $A^+/A^- = 1.06$, close to the expected value.

in C_{sing} for $T < T_c$ has been fit by other researchers by adding Gaussian fluctuations to the fit[78]. Gaussian fluctuations are expected to be significant outside the critical regime.

Finally, we must ask: Is there any way we could make this specific heat data agree with the values for ν we have found in our films and are reported elsewhere? Examining the data, it is highly unlikely that we can fit our data for $\nu > 1$. If $\nu > 1$, then from $\alpha = 2 - D\nu$, $\alpha < -1$. This in turn implies that $C_{sing} \sim |t|^A$, where A is some power greater than one. This means that C_{sing} and $|t|$ will be a straight line on a log-log plot, but not on a semi-log plot. Our trick (Eq. 6.5) only works for $\alpha \approx 0$. This is a major blow against $\nu > 1$.

Because scaling is so flexible, it should not surprise us when the log-log plot as described above looks more-or-less linear, as shown in Fig. 6.8. We can find the exponent α from these fits. However, we must find different values for α above and below T_c, which does not agree with theory. Even assuming these values for α ($\alpha = 0.14$ and $\alpha = 0.3$), the values for ν still do not agree with $\nu > 1$.[4] In fact, the negative slope in Fig. 6.8 implies $\nu \leq \frac{2}{3}$. Any value for $\nu > \frac{2}{3}$ would imply that $\alpha < 0$ giving a positive slope in Fig. 6.8. Thus, the only reasonable values for ν from our data are those from 3D-XY theory or GL theory.

Finally, with so many free parameters, we can force a fit to our data with $\alpha < -1$ (meaning $\nu > 1$). Doing so forces us to choose values such that $A^+/A^- \neq 1.06$ and $B^+ \neq B^-$, in addition to the fact that the fits have higher residuals than the 3D-XY fit with $\alpha = -0.013$. We must conclude that the data simply do not agree with $\nu > 1$.

[4]From this plot, however, it is easy to see why we could fit our data using $\alpha = 0.5$ (GL theory plus fluctuations), as for these values of α, $\nu = 0.66$ and $\nu = 0.57$.

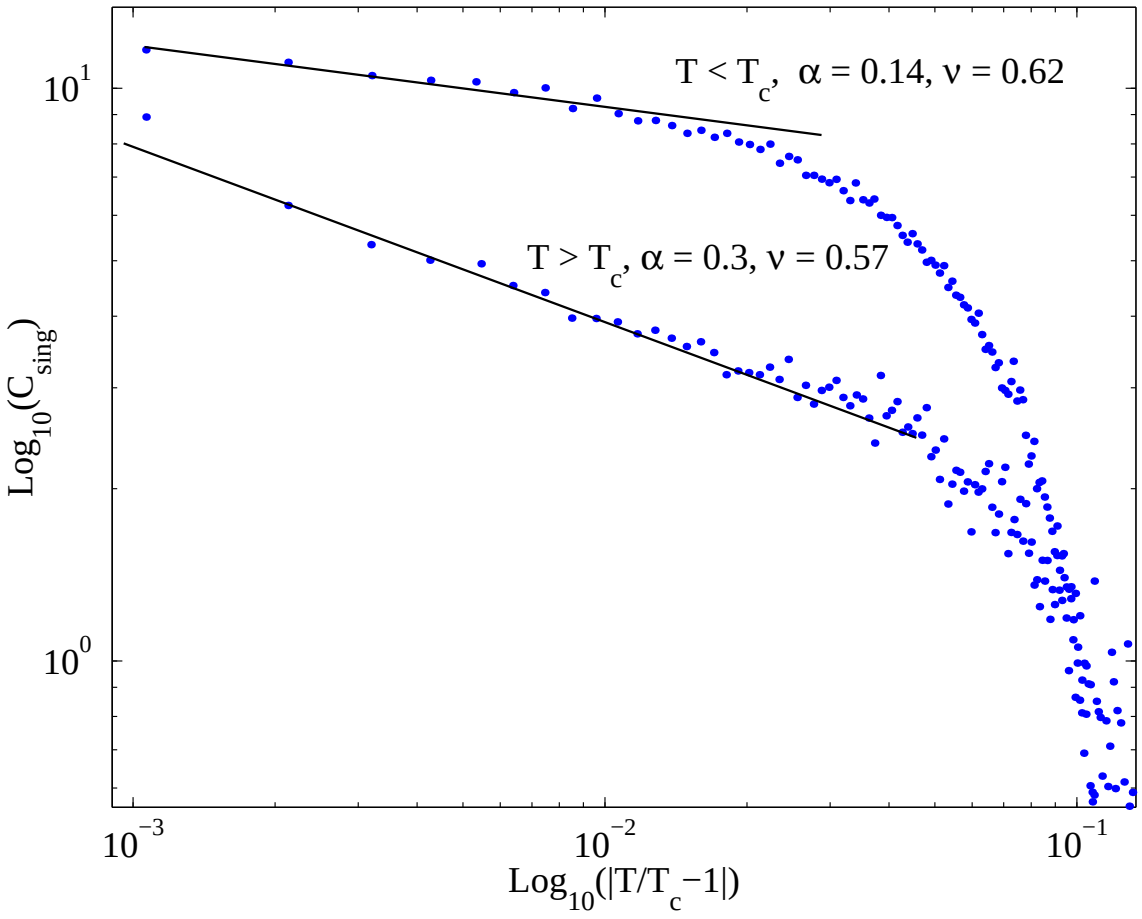

Figure 6.8: Fit of C_{sing} when α is not small. We can see that over the same range in temperature as in Fig. 6.7, the data looks linear. However, we are forced to pick exponents that are not equal above and below T_c, which is not predicted. And even this does not alter the values for ν to agree with the high-current analysis.

6.2 dc Transport in Crystals

It was our hope, and part of the reason we began working with crystals, that we could quickly measure dc transport in crystals to confirm our results regarding finite size effect in films. As is so often the case in experimental physics, the dc transport measurement in crystals proved to be far more difficult than anticipated, and in fact has not been resolved in our lab to date.

In this section, we will present our dc transport measurements on crystals. While, from the measurements, it is clear that a phase transition exists, the data have unexplained problems which preclude analysis of the data.

UBC transport crystals

Along with our specific heat crystal, the UBC generously supplied us with several crystals the rough size and shape for transport measurements. One such crystal was shown in Fig. 2.19. With the electrical contacts placed on the crystal as described in Ch. 2, we measured the crystals. The R vs. T for one crystal, ubc2, we have shown previously in Fig. 2.17. This crystal has dimensions 0.3 mm $\times$ 1 mm $\times$ 100 μm, although the voltage leads are only separated by ≈ 0.7 mm. In Fig. 6.9 we plot the $I-V$ curves for this crystal.

This figure shows very similar behavior to our measurements in films – albeit on a much smaller temperature scale, as the isotherms in Fig. 6.9 are only separated by 10 mK! The highest temperatures are ohmic, changing rapidly to non-linear behavior. However, at the lowest temperatures, we see nearly ohmic behavior (although they look ohmic, $\partial \log V/\partial \log I$ is not precisely 1). This signal should not be present in our $I-V$ curves.

Initially, we attributed this to common mode, as the signal looks similar to that of Fig. 3.5. However, the $I-V$ curves do not line up exactly, as we would expect, and the signal is not quite ohmic. To be safe, we ran the $I-V$ curves again with a

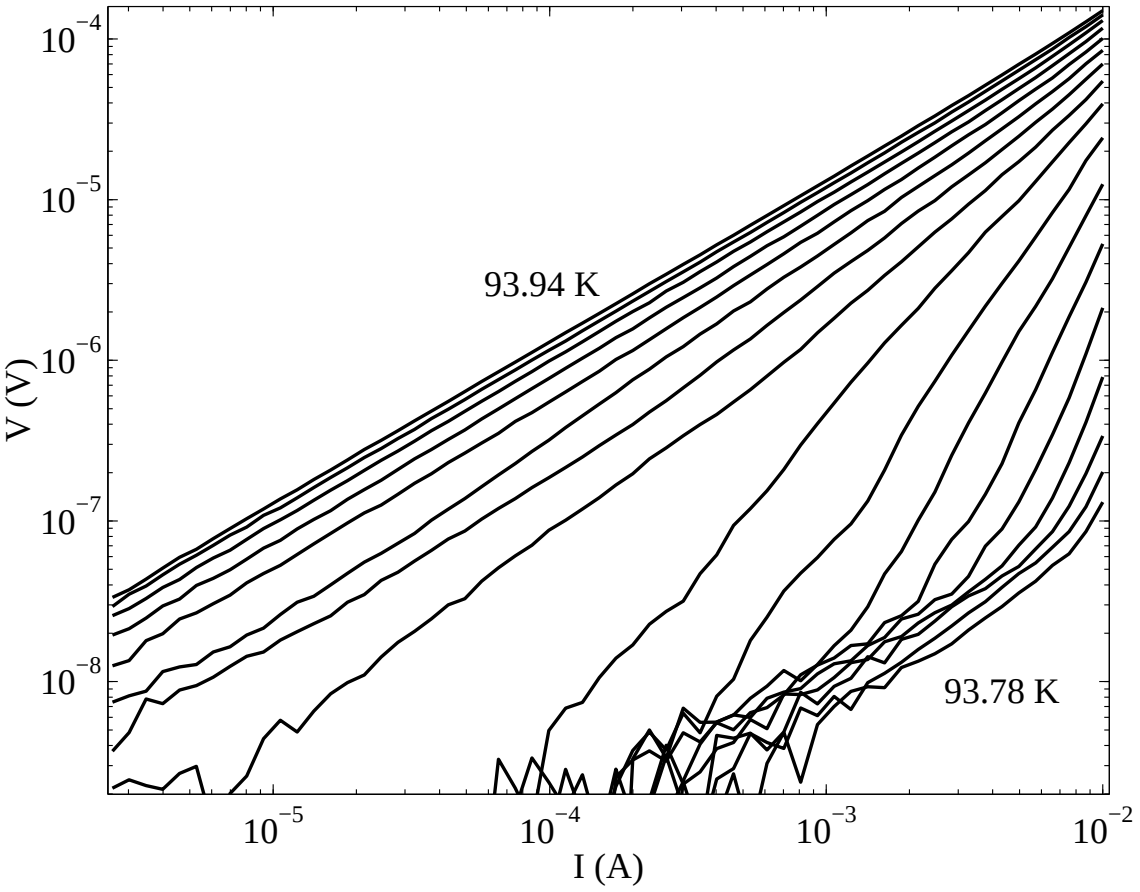

Figure 6.9: $I-V$ curves for crystal ubc2. Much of the behavior is similar to that of films, only on a much narrower temperature scale. Here isotherms are separated by only 10 mK. At the lowest temperatures, we see unexpected nearly-ohmic behavior.

voltmeter with a higher CMRR, with no change in the data, ruling out CMRR as a problem.

The most likely cause is the problem most experimenters have in crystals: non-uniform current density. Our crystal is not exactly rectangular, and a 10% difference from one side to the other might be enough to alter our measurement. This also might not be so noticeable in the films, because in films, although we are applying roughly the same current, the current density in films is many order of magnitude larger than in crystals. If the current density bunches up on the narrower or thinner side of the crystal, this might create the signal we see. Unfortunately, we cannot increase the current in the crystal, as higher currents cause large amounts of heating.

CSR crystals

With the arrival of a new post-doc to our lab came the knowledge of how to grow crystals, as well as several high-quality YBCO crystals. Although Bing Liang's crystals are not on par with the UBC crystals, they are of quality comparable as our films, with $T_c \approx 89$ K and $\Delta T_c \approx 1$ K from the magnetization measurement.

With these crystals, we tried to decrease any effects of non-uniform shape. In order to do so, we glued the crystal to a piece of sapphire. Then, using typical transmission electron microscope techniques, we polished the crystal down in size, making it thinner such that we could pass a larger current density without heating the crystal, while also making sure the sides were parallel. The drawback, of course, was that we lost a good deal of the crystal in the polishing process.

We measured the $I - V$ curves of one of the crystals we polished, bl1a. The crystal was of size 0.8 mm $\times$ 2.5 mm $\times$ 50 μm. We can, in fact, polish it thinner than 50 μm, but the polisher[5] became nervous and stopped at $d \approx 50$ μm. The $I - V$ curves are shown in Fig. 6.10.

[5]The author.

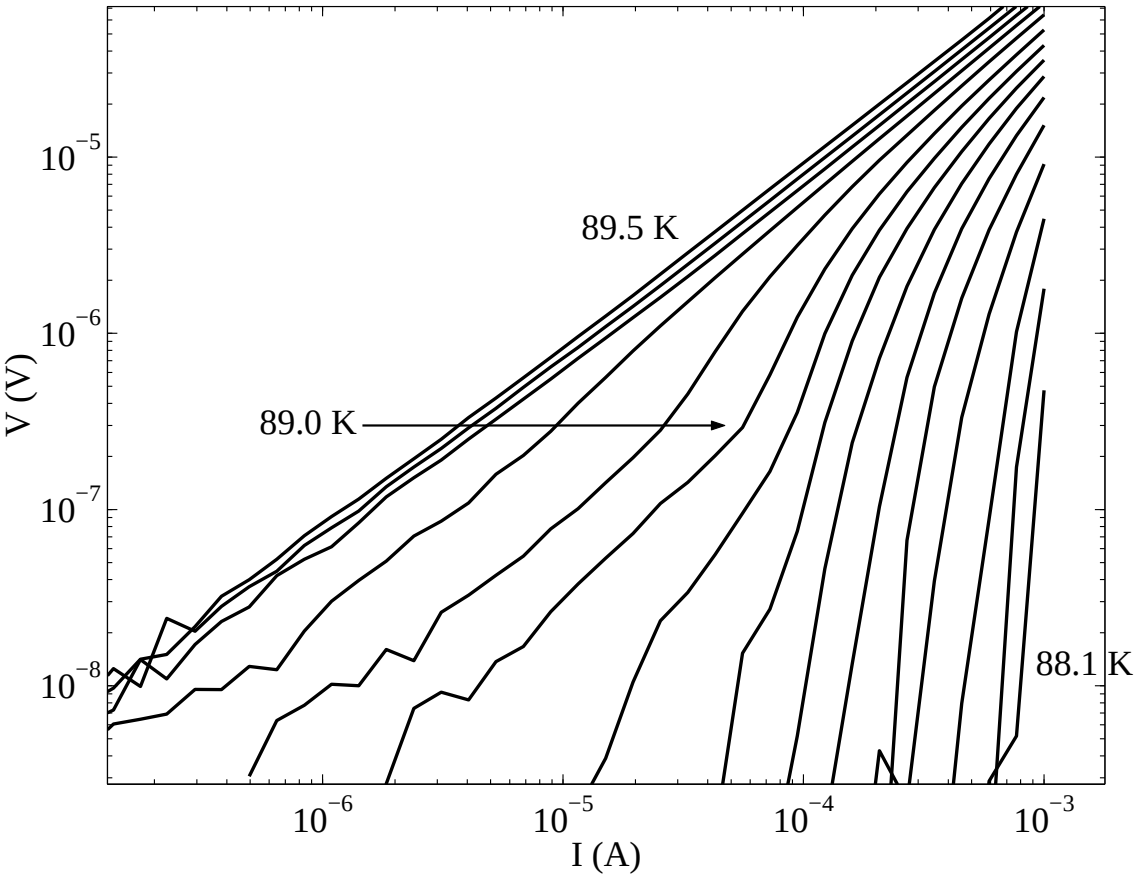

Figure 6.10: $I - V$ curves for crystal bl1a, polished such that we can apply higher current densities. The isotherms are separated by 100 mK. There is still unexplained ohmic behavior, only now in the middle of the $I - V$ curves, at 89.0 K, and in the surrounding isotherms.

It is obvious that this crystal is not on par with the UBC crystals, as here the temperature is lower and the isotherms are separated by 100 mK. Nonetheless, this data looks much more familiar, and similar to the $I - V$ curves from the films. Unfortunately, this data is also marred by the unexplained ohmic tails occurring abruptly in the middle of the non-linear isotherms at 89.0 K, and in the surrounding isotherms.

As yet, we have no explanation for this ohmic behavior. We are currently working to reduce the size of the voltage contacts. Because the gold voltage contacts will be an equipotential surface, their large size may alter the current flow.

Chapter 7

Future Work

Although it would be nice to finish this dissertation with a summary of all we have accomplished (in addition to the summary at the end of Ch. 5), it seems more fitting to end with a list of things yet to be done. We feel there is still much left to be studied, despite the opinions of many researchers who believe that the second-order phase transition in field and in zero field is a done deal.

What follows is a short list of some of the many possible experiments possible.

Finite size effect in field

It would be very interesting to perform the same measurements we have done in zero field in a field. The equations we derived in Ch. 5 should hold for the transition in field, and so we expect to see significant finite size effects not only in the zero-field transition, but also in the vortex-glass transition. Perhaps we can look at the transition in field to determine the exponents of the vortex-glass transition with greater accuracy. In fact, preliminary measurements indicate $z \approx 2$, a far cry from the consensus value for the transition of $z \approx 5$.

There is work, also, that predicts that the magnetic field will create a finite size effect[100] similar to that created by the thickness of the film. It would be a relatively easy task to investigate these possible effects, and make a graph similar to that of Fig. 5.39 as a function of field or thickness, depending on what is actually

creating the finite size effect.

ac specific heat

One of the problems with our data on specific heat is the fact that it is simply not sensitive enough. We would like to improve the data, and the simplest method to do so is ac specific heat.

Our stages are similar to those used by other researchers to measure ac specific heat[102], and with some adjustments to the electronics, it should be possible to decrease the error in our measurement by an order of magnitude or more. This improvement would afford us several opportunities. We would be able to wade into the $\nu = 0.5$ or $\nu = 0.67$ debate, and we would be able to fit our data allowing more parameters to vary. Most significantly, the increased sensitivity would allow us to take the derivative of the data numerically without introducing large uncertainties in the data. This should allow us to see the exponent without any further data analysis or fits.

dc transport in crystals

It is curious that the future work should have the same title as a section of current work presented here. However, there are many unresolved problems in this experiment. Is the current uniform? Can we apply a larger current density? Although we seem to have made some improvements by polishing the crystal to a thinner, more uniform size, there are still many experiments to run. The fundamental question still remains: Do the data agree with 3D-XY theory, as reported[46], and are they immune to finite seize effects, as we predict?

We have made a strong claim that finite size effects obscure the transition. If we are correct, then the same transition in a crystal should be free from these problems. This is the most fundamental question that needs to be answered regarding our work presented here.

Microwave conductivity

As mentioned at the beginning of Ch. 5, Strachan made preliminary measurements of $\sigma(\omega)$ at frequencies from 45 MHz to 45 GHz. These measurements offer us the chance to measure T_c, ν, and z on the same sample in two different experiments. As such, though the data analysis of the microwave experiment is non-trivial, it is a very useful experiment.

BIBLIOGRAPHY

[1] H. K. Onnes, Leiden Comm. **120b, 122b, 124c** (1911).

[2] T. P. Orlando and K. A. Delin, *Foundations of Applied Superconductivity* (Addison-Wesley, Reading, MA, 1991).

[3] M. Tinkham, *Introduction to Superconductivity*, 2nd ed. (McGraw-Hill, New York, 1996).

[4] D. L. Goodstein, *States of Matter* (Dover, Mineola, NY, 2002).

[5] J. G. Bednorz and K. A. Müller, Zeit. Phys. B **64**, 189 (1986).

[6] M. K. Wu, J. R. Ashburn, C. J. Torng, P. H. Hor, R. L. Meng, L. Gao, Z. J. Huang, Y. Q. Wang, and C. W. Chu, Phys. Rev. Lett. **58**, 908 (1987).

[7] S. Hikami, T. Hiriai, and S. Kagoshima, Jpn. J. Appl. Physics **26**, L314 (1987).

[8] Z. X. Zhao, L. Q. Chen, Q. S. Yang, Y. Huang, G. Chen, R. M. Tang, G. Liu, C. G. Cui, L. Chen, L. H. Wang, S. Q. Guo, S. L. Li, and J. Q. Bi, Kexue Tongbao **33**, 661 (1987).

[9] M. P. A. Fisher, Phys. Rev. Lett. **62**, 1415 (1989).

[10] D. S. Fisher, M. P. A. Fisher, and D. A. Huse, Phys. Rev. B **43**, 130 (1991).

[11] D. A. Huse, D. S. Fisher, and M. P. A. Fisher, Nature **358**, 553 (1992).

[12] D. R. Strachan, M. C. Sullivan, P. Fournier, S. P. Pai, T. Venkatesan, and C. J. Lobb, Phys. Rev. Lett. **87**, 067001 (2001).

[13] N. W. Ashcroft and N. D. Mermin, *Solid State Physics* (Harcourt Brace College Publishers, Philadelphia, 1976).

[14] R. Liang, D. A. Bonn, and W. N. Hardy, Physica C **304**, 105 (1998).

[15] D. R. Strachan, *The Superconducting Transition of YBCO*, PhD thesis, University of Maryland, 2002.

[16] W. F. McClune, *Powder Diffraction File* (International Centre for Diffraction Data, Swarthmore PA, 1991).

[17] Y. Dagan, private communication.

[18] R. Liang, P. Dosanjh, D. J. Barr, J. F. Carolan, and W. N. Hardy, Physica C **195**, 51 (1992).

[19] R. H. Koch, V. Foglietti, W. J. Gallagher, G. Koran, A. Gupta, and M. P. A. Fisher, Phys. Rev. Lett. **63**, 1511 (1989).

[20] P. Wöltgens, C. Dekker, R. Koch, B. Hussey, and A. Gupta, Phys. Rev. B **52**, 4536 (1995).

[21] J. M. Repaci, *The Superconducting Phase Transition of thin YBCO films*, PhD thesis, University of Maryland, 1997.

[22] A. Junod, J. Phys. E-Sci. Instrumen. **12**, 945 (1979).

[23] P. F. Sullivan and G. Seidel, Phys. Rev. **173**, 679 (1968).

[24] R. Bachmann, F. DiSalvo, T. H. Geballe, R. L. Greene, R. E. Howard, C. N. King, H. C. Kirsch, K. N. Lee, R. E. Schwall, H.-U. Thomas, and R. B. Zubeck, Review of Scientific Instruments **43**, 205 (1972).

[25] Y. Kraftmakher, Phys. Rep. **356**, 1 (2002).

[26] V. N. Smolyaniniva, *Thermal and Magnetic Properties of Manganese Oxides*, PhD thesis, University of Maryland, 1999.

[27] K. A. Moler, *Specific Heat of Cuprate Superconductors*, PhD thesis, Stanford University, 1995.

[28] H. Balci, *Specific Heat and Nernst Effect of Electron-Doped Cuprate Superconductors*, PhD thesis, University of Maryland, 2003.

[29] V. L. Ginzburg and L. D. Landau, Zh. Eksperim. i. Teor. Fiz. **20**, 1064 (1950).

[30] J. Bardeen, L. Cooper, and J. R. Schrieffer, Phys. Rev. **108** (1957).

[31] C. J. Lobb, Phys. Rev. B **36**, 3930 (1987).

[32] C. J. Lobb, private communication.

[33] W. J. Skocpol and M. Tinkham, Rep. Prog. Phys. **38**, 1049 (1975).

[34] G. D. Zally and J. M. Mochel, Phys. Rev. B **6**, 4142 (1972).

[35] D. Naugle and R. E. Glover, Phys. Lett. **28A**, 611 (1969).

[36] V. L. Ginzburg, Fiz. Tverd. Tela **2**, 2031 (1960).

[37] P. M. Chaikin and T. C. Lubensky, *Principles of Condensed Matter Physics* (Cambridge University press, 1995).

[38] L. P. Kadanoff, W. Gotze, D. Hamblen, R. Hecht, E. A. S. Lewis, V. V. Palciaus, M. Rayl, J. Swift, D. Aspnes, and J. Kane, Rev. Mod. Phys. **39**, 395 (1967).

[39] J. J. Binney, N. J. Dowrick, A. J. Fisher, and M. E. J. Newman, *The Theory of Critical Phenomena: An Introduction to the Renormalization Group* (Oxford University Press, New York, 1995).

[40] S.-K. Ma, *Modern Theory of Critical Phenomena* (W. A. Benjamin, Inc., Reading, MA, 1976).

[41] J. C. LeGuillou and J. Zinn-Justin, Phys. Rev. B **21**, 3976 (1980).

[42] D. Z. Albert, Phys. Rev. B **25**, 4810 (1982).

[43] C. Kittel and H. Kroemer, *Thermal Physics*, 2nd ed. (W.H. Freeman and Co., New York, 1995).

[44] P. C. Hohenberg and B. I. Halperin, Rev. Mod. Phys **49**, 435 (1977).

[45] D. R. Strachan, M. C. Sullivan, and C. J. Lobb, Probing the limits of superconductivity, in *Superconductivity and Related Oxides: Physics and Nanoengineering V*, edited by I. Bozovic and D. Pavuna Vol. 4811, pp. 65–77, SPIE, 2002.

[46] N. C. Yeh, W. Jiang, D. S. Reed, U. Kriplani, and F. Holtzberg, Phys. Rev. B **47**, 6146 (1993).

[47] J. Lidmar, Phys. Rev. Lett. **91**, 097001 (2003).

[48] S. N. Coppersmith, M. Inui, and P. B. Littlewood, Phys. Rev. Lett. **64**, 2585 (1990).

[49] H. S. Bokil and A. P. Young, Phys. Rev. Lett. **74**, 3021 (1995).

[50] C. Wengel and A. P. Young, Phys. Rev. B **54**, R6869 (1996).

[51] C. Reichhardt, A. van Otterlo, , and G. T. Zimányi, Phys. Rev. Lett. **84**, 1994 (2000).

[52] D. A. Huse, M. Fisher, and D. S. Fisher, Nature **358**, 6387 (1992).

[53] D. R. Strachan, private communication.

[54] J. A. Lipa, D. R. Swanson, J. A. Nissen, T. C. P. Chui, and U. E. Israelsson, Phys. Rev. Lett. **76**, 944 (1996).

[55] J. A. Lipa and T. C. P. Chui, Phys. Rev. Lett. **51**, 2291 (1983).

[56] R. H. Koch, V. Foglietti, and M. P. A. Fisher, Phys. Rev. Lett. **64**, 2586 (1990).

[57] Y. Ando, H. Kubota, and S. Tanaka, Phys. Rev. Lett. **69**, 2851 (1992).

[58] P. J. M. Wöltgens, C. Dekker, J. Swste, and H. W. de Wijn, Phys. Rev. B **48**, 16826 (1993).

[59] C. Dekker, W. Eidelloth, and R. H. Koch, Phys. Rev. Lett. **68**, 3347 (1992).

[60] T. K. Worthington, E. Olsson, C. S. Nichols, T. M. Shaw, and D. R. Clarke, Phys. Rev. B **43**, 10538 (1991).

[61] M. Charalambous, R. H. Koch, T. Masselink, T. Doany, C. Feild, and F. Holtzberg, Phys. Rev. Lett. **75**, 2578 (1995).

[62] M. Charalambous, R. Koch, A. D. Kent, and W. T. Masselink, Phys. Rev. B **58**, 9510 (1997).

[63] M. Friesen, J. Deak, L. Hou, and M. McElfresh, Phys. Rev. B **54**, 3525 (1996).

[64] L. Hou, J. Deak, P. Metcalf, and M. McElfresh, Phys. Rev. B **50**, 7226 (1994).

[65] P. L. Gammel, L. F. Schneemeyer, and D. J. Bishop, Phys. Rev. B **66**, 953 (1991).

[66] M. A. Howson, N. Overend, I. D. Lawrie, and M. B. Salamon, Phys. Rev. B **51**, 11984 (1995).

[67] M. B. Salamon, J. Shi, N. Overend, and M. A. Howson, Phys. Rev. B **47**, 5520 (1993).

[68] J. M. Roberts, B. Brown, J. Tate, X. X. Xi, and S. N. Mao, Phys. Rev. B **51**, 15281 (1995).

[69] N. Yeh, D. S. Reed, W. Jiang, U. Kriplani, C. C. Tsuei, C. C. Chi, and F. Holtzberg, Physica C **185-189**, 1799 (1991).

[70] H. Yamasaki, K. Endo, S. Kosaka, S. Y. M. Umeda, and K. Kajimura, Phys. Rev. B **50**, 12959 (1994).

[71] J. M. Roberts, B. Brown, B. A. Hermann, and J. Tate, Phys. Rev. Lett. **49**, 6890 (1994).

[72] K. Moloni, M. Friesen, S. Li, V. Souw, P. Metcalf, L. Hou, and M. McElfresh, Phys. Rev. Lett. **78**, 3173 (1997).

[73] N. Yeh, D. S. Reed, W. Jiang, U. Kriplani, F. Holtzberg, A. Gupta, B. D. Hunt, R. P. Vasquez, M. C. Foote, and L. Bajuk, Phys. Rev. B **45**, 5654 (1992).

[74] B. Brown, Phys. Rev. B **61**, 3267 (2000).

[75] P. V. de Haan, G. Jakob, and H. Adrian, Phys. Rev. B **60**, 12443 (1999).

[76] P. V. de Haan, G. Jakob, and H. Adrian, Physica C **341-348**, 1387 (2000).

[77] J. M. Repaci, C. Kwon, Q. Li, X. Jiang, T. Venkatessan, R. E. Glover, III, C. J. Lobb, and R. S. Newrock, Phys. Rev. B **54**, R9674 (1996).

[78] V. Pasler, P. Schweiss, C. Meingast, B. Obst, H. Wühl, A. I. Rykov, and S. Tajima, Phys. Rev. Lett. **81**, 1094 (1998).

[79] N. Overend, M. A. Howson, and I. D. Lawrie, Phys. Rev. Lett. **72**, 3238 (1994).

[80] S. E. Inderhees, M. B. Salamon, J. P. Rice, and D. M. Ginsberg, Phys. Rev. Lett. **66**, 232 (1991).

[81] V. Breit, P. Schweiss, R. Hauff, H. Wühl, H. Claus, H. Rietschel, A. Erb, and G. MüllerVogt, Phys. Rev. B **52**, R15727 (1995).

[82] Z. H. Lin, G. C. Spalding, A. M. Goldman, B. F. Bayman, and O. T. Valls, Europhys. Lett. **32**, 573 (1995).

[83] G. Mozurkewich, M. B. Salamon, and S. E. Inderhees, Phys. Rev. B **46**, 11914 (1992).

[84] M. Roulin, A. Junod, and E. Walker, Physica C **260**, 257 (1996).

[85] S. Kamal, D. A. Bonn, N. Goldenfeld, P. J. Hirschfeld, R. Liang, and W. N. Hardy, Phys. Rev. Lett. **73**, 1845 (1994).

[86] W. J. Skocpol, M. R. Beasley, and M. Tinkham, J. Appl. Phys. **45**, 4054 (1974).

[87] V. B. Efimov and L. P. Mezhov-Deglin, Low Temp. Phys. **23**, 204 (1997).

[88] M. Matsukawa, T. Mizukoshi, K. Noto, and Y. Shiohara, Phys. Rev. B **53**, R6034 (1996).

[89] S. J. Hagen, Z. Z. Wang, and N. P. Ong, Phys. Rev. B **40**, 9389 (1989).

[90] N.-C. Yeh, private communication.

[91] J. S. Moodera, R. Meservey, J. E. Tkaczyk, C. X. Hao, G. A. Gibson, and P. M. Tedrow, Phys. Rev. B **37**, 619 (1988).

[92] H. C. Lee, R. S. Newrock, D. B. Mast, S. E. Hebboul, J. C. Garland, and C. J. Lobb, Phys. Rev. B **44**, R921 (1991).

[93] J. B. Johnson, Phys. Rev. **32**, 97 (1928).

[94] H. Nyquist, Phys. Rev. **32**, 110 (1928).

[95] A. J. Berkley, *A Josephson Junction Qubit*, PhD thesis, University of Maryland, 2003.

[96] T. Frederiksen, private communication.

[97] C. Dekker, R. Koch, B. Oh, and A. Gupta, Physica C **185-189**, 1799 (1991).

[98] A. Sawa, H. Yamasaki, Y. Mawatari, H. Obara, M. Umeda, and S. Kosaka, Phys. Rev. B **58**, 2868 (1996).

[99] Z. L. Xiao, E. Y. Andrei, Y. Paltiel, E. Zeldov, P. Shuk, and M. Greenblatt, Phys. Rev. B **65**, 094511 (2002).

[100] T. Schneider, arXiv:condmat/0210702 (2002).

[101] M. B. Salamon, J. Shi, N. Overend, and M. A. Howson, Phys. Rev. B **47**, 5520 (1993).

[102] M. Charalambous, O. Riou, P. Gandit, B. Billon, P. Lejay, J. Chaussy, W. N. Hardy, D. A. Bonn, and R. Liang, Phys. Rev. Lett. **83**, 2042 (1999).

[103] J. W. Loram, K. A. Mirza, J. R. Cooper, and W. Y. Liang, Phys. Rev. Lett. **71**, 1740 (1993).

[104] F. W. de Wette, A. D. Kulkarni, J. Prade, U. Schröder, and W. Kress, Phys. Rev. Lett. **42**, 6707 (1990).

[105] R. Shaviv, J. E. F. Westrum, R. J. C. Brown, M. Sayer, X. Yu, and R. D. Weir, J. Chem. Phys. **92**, 6794 (1990).

[106] J. Zinn-Justin, *Quantum Field Theory and Critical Phenomena* (Oxford University Press, Oxford, 1989).